Interplay of Spin-Orbit Coupling and Electronic Coulomb Interactions in Strontium Iridate Sr2IrO4

Cyril Martins

ÉCOLE POLYTECHNIQUE
ParisTech

Thèse présentée pour obtenir le grade de

DOCTEUR DE L'ECOLE POLYTECHNIQUE

Spécialité : Physique des Matériaux et Milieux Denses

Cyril MARTINS

Couplage Spin-Orbite et Interaction de Coulomb dans l'Iridate de Strontium Sr_2IrO_4

Interplay of Spin-Orbit Coupling and Electronic Coulomb Interactions in Strontium Iridate Sr_2IrO_4

Soutenue publiquement le 26 Novembre 2010 à l'Ecole Polytechnique
devant le jury composé de :

Président du jury	:	**Luca**	**PERFETTI**	Ecole Polytechnique, Palaiseau
Rapporteurs	:	**Alexander**	**LICHTENSTEIN**	Hamburg Universität
		Marcelo	**ROZENBERG**	Université Paris-Sud, Orsay
Directrice de thèse	:	**Silke**	**BIERMANN**	Ecole Polytechnique, Palaiseau

Cyril MARTINS

Couplage Spin-Orbite et Interaction de Coulomb dans l'Iridate de Strontium Sr_2IrO_4

Interplay of Spin-Orbit Coupling and Electronic Coulomb Interactions in Strontium Iridate Sr_2IrO_4

2010

Centre de Physique Théorique (CPhT)
Ecole Polytechnique
France

Remerciements

Il est assez paradoxal que les premières (et peut-être seules) lignes que tu liras, ô curieux et/ou courageux lecteur, correspondent en fait pour moi, auteur, aux dernières pages que j'ajouterai dans ce recueil. Et c'est avec plaisir que je retrouve ma chère langue de Molière pour parachever ce qui a été une longue, et souvent difficile, entreprise.

En ce jour, l'heure est pour moi au bilan, je contemple avec une certaine satisfaction, mais aussi une petite pointe de nostalgie, le chemin parcouru pendant ces trois dernières années et que ces quelques 200 pages ont pour vocation de résumer.

En ce jour, il y a bien sûr une grande fierté qui m'emplit quand je relis le titre "docteur de l'Ecole Polytechnique" apposé sur la première page de cet ouvrage mais il y a aussi et surtout un souvenir, une image qui me revient en tête: celle d'une assemblée debout en amphi Carnot un vendredi après-midi de novembre, le sourire aux lèvres, le regard soulagé et heureux, faisant résonner la salle de leurs applaudissements chaleureux. Cinq mois se sont peut-être écoulés depuis, mais je garde encore intact en ma mémoire et dans mon coeur le sentiment que j'ai ressenti à ce moment-là.

Et en ce jour, c'est à chacune de ces mains qui battaient l'air avec enthousiasme, mais aussi à celles qui n'ont pu être là mais ont tout autant participé à ma réussite, que je voudrais témoigner ma reconnaissance.

Je tiens à remercier tout d'abord Silke, ma directrice de thèse, pour m'avoir donné l'opportunité de travailler dans un contexte scientifique de grande qualité pendant ces trois années. Merci d'avoir cru en "ce jeune Supaéro qui avait abandonné les avions pour la mécanique quantique" dès le premier jour et merci surtout pour ton investissement et l'intérêt que tu as toujours porté à mon travail, même jusqu'à des heures incroyablement tardives. Merci aussi pour ton encadrement malgré tes fréquents et nombreux déplacements et pour ton enthousiasme communicatif, même dans les moments de doute où mon pessimisme tendait à prendre le dessus.

Je tiens également à remercier mes rapporteurs Alexander Lichtenstein et Marcelo Rozenberg ainsi que Luca Perfetti qui tenait le rôle de président du jury. Vous m'avez tous les trois fait un grand honneur en acceptant d'être présents à ma soutenance et en prenant le temps de lire attentivement mon manuscrit. Vos questions et remarques, aussi difficiles fussent-elles sur le moment, m'ont été autant de précieux moyens pour améliorer mon travail et approfondir encore mes connaissances dans le domaine de la physique des matériaux.

Ma reconnaissance va aussi à tous les membres du groupe Matière Condensée du Centre de Physique Théorique (CPhT) de l'Ecole Polytechnique, que j'ai pu côtoyer depuis septembre 2007. Chacun d'entre vous a contribué à sa manière au résultat que vous voyez aujourd'hui.

En premier lieu, je souhaite remercier Antoine Georges, notre "chef de labo", avec qui j'aurais aimé encore plus intéragir. Merci pour m'avoir accueilli au sein de cet équipe formidable, pour m'avoir dispensé tes cours à l'ENS, l'X ou au Collège de France et pour avoir toujours su me mettre à l'aise au sein du laboratoire.

Un grand merci aussi et surtout à tous mes collègues, avec qui j'ai partagé mes doutes, mes (fausses) joies, mes galères et mes découvertes au quotidien durant ces trois ans. Ce fut un véritable plaisir de travailler, collaborer, échanger mais aussi et surtout de rire et s'amuser avec vous. La grande convivialité que vous faites (ou avez fait) régner au labo a été un élément fondamental dans mon épanouissement, au moins autant que votre enthousiasme et votre passion pour la physique que vous me transmettiez. Merci donc à Corinna Kollath, Veronica Vildosola, Donat Adams, Peter Barmettler, Pablo Cornaglia, Xiaoyu Deng, Michel Ferrero, Hartmut Hafermann, Igor Krivenko, Lorenzo de Leo, Luca de Medici, Olivier Parcollet, Dario Poletti, Alexander Poteryaev et Leonid Pourovskii.

Merci à mes prédécesseurs Jan et Lam pour leur exemple et leurs utiles conseils. Merci à mes stagiaires Matthieu et Samuel. Merci à Loïg, mon compagnon de route (et successeur) avec qui j'ai "senti la ville" de Tokyo, découvert la face cachée de L.A. (Ah, Venice Beach by night !) et surtout traversé le désert (de Californie. Il faudra qu'on retourne voir les champs de coton d'ailleurs !).

Enfin, un immense Merci au quatuor de post-docs qui m'ont énomément aidé et soutenu dans mes travaux et dans la rude tâche qu'a été la rédaction de ce manuscrit. Grazie Mille à Michele pour ton bel accent chantant qui me faisait voyager durant tes coups de téléphone interminables mais aussi et surtout pour tes nombreux conseils et ton écoute. Vielen Dank à Markus pour tes "réponses à tout sur tout et bien plus encore" et ton fameux "Pole Pole" qui m'a remonté le moral en septembre. Hvala à Jernej pour ton optimisme débordant. Grâce à toi, j'ai appris que les problèmes pouvaient toujours devenir aussi simples qu'un "Ciao Ragazzi". Merci à Jean-Sébastien pour ton accent Québecois qui me fera toujours rêver et pour l'efficacité de tes recherches sur Internet (surtout quand il ne s'agit pas de physique !).

Mais le CPhT ne se résume pas qu'au groupe de Matière Condensée. Je tiens à remercier aussi nos quatre secretaires (en particulier Fadila et Florence) et nos trois informaticiens (tout spécialement Stéphane) sans qui le labo ne fonctionnerait pas aussi bien.

Je remercie aussi chaleureusement Christoph Kopper qui m'a permis de peaufiner mes connaissances en physique mathématique et m'a fourni un soutien financier pour la fin de ma thèse.

Merci aux membres du groupe Hautes Energies pour "leurs discussions quotidiennes en anglais dans la salle café, si animées et si distrayantes". Je remercie enfin Patrick Mora, le directeur du CPhT, et Marios Petropoulos du groupe des Cordes pour leurs signatures annuelles et leurs conseils lors des renouvellements d'allocation de bourse de thèse à chaque automne.

A ce sujet, merci à l'Ecole Doctorale (EDX) pour son soutien financier pendant ces trois ans à travers l'allocation internationale de thèse Gaspard Monge ainsi que pour l'allocation post-doctoral de l'X qui m'a été atribuée et me permet de poursuivre actuellement mes recherches. Plus particulièrement, merci à Fabrice et Audrey pour leur disponibilité et leur écoute.

Je souhaite enfin exprimer toute ma gratitude envers mes "sensei" Ferdi Aryasetiawan, Takashi Miyake, Rei Sakuma et Masatoshi Imada qui m'ont accueilli et fait découvrir leur culture lors de mes deux séjours au Japon en 2005 et 2006. Plus encore, je leur suis très reconnaissant pour m'avoir accueilli en stage post-doctoral depuis février et pour m'avoir aidé bien au delà de leurs attributions pendant ce séjour (tout particulièrement pendant les jours qui ont suivi le grand séisme de Sendaï). Collaborer avec vous est un grand plaisir et une source constante d'enrichissement, j'espère de tout coeur pouvoir retourner au pays du Soleil Levant très bientôt pour poursuivre nos travaux ensemble "de vive voix".

Mes derniers mots iront à tous ces gens pour qui les pages qui suivent demeureront sûrement un royaume quasi-incompréhensible mais qui ont contribué par leur soutien quotidien à cette réussite bien plus qu'ils ne peuvent l'imaginer.

Merci à Nicolas mon Binôme et Cyril mon alter ego. Merci à tous mes amis "râleurs" de Supaéro: Alexis l'improvisateur Toulousaing, Damien le financier devenu contrôleur aérien, les Vernonais Benoît

et Julien, ce sacré Charles, Jérôme l'Alsacien, les deux Romain de Paris et Berlin. Merci à Sébastien l'astrophysicien expatrié et sa petite femme Charlotte (revenez nous vite des US !), à Pascal et Angela mon couple de "geeks" préféré. Mes pensées vont aussi à JC, notre grand montagnard, j'aurais aimé pouvoir trinquer aussi avec toi à la fin de ma thèse.

Merci à mon Québécois Olivier qui, je crois, est le seul à comprendre mes divagations quantiques et à mes compagnons de prépa qui sont aujourd'hui dans la même situation que moi il y a quelques mois : Olivier le Londonien qui m'a fait découvrir l'X sous d'autres aspects, Baptiste et Damien, les matheux dont j'attends les soutenances avec impatience.

Merci à Cécile, Dominique Devernay, Christian Teichteil et Emmanuel Fromager, Pierre Pujol et David Dean pour m'avoir lancer dans cette grande aventure en me faisant partager votre passion au cours de ma scolarité.

Merci aux Xdoc et au Binet Impro de l'X qui m'ont accueilli les bras ouverts en 2007. Merci à la troupe OnOff pour sa joie, sa bonne humeur et son talent. Grâce à vous, j'ai pu continuer à cultiver le plaisir d'improviser sur scène et j'ai même pu brûler les planches à Paris... OnOff un jour, OnOff toujours...

Je termine ces remerciements avec ces personnes qui ont souffert et vibré tout autant, voire même plus, que moi pendant ces trois années. Ceux dont le soutien étaient là quoiqu'il arrive, et ceux dont les applaudissements résonnaient le plus fortement à mes oreilles en ce vendredi 26 novembre. A eux, je veux tirer mon chapeau et les mots me manquent pour vous dire à quel point vous compter pour moi et à quel point la saveur de la réussite n'aurait pas été la même sans vous. Merci à Papa, Maman, Jul, Val, Papys et Mamies ainsi qu'à tout le reste de la famille. Merci à vous tous et désolé si ces pages demeurent "une énigme" et ne vous aident pas plus à répondre à la fameuse question "Mais sur quoi tu travailles alors?" =)

Et non, je ne t'ai pas oubliée. Toi qui a dû me supporter tous les jours depuis septembre 2007 (avec parfois barbe et mauvaise humeur), qui m'a entouré de ton amour et de ton soutien à chaque instant, qui est venue me chercher à 3h00 du matin au labo en octobre et se demande encore si on écrit "plane waves" ou "planewaves". Merci à ce cours d'anglais du 10 septembre 2007 qui nous a permis de se rencontrer et merci à toi d'être là auprès de moi tout simplement. Spassiba Bolchoï ma Taniouchka.

le 26 avril 2011, à Palaiseau
Cyril M.

Introduction

Solid state physics is certainly the physical science which has the most impact on our daily life. From the fabrication of the first transistor in 1947 to the discovery of giant magneto-resistance (GMR) in 1988 [18, 22], the discoveries made in this field have led to numerous technological and industrial applications. Current telecommunication and computing devices would not exist without the development of condensed matter physics. Even after all these years, solid state research still remains extremely active as many new applications will surely emerge from a better understanding of high-temperature superconductors, spintronics devices and carbon nanotubes, to only name a few.

This fast-pace technological development would not have been possible without the joint effort of innovative experiments and good theories. Actually, theoretical condensed matter physics has kept busy some of the greatest minds of our century. Indeed, understanding the large realm of phenomena displayed by solid state materials requires the development of new sophisticated theories. This is true even for the "simplest" of phenomenon. A good example of this false simplicity is given by insulating materials. Experimentally, insulators are merely compounds which cannot conduct electricity, but are they all insulating for the same reasons?

The first theory developed to explain insulating behavior was based on band theory. In this framework, electrons are described as independent particles moving in an effective potential induced by the crystal lattice and by their fellow electrons. The system can then be understood in terms of "*energy bands*" and an insulating state occurs only when all bands are filled. With this physical picture in mind, the development of "*density functional theory*" (DFT) [70, 93] in conjunction with the local density approximation (LDA) has enabled physicists to improve our understanding of many compounds.

However, the picture is not perfect yet. DFT calculations fail to capture the physics of some transition metal oxides or rare-earth compounds, which contain open d and f-shells. In these "*strongly correlated materials*", the previous single-particle picture is not suitable at all as the repulsive Coulomb interaction between electrons plays a significant role. In the extreme limit, the energy cost of electronic correlations may be so overwhelming that the system can be an insulator even if its energy bands are not filled. Such a material for which electronic correlations prevent the motion of the electrons is called a "*Mott insulator*" [120, 121].

An important breakthrough in our understanding of this new class of insulators was made in the early nineties with the development of "*dynamical mean-field theory*" (DMFT) [57, 98]. Within this new framework, the lattice model is mapped onto a local impurity problem embedded in an electronic bath. By combining DFT band structure calculations with DMFT in the so-called "*LDA+DMFT formalism*", a successful description of strongly correlated materials was then possible.

However, physicists cannot just rest on their laurels as nature always provides new challenges, even for well-established theories. Strontium iridate (Sr_2IrO_4) is one of these challenging materials that evades our understanding. Whereas $5d$-transition metal oxides are usually considered as "weakly" correlated, this material exhibits an insulating state despite its odd number of electrons per unit cell. This puzzling affair remained a mystery for decades. Recently, the model of "*spin-orbit driven Mott*

insulator" has been proposed [84]. According to this picture, the cooperative interaction between electronic correlations and the strong spin-orbit coupling explains the insulating state of this material.

Sr_2IrO_4 is however not an isolated example. spin-orbit interaction was found to play a significant role in the properties of a growing variety of correlated compounds such as strontium rhodate [107], iron-spinel [37] and many other iridium-based transition metal oxides [116, 125, 146]. In addition, the recent discovery of topological band insulators [21, 94, 118] has shown that spin-orbit coupling can also modify significantly the band structure of weakly correlated solids, thus leading to a distinct phase of matter. Whereas spin-orbit interaction was commonly thought as a "small relativistic correction" in solid state physics and even more so for strongly correlated materials, it appears now that this assumption has been a mistake.

This thesis takes all this importance in this new context where studying the interplay between the electronic correlations and the spin-orbit interaction has become essential. The main purpose of our work was to study the paramagnetic insulating phase of Sr_2IrO_4 within LDA+DMFT. This study required the extension of the current implementation of LDA+DMFT to take into account the spin-orbit coupling. In regards of this objective, this thesis is organized in two parts:

- In the first part, we introduce definitions and concepts that are of great use to the study of strongly correlated materials. More precisely, the first chapter is focused on *density functional theory* (DFT) and *dynamical mean-field theory* (DMFT). Having presented these two theories independently, we then explain in the second chapter how to treat correlations in materials within the *LDA+DMFT formalism*. The implementation of LDA+DMFT developed in the *linearized augmented planewaves* (LAPW) framework by Aichhorn *et al.* [1] is then described. This description is essential since our work particularly consisted in extending it so that the spin-orbit interaction may be included (more precisely, to define the Wannier orbitals on which the local impurity problem is based). A general presentation of this new "*LDA+SO+DMFT implementation*" is finally given in the third chapter after a brief review of the effects of the spin-orbit coupling in atoms and solids.

- The second part is devoted to the $5d$ transition metal oxide Sr_2IrO_4 whose study has motivated the technical developments achieved in this thesis. In the fourth chapter, we give an exhaustive review of the existing experimental and theoretical works performed on this compound, in order to put our results into context. Our LDA+DMFT study is then presented in the last chapter. On the one hand, we confirm that Sr_2IrO_4 is a Mott insulator in its paramagnetic phase. On the other hand, we highlight the respective roles played by the spin-orbit interaction and the structural distortions to reach the Mott insulating state. By systematically varying the correlation strength in the absence and presence of both these elements, we indeed argue that only their *acting together* may open the Mott gap in Sr_2IrO_4.

Finally, this thesis ends with a series of appendices, where additional information on crystal field effects in the presence of spin-orbit coupling, technical issues about the new implementation of projector scheme and a discussion on many-body treatment of the spin-orbit interaction, invoking spin-same-orbit and spin-other-orbit terms, can be found.

Contents

Part I

Methods

Chapter 1

A (not so) brief introduction to the domain

What is a "*strongly correlated material*"? The best way to answer this question would certainly be to give an exhaustive list of the compounds which are considered so and the solved and still open questions related to them. With such an approach, we could cite the transition metal and transition metal oxides, the cuprates or new iron-based superconductors, the rare-earth and actinide or lanthanide compounds. However, making such an exhaustive overview is a really tough task, above all in a few pages, and for the interested reader we particularly recommend the review of Imada *et al.* [76]. Nevertheless, despite the large number of compounds and the variety of their features, some general behaviors can still be extracted and finding the key-physical concepts which are hidden below this diversity of phenomena is precisely the aim of the theoretical branch of this scientific domain.

In this chapter, we introduce the main physical ideas which are at stake in this field. Starting from a short reminder of elementary notions which are of great use in all the condensed matter physics, we then present the "*density functional theory*" (DFT) which was an important breakthrough in the domain in the early sixties. To understand the limits of this theory, the concept of "*electronic correlations*" must be introduced and is the subject of the second part of this chapter. The Hubbard model is then presented and the Mott physics is described. The last part of this chapter is devoted to the "*dynamical mean-field theory*" (DMFT) which is now well-established in the community to describe the correlated states in materials.

1.1 Basics of solid state physics

Any solid is a polyatomic system which is composed of two coupled subsystems: a set of N_n atomic nuclei and a set of N_e electrons, these two entities being of the order of a few Avogadro's number $\mathcal{N}_A = 6.022 \times 10^{23}$. The quantum mechanical description of this system relies on the following Hamiltonian:

$$\begin{aligned} H &= \sum_{i=1}^{N_n} -\frac{\hbar^2}{2M_i}\nabla^2_{\mathbf{R_i}} + \sum_{\substack{i,j=1 \\ i<j}}^{N_n} \frac{(Z_i e)(Z_j e)}{4\pi\varepsilon_0 |\mathbf{R}_i - \mathbf{R}_j|} \\ &+ \sum_{j=1}^{N_e} -\frac{\hbar^2}{2m_0}\nabla^2_{\mathbf{r_j}} + \sum_{\substack{i,j=1 \\ i<j}}^{N_e} \frac{e^2}{4\pi\varepsilon_0 |\mathbf{r}_i - \mathbf{r}_j|} - \sum_{i=1}^{N_n}\sum_{j=1}^{N_e} \frac{Z_i e^2}{4\pi\varepsilon_0 |\mathbf{R}_i - \mathbf{r}_j|} \end{aligned} \tag{1.1}$$

where M_i is the mass of the i^{th} nucleus, $Z_i e$ its charge and m_0 the electronic mass. The first two terms correspond to the kinetic energy of the atomic nuclei and the Coulomb interaction energy between

them. The third and fourth terms are the same physical quantities for the electrons and the fifth term stands for the Coulomb interaction energy between the electrons and the nuclei.

However, the mass of the nuclei is several orders of magnitude larger than that of the electrons: $m_0/M_i \approx 10^{-4}$-10^{-6}. As a result, a solid is described by two extremely different dynamical regimes, the velocities of the nuclei being considerably smaller than those of the electrons. The "*adiabatic*" or "*Born-Oppenheimer approximation*" takes advantage of this physical observation and allows studying the dynamics of the electrons separately from that of the nuclei. The initial problem (1.1) reduces then to a system of N_e interacting electrons in the static electric field $V(\mathbf{r})$ induced by the fixed N_n nuclei:

$$H = \sum_{j=1}^{N_e} \left[-\frac{\hbar^2}{2m_0} \nabla^2_{\mathbf{r_j}} + V(\mathbf{r}_j) \right] + \frac{e^2}{4\pi\varepsilon_0} \sum_{\substack{i,j=1 \\ i<j}}^{N_e} \frac{1}{|\mathbf{r}_i - \mathbf{r}_j|}. \tag{1.2}$$

In the following, we will consider only crystalline solids, in which the atomic nuclei are arranged in an orderly periodic pattern in the three spatial dimensions. We furthermore assume that crystals are infinite in space. As a consequence, it is possible to find a set of discrete translations and a set of symmetry operations – like rotations and reflections – which leave the system invariant after applying any of these operations to it. The former defines the "*Bravais lattice*" $\mathcal{B}$ of the compound and the latter its "*crystallographic point group*" [2, 16, 25].

By performing all these approximations, we have neglected the dynamic lattice deviations, the impact of disorder or defaults and the surface effects, which are important subjects in solid-state physics on their own. Nevertheless, even such an idealistic description of the problem remains almost impossible to solve because of its many-body character. Each of the 10^{23} electrons indeed interacts with all the others via the Coulomb interaction – the last term of (1.2) – : their behaviors are "*correlated*" with each other.

The simplest way to take into account this effect is to approximate the last term of (1.2) in a "*mean-field approach*". This is precisely the aim of the "*Hartree approximation*", in which each electron feels only the electric field induced by the mean charge density $\rho(\mathbf{r})$ corresponding to all the other electrons:

$$H \approx \sum_{j=1}^{N_e} \left[-\frac{\hbar^2}{2m_0} \nabla^2_{\mathbf{r_j}} + V(\mathbf{r}_j) + V_H(\mathbf{r}_j) \right] \qquad \text{with} \qquad V_H(\mathbf{r}) = \frac{e^2}{4\pi\varepsilon_0} \int_{\mathbb{R}^3} d^3\mathbf{r}' \frac{\rho(\mathbf{r}')}{|\mathbf{r} - \mathbf{r}'|}. \tag{1.3}$$

Consequently, the Hamiltonian becomes separable and it is then possible to solve the problem by using standard methods developed for independent particle system.

Within this independent particle picture, the periodicity of the lattice results into two main concepts which form the base of solid-state physics:

Bloch's theorem (1929) [24] which states that the wavefunction of a particle or pseudo-particle can be written as:

$$\psi_{\mathbf{k}}(\mathbf{r}) = e^{i\mathbf{k}.\mathbf{r}} u_{\mathbf{k}}(\mathbf{r}) \quad \text{with} \quad u_{\mathbf{k}}(\mathbf{r} + \mathbf{R}) = u_{\mathbf{k}}(\mathbf{r}) \quad \forall\, \mathbf{R} \in \mathcal{B} \tag{1.4}$$

where $\mathbf{k}$ is a reciprocal lattice vector which belongs to the "*first Brillouin zone*" (1BZ) of the crystal and is called the "*crystal momentum*" of the particle. Bloch functions can also be written in the following form, where the sum runs over all the reciprocal lattice vectors $\mathbf{K}$:

$$\psi_{\mathbf{k}}(\mathbf{r}) = \sum_{\mathbf{K}} c_{\mathbf{k}-\mathbf{K}} e^{i(\mathbf{k}-\mathbf{K}).\mathbf{r}}. \tag{1.5}$$

The formation of "*band structure*": In the crystal, electrons are confined to some intervals of energy, and forbidden from other regions. According to Pauli's principle, each "*band*" can accommodate two electrons with opposite spins by unit cell. Two different kinds of solid can then be distinguished:

- the "*metals*", whose band structure contains one or several partially-filled bands. An itinerant behavior of the charge carriers is then realized and the energy ε_F up to which the bands are filled is called the "*Fermi level*". The density of states at the Fermi level of such a compound is finite.
- the "*band-insulators*", with an even number of electrons by unit cell, for which all the energy bands are filled. These compounds are characterized by an "*energy gap*", which is the energy difference between the top of the highest occupied band – or "*valence band*" – and the bottom of the lowest unoccupied band – or "*conduction band*" –. The density of states inside the gap is of course zero.

Before concluding this section, we would like to focus the reader's attention on the "*mean-field*" concept, introduced to establish equation (1.3). To treat the many-body Hamiltonian (1.2) of the electronic system, we have considered an equivalent problem of independent particles, described by a set of single-particle Schrödinger-like equations:

$$H\psi_{\mathbf{k}}(\mathbf{r}) = \varepsilon_{n\mathbf{k}}\psi_{\mathbf{k}}(\mathbf{r}) \qquad \text{with} \qquad H = \sum_{j=1}^{N_e}\left[-\frac{\hbar^2}{2m_0}\nabla^2_{\mathbf{r_j}} + V(\mathbf{r}_j) + V_H(\mathbf{r}_j)\right] \tag{1.6}$$

in which the two-body interaction is replaced by the *effective Hartree potential* $V_H(\mathbf{r})$ based on the following approximation:

$$\frac{e^2}{4\pi\varepsilon_0}\sum_{\substack{i,j=1\\ i<j}}^{N_e}\frac{1}{|\mathbf{r}_i-\mathbf{r}_j|} \;\approx\; \sum_{i=1}^{N_e} V_H(\mathbf{r_i}) = \sum_{i=1}^{N_e}\frac{e^2}{4\pi\varepsilon_0}\int_{\mathbb{R}^3} d^3\mathbf{r}'\frac{\rho(\mathbf{r}')}{|\mathbf{r}_i-\mathbf{r}'|}. \tag{1.7}$$

This describes the effect of a *mean-field interaction* which becomes a functional of the electronic density $\rho(\mathbf{r})$ defined as:

$$\rho(\mathbf{r}) = \sum_{\varepsilon_{n\mathbf{k}}\leq\varepsilon_F}|\psi_{\mathbf{k}}(\mathbf{r})|^2. \tag{1.8}$$

Since the density of the electrons $\rho(\mathbf{r})$ is precisely unknown when one intends to solve equations (1.6), the problem must be solved iteratively by performing a self-consistency loop: starting from an initial guess of the mean density, the eigenstates $\psi_{\mathbf{k}}(\mathbf{r})$ of (1.6) are found and the charge density associated to the corresponding ground-state is calculated with (1.8). The Hamiltonian (1.6) is then solved again with this new guess of $\rho(\mathbf{r})$. The iterations stop when the convergence is achieved.

However, going beyond the *mean-field approximation* is essential in electronic structure calculations to get the quantitative physics out of the solution. From this point of view, the real breakthrough in the field is represented by the "*density functional theory*" (DFT), which is the subject of the next section.

1.2 The Density Functional Theory (DFT)

The formalism of the "*density-functional theory*" (DFT) was introduced by Hohenberg and Kohn in 1964 [70]. In 1965, Kohn and Sham established a set of equations to treat any interacting electron

system within this formalism [93]. Nevertheless, as we will see, some drastic simplifications in the many-body problem must be introduced to use in practice this approach. Despite these approximations, this scheme has turned out to be reliable for describing the ground-state of numerous compounds and has become the most popular *ab initio* method in quantum chemistry and solid-state physics to study electronic structures.

The brief overview of DFT presented here follows the traditional – historical – approach. A thorough introduction to this theory can be found in [32, 80]. We also mention, for the interested reader, the alternative presentation of [14], based on the analogy with thermodynamics.

1.2.1 The Hohenberg-Kohn theorems

In 1964, Hohenberg and Kohn formulated two theorems [70], which formally justified the use of the density $\rho(\mathbf{r})$ as the basic variable in determining the total energy of a system composed of N_e interacting electrons and described by the Hamiltonian (1.2). Such a statement was a real breakthrough in the domain, since the ground-state of such a system is typically described by $3N_e$ variables in the wavefunction:

$$H|\Psi\rangle = E|\Psi\rangle \qquad \text{with} \qquad |\Psi\rangle = \int \Psi(\mathbf{r}_1, \ldots, \mathbf{r}_N)|\mathbf{r}_1, \ldots, \mathbf{r}_{N_e}\rangle d^3\mathbf{r}_1 \ldots d^3\mathbf{r}_{N_e} \tag{1.9}$$

whereas the electronic density distribution counts only 3 parameters:

$$\rho(\mathbf{r}) = N_e \int |\Psi(\mathbf{r}, \mathbf{r}_2, \ldots, \mathbf{r}_{N_e})|^2 d^3\mathbf{r}_2 \ldots d^3\mathbf{r}_{N_e}. \tag{1.10}$$

First Hohenberg-Kohn theorem

Using the index "$_0$" for ground-state quantities, the first Hohenberg-Kohn theorem states:

> *The external potential $V(\mathbf{r})$ is (to within a constant) a unique functional of $\rho_0(\mathbf{r})$; since in turn $V(\mathbf{r})$ fixes the Hamiltonian H, we see that the full many particle ground-state is a unique functional of $\rho_0(\mathbf{r})$.*

Thus it exists a one-to-one mapping between a given external potential $V(\mathbf{r})$ and the ground-state density $\rho_0(\mathbf{r})$. This theorem also implies that all the ground-state properties of the interacting particle system are *exactly* determined through the knowledge of $\rho_0(\mathbf{r})$. We will not display here the historical proof of the theorem, which shows the existence of this relation by *reductio ad absurdum*. No explicit formula to calculate the potential $V(\mathbf{r})$ from $\rho_0(\mathbf{r})$ is actually known and in practice, some approximation must thus be used.

Second Hohenberg-Kohn Theorem

The second Hohenberg-Kohn theorem extends the Rayleigh-Ritz variational principle for all density distributions $\rho(\mathbf{r})$ which can be represented by N_e-body wave-function. The ground-state energy $E_0 = E[\rho_0(\mathbf{r})]$ indeed minimizes the following functional of the density:

$$E[\rho(\mathbf{r})] = F[\rho(\mathbf{r})] + \int V(\mathbf{r})\rho(\mathbf{r})d^3\mathbf{r} \tag{1.11}$$

where $F[\rho(\mathbf{r})]$ is a *universal functional* which contains the potential energy of the electron-electron interactions and the kinetic energy of the interacting electrons.[1] Since the expression of the Hartree

[1] This functional is said "*universal*" since it is identical for any system of N_e interacting electrons. In the formulation of Levy and Lieb [102, 106], $F[\rho(\mathbf{r})]$ can be formally expressed as the minimum of the expectation values of the exact

energy as a function of the density is explicitly known, the functional $F[\rho(\mathbf{r})]$ can be further decomposed into:

$$F[\rho(\mathbf{r})] = \frac{1}{2}\int d^3\mathbf{r}\int d^3\mathbf{r}'\frac{e^2}{4\pi\varepsilon_0}\frac{\rho(\mathbf{r})\rho(\mathbf{r}')}{|\mathbf{r}-\mathbf{r}'|} + G[\rho(\mathbf{r})]. \tag{1.13}$$

Even with this last expression of $F[\rho(\mathbf{r})]$, the variational principle still remains tricky to solve, since an explicit expression of $G[\rho(\mathbf{r})]$ in function of $\rho(\mathbf{r})$ remains unknown.

1.2.2 The Kohn-Sham equations

In 1965, Kohn and Sham suggested to solve the complex interacting electronic system by using an "*effective model of independent particles with the same ground-state density*" [93]. In the same spirit as previously explained about the Hartree – and Hartree-Fock – approximation, they considered a fictitious non-interacting system described by a set of single-particle Schrödinger-like equations:

$$\left[-\frac{\hbar^2}{2m_0}\nabla^2 + V_{KS}(\mathbf{r})\right]\psi_{\mathbf{k}}(\mathbf{r}) = \varepsilon_{n\mathbf{k}}\psi_{\mathbf{k}}(\mathbf{r}) \tag{1.14}$$

where the "*effective Kohn-Sham potential*" $V_{KS}(\mathbf{r})$ must be chosen such that the value of the ground-state density $\rho_0(\mathbf{r})$ of the interacting system is accurately reproduced:

$$\rho_0(\mathbf{r}) = \sum_{\varepsilon_{n\mathbf{k}}\leq\varepsilon_F}|\psi_{\mathbf{k}}(\mathbf{r})|^2. \tag{1.15}$$

The energy functional $E_{ni}[\rho(\mathbf{r})]$ of such a non-interacting system is explicitly known:

$$E_{ni}[\rho(\mathbf{r})] = T_0[\rho(\mathbf{r})] + \int V_{KS}(\mathbf{r})\rho(\mathbf{r})d^3\mathbf{r} \qquad \text{with} \qquad T_0[\rho(\mathbf{r})] = \sum_{\varepsilon_{n\mathbf{k}}\leq\varepsilon_F}\langle\psi_{\mathbf{k}}| - \frac{\hbar^2}{2m_0}\nabla^2_{\mathbf{r}}|\psi_{\mathbf{k}}\rangle. \tag{1.16}$$

Moreover, it is formally possible to write the energy functional $E[\rho(\mathbf{r})]$ of the initial interacting electronic system (1.11) as follows:

$$E[\rho(\mathbf{r})] = T_0[\rho(\mathbf{r})] + \frac{1}{2}\int d^3\mathbf{r}\int d^3\mathbf{r}'\frac{e^2}{4\pi\varepsilon_0}\frac{\rho(\mathbf{r})\rho(\mathbf{r}')}{|\mathbf{r}-\mathbf{r}'|} + E_{xc}[\rho(\mathbf{r})] + \int V(\mathbf{r})\rho(\mathbf{r})d^3\mathbf{r} \tag{1.17}$$

where $E_{xc}[\rho(\mathbf{r})] = G[\rho(\mathbf{r})] - T_0[\rho(\mathbf{r})]$ is the "*exchange-correlation energy*" which contains all the many-body effects.

Consequently, in order that $E[\rho(\mathbf{r})]$ and $E_{ni}[\rho(\mathbf{r})]$ can have the same ground-state density $\rho_0(\mathbf{r})$ – or the same global minimum under the same constraint of particle number $N_e = \int\rho(\mathbf{r})d^3\mathbf{r}$ –, the condition on $V_{KS}(\mathbf{r})$ reads finally:

$$V_{KS}(\mathbf{r}) = V(\mathbf{r}) + V_H(\mathbf{r}) + V^{xc}(\mathbf{r}) \tag{1.18}$$

where $V_H(\mathbf{r})$ is the Hartree potential already defined in (1.3) – calculated with $\rho_0(\mathbf{r})$ – and $V^{xc}(\mathbf{r})$ is the "*exchange-correlation potential*" defined by

$$V^{xc}(\mathbf{r}) = \left.\frac{\delta E_{xc}[\rho(\mathbf{r})]}{\delta\rho(\mathbf{r})}\right|_{\rho_0(\mathbf{r})}. \tag{1.19}$$

---

kinetic energy $\widehat{T}$ and electron-electron interaction $\widehat{V}_{ee}$, taken over the class of wavefunctions that yield the density $\rho(\mathbf{r})$:

$$F[\rho(\mathbf{r})] = \min_{\Psi\to\rho(\mathbf{r})} <\Psi_{[\rho(\mathbf{r})]}|\widehat{T}+\widehat{V}_{ee}|\Psi_{[\rho(\mathbf{r})]}> \quad \text{with} \quad \widehat{T} = -\frac{\hbar^2}{2m_0}\sum_{i=1}^{N_e}\nabla^2_{\mathbf{r_i}} \quad \text{and} \quad \widehat{V}_{ee} = \frac{e^2}{4\pi\varepsilon_0}\sum_{\substack{i,j=1\\ i<j}}^{N_e}\frac{1}{|\mathbf{r}_i-\mathbf{r}_j|}. \tag{1.12}$$

As already observed at the end of section 1.1, a "*self-consistency condition*" appears since the effective potential depends on the density $V_{KS}(\mathbf{r}) = V_{KS}[\rho_0(\mathbf{r})]$. However, no approximation has been introduced so far by describing the interacting electronic system by such an *effective model of non-interacting particles*. Actually, the mapping between the initial many-body problem and the auxiliary non-interacting effective system would be *exact* if an expression of the exchange-correlation potential $V^{xc}(\mathbf{r})$ was known. Unfortunately, not only the expression of $E_{xc}[\rho(\mathbf{r})]$ but also a systematic series of approximation converging to the exact result is missing. An approximation on the form of the exchange-correlation potential $V^{xc}(\mathbf{r})$ must thus be made, in order to solve *self-consistently* the Kohn-Sham equations defined by (1.14) and (1.18).

1.2.3 Approximations to the exchange-correlation functional $\mathbf{E_{xc}}[\rho(\mathbf{r})]$

As we have previously said, the total energy functional (1.17) is known except for its exchange-correlation term $E_{xc}[\rho(\mathbf{r})]$. Various approximations to the exchange-correlation functional have been devised [32] but only the most popular of them will be described now.

The Local Density Approximation (LDA)

The most commonly adapted is the so-called "*local density approximation*" (LDA), initially proposed in the original article of Kohn and Sham [93]:

$$E_{xc}^{LDA}[\rho(\mathbf{r})] = \int \rho(\mathbf{r})\ \varepsilon_{xc}[\rho(\mathbf{r})]\ d^3\mathbf{r}. \tag{1.20}$$

In this expression, $\varepsilon_{xc}[\rho]$ is the exchange-correlation energy per particle of the *homogeneous electron gas* evaluated with the density ρ. The approximation thus relies on the following postulate: the exchange-correlation energy associated to a particular density $\rho(\mathbf{r})$ is "*locally*" equal to the exchange correlation energy of an homogeneous electron gas, which has the same overall density as the initial density evaluated at the point $\mathbf{r}$.

Although the exchange contribution $\varepsilon_x[\rho]$ can be obtained analytically [48]:

$$\varepsilon_x[\rho] = -\frac{3}{4}\left[\frac{3}{\pi}\rho\right]^{\frac{1}{3}} \tag{1.21}$$

the correlation contribution $\varepsilon_c[\rho]$ remains unknown. In 1980, Ceperley and Adler performed a set of Quantum Monte Carlo (QMC) calculations for the homogeneous electron gas with different densities [35]. They also provided a correlation energy parametrization based on this ground-state energy results, which are nowadays of great use in the context of the local density mapping.

The Generalized Gradient Approximation (GGA)

The "*generalized gradient approximation*" (GGA) is as popular as the LDA, especially in quantum chemistry. Introduced in the late eighties, this approach refines the LDA by including the dependence on the gradient of the density in the exchange-correlation energy per particle:

$$E_{xc}^{GGA}[\rho(\mathbf{r})] = \int \rho(\mathbf{r})\ \varepsilon_{xc}[\rho(\mathbf{r}), \nabla\rho(\mathbf{r})]\ d^3\mathbf{r}. \tag{1.22}$$

Many choices for the parametrization of ε_{xc} are nowadays available in this framework, but we will not describe them since their theoretical foundation is often not completely rigorous – or at best empirical. The interested reader can find more details about the exact properties of exchange-correlation energy $E_{xc}[\rho(\mathbf{r})]$ and all the other existing approximations in the review [32].

The Local Spin Density Approximation (LSDA)

In many applications, going beyond the LDA is needed in order to include non-homogeneous spin densities, such as spin density wave instabilities, local spin moment formation and spin-orbit coupling. Therefore the density has to be resolved into its spin components $\rho_\uparrow(\mathbf{r})$ and $\rho_\downarrow(\mathbf{r})$. The DFT formulation based on these two fundamental variables[2] has been developed in the mid seventies [62, 160], and the LDA has then been extended to the "*local spin-density approximation*" (LSDA).

The Hohenberg-Kohn theorems and the Kohn-Sham equations can be immediately rephrased, just by attaching a suitable spin-index to the densities. There are, however, some exceptions to this simple rule, and among them the construction of the exchange-correlation functional. For instance, it is known that the exchange energy must be calculated by:

$$E_x^{LSDA}[\rho_\uparrow(\mathbf{r}), \rho_\downarrow(\mathbf{r})] = \frac{1}{2}\left(E_x^{LDA}[2\rho_\uparrow(\mathbf{r})] + E_x^{LDA}[2\rho_\downarrow(\mathbf{r})]\right) \tag{1.24}$$

For the correlation energy however, no scaling relation of this type holds, so that $E_c^{LSDA}[\rho_\uparrow(\mathbf{r}), \rho_\downarrow(\mathbf{r})]$ is in practice either directly constructed in terms of the spin-densities or written by using, without formal justification, the same interpolation as here-above for the exchange energy [80, 160].

1.2.4 Success and limitations of DFT

Despite the approximation in the form for the exchange-correlation energy – which makes the theory applicable in practice –, DFT is widely used in the solid-state community. This is first of all because its implementations can yield astonishingly good results with respect to experiments for describing ground-state properties of a wide class of materials. For instance, the lattice constants of simple crystals are obtained with an accuracy of about 1%, within the LDA [14]. Another advantage of DFT is doubtlessly the high computational efficiency of its implementations.

Nevertheless, according to the Hohenberg-Kohn theorems, DFT is *only* a ground-state theory. This approach provides no information on the excitation spectrum of the compounds, which is directly observed in experiments such as photo-emission spectroscopy, optics or transport. It is however common nowadays to interpret the Kohn-Sham eigenvalues as the single-particle excitations of the system. This identification is strictly speaking unjustified since the Kohn-Sham eigenvalues are merely auxiliary quantities, without any physical meaning. By using it, people actually do a tacit assumption: the electrons in the physical system are indeed considered to be well-described by a model of independent particles.

In practice, this procedure yields reasonable results in many solids but fails for some systems, like transition metals, transition metal oxides or rare-earth compounds, which contain open d and f-shells. Such materials are said to be "*strongly correlated*". In these cases, the electronic band structure obtained at the end of a DFT calculation and the true excitation spectrum of the compound do not match, highlighting that their electrons can not be well-described with a single-particle picture. For some of them called "*Mott insulators*", both the Kohn-Sham ground-state and spectrum are even qualitatively wrong, since the insulating behavior of the material is not found and a metallic state is predicted. The next sections are devoted to describe the main features of such compounds.

[2] The formalism can also be reformulated in terms of the total charge density $\rho(\mathbf{r})$ and the spin-magnetization density $m(\mathbf{r})$:

$$\rho(\mathbf{r}) = \rho_\uparrow(\mathbf{r}) + \rho_\downarrow(\mathbf{r}) \qquad \text{and} \qquad m(\mathbf{r}) = \frac{e\hbar}{2m_0 c}\big[\rho_\uparrow(\mathbf{r}) - \rho_\downarrow(\mathbf{r})\big] \tag{1.23}$$

1.3 Electronic correlations

The methods presented so far have described the physical properties of electrons in solids by assuming a single-particle picture. In the two previous sections, the electron-electron Coulomb interaction term of the general Hamiltonian (1.2) was indeed approximated by an effective potential $V_{\text{eff}}(\mathbf{r}) = V_H(\mathbf{r}) + V^{xc}(\mathbf{r})$ felt *independently* by all electrons. However, Nature is – fortunately – far more complicated: the "*electronic correlations*" can induce a huge range of physical phenomena, requiring new models and methods to describe them.

1.3.1 Introduction to strong correlations and Mott insulators

In many solids, the physical properties of electrons can be described – to a good approximation – by assuming an independent particle picture. This is particularly successful when one deals with broad energy bands associated with a large value of the kinetic energy. In such cases, the valence electrons are "*highly itinerant*": they are *delocalized all over the solid*. As a result, a description based on the *nearly-free electron approximation* is appropriate since the typical time spent by an electron near a specific atom in the crystal lattice is very short.

For some materials however – generally associated with moderate values of the bandwidth –, a description based on a particle-like picture – with a *tight-binding model* – appears then more suitable since valence electrons spend a larger time around a given atom in the crystal lattice. In these conditions, electrons "have enough time to see each other on each atomic site" – via the Coulomb interaction – and the motions of individual electrons become "*correlated*". If the energy cost of this interaction is sufficiently large, delocalizing the valence electrons over the whole solid may become less favorable energetically. In extreme cases, the electrons may even remain "*localized*" on their respective atom.

If this occurs to all electrons close to the Fermi level, the solid becomes an insulator. This insulating state is difficult to understand from a wave-like picture. It does not come from destructive interference in **k**-space resulting in the absence of available one-electron states, as in conventional band insulators. However, this state is easily described with a particle-like picture in real space, as we have just done. This mechanism was explained long ago by Mott and Peierls [120, 121], that is why such compounds are called "*Mott insulators*".

The most interesting situation – but also the hardest to handle theoretically – arises when the localized character on short time-scales (or high energy scales) and the itinerant character on long time-scales (or short energy scales) coexist. In such cases, the electrons can be naively seen as "*hesitating*" between being itinerant and being localized. Such materials are said to be "*strongly correlated*".

In these compounds, a plethora of physical phenomena can not be described by the standard band theory and DFT, as already mentioned in section 1.2. It is thus necessary to develop new techniques in order to understand these properties. The most famous models in the domain were derived by Hubbard in 1963 [73] and 1964 [74, 75]. Despite their apparent simplicity, these "*Hubbard models*" embody well the necessity to think both in **k**-space and in real space to describe the physics of correlation.

1.3.2 The Hubbard model

For the sake of simplicity, we will derive here the "*Hubbard model*" for an electronic system in a crystal composed of a cubic lattice with one atom by unit cell. Moreover, it is more convenient to use the formalism of "*second quantization*" to express the Hamiltonian (1.2). This consists in replacing the wavefunction by an operator acting on a quantum field with a fluctuating particle number. As

described in standard textbooks [17], the Hamiltonian (1.2) becomes in terms of field operators:

$$\begin{aligned} H &= \sum_{\sigma=\uparrow,\downarrow} \int_{\mathbb{R}^3} d^3\mathbf{r}\ \psi^\dagger_\sigma(\mathbf{r}) \left[-\frac{\hbar^2}{2m_0}\nabla^2_{\mathbf{r}} + V(\mathbf{r})\right] \psi_\sigma(\mathbf{r}) \\ &+ \frac{1}{2}\sum_{\sigma,\tau=\uparrow,\downarrow} \frac{e^2}{4\pi\varepsilon_0}\int_{\mathbb{R}^3} d^3\mathbf{r}\int_{\mathbb{R}^3} d^3\mathbf{r}'\ \psi^\dagger_\sigma(\mathbf{r})\psi^\dagger_\tau(\mathbf{r}')\left[\frac{1}{|\mathbf{r}-\mathbf{r}'|}\right]\psi_\tau(\mathbf{r}')\psi_\sigma(\mathbf{r}) \end{aligned} \tag{1.25}$$

where $\psi^\dagger_\sigma(\mathbf{r})$ and $\psi_\sigma(\mathbf{r})$ respectively creates and annihilates an electron with spin σ at the point $\mathbf{r}$. The proper fermion statistics is imposed through the anticommutation relations of the field operators:

$$\psi_\sigma(\mathbf{r})\psi_\tau(\mathbf{r}') + \psi_\tau(\mathbf{r}')\psi_\sigma(\mathbf{r}) = 0 \qquad \text{and} \qquad \psi_\sigma(\mathbf{r})\psi^\dagger_\tau(\mathbf{r}') + \psi^\dagger_\tau(\mathbf{r}')\psi_\sigma(\mathbf{r}) = \delta_{\sigma\tau}\delta(\mathbf{r}-\mathbf{r}'). \tag{1.26}$$

It is generally of little use to start with the bare ion-electron potential $V(\mathbf{r})$ and the long-range Coulomb interaction in (1.25), since a *collective screening* of the core and valence electrons may be large. Much of this *screening* effect can be incorporated into the single particle part of H by modifying locally the potential[3]. As a result, the electron-electron interaction is renormalized in a residual interaction term[4]:

$$\widetilde{V}_{ee}(\mathbf{r},\mathbf{r}') = \frac{e^2}{4\pi\varepsilon_0}\frac{1}{|\mathbf{r}-\mathbf{r}'|} - \frac{1}{N_e}[V_{\text{eff}}(\mathbf{r}) + V_{\text{eff}}(\mathbf{r}')] \tag{1.28}$$

with $V_{\text{eff}}(\mathbf{r}) = V_H(\mathbf{r}) + V^{xc}(\mathbf{r})$ and we can finally rewrite the Hamiltonian as:

$$\begin{aligned} H &= \sum_{\sigma=\uparrow,\downarrow} \int_{\mathbb{R}^3} d^3\mathbf{r}\ \psi^\dagger_\sigma(\mathbf{r}) \left[-\frac{\hbar^2}{2m_0}\nabla^2_{\mathbf{r}} + V_{KS}(\mathbf{r})\right] \psi_\sigma(\mathbf{r}) \\ &+ \frac{1}{2}\sum_{\sigma,\tau=\uparrow,\downarrow} \int_{\mathbb{R}^3} d^3\mathbf{r}\int_{\mathbb{R}^3} d^3\mathbf{r}'\ \psi^\dagger_\sigma(\mathbf{r})\psi^\dagger_\tau(\mathbf{r}')\ \widetilde{V}_{ee}(\mathbf{r},\mathbf{r}')\ \psi_\tau(\mathbf{r}')\psi_\sigma(\mathbf{r}). \end{aligned} \tag{1.29}$$

Introduced by Wannier in 1937 [163], the "*Wannier states*" provide a representation which is more appropriate to our purpose. They are indeed *localized around each atomic site* $\mathbf{R}_j$ and defined as the Fourier transformation of the Bloch states:

$$\chi^{\mathbf{R}_j}_{L\sigma}(\mathbf{r}) = \frac{1}{\sqrt{\mathcal{N}}}\sum_{\mathbf{k}} e^{-i\mathbf{k}.\mathbf{R}_j}\psi^\sigma_{\mathbf{k}\nu_L}(\mathbf{r}) \tag{1.30}$$

where $\mathcal{N}$ is the number of lattice sites, L the combined index (l,m) denoting the orbital and ν_L the band index associated to the L character[5]. Defining the creation and annihilation operator of a Wannier state as $c^{\sigma\dagger}_{\mathbf{R}_jL}$ and $c^\sigma_{\mathbf{R}_jL}$, the field operators can be written as:

$$\psi^\dagger_\sigma(\mathbf{r}) = \sum_{\mathbf{R}_j,L}\left[\chi^{\mathbf{R}_j}_{L\sigma}(\mathbf{r})\right]^* c^{\sigma\dagger}_{\mathbf{R}_jL} \qquad \text{and} \qquad \psi_\sigma(\mathbf{r}) = \sum_{\mathbf{R}_j,L}\chi^{\mathbf{R}_j}_{L\sigma}(\mathbf{r})c^\sigma_{\mathbf{R}_jL}. \tag{1.31}$$

[3]This is precisely what is done with the effective Kohn-Sham potential $V_{KS}(\mathbf{r})$ in DFT where:

$$V_{KS}(\mathbf{r}) = V(\mathbf{r}) + V_H(\mathbf{r}) + V^{xc}(\mathbf{r}) = V(\mathbf{r}) + V_{\text{eff}}(\mathbf{r}). \tag{1.27}$$

[4]In reality, *screening* is a dynamical process which involves collective charge fluctuations with a plasma frequency scale. However, if the plasma frequency is higher than the excitation energies of interest – as in our case –, $\widetilde{V}_{ee}(\mathbf{r},\mathbf{r}')$ can be taken as instantaneous.

[5]Contrary to the most general case presented in section 2.3, the definition for the *Wannier states* given here has no ambiguity, since we are considering a very simple example.

The Hamiltonian becomes then the following lattice model:

$$\begin{aligned} H &= \sum_{i,j} \sum_{L,L'} \sum_{\sigma} t_{ij}^{LL'\sigma} c^{\sigma\dagger}_{\mathbf{R}_i L} c^{\sigma}_{\mathbf{R}_j L'} \\ &+ \frac{1}{2} \sum_{i,j,k,l} \sum_{L,L',M,M'} \sum_{\sigma,\sigma'} U_{i\ j\ k\ l}^{LL'MM'\sigma\sigma'} c^{\sigma\dagger}_{\mathbf{R}_i L} c^{\sigma'\dagger}_{\mathbf{R}_j L'} c^{\sigma'}_{\mathbf{R}_l M'} c^{\sigma}_{\mathbf{R}_k M} \end{aligned} \tag{1.32}$$

where the real-space *hopping amplitudes* $t_{ij}^{LL'\sigma}$ and the *interaction parameters* $U_{i\ j\ k\ l}^{LL'MM'\sigma\sigma'}$ are respectively given by:

$$\begin{aligned} t_{ij}^{LL'\sigma} &= \int_{\mathbb{R}^3} d^3\mathbf{r} \quad \left[\chi^{\mathbf{R}_i}_{L\sigma}(\mathbf{r})\right]^* \left[-\frac{\hbar^2}{2m_0}\nabla^2_{\mathbf{r}} + V_{KS}(\mathbf{r})\right] \chi^{\mathbf{R}_j}_{L'\sigma}(\mathbf{r}) \\ U_{i\ j\ k\ l}^{LL'MM'\sigma\sigma'} &= \int_{\mathbb{R}^3}\int_{\mathbb{R}^3} d^3\mathbf{r} d^3\mathbf{r}' \quad \left[\chi^{\mathbf{R}_i}_{L\sigma}(\mathbf{r})\right]^* \left[\chi^{\mathbf{R}_j}_{L'\sigma'}(\mathbf{r})\right]^* \widetilde{V}_{ee}(\mathbf{r},\mathbf{r}')\ \chi^{\mathbf{R}_l}_{M'\sigma'}(\mathbf{r}) \chi^{\mathbf{R}_k}_{M\sigma}(\mathbf{r}). \end{aligned} \tag{1.33}$$

For the study of the basic physical mechanisms, simpler lattice model Hamiltonians are traditionally used. They are derived from the general expression (1.32) by reducing the number of matrix elements to the dominant contributions. For instance, to derive the *single band* [73] or the *multi-orbital Hubbard models* [74, 75], the hopping elements $t_{ij}^{LL'\sigma}$ are usually restricted to nearest-neighbor and next-nearest-neighbor terms and the *local* intra-atomic interaction parameters $U_{i\ i\ i\ i}^{LL'MM'\sigma\sigma'}$ are expected to strongly dominate.

Consequently, the resulting Hamiltonian for the *single-band Hubbard model* reads:

$$H = \sum_{\langle i,j\rangle,\sigma} t_{ij}\ c_i^{\sigma\dagger} c_j^{\sigma} + U \sum_i n_{i\uparrow} n_{i\downarrow} + (\varepsilon_0 - \mu) \sum_{i,\sigma} c_i^{\sigma\dagger} c_i^{\sigma} \tag{1.34}$$

where we used i instead of $\mathbf{R}_i$ and the operator $n_{i\sigma} = c_i^{\sigma\dagger} c_i^{\sigma}$ to simplify the notations. Because of the translational invariance of the system, the hopping amplitude t_{ij} is t for all nearest-neighbors i and j, t' for all next-nearest-neighbors i and j, and 0 otherwise. Moreover, this one-particle part of the Hamiltonian (1.34) can be diagonalized in $\mathbf{k}$-space. The chemical potential μ and the energy ε_0 of the single-electron atomic level have been introduced to write the Hamiltonian in its more general form.

Using similar shortened notations, the *multi-orbital Hubbard model* reads:

$$H = \sum_{\langle i,j\rangle,\sigma} \sum_{L,L'} t_{ij}\ c_{iL}^{\sigma\dagger} c_{jL}^{\sigma} + \sum_i \sum_{L,L',\sigma,\sigma'} U_{LL'}^{\sigma\sigma'}\ n_{iL\sigma} n_{iL'\sigma'} + \sum_{i,L,\sigma} (\varepsilon_L - \mu)\ c_{iL}^{\sigma\dagger} c_{iL}^{\sigma} \tag{1.35}$$

where the on-site interaction term $U_{LL'}^{\sigma\sigma'}$ is generally parametrized as follows:

$$\begin{aligned} &\sum_L U\ n_{L\uparrow} n_{L\downarrow} + \sum_{L>M} \sum_{\sigma} U'\ n_{L\sigma} n_{M\bar{\sigma}} + (U' - J)\ n_{L\sigma} n_{M\sigma} \\ &- \sum_{L\neq M} J\ \left[\psi^{\dagger}_{L\downarrow}\psi^{\dagger}_{M\uparrow}\psi_{M\downarrow}\psi_{L\uparrow} + \psi^{\dagger}_{M\uparrow}\psi^{\dagger}_{M\downarrow}\psi_{L\uparrow}\psi_{L\downarrow} + h.c.\ \right]. \end{aligned} \tag{1.36}$$

Moreover, if one considers a lattice model restricted only to the t_{2g} orbitals[6] for each atom, the

[6] A brief reminder about the definition of the e_g and t_{2g} atomic orbitals can be found in Appendix A.

parameter U' takes the value $U - 2J$ and the multi-orbital Hubbard model can then be rewritten as:

$$\begin{aligned} H &= \sum_{\langle i,j\rangle,\sigma} \sum_{L,L'} t_{ij}\ c^{\sigma\dagger}_{iL} c^{\sigma}_{jL} + \sum_{i,L,\sigma} (\varepsilon_L - \mu)\ c^{\sigma\dagger}_{iL} c^{\sigma}_{iL} \\ &+ \sum_{L} U\ n_{L\uparrow} n_{L\downarrow} + \sum_{L>M} \sum_{\sigma} (U - 2J)\ n_{L\sigma} n_{M\bar{\sigma}} + (U - 3J)\ n_{L\sigma} n_{M\sigma} \\ &- \sum_{L\neq M} J\ \left[\psi^{\dagger}_{L\downarrow}\psi^{\dagger}_{M\uparrow}\psi_{M\downarrow}\psi_{L\uparrow} + \psi^{\dagger}_{M\uparrow}\psi^{\dagger}_{M\downarrow}\psi_{L\uparrow}\psi_{L\downarrow} + h.c.\ \right]. \end{aligned} \tag{1.37}$$

The Hamiltonian (1.37) with U and J has been constructed such that it is rotationally invariant both in orbital and spin space. If we assume that the *Hund's coupling* J is small compared to the *on-site Coulomb repulsion* U, we can either set it to zero entirely or just set the exchange and pair-hopping terms – of the third line – to zero. In both cases, the Hamiltonian will finally contain only density-density terms.

1.3.3 Examples of strongly correlated materials

Strongly correlated materials are generally associated with partially filled d or f-shells. As a result, these materials are made of:

- transition metal elements, particularly from the $3d$-shell from Titane (Ti) to Copper (Cu), and to a lesser extent from the $4d$-shell from Zirconium (Zi) to Silver (Ag),
- rare earth ($4f$-shell) from Lanthanum (La) to Ytterbium (Yb), or actinide elements ($5f$-shell) from Actinium (Ac) to Nobellium (No).

In the following, we briefly describe the key issues arising in these compounds and give a few representative examples in each case. The interested reader can find in reviews [55, 66, 76] more important discussions on this topic.

Transition metals

In $3d$-transition metals, the $4s$ orbitals have lower energy than the $3d$ and are thus filled first. Moreover, the $4s$ orbitals extend much further from the nucleus and overlap strongly. This holds the atoms sufficiently so that the $3d$ orbitals have a small direct overlap, hence forming band neither extremely narrow nor really wide.

In addition, the $3d$ orbital wavefunctions are confined closer to the nucleus than the other orbitals. They then undergo an efficient Coulomb repulsion, despite the screening of the $4s$ orbitals. For these two reasons, electron correlations do have important physical effects for $3d$-transition metals, but not extreme ones leading to a complete localization.

Consequently, band structure calculations based on DFT-LDA methods generally overestimate the width of the occupied d-band – by about 30% in the case of Nickel (Ni), for instance [55]. Furthermore, some features observed in spectroscopy experiments – such as the 6 eV satellite in Ni – are also signatures of correlation effects, and are not reproduced by standard electronic structure calculations.

Transition metal oxides

In transition metal compounds – oxides or chalcogenides –, the direct overlap between d-orbitals is generally so small that d electrons can only move through hybridization with the ligand atoms. This leads then to the formation of quite narrow bands and the correlation can then play an even more significant role than in simple transition metals.

As a result, these systems can even turn into Mott insulator, like the d^1-compounds lanthanum titanate ($LaTiO_3$) or yttrium titanate ($YTiO_3$) [130]. For such system, band structure calculations

based on DFT-LDA methods completely fail as a metallic behavior is always predicted. For the same reason, DFT calculations also failed in describing the metal-insulator transition in compounds like vanadium dioxide (VO_2) and vanadium sesquioxide (V_2O_3) [158].

But even for *metallic* transition metal oxides, the LDA band structure can be found to disagree with experimental observations: this is for instance the case for strongly correlated metal strontium vanadate ($SrVO_3$) [101].

Rare earth and actinides

A distinctive character of the physics of rare-earth metals is that the $4f$ electrons tend to be localized rather than itinerant at ambient pressure. The f-electrons then contribute little to the cohesive energy of the solid, and the unit cell volume depends very weakly on the filling of the $4f$-shell.

For these materials, ground-state properties, such as equilibrium unit cell volume, are not accurately predicted from LDA calculations. A spectacular example is the δ-phase of metallic Plutonium (Pu) in which the unit cell volume is underestimated (compared to the experimental value) by as much as 35% [55].

All these examples illustrate the need of a a method which is able to handle intermediate situations between "fully localized" and "fully itinerant" electrons. The "*dynamical mean-field theory*" (DMFT) is a technique which was developed in the early nineties with this aim in view.

1.4 The Dynamical Mean-Field Theory (DMFT)

In this section, we introduce the "*dynamical mean-field theory*" (DMFT) [57, 98], which can be seen as an extension to quantum many-body systems of classical mean-field approach. This theory has been a major breakthrough in the understanding of correlated materials since it allowed a consistent description of both the low-energy coherent features – the long-lived quasiparticle excitations – and the incoherent high-energy excitations due to the Coulomb repulsion, acting on short timescales.

In the following, we first present the main features of this quantitative method, assuming that the reader is familiar with the fundamentals of many-body physics and Landau's theory of Fermi liquid. We then provide a general description of the Mott transition within the DMFT framework by basing our discussion on the example of the half-filled one-band Hubbard model (1.34) on a Bethe lattice in infinite dimensions.

1.4.1 Introduction to the theory

The underlying physical idea in a mean-field approach of a lattice problem is that the dynamics at a given site of the can be understood as the interaction of the *local degrees of freedom* at this site with an "*external bath*" created by all other degrees of freedom on the other sites. To make it simple, one obtains the "*dynamical mean-field theory*" (DMFT) by merely applying this idea to the quantum case.

Historically, the most important steps leading to this quantum generalization were the introduction of the limit of large lattice coordination for interacting fermion models in 1989 by Müller-Hartmann [123] and Metzner and Vollhardt [113] and the mapping of the reference system onto a self-consistent quantum impurity model in 1992 by Georges and Kotliar [56].

We derive here DMFT equations on the simplest example of the single-band Hubbard model:

$$H = \sum_{\langle i,j\rangle,\sigma} t_{ij}\; c_i^{\sigma\dagger} c_j^{\sigma} + U \sum_i n_{i\uparrow} n_{i\downarrow} + (\varepsilon_0 - \mu) \sum_{i,\sigma} c_i^{\sigma\dagger} c_i^{\sigma}. \tag{1.34}$$

With this Hamiltonian and in the absence of hopping $t_{ij} = 0$, each atom has four eigenstates:

- $|0\rangle$ with energy 0,
- $|\uparrow\rangle$ and $|\downarrow\rangle$, both with energy $\varepsilon_0 - \mu$,
- $|\uparrow\downarrow\rangle$ with energy $2(\varepsilon_0 - \mu) + U$.

The key quantity on which DMFT focuses is the local Green's function at a given lattice site i, defined by:

$$\forall\tau,\tau' \qquad \forall\sigma =\uparrow,\downarrow \qquad G_{ii}^{\sigma}(\tau-\tau') = -\langle T[c_i^{\sigma}(\tau)c_i^{\sigma\dagger}(\tau')]\rangle. \tag{1.38}$$

Because of the translational invariance of the system, this quantity is the same for all site i and we will merely refer to it as $G_{loc}^{\sigma}(\tau-\tau')$ in the following. In a completely similar manner as in the classical mean-field theory, one then introduces a representation of the local Green's function as a function of "*a single atom coupled to an effective bath*". This step can be performed by using the Hamiltonian of an Anderson impurity model (AIM) [7]:

$$H_{AIM} = H_{atom} + H_{bath} + H_{coupling} \tag{1.39}$$

where H_{atom} describes the local energy on the "*atomic (or impurity) site*":

$$H_{atom} = U\ n_{i\uparrow}n_{i\downarrow} + (\varepsilon_0 - \mu)(n_{i\uparrow} + n_{i\downarrow}) \tag{1.40}$$

a set of non-interacting fermions (described by the field operators $a_{l\sigma}^{\dagger}$ and $a_{l\sigma}$) has been introduced to describe the "*effective external bath*":

$$H_{bath} = \sum_{l\sigma} \widetilde{\varepsilon}_l\ a_{l\sigma}^{\dagger}a_{l\sigma} \tag{1.41}$$

and $H_{coupling}$ describes the processes of bath fermions hopping on or off the atomic site with amplitude V_l:

$$H_{coupling} = \sum_{l\sigma} V_l\ (a_{l\sigma}^{\dagger}c_i^{\sigma} + c_i^{\sigma\dagger}a_{l\sigma}) \tag{1.42}$$

The parameters $\widetilde{\varepsilon}_l$ and V_l should be chosen in such a way that the impurity Green's function $G_{imp}^{\sigma}(\tau-\tau')$ of (1.39) coincides with the local Green's function $G_{loc}^{\sigma}(\tau-\tau')$ of the lattice Hubbard model under consideration:

$$\forall\tau,\tau' \qquad \forall\sigma =\uparrow,\downarrow \qquad G_{imp}^{\sigma}(\tau-\tau') = G_{loc}^{\sigma}(\tau-\tau'). \tag{1.43}$$

They also enable to define an *hybridization function*:

$$\Delta(i\omega_n) = \sum_l \frac{|V_l|^2}{i\omega_n - \widetilde{\varepsilon}_l}. \tag{1.44}$$

This is easily seen when the effective on-site problem is recast in a form which does not explicitly involves the effective bath degrees of freedom. However, this requires the use of an effective action S_{eff} based on the functional integral formalism rather than a simple Hamiltonian formalism. Integrating out the bath degrees of freedom, this effective action can indeed be written as:

$$S_{\text{eff}} = -\int_0^{\beta} d\tau \int_0^{\beta} d\tau' \sum_{\sigma} c_i^{\sigma\dagger}(\tau)\mathcal{G}_0^{-1}(\tau-\tau')c_i^{\sigma}(\tau') + U\int_0^{\beta} d\tau\ n_{i\uparrow}n_{i\downarrow} \tag{1.45}$$

where $c_i^{\sigma\dagger}$ and c_i^{σ} are the Grassmann variables corresponding to the local "atomic" state and

$$\mathcal{G}_0^{-1}(i\omega_n) = i\omega_n + \mu - \varepsilon_0 - \Delta(i\omega_n). \tag{1.46}$$

In expression (1.45), $\mathcal{G}_0$ plays the role of a *bare Green's function* for the effective action S_{eff}, but it should not be confused with the non-interacting local Green's function of the original lattice model (obtained for $U = 0$). Moreover, one can interpret $\mathcal{G}_0^{-1}(\tau - \tau')$ – or equivalently $\Delta(i\omega_n)$ – as the quantum generalization of the Weiss effective field in the classical case. The main difference with the classical case is that this "*dynamical mean-field*" is a function of energy – or time – instead of a single number.

The local action (1.45) represents the effective dynamics of the local site under consideration: a fermion is created on the site i at time τ (coming from the *external bath*, in other words from the other sites of the lattice) and is destroyed at time τ' (going back to the bath). Whenever two fermions – with opposite spins – are present at the same time, an energy cost U is included. This effective action thus describes the fluctuations between the four atomic states $|0\rangle$, $|\uparrow\rangle$, $|\downarrow\rangle$ and $|\uparrow\downarrow\rangle$ induced by the coupling to the bath, as displayed on figure 1.1. Taking full account of these local quantum fluctuations is precisely the main purpose of DMFT.

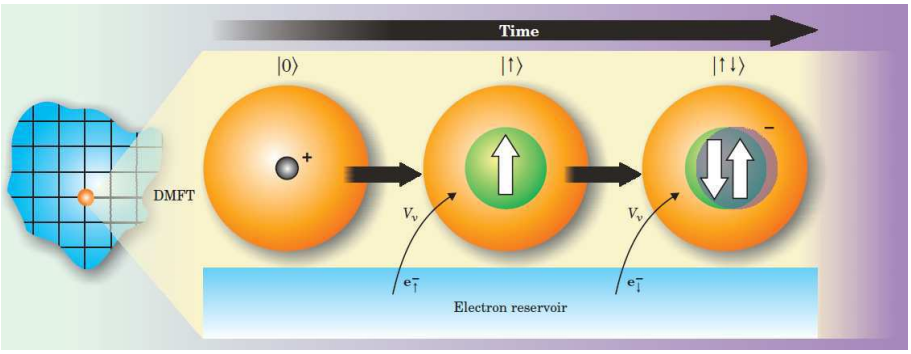

Figure 1.1: DMFT enables to describe the fluctuations on a lattice site between the four atomic states $|0\rangle$, $|\uparrow\rangle$, $|\downarrow\rangle$ and $|\uparrow\downarrow\rangle$ induced by the coupling to an *external effective bath*. From [99].

So far, we have introduced the quantum generalization of the Weiss effective field and have represented the local Green's function $\mathbf{G}_{loc}(\tau - \tau')$ as that of a single atom coupled to an effective bath. This can be viewed as an exact representation. We now have to generalize to the quantum case the *mean-field approximation* relating the Weiss function $\mathcal{G}_0^{-1}(\tau - \tau')$ to $\mathbf{G}_{loc}(\tau - \tau')$. The simplest manner to explain it is to observe that, in the effective impurity model (1.45), we can define a local self-energy from the interacting Green's function $G^{\sigma}_{imp}(\tau - \tau') = -\langle T[c_i^{\sigma}(\tau)c_i^{\sigma\dagger}(\tau')]\rangle_{S_{\text{eff}}}$ and the Weiss dynamical mean-field as:

$$\mathbf{\Sigma}_{imp}(i\omega_n) = \mathcal{G}_0^{-1}(i\omega_n) - \mathbf{G}_{imp}^{-1}(i\omega_n) = i\omega_n + \mu - \varepsilon_0 - \Delta(i\omega_n) - \mathbf{G}_{imp}^{-1}(i\omega_n). \tag{1.47}$$

On the contrary, the self-energy of the original lattice model can be defined as usual from the full Green's function $G^{\sigma}_{i-j}(\tau - \tau') = -\langle T[c_i^{\sigma}(\tau)c_j^{\sigma\dagger}(\tau')]\rangle$ by:

$$\mathbf{G}(\mathbf{k}, i\omega_n) = \frac{1}{i\omega_n + \mu - \varepsilon_0 - \varepsilon_{\mathbf{k}} - \mathbf{\Sigma}(\mathbf{k}, i\omega_n)} \tag{1.48}$$

in which $\varepsilon_{\mathbf{k}}$ is the Fourier transform of the hopping integral:

$$\varepsilon_{\mathbf{k}} = \sum_j t_{ij} e^{i\mathbf{k}\cdot(\mathbf{R}_i - \mathbf{R}_j)}. \tag{1.49}$$

The "*DMFT approximation*" then consists in identifying the lattice self-energy and the impurity self-energy. In real-space, this means that all non-local components $\mathbf{\Sigma}_{ij}(i\omega_n)$ are neglected and the on-site components are approximated by $\mathbf{\Sigma}_{imp}(i\omega_n)$:

$$\forall i\omega_n \qquad \forall i \qquad \mathbf{\Sigma}_{ii}(i\omega_n) \approx \mathbf{\Sigma}_{imp}(i\omega_n) \qquad \text{and} \qquad \forall i,j \qquad \mathbf{\Sigma}_{ij}(i\omega_n) \approx 0. \tag{1.50}$$

Summing (1.48) over $\mathbf{k}$ in order to obtain the on-site component $\mathbf{G}_{loc}(i\omega_n)$ of the the lattice Green's function, and using (1.47), one finally gets the "*self-consistency condition*":

$$\sum_{\mathbf{k}} \frac{1}{i\omega_n + \mu - \varepsilon_0 - \varepsilon_{\mathbf{k}} + \mathbf{G}^{-1}(i\omega_n) - \mathcal{G}_0^{-1}(i\omega_n)} = \mathbf{G}(i\omega_n) \tag{1.51}$$

or by considering explicitly the hybridization function:

$$\sum_{\mathbf{k}} \frac{1}{\Delta(i\omega_n) + \mathbf{G}^{-1}(i\omega_n) - \varepsilon_{\mathbf{k}}} = \mathbf{G}(i\omega_n). \tag{1.52}$$

The expression (1.52) can also be written as:

$$\int d\varepsilon \frac{D(\varepsilon)}{\Delta(i\omega_n) + \mathbf{G}^{-1}(i\omega_n) - \varepsilon} = \mathbf{G}(i\omega_n) \qquad \text{with} \qquad D(\varepsilon) = \sum_{\mathbf{k}} \delta(\varepsilon - \varepsilon_{\mathbf{k}}). \tag{1.53}$$

where $D(\varepsilon)$ is the non-interacting density of states.

This *self-consistency condition* relates, for each frequency, the dynamical mean-field $\Delta(i\omega_n)$ – or $\mathcal{G}_0(i\omega_n)$ – and the local Green's function $\mathbf{G}(i\omega_n)$. Furthermore, $\mathbf{G}(i\omega_n)$ is also the interacting Green's function of the effective impurity model (1.39) – or (1.45) – since by construction:

$$\forall i\omega_n \qquad \mathbf{G}_{loc}(i\omega_n) = \mathbf{G}_{imp}(i\omega_n) = \mathbf{G}(i\omega_n). \tag{1.43}$$

Therefore, the set of DMFT equations is closed and fully determines in principle the two functions Δ and $\mathbf{G}$ – or $\mathcal{G}_0$ and $\mathbf{G}$.

In practice, one uses an iterative procedure based on a self-consistency loop to solve this problem. In many cases, this iterative procedure converges to a unique solution independently of the initial choice of $\Delta(i\omega_n)$. In some cases however, more than one stable solution can be found, especially close to the Mott transition.

1.4.2 Limits in which DMFT becomes exact

The DMFT equations yield the exact answer in three simple limits:

Infinite coordination limit

As the classical mean-field theory, DMFT becomes exact in the limit where the connectivity z of the lattice is taken to infinity. Apart from the intrinsic interest of solving strongly correlated fermion models in the limit of infinite coordination, this property guarantees that exact constraints – such as the causality of the self-energy, the non-negativity of the spectral functions, the Luttinger theorem or other sum rules – are preserved by the DMFT approximation.

Non-interacting limit

In the non-interacting limit – that is to say when $U = 0$ in (1.34) –, the *DMFT approximation* (1.50) is trivially exact since the self-energy is not only **k**-independent but merely vanishes. As a result, solving the impurity problem (1.45) yields $\mathbf{G}(i\omega_n) = \mathcal{G}_0(i\omega_n)$ and, by using the condition (1.51), $\mathbf{G}(i\omega_n)$ reduces to the free on-site Green's function, as expected:

$$\forall \quad \sigma = \uparrow, \downarrow \qquad G^\sigma(i\omega_n) = \sum_{\mathbf{k}} \frac{1}{i\omega_n + \mu - \varepsilon_0 - \varepsilon_{\mathbf{k}}}. \tag{1.54}$$

Atomic limit

In the atomic limit – that is to say when $t_{ij} = 0$ in (1.34) –, the model consists in a collection of isolated atoms on each site. As a result, the *DMFT approximation* is again exact since the self-energy has only on-site components. In this case, the dynamical mean field $\mathcal{G}_0(i\omega_n)$ vanishes in (1.45) and the action S_{eff} merely corresponds to the quantization of the atomic Hamiltonian H_{atom} (1.40). This yields:

$$\begin{aligned} \forall \quad \sigma = \uparrow, \downarrow \quad G^\sigma(i\omega_n) &= \left(1 - \frac{n}{2}\right) \frac{1}{i\omega_n + \mu - \varepsilon_0} + \frac{n}{2} \frac{1}{i\omega_n + \mu - \varepsilon_0 - U} \\ \text{and} \qquad \Sigma^\sigma(i\omega_n) &= \frac{n}{2} U \;+\; \frac{n}{2}\left(1 - \frac{n}{2}\right) \frac{U^2}{i\omega_n + \mu - \varepsilon_0 - (1 - \frac{n}{2})U} \\ \text{with} \qquad \frac{n}{2} &= \frac{e^{\beta(\mu - \varepsilon_0)} + e^{\beta(2(\mu - \varepsilon_0) + U)}}{1 + 2e^{\beta(\mu - \varepsilon_0)} + e^{\beta(2(\mu - \varepsilon_0) + U)}}. \end{aligned} \tag{1.55}$$

Thus, besides the case of infinite dimensions, DMFT is exact in the two limits of the *non-interacting band* and of the *isolated atoms* and can then be seen as providing an interpolation between them.

1.4.3 Impurity solvers

Using reliable methods for calculating the impurity Green's function and self-energy is a key step in solving the DMFT equations. "*Impurity solvers*" can be classified into two main types:

- the analytical methods, like the iterated perturbation theory (IPT) [56, 81] or the non-crossing approximation (NCA) [98],
- the numerical techniques, such as the exact diagonalization [30, 138], the renormalization group (NRG) [28] and the quantum Monte Carlo algorithms (QMC) [69, 141, 165].

We provide here only a short introduction to the QMC methods since our calculations on strontium iridate (Sr_2IrO_4) were performed by using a continuous time QMC (CTQMC) technique [141, 165]. A more thorough description and analysis of *impurity solvers* can be found in [57].

The major advantage of QMC solvers over other impurity solvers is that they are numerically exact, easily adapted to multiple orbital systems or clusters, and fast enough to reach low temperatures. However, their main disadvantage is that they work on the imaginary time (or Matsubara axis). Real frequency data like spectra or optical conductivities have thus to be extracted via analytical continuation [78]. Two main QMC algorithms are in wide use in the community:

The algorithm of Hirsch and Fye [69] was developed long before DMFT as an algorithm to solve the Anderson impurity model. It was the first QMC algorithm applied to the DMFT impurity

problem and is still very popular. This algorithm is based on a Trotter-Suzuki decomposition of the effective action S_{eff} (1.45) and a discrete Hubbard-Stratonovich transformation [67, 68]. It therefore requires a discretization of imaginary time into N so-called "*time slices*" $\Delta\tau = \beta/N$.

The CTQMC algorithms: In 2005 Rubtsov *et al.* [141] introduced the "*weak-coupling CTQMC algorithm*" for fermions and in 2006 Werner *et al.* [165] the "*strong-coupling CTQMC algorithm*". The interested reader can find a detailed presentation of these techniques in [61, 63]. Both these methods have the main advantage of relying on *continuous* time. As a result, they are free of any systematic error due to a time discretization and can resolve accurately the behavior of the Green's function for lower temperatures and stronger interaction regime than the Hirsch-Fye algorithm[7]. For these main reasons, CTQMC methods are steadily gaining importance in the field.

1.4.4 Theory of the Mott transition within DMFT

By applying DMFT on the Hubbard model, huge progress in the understanding of the Mott transition have been made. In the following, we briefly review the key features of this phenomenon. More details on the Mott metal-insulator transition are available in the review [57] and in the following original references [56, 58, 59, 100, 139, 140].

To illustrate our discussion, we will consider the half-filled one-band Hubbard model (1.34) on a Bethe lattice in infinite dimensions. In this case, the density of states (DOS) of the band is semi-circular, as depicted in figure 1.2. The schematized phase diagram of this model represented as a function of the interaction U and the temperature T is shown in figure 1.3.

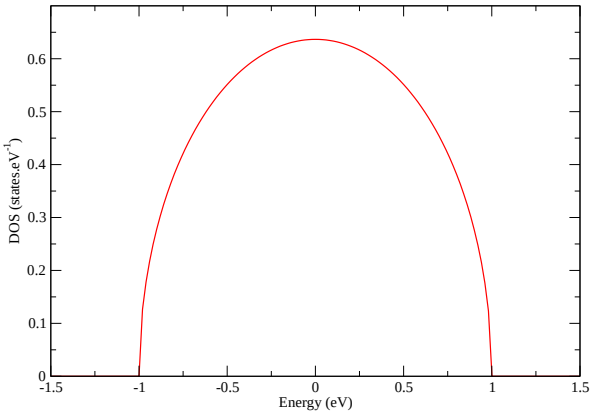

Figure 1.2: Density of states of the Bethe lattice in infinite dimensions, with an half bandwidth $D = 1.0$ eV.

Non-interacting limit

As already mentioned, in the non-interacting limit ($U = 0$), the Hamiltonian (1.34) is diagonal in $\mathbf{k}$-space. As a result, the spectral function of the system at a given momentum is a Dirac distribution:

$$A(\mathbf{k},\omega) = -\frac{1}{\pi}\mathfrak{Im}\left[G(\mathbf{k},\omega)\right] = \delta(\omega - \varepsilon_{\mathbf{k}}) \tag{1.56}$$

[7] Indeed, the computation time of Hirsch-Fye algorithm approximately scales as $O(N^3)$ whereas its grid spacing is generally required to be $N \approx 5\ \beta U$ to ensure a sufficient resolution.

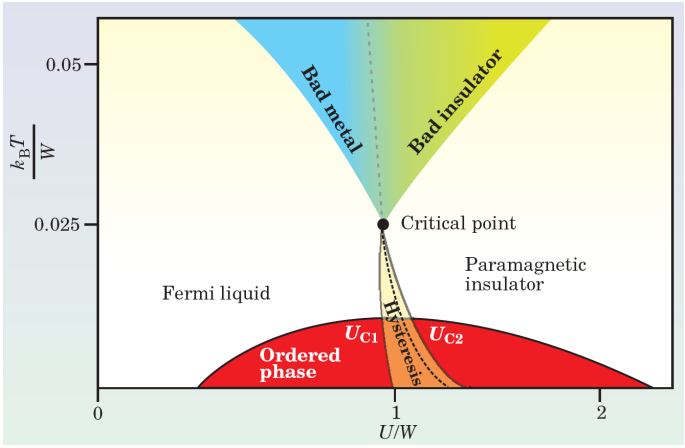

Figure 1.3: Schematic phase diagram of the one band half-filled Hubbard model (1.34) within DMFT. The axes correspond to the temperature T and the Coulomb repulsion U. Energies are normalized by the bandwidth of the model $W = 2D$. From [99].

and the self-energy is of course zero. The total local spectral function $A(\omega) = \sum_{\mathbf{k}} A(\mathbf{k}, \omega)$ coincides with the density of states shown in figure 1.2.

The Fermi liquid regime

At low temperature and moderate interaction strength, the system exhibits the "*Fermi liquid regime*". The DMFT spectral function $A(\omega)$ – at T=0 K – presented in figure 1.4-a displays the famous "*three-peak structure*", made of a quasi-particle band close to the Fermi energy surrounded by the lower and upper Hubbard bands. The quasi-particle part has a reduced bandwidth of order $Z.D \sim \varepsilon_F^*$, where D is the half-bandwidth of the non-interacting initial system and Z the quasi-particle weight. This energy scale can also be interpreted as the coherence-scale for the quasi-particles. Moreover, the value $A(\omega = 0)$ is pinned to its non-interacting value, which means that the correlations do not modify the Fermi surface [124]. In addition to low energy quasi-particles, the preformed Hubbard bands accommodate the weight $1 - Z$ which is transferred from lower energies. They can be associated to the atomic-like transitions corresponding to the addition or removal of one electron on an atomic site.

When looking at the corresponding self-energy presented in figure 1.4-b, the characteristics of the Fermi liquid are present: the real-part is linear in frequency, with a negative slope, around the Fermi-level and the imaginary part is proportional to ω^2. However, already at rather low energies, the self-energy deviates substantially from its low-energy behavior. Furthermore, the real-part has the same behavior at high energy as the atomic limit: $\Sigma(\omega \to +\infty) \approx U^2/4\omega$ and approaches the constant Hartree term, which is zero at half-filling. The matching of these two very different behaviors results in a pronounced frequency dependence in the intermediate regime, leading to the observed prominent peak in the imaginary part.

An increase in temperature induces a finite scattering rate even at the Fermi level. This scattering rate corresponds to a finite value in the imaginary part of the self-energy at zero energy and results into the violation of the previously mentioned pinning condition: the spectral function at zero energy is no longer bound to its non-interacting value, but is considerably reduced.

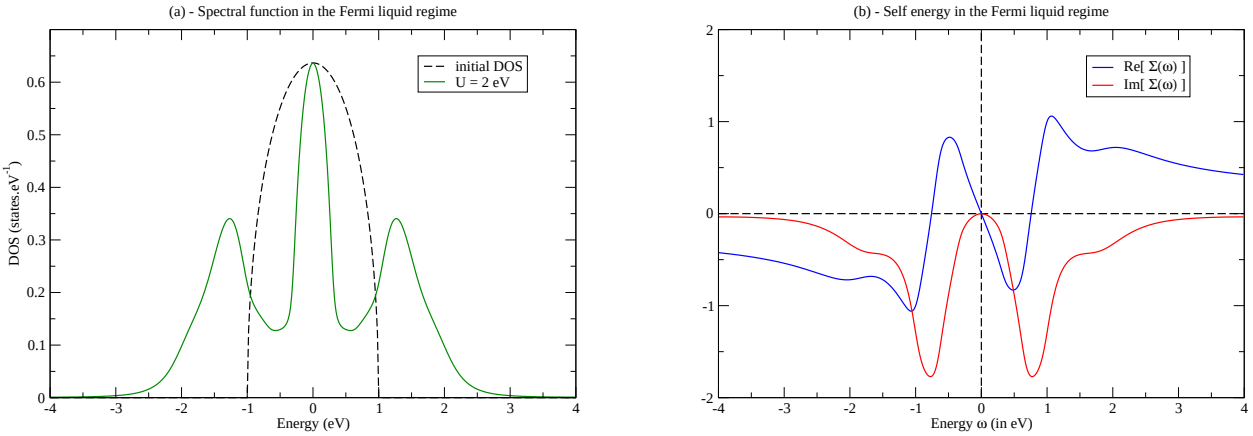

Figure 1.4: DMFT spectral function $A(\omega)$ (panel a) and self-energy $\Sigma(\omega)$ (panel b) for the one band half-filled Hubbard model (1.34) on the Bethe lattice in infinite dimensions with U=2 eV. The calculations were performed at T=0 K with the iterated perturbation theory (IPT).

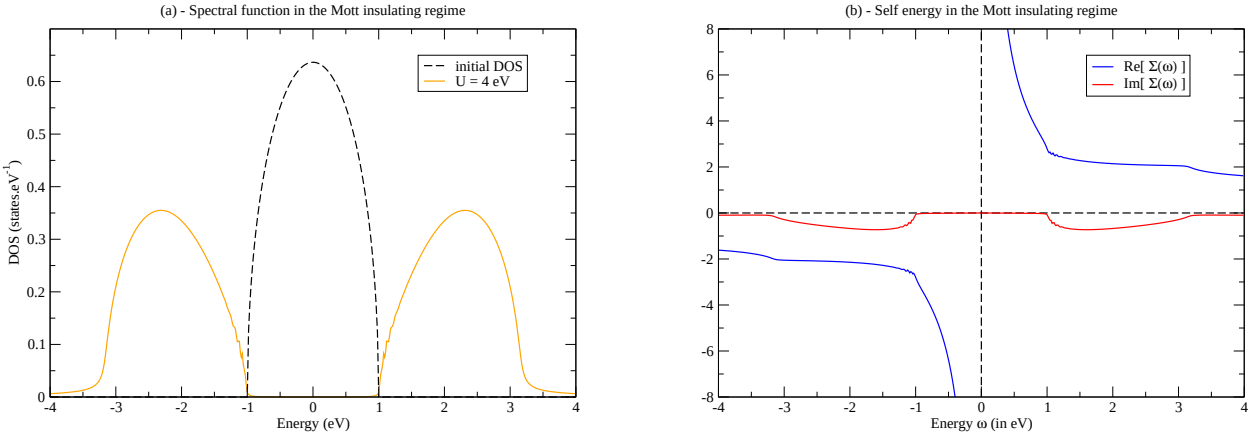

Figure 1.5: Same as figure 1.4, but with U=4 eV.

The Mott insulating state

At strong enough coupling, the system becomes a "*Mott insulator*". The gap $\Delta \approx U$ is indeed clearly seen on the corresponding DMFT spectral function $A(\omega)$ – at T=0 K – displayed in figure 1.5-a. Since at half-filling, the real part of the self-energy is an anti-symmetric function, it has to vanish at zero frequency. As a consequence the elimination of spectral weight at the Fermi level can only be achieved by a divergence of the imaginary part, as observed on figure 1.5-b.

In addition, this insulating phase is characterized by unscreened local moments, associated with a Curie law for the local susceptibility $\sum_{\mathbf{q}} \chi_{\mathbf{q}} \approx \frac{1}{T}$ and an extensive entropy. As temperature is lowered, these local moments order into an *antiferromagnetic phase*. On the contrary, upon heating, thermal fluctuations lead to a filling of the gap and a curing of the divergence in the imaginary part of the self-energy. The latter thus reaches a finite value at zero frequency.

The transition lines

The Mott metal-insulator transition is of *first order*, and thus exhibits a *coexistence region* in the phase diagram, as seen on figure 1.3. At $T = 0$ K, the mean-field solution corresponding to the paramagnetic metal indeed disappears at a critical coupling U_{c2} whereas the mean-field insulating solution is found for $U > U_{c1}$. More precisely, at the point U_{c2} the quasi-particle weight vanishes ($Z \approx 1 - U/U_{c2}$) as in the Brinkman-Rice theory [27] while the Mott gap Δ opens up at U_{c1}. For the half-filled one-band Hubbard model, the value for U_{c1} and U_{c2} at T=0 K are 3 D and 2.5 D respectively.

These two critical couplings extend at finite temperature into two spinodal lines $U_{c1}(T)$ and $U_{c2}(T)$ and end in a critical point, above which the transition from a high-conductivity to the high-resistivity phase is continuous. The phase diagram is thus similar to the one of the liquid-gas transition, casting the metal-insulator Mott transition into the Ising universality class [96, 97].

In a realistic multi-band setup, the situation becomes more involved [133]. In particular, a modification of the Fermi surface becomes possible through a local self-energy that causes charge transfers between different orbitals. Moreover the necessity of a divergent mass for a Mott transition gets relaxed. Indeed a correlation enhancement of crystal field splittings may cause a shifting of spectral weight and thus lead to the separation of former bands at the Fermi level. Responsible for this will be the orbital dependence in the real-parts in the self-energy, which need no longer vanish at zero energy, as was the case for the half-filled one-band model.

Chapter 2

Combining DFT-LDA calculations with DMFT: the LDA+DMFT approach

As emphasized in sections 1.2 and 1.3, the screened Coulomb interaction is responsible for the failure of DFT-LDA calculations in giving a reliable independent-particle description of correlated materials. Indeed, in these systems, the band formation – well-described in the **k**-space – and the tendency to localization – rather described in real space – coexist and a theoretical framework in which these both issues are treated on an equal footing is necessary.

The dynamical mean-field theory (DMFT), introduced in section 1.4, is a quantitative method which was precisely developed in the early nineties for handling electron correlations. Since then, it has led to significant advances in the understanding of strong correlation physics, especially by allowing to describe the Mott metal-insulator transition.

In order to overcome the shortcomings of DFT-LDA for strongly correlated materials, the combination of the electronic band structure techniques with DMFT was suggested [57] and the first descriptions of the so-called "*LDA+DMFT formalism*" appeared in 1997-1998 [11, 104]. The success of this approach was such that numerous implementations have been developed and applied to the calculations of the spectral properties of many materials over the past decades [98].

In this chapter, we first introduce the key steps involved in performing an LDA+DMFT calculation. This description is meant to be as general as possible, irrespective of any specific basis set, any band structure code or any impurity solver chosen to implement the method. On the contrary, the following sections focus on the technicalities of the implementation we have extended to perform our calculations on Sr_2IrO_4: this implementation is based on the "*linear augmented plane waves (LAPW) approach*" – and more precisely on the Wien2k program – and uses a "*projection scheme to localized Wannier-type orbitals*" [1] .

2.1 The LDA+DMFT formalism

2.1.1 General description of the method

The "*LDA+DMFT approach*" [104, 11] to electronic structure is based on the following "philosophy" : one extracts from an initial LDA calculations the part of the system which is assumed to exhibit *the most significant correlation effects* in order to treat it within DMFT, whereas the other part – considered as *less correlated* – is assumed well-described by the standard LDA approach. Consequently, its starting point is very similar to that of the "*LDA+U approach*" [13, 9], which combines LDA calculations with a static repulsion U.

However, DFT and DMFT rely on two different key quantities. On the one hand, a DFT cycle is built around the *total electronic charge density* $\rho(\mathbf{r})$ of the system but gives a description of the electronic wavefunctions based on the Bloch basis $|\psi^{\sigma}_{\mathbf{k}\nu}\rangle$, with ν the band index, σ the spin degree of freedom and $\mathbf{k}$ the momentum (cf. section 1.2). On the other hand, DMFT can be described as an effective atom approach and is based on the self-consistently determination of the *local one-particle Green's function* $\mathbf{G}_{loc}(i\omega_n)$ of the system.

In the LDA+DMFT formalism, both these quantities – namely $\rho(\mathbf{r})$ and $\mathbf{G}_{loc}(i\omega_n)$ – must be determined self-consistently, following an iterative cycle which is summarized on figure 2.1. The present description of LDA+DMFT follows this cycle, starting from a given charge density $\rho(\mathbf{r})$:

i) The DFT calculation

The first step is merely based on the Kohn-Sham equations introduced in section 1.2. A Kohn-Sham potential $V_{KS}[\rho(\mathbf{r})]$ is indeed found and the related one-particle Hamiltonian is diagonalized:

$$H|\psi^{\sigma}_{\mathbf{k}\nu}\rangle = \varepsilon^{\sigma}_{\mathbf{k}\nu}|\psi^{\sigma}_{\mathbf{k}\nu}\rangle. \tag{2.1}$$

Since the Bloch basis $|\psi^{\sigma}_{\mathbf{k}\nu}\rangle$ is a natural output of any electronic structure calculation, we will choose it in the following as the complete basis set to describe the full Hilbert space of the system.

ii) The "*projection operators*"

In order to formulate the *local effective atomic problem* for DMFT, one must build a set of localized basis functions $|\chi^{\alpha}_{L}\rangle$, where α labels an atom in the unit cell and L stands for all orbital indices $L = \{l, m, \sigma\}$. These functions will span the "*correlated*" subspace $\mathcal{C}$ of the full Hilbert space, in which many-body correlation effects – beyond the LDA – will be taken into account.

This set of orbitals $|\chi^{\alpha}_{L}\rangle$ is seldom the same as the complete basis set used to expand the Kohn-Sham eigenstates $|\psi^{\sigma}_{\mathbf{k}\nu}\rangle$ in the band structure code. The way to construct them is highly dependent on the implementation used and we will come back to this point later. For the current description, it is enough to introduce the following "*projection operator*" onto the subspace $\mathcal{C}$:

$$\mathbf{P}^{(\mathcal{C})}_{\alpha} = \sum_{|\chi^{\alpha}_{L}\rangle \in \mathcal{C}} |\chi^{\alpha}_{L}\rangle\langle\chi^{\alpha}_{L}|. \tag{2.2}$$

Building this projector corresponds to the second step of the cycle, called "*interfacing*" on figure 2.1. For simplicity, we will consider in the following that only a single type of atom is included in this projection, or in other words is correlated.

iii) The DMFT self-consistent loop

Once defined the correlated subspace $\mathcal{C}$, it is possible to construct the effective impurity model, defined by the bare Green's function – or *dynamical mean-field* – $[\mathcal{G}_0]^{\sigma}_{LL'}(i\omega_n)$ and the many-body interaction term H_U (1.36). Its action $\mathcal{S}_{\text{eff}}$ reads:

$$\mathcal{S}_{\text{eff}} = -\int_0^{\beta} d\tau \int_0^{\beta} d\tau' \sum_{LL'} c^{\dagger}_{L}(\tau) \left[\mathcal{G}_0^{-1}\right]_{LL'}(\tau - \tau') c_{L'}(\tau') + \int_0^{\beta} d\tau H_U(c^{\dagger}_{L}; c_{L}) \tag{2.3}$$

where $c^{\dagger}_{L}$ and c_{L} are the Grassmann variables corresponding to the correlated orbitals $|\chi_{L}\rangle$.

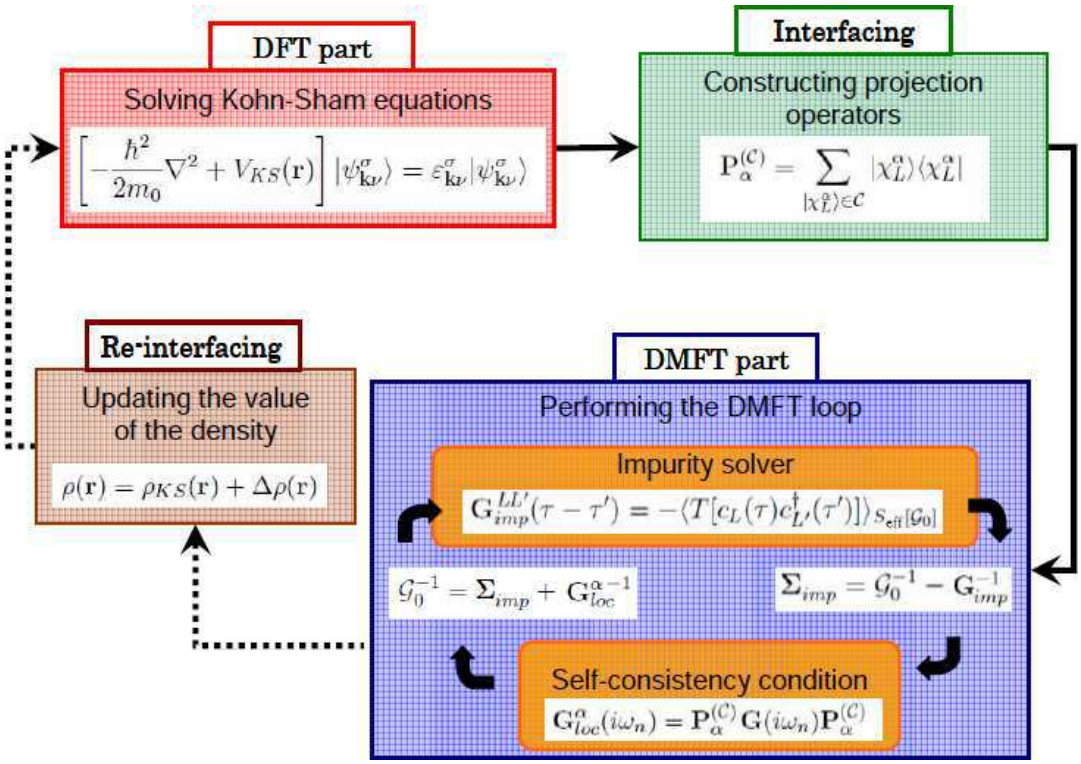

Figure 2.1: The complete self-consistent loop for LDA+DMFT:

*The charge $\rho(\mathbf{r})$ determines the Kohn-Sham potential from which the eigenvalues $\varepsilon^\sigma_{\mathbf{k}\nu}$ and Bloch states $|\psi^\sigma_{\mathbf{k}\nu}\rangle$ are calculated (**i**).*
*The correlated orbitals are then defined and their projector $\mathbf{P}^{(\mathcal{C})}_\alpha$ are constructed (**ii**) in order to perform the DMFT loop. The latter (**iii**) consists in:*
- solving the effective impurity problem for the impurity Green's function $\mathbf{G}_{imp}$, hence obtaining an impurity self-energy $\mathbf{\Sigma}_{imp}$;
- combining the self-energy correction with the Green's function of the solid $\mathbf{G}(i\omega_n)$ in order to calculate the local Green's function $\mathbf{G}^\alpha_{loc}(i\omega_n)$ – cf. equations (2.6),(2.7) and (2.8) –;
- finally obtaining an updated dynamical mean-field $\mathcal{G}_0$ for the impurity problem.
*Once the DMFT loop has converged, the chemical potential is updated and the new charge density – including many-body effects – is constructed (**iv**).*

As explained in section 1.4, the dynamical mean-field $\mathcal{G}_0$ is the relevant link in the inner self-consistent DMFT loop. Starting from the following initial guess:

$$\mathcal{G}_0(i\omega_n) = \mathbf{P}_\alpha^{(\mathcal{C})} \mathbf{G}_{KS}(i\omega_n) \mathbf{P}_\alpha^{(\mathcal{C})} \qquad \text{with} \qquad [\mathbf{G}_{KS}(\mathbf{k}, i\omega_n)]^\sigma_{\nu\nu'} = \frac{1}{i\omega_n + \mu - \varepsilon^\sigma_{\mathbf{k}\nu}} \delta_{\nu\nu'} \tag{2.4}$$

the effective impurity model is solved by using a suitable impurity solver. One then obtains the impurity Green's function $\mathbf{G}_{imp}(i\omega_n)$ as well as the impurity self-energy:

$$\left[\mathbf{\Sigma}_{imp}(i\omega_n)\right]_{LL'} = \left[\mathcal{G}_0^{-1}(i\omega_n)\right]_{LL'} - \left[\mathbf{G}_{imp}^{-1}(i\omega_n)\right]_{LL'} \qquad \forall\ |\chi_L^\alpha\rangle\ ,\ |\chi_{L'}^\alpha\rangle\ \in \mathcal{C}. \tag{2.5}$$

In order to have a full set of self-consistent equations, the effective impurity problem is related to the whole solid thanks to the *DMFT approximation* (1.50). It states that the self-energy correction in the solid must be non-zero only inside the (lattice-translated) correlated subspace and moreover exhibits only local components in the basis set $|\chi_L^\alpha\rangle$. The lattice self-energy correction $\Sigma^\sigma_{\nu\nu'}(\mathbf{k}, i\omega_n)$ is therefore obtained by the following relation:

$$\begin{aligned} \Sigma^\sigma_{\nu\nu'}(\mathbf{k}, i\omega_n) \quad &= \langle \psi^\sigma_{\mathbf{k},\nu} | \mathbf{P}_\alpha^{(\mathcal{C})} \left[\mathbf{\Delta\Sigma}^\alpha_{imp}(i\omega_n)\right]_{LL'} \mathbf{P}_\alpha^{(\mathcal{C})} | \psi^\sigma_{\mathbf{k},\nu'} \rangle \\ \text{with} \quad \left[\mathbf{\Delta\Sigma}^\alpha_{imp}(i\omega_n)\right]_{LL'} \quad &= \left[\mathbf{\Sigma}_{imp}(i\omega_n)\right]_{LL'} - \left[\mathbf{\Sigma}_{dc}\right]_{LL'}. \end{aligned} \tag{2.6}$$

In this expression, $\mathbf{\Sigma}_{dc}$ is the "*double-counting term*" for the local orbitals, which correct for correlation effects already included in conventional DFT.

Using then Dyson's equation, the Green's function of the solid $\mathbf{G}(\mathbf{k}, i\omega_n)$ is given by

$$[G^\sigma(\mathbf{k}, i\omega_n)]^{-1}_{\nu\nu'} = (i\omega_n + \mu - \varepsilon^\sigma_{k\nu})\delta_{\nu\nu'} - \Sigma^\sigma_{\nu\nu'}(\mathbf{k}, i\omega_n) \tag{2.7}$$

and the local Green's function $\mathbf{G}^\alpha_{loc}$ is then obtained by projecting the Green's function of the solid to the set of correlated orbitals L of the correlated atom α:

$$\mathbf{G}^\alpha_{loc}(i\omega_n) = \mathbf{P}_\alpha^{(\mathcal{C})} \mathbf{G}(i\omega_n) \mathbf{P}_\alpha^{(\mathcal{C})}. \tag{2.8}$$

Finally, since by construction the local Green's function must coincide with the one obtained from the effective impurity problem:

$$\mathbf{G}^\alpha_{loc}(i\omega_n) = \mathbf{G}_{imp}(i\omega_n) \tag{2.9}$$

a new dynamical mean-field $\mathcal{G}_0$ can be found thanks to the self-energy of the impurity model:

$$\left[\mathcal{G}_0^{-1}(i\omega_n)\right]_{LL'} = \left[\mathbf{\Sigma}_{imp}(i\omega_n)\right]_{LL'} + \left[\mathbf{G}^\alpha_{loc}(i\omega_n)^{-1}\right]_{LL'}. \tag{2.10}$$

This new $\mathcal{G}_0^{-1}$ allow to solve a new effective impurity model and the cycle is repeated until convergence is reached.

iv) The *updating of the charge*

The last step of the LDA+DMFT loop is the "*updating of the charge*" $\rho(\mathbf{r})$. Without introducing any specific basis set, the charge density is calculated from the full Green's function of the solid by:

$$\rho(\mathbf{r}) = \frac{1}{\beta} \sum_n \langle \mathbf{r} | \mathbf{G}(i\omega_n) | \mathbf{r} \rangle e^{i\omega_n . 0^+}. \tag{2.11}$$

In this expression, it is more convenient to split $\rho(\mathbf{r})$ as follows:

$$\rho(\mathbf{r}) = \rho_{KS}(\mathbf{r}) + \Delta\rho(\mathbf{r}) \qquad \text{with} \qquad \rho_{KS}(\mathbf{r}) = \langle \mathbf{r} | \mathbf{G}_{KS} | \mathbf{r} \rangle = \sum_{\substack{\mathbf{k},\nu,\sigma \\ \varepsilon^\sigma_{\mathbf{k},\nu} \leq \mu}} |\psi^\sigma_{\mathbf{k},\nu}|^2. \tag{2.12}$$

It is important to point out here that the demand for charge neutrality is not imposed on $\rho_{KS}(\mathbf{r})$ but rather on $\rho(\mathbf{r})$. As a result, the chemical potential μ must be explicitly determined at the end of a DMFT loop in such a way that the total number of electrons N_e is the correct one:

$$N_e = \mathrm{tr}(\mathbf{G}) = \int d\mathbf{r}\rho(\mathbf{r}). \tag{2.13}$$

This value of the chemical potential will in general not be such that $\mathrm{tr}(G_{KS}) = \int d\mathbf{r}\rho_{KS}(\mathbf{r}) = N_e$. This is actually not surprising: since correlation effects were introduced, the Kohn Sham representation of the charge density by independent Kohn Sham wave-functions no longer holds.

With this new charge density $\rho(\mathbf{r})$ a new Kohn-Sham potential can be determined, and the whole cycle can be iterated again, until the charge density $\rho(\mathbf{r})$, the impurity self-energy $\mathbf{\Sigma}_{imp}(i\omega_n)$ and the chemical potential μ are converged.

However, in practice, the calculations using the self-consistency over the charge density in the LDA+DMFT framework still remains rare. So far, this has been implemented only within the linear muffin-tin orbital (LMTO) framework [134, 142, 143] or within the Korringa-Kohn-Rostoker (KKR) method [114]. Very recently, an implementation based on the projector-augmented wave (PAW) formalism was also presented [60]. In most cases however, the global self-consistency on the charge density is not implemented. The LDA+DMFT calculations are thus performed by starting from the already converged density $\rho(\mathbf{r})$ obtained at the DFT-LDA level and by then iterating the DMFT loop until convergence of the impurity self-energy. The LDA+DMFT calculations performed on Sr_2IrO_4 in this thesis were done within this "*one-shot*" approach.

2.1.2 The double-counting correction

Since electronic correlations are already – but partially – taken into account within the DFT approach through the LDA – or GGA – exchange-correlation potential, the double-counting correction $\mathbf{\Sigma}_{dc}$ must correct for this in the LDA+DMFT method. However, defining the double counting correction is actually a tricky problem in the framework of conventional DFT [42, 132] since this theory is not orbitally resolved. Furthermore the LDA – or even GGA – exchange-correlation potential does not have a diagrammatic interpretation which would allow to subtract the corresponding terms from the DMFT many-body correction.

One could then think of subtracting the matrix elements of $V_H(\mathbf{r})$ and $V^{xc}(\mathbf{r})$ in the orbitals of the correlated subspace $\mathcal{C}$ from the Green's function $\mathbf{G}_{KS}(i\omega_n)$ to which the many-body self-energy is applied. However, this option is not chosen because the DMFT approach is meant to treat the low-energy screened interaction. As a result, the Hartree approximation is not an appropriate starting point and one wants to benefit from the spatially resolved screening effects which are already partially captured in the LDA description of the system.

Systematic approaches to avoid the double-counting problem are still being developed. Nevertheless, various schemes for the double counting correction currently exist. Among them, the following are the most used:

- the "*fully localized limit*", originally introduced in the LDA+U context [12]:

$$\left[\mathbf{\Sigma}_{dc}\right]^{\sigma}_{mm'} = \left[U\left(N_c - \frac{1}{2}\right) - J\left(N_c^{\sigma} - \frac{1}{2}\right)\right]\delta_{mm'}. \tag{2.14}$$

  In this expression, U is the average Coulomb interaction, J the Hund's coupling, N_c^{σ} the spin-resolved occupancy of the correlated orbital and $N_c = N_c^{\uparrow} + N_c^{\downarrow}$. As usual, the parameters m ans σ refer to the orbital index and the spin degree of freedom respectively.

- the "*around mean-field*" correction, also originally introduced in the LDA+U context [13]:

$$\left[\mathbf{\Sigma}_{dc}\right]^{\sigma}_{mm'} = \frac{U}{2} N_c(N_c - 1)\delta_{mm'}. \tag{2.15}$$

- the recent "Held's convention", which is specially adapted for a description where only the t_{2g} orbitals are considered correlated on an atom [66]:

$$\left[\mathbf{\Sigma}_{dc}\right]^{\sigma}_{mm'} = (U - 2J)(N_c - \frac{1}{2})\delta_{mm'}. \tag{2.16}$$

- the "Lichtenstein's correction", which was suggested for metallic systems since the static part of the correlation effects are already well described in DFT[105]:

$$\left[\mathbf{\Sigma}_{dc}\right]^{\sigma}_{mm'} = \frac{1}{2} Tr[\mathbf{\Sigma}(\omega = 0)]. \tag{2.17}$$

A recent work [83] has systematically investigated the effects of these different choices on the spectral function.

2.1.3 Choice of the localized basis set

In LDA+DMFT, the main physical issue is to construct the localized basis set $|\chi^{\alpha}_{L}\rangle$ and define among them the correlated orbitals of the system. As observed in section 1.3, a suitable concept is that of "*Wannier functions*" (1.30), formally built from the Bloch basis $|\psi^{\sigma}_{\mathbf{k},\nu}\rangle$ and centered on the atomic positions $\mathbf{R}_i$ in the crystal lattice. However, their implementations are highly dependent on the basis set used in the electronic structure code.

Among them, the "*muffin-tin orbitals*" in their linear version (LMTO) [5] form an adaptive minimal set of basis functions. They have each a well-defined momentum and are already well-localized. Most implementations have up to now used –almost directly – this basis set to span the correlated subspace $\mathcal{C}$. Nevertheless, there are several possible choices of basis even within the LMTO-NMTO method. Basically, a compromise has to be made between the degree of localization and the orthogonality of the basis set. The most localized basis functions are not orthogonal and will therefore involve an overlap matrix. Since DMFT neglects non-local correlations, they may be the best one to choose. However, a non-orthogonal basis set may not be simple to implement for technical reasons[1]. On the contrary, orthogonal LMTO-NMTO basis sets are somewhat more extended.

Recently, some approaches were developed to really construct *Wannier functions*. In 2000, Andersen *et al.* proposed the N^{th} order version of muffin-tin orbitals (NMTO) scheme [6] in which Wannier-like functions can be designed by using a "downfolding" procedure. Within such a Wannier basis, LDA+DMFT has been implemented and successfully applied to investigate the Mott transition in orthorhombic $3d^1$ pervoskites [130].

The "*maximally-localized Wannier functions*" proposed by Marzari, Vanderbilt and Souza [111, 155] were used in a LDA+DMFT implementation in 2006 [101]. The alternative projection procedure developed by Anisimov *et al.* [10] was also recently applied within the LDA+DMFT framework [1, 3]. Since the study carried out on Sr_2IrO_4 and presented in this thesis was performed with the latter method, we will describe it more precisely in section 2.3.

[1] This is mostly related to the use of impurity solvers, like QMC methods.

2.1.4 Approximations in the LDA+DMFT method

The important success of the LDA+DMFT approach must not hide the limitations of the formalism. In order to put into perspective this formalism, we summarize here the approximations performed on various level of the theory and try to justify them as far as possible.

The choice of the "*correlated orbitals*"

Only a few number of orbitals, the "*correlated*" ones, are treated with DMFT in contrast to the "*weakly correlated*" other orbitals. This arbitrariness is justified by physical considerations: by looking at the LDA band structure, the s and p bands are much broader than the d bands. The former are thus less correlated than the latter. The ultimate test, of course, would involve treating all the orbitals within DMFT, but still remains impractical nowadays.

The DMFT approximation

By using DMFT to solve the original lattice model, one assumes that the self energy is local – or momentum-independent.

$$\forall i\omega_n \qquad \forall i \qquad \mathbf{\Sigma}_{ii}(i\omega_n) \approx \mathbf{\Sigma}_{imp}(i\omega_n) \qquad \text{and} \qquad \forall i,j \qquad \mathbf{\Sigma}_{ij}(i\omega_n) \approx 0. \tag{1.50}$$

As explained in section 1.4, this approximation becomes exact in the limit of infinite coordination number. The usual justification is that the coordination number of the considered system – like a perovskite structure – is "large enough". A more rigorous argument could be provided by the comparison to cluster calculations which reintroduce some momentum dependence. However, these simulations are often not within reach of our computer systems.

The choice of the interaction Hamiltonian H_U

This point was not really discussed. In practice, one often chooses to work with pure density-density interactions. As a result, Coulomb and Ising-like Hund's coupling terms are included, but the full rotational symmetry in spin space is not conserved anymore. It is clear that this simplification might change the physics, and the approximation is not really controlled.

The choice of "*double-counting correction*" $\mathbf{\Sigma}_{dc}$

The choice of the correction for the wrongly assumed weak correlation within the LDA is not at all clear. While some schemes have been proposed, they are neither unique nor thoroughly derivable. The effect of these terms is a major source of uncertainty.

The "*one-shot*" implementation of LDA+DMFT

The LDA+DMFT cycle summarized on figure 2.1 should be iterated until the charge density $\rho(\mathbf{r})$, the impurity self-energy $\mathbf{\Sigma}_{imp}(i\omega_n)$ and the chemical potential μ are converged. As already explained, most implementations do not perform the self-consistency over the charge density. This introduces a new approximation in the calculation, which is not really controlled. It is however commonly thought that the "*one-shot*" results are really close to those which would be obtained with a full self-consistently implementation. Some developments in the field – allowed by the growing computer power – are currently in progress to determine the validity of this belief.

2.2 Introduction to (linearized) augmented planewaves ((L)APW)

We have chosen to implement the LDA+DMFT formalism within the "*linearized augmented planewaves (LAPW) framework*", since recent developments proved the accuracy of using this kind of basis for many materials. More precisely, our implementation is based on the electronic structure code Wien2k [23], which is an *all-electron full-potential LAPW method*.

In this section, we first introduce the main characteristics of this code and then describe thoroughly the construction of the APW and LAPW bases. For the interested reader, additional details about the (L)APW bases and Wien2k can be found in the following extensive reviews and books [23, 40, 149].

2.2.1 Wien2k, an *all-electron full-potential LAPW method*

In this part, we introduce the main concepts on which the program Wien2k relies. The interested reader may find more details on the structure and the implementation of this code in the tutorial [23]. Some additional technicalities are also described in Appendix C.

In Wien2k, the space contained in the unit cell of a given compound is partitioned into two regions:

- a set of non-overlapping spheres S^{α}_{MT} of radius R^{α}_{MT} around each atom α. They are called the "*muffin tin spheres*" and define the first region.
- the second region corresponds to the remaining space outside the spheres. It is called the "*interstitial region*" and labeled I.

This spatial division is linked to the different behaviors of the electronic wavefunctions in a crystal. Far away from the atomic nuclei, only the valence electrons can be found. In this region – which corresponds to I –, they are delocalized all over the solid and can be described by planewaves. Close to the nuclei however, the core electrons, which do not participate significantly in chemical bonding with other atoms, lie in atomic-like orbitals.

This partition in two regions of the unit cell was originally proposed by Slater in 1953 [152] and two different types of basis were then developed from this idea:

- the "*linear muffin-tin orbitals*" (LMTO) [5] or its most recent Nth order version (NMTO) [6],
- the "*augmented planewaves*" (APW) and their descendants. These bases can be seen as made of oscillating functions – like planewaves – that run through the unit cell. However, this simple oscillating behavior is changed into something more complex inside the muffin-tin sphere of each atom.

The Wien2k program is based on this last type of basis set, namely the "*linearized augmented planewave*" (LAPW).

However not all the electronic wavefunctions are expanded within this basis set. Wien2k indeed introduces the following difference:

- a "*core state*" is *entirely* contained in a muffin-tin sphere and is thus calculated by solving the relativistic radial Schrödinger equation for the considered free atom.
- a "*valence state*" requires on the contrary a description by (L)APW, since their wavefunctions leak outside the muffin-tin spheres. A small subtlety is moreover considered here: the electron can indeed be "*pure valence*" state or "*semi-core*" valence state. The latter are distinguished from the former because they lie high enough in energy so that their charge is not completely confined

inside the muffin-tin sphere, but they have only a few percent of it outside the sphere. For instance, in the case of Sr_2IrO_4, the orbitals Ir-5p and 4f are *semi-core* states. This distinction induces slight differences in the basis expansion, which is explained later.

Despite, Wien2k is an "*all-electron*" method: although *core* and *valence* electrons are not treated in the same way, both of these states are indeed calculated self-consistently. The influence of the core states on the valence is carried out by the inclusion of the core density $\rho_{core}(\mathbf{r})$ in the Hartree $V_H[\rho(\mathbf{r})]$ and exchange-correlation potentials $V^{xc}[\rho(\mathbf{r})]$ used to calculate the valence states, since:

$$\rho(\mathbf{r}) = \rho_{core}(\mathbf{r}) + \rho_{valence}(\mathbf{r}). \tag{2.18}$$

Reciprocally, the core states are calculated using the spherical average of the total electronic potential $\rho(\mathbf{r})$ inside each muffin-tin sphere.

Moreover, the division of the unit cell into two domains induces also a dual representation for the density $\rho(\mathbf{r})$ and the potential $V_{KS}(\mathbf{r})$. For instance, the Kohn-Sham potential $V_{KS}(\mathbf{r})$ is expanded as follows:

$$V_{KS}(\mathbf{r}) = \begin{cases} \sum_{\mathbf{G}} V_{\mathbf{G}} e^{i\mathbf{G}\cdot\mathbf{r}} & \text{if } \mathbf{r} \in I \\ \sum_{L=0}^{L_{max}} \sum_{M=-L}^{+L} V_{LM} Y_M^L(\hat{\mathbf{r}^\alpha}) & \text{if } \mathbf{r} \in S_{MT}^\alpha \quad (\alpha = 1, ..., N_{at}) \end{cases} \tag{2.19}$$

where $\mathbf{G}$ are the reciprocal lattice vectors and $Y_M^L(\hat{\mathbf{r}})$ the spherical harmonics. Since there is no shape approximation for $V(\mathbf{r})$, this method is also called "*full-potential*". This represents the main advantage of the APW method to the LMTO-NMTO framework: within LMTO-NMTO, the decomposition of the potential corresponds to retaining only the $L = 0$ component inside the spheres and the $\mathbf{G} = 0$ component in the interstitial space. The recent introduction of the atomic sphere approximation (ASA) [4] has allowed to improve significantly the description of the potential but holds mainly for closely packed structure. On the contrary, the APW method is free of any approximation and can then be considered as more accurate, especially for non-compact structures.

2.2.2 APW and LAPW bases

In Wien2k, the eigenfunctions of the Kohn-Sham Hamiltonian $\psi_{\mathbf{k}\nu}^\sigma(\mathbf{r})$ are expanded as follows:

$$\psi_{\mathbf{k}\nu}^\sigma(\mathbf{r}) = \sum_{|\mathbf{K}| \leq K_{max}} c_{\mathbf{K}\nu}^\sigma(\mathbf{k}) \phi_{\mathbf{K}}^{\mathbf{k}\sigma}(\mathbf{r}) \tag{2.20}$$

with ν the band index, σ the spin degree of freedom and $\mathbf{K}$ the reciprocal lattice vectors. The basis functions $\phi_{\mathbf{K}}^{\mathbf{k}\sigma}(\mathbf{r})$ are of course the APW or LAPW functions and the parameter K_{max} defines the cutoff of the basis expansion. We now describe thoroughly the construction of these APW and LAPW functions. For this, we follow the historical development of the method in order to be as clear as possible, as it is done in [40, 103, 149].

The augmented planewaves (APW) basis

The notion of "*augmented planewaves*" (APW) was originally introduced in 1953 by Slater [152]. In this seminal work, the division of the unit cell is also exposed. However, the potential is taken as spherically symmetric inside the spheres and constant outside.

In order to describe at best the behavior of the electrons in each region, the basis functions $\phi_{\mathbf{K}}^{\mathbf{k}\sigma}(\mathbf{r})$ are expanded in planewaves in the interstitial region I and in atomic-like orbitals in the muffin-tin

spheres:

$$\phi_{\mathbf{K}}^{\mathbf{k}\sigma}(\mathbf{r}) = \begin{cases} \frac{1}{\sqrt{\Omega}} e^{i(\mathbf{k}+\mathbf{K})\cdot\mathbf{r}} & \text{if } \mathbf{r} \in I \\ \sum_{l}^{l_{max}} \sum_{m=-l}^{+l} A_{lm}^{\alpha,\mathbf{k}+\mathbf{K}} u_l^{\alpha,\sigma}(r^\alpha, \varepsilon) Y_m^l(\hat{\mathbf{r}^\alpha}) & \text{if } \mathbf{r} \in S_{MT}^\alpha \end{cases} \tag{2.21}$$

where in this expression,

- $\mathbf{K}$ are the reciprocal lattice vectors, Ω is the unit cell volume, N_{at} is the total number of atoms in the cell, and ε has the dimension of an energy.
- $\mathbf{r}^\alpha = \mathcal{T}_\alpha(\mathbf{r}) = \mathcal{R}_\alpha(\mathbf{r} - \mathbf{r}_\alpha)$ is the position inside the muffin-tin sphere S_{MT}^α, given with respect to the center of the sphere $\mathbf{r}_\alpha$. $\mathcal{T}_\alpha$ is the transformation from the global coordinates of the crystal to the local coordinates associated to the atom α, which is composed of the rotation $\mathcal{R}_\alpha$ and the translation by the vector $\mathbf{r}_\alpha$. The length of $\mathbf{r}^\alpha$ is denoted r^α, and the angles θ^α and ϕ^α specifying the direction of the vector in spherical coordinates, are indicated as $\hat{\mathbf{r}^\alpha}$.
- $Y_m^l(\hat{\mathbf{r}})$ are the spherical harmonics within the standard convention of Condon-Shortley (a factor $(-1)^m$ is included in the definition).
- $u_l^{\alpha,\sigma}(r,\varepsilon)$ is the radial solution of the Schrödinger equation for the free atom α at the energy ε:

$$\left[-\frac{d^2}{dr^2} + \frac{l(l+1)}{r^2} + V(r) - \varepsilon\right] r u_l^{\alpha,\sigma}(r,\varepsilon) = 0 \tag{2.22}$$

  However, the boundary condition is changed: for a true free atom, the boundary condition is that $u_l^{\alpha,\sigma}(r,\varepsilon)$ should vanish for $\mathbf{r} \to +\infty$. In the APW method, it is required that the planewave outside the sphere matches the function inside the sphere over the complete surface of the sphere – in value, not in slope. If an eigenfunction was discontinuous, its kinetic energy would indeed not be well-defined. In addition, the following normalization condition is specified:

$$\int_0^{R_{MT}^\alpha} r^2 |u_l^{\alpha,\sigma}(r,\varepsilon)|^2 dr = 1 \quad \forall \alpha, \sigma, l, \varepsilon \tag{2.23}$$

- the $A_{lm}^{\alpha,\mathbf{k}}$ are the expansion coefficients which are uniquely defined by requiring the continuity of the basis wavefunction at the sphere boundary and are given by:

$$A_{lm}^{\alpha,\mathbf{k}+\mathbf{K}} = \frac{4\pi}{\sqrt{\Omega}} i^l \; Y_l^{m*}(\mathcal{R}_\alpha(\widehat{\mathbf{k}+\mathbf{K}})) \; \frac{j_l(\|\mathbf{k}+\mathbf{K}\| R_{MT}^\alpha)}{u_l^{\alpha,\sigma}(R_{MT}^\alpha, \varepsilon)} \; e^{i(\mathbf{k}+\mathbf{K})\cdot\mathbf{r}_\alpha} \tag{2.24}$$

  where $j_l(x)$ is the Bessel function of order l.

To obtain this expression, the expansion of the planewaves in spherical harmonics around the origin $\mathbf{r}_\alpha$ of the sphere of atom α were used:

$$\frac{1}{\sqrt{\Omega}} e^{i\mathbf{K}\cdot\mathbf{r}} = \frac{4\pi}{\sqrt{\Omega}} \sum_{l=0}^{+\infty} \sum_{m=-l}^{+l} i^l \; j_l(\|\mathbf{K}\|\|\mathbf{r}\|) \; Y_l^{m*}(\mathcal{R}_\alpha(\widehat{\mathbf{K}}) \; Y_l^m(\widehat{\mathbf{r}^\alpha}) \tag{2.25}$$

In expression (2.25), the sum on the right-hand side is infinite. In practice, however, this sum must be truncated at some value l_{max}.

The APW method, as it is presented here, is not used anymore because of a major drawback. Indeed, to describe accurately an eigenstate $\psi_{\mathbf{k}\nu}^\sigma$ with the APW basis set, one has to solve inside the

muffin-tin sphere the radial Schrödinger equation at the band energy $\varepsilon = \varepsilon^{\sigma}_{\mathbf{k}\nu}$. Consequently, the final eigenvalue equation becomes non-linear and its solution much more computationally demanding for each $\mathbf{k}$-point. Another shortcoming of the APW method, known as the *asymptote problem*, is related to the indetermination of the expansion coefficients when the radial function $u_l^{\alpha,\sigma}$ has a node at the muffin-tin radius R^{α}_{MT}. In the vicinity of this region, the relation between $A_{lm}^{\alpha,\mathbf{k}+\mathbf{K}}$ and $c^{\sigma}_{\mathbf{K}\nu}(\mathbf{k})$ becomes numerically unstable since $u_l^{\alpha,\sigma}(R^{\alpha}_{MT},\varepsilon)$ is actually in the denominator of (2.24).

The regular LAPW method

In 1975, Andersen proposed a modification of the APW method [5] with the aim of overcoming its limitations. In this approach, both the wavefunctions and their derivatives are made continuous at the muffin-tin radius by matching the interstitial planewaves to a linear combination of the radial functions, and their energy derivative, calculated at a fixed reference energy.

By making a Taylor expansion of the radial wavefunction $u_l^{\alpha,\sigma}$ around a reference energy ε_0, one gets:

$$\begin{aligned} u_l^{\alpha,\sigma}(r^{\alpha},\varepsilon) &= u_l^{\alpha,\sigma}(r^{\alpha},\varepsilon_0) + (\varepsilon-\varepsilon_0)\dot{u}_l^{\alpha,\sigma}(r^{\alpha},\varepsilon_0) + O\big((\varepsilon-\varepsilon_0)^2\big) \\ &\text{with} \quad \dot{u}_l^{\alpha,\sigma}(r^{\alpha},\varepsilon_0) = \left.\frac{\partial u_l^{\alpha,\sigma}(r^{\alpha},\varepsilon)}{\partial\varepsilon}\right|_{\varepsilon=\varepsilon_0} \end{aligned} \tag{2.26}$$

In this expression, it is advantageous to choose ε_0 near the center of the considered band. As a result one should not choose one universal value ε_0, but a set of well-chosen E^{α}_{1l} up to $l = l_{max}$.

The definition of the LAPW basis set is then given by substituting the first two terms of the expansion in the APW description (2.21), for a fixed E^{α}_{1l} for each atom α and each value of l:

$$\phi^{\mathbf{k}\sigma}_{\mathbf{K}}(\mathbf{r}) = \begin{cases} \dfrac{1}{\sqrt{\Omega}} e^{i(\mathbf{k}+\mathbf{K})\cdot\mathbf{r}} & \text{if } \mathbf{r}\in I \\ \displaystyle\sum_{l}^{l_{max}} \sum_{m=-l}^{+l} \Big[A_{lm}^{\alpha,\mathbf{k}+\mathbf{K}} u_l^{\alpha,\sigma}(r^{\alpha},E^{\alpha}_{1l}) + B_{lm}^{\alpha,\mathbf{k}+\mathbf{K}} \dot{u}_l^{\alpha,\sigma}(r^{\alpha},E^{\alpha}_{1l})\Big] Y_m^l(\hat{\mathbf{r}^{\alpha}}) & \text{if } \mathbf{r}\in S^{\alpha}_{MT} \end{cases} \tag{2.27}$$

A yet undetermined coefficient $B_{lm}^{\alpha,\mathbf{k}+\mathbf{K}}$ is introduced because of the linearization. The expansion coefficients $A_{lm}^{\alpha,\mathbf{k}+\mathbf{K}}$ and $B_{lm}^{\alpha,\mathbf{k}+\mathbf{K}}$ are then obtained by requiring that $\phi^{\mathbf{k}\sigma}_{\mathbf{K}}(\mathbf{r})$ is continuous in value *and* slope at the sphere boundary S^{α}_{MT}. This leads to:

$$A_{lm}^{\alpha,\mathbf{k}+\mathbf{K}} = \frac{4\pi}{\sqrt{\Omega}} i^l \; Y_l^{m*}(\mathcal{R}_{\alpha}(\widehat{\mathbf{k}+\mathbf{K}})) \; {R^{\alpha}_{MT}}^2 \; a_l^{\alpha}(\mathbf{k}+\mathbf{K}) \; e^{i(\mathbf{k}+\mathbf{K})\cdot\mathbf{r}_{\alpha}} \tag{2.28}$$

$$B_{lm}^{\alpha,\mathbf{k}+\mathbf{K}} = \frac{4\pi}{\sqrt{\Omega}} i^l \; Y_l^{m*}(\mathcal{R}_{\alpha}(\widehat{\mathbf{k}+\mathbf{K}})) \; {R^{\alpha}_{MT}}^2 \; b_l^{\alpha}(\mathbf{k}+\mathbf{K}) \; e^{i(\mathbf{k}+\mathbf{K})\cdot\mathbf{r}_{\alpha}} \tag{2.29}$$

where

$$\begin{aligned} a_l^{\alpha}(\mathbf{k}+\mathbf{K}) &= \|\mathbf{k}+\mathbf{K}\| \; j_l'(\|\mathbf{k}+\mathbf{K}\|R^{\alpha}_{MT}) \; \dot{u}_l^{\alpha,\sigma}(R^{\alpha}_{MT},E^{\alpha}_{1l}) - j_l(\|\mathbf{k}+\mathbf{K}\|R^{\alpha}_{MT}) \; \big[\dot{u}_l^{\alpha,\sigma}\big]'(R^{\alpha}_{MT},E^{\alpha}_{1l}) \\ b_l^{\alpha}(\mathbf{k}+\mathbf{K}) &= j_l(\|\mathbf{k}+\mathbf{K}\|R^{\alpha}_{MT}) \; \big[u_l^{\alpha,\sigma}\big]'(R^{\alpha}_{MT},E^{\alpha}_{1l}) - \|\mathbf{k}+\mathbf{K}\| \; j_l'(\|\mathbf{k}+\mathbf{K}\|R_{\alpha}) \; u_l^{\alpha,\sigma}(R^{\alpha}_{MT},E^{\alpha}_{1l}). \end{aligned} \tag{2.30}$$

We used the notation $[...]' = \partial[...]/\partial r$ in the previous formula and we remind that $u_l^{\alpha,\sigma}$ and $\dot{u}_l^{\alpha,\sigma}$ are orthogonal because of the normalization condition (2.23).

Within this linearized treatment, the error in the wavefunction is of second order in $(\varepsilon - E^{\alpha}_{1l})$. Taking into account the variational principle, this leads to an error of fourth order, $(\varepsilon^{\sigma}_{\mathbf{k}\nu} - E^{\alpha}_{1l})^4$, in the band energy. In other words, the LAPW basis set forms a good basis over a relatively large energy region, typically allowing the calculation of all the valence bands with a single set of reference energies E^{α}_{1l}. Inded, the method rapidly demonstrated its power and accuracy. It has even become the benchmark for electronic structure calculations within the Kohn-Sham scheme for decades.

The LAPW with Local Orbitals (LO) basis

There are situations in which the use of a single set of reference energies E^{α}_{1l} is inadequate for all the bands of interest. Such a situation arises when two (or more, but rarely) states with the same l number are involved in a chemical bonding or when bands over an unusually large energy region are required. This is precisely the case for the so-called "*semi-core*" states. To describe at best such states, the *local orbitals* (LO) were introduced by D. J. Singh in 1991 [148]:

$$\phi^{LO}_{lm,\alpha}(\mathbf{r}) = \begin{cases} 0 & \text{if } \mathbf{r} \in I \\ \left[A^{\alpha,LO}_{lm} u^{\alpha,\sigma}_{l}(r^{\alpha}, E^{\alpha}_{1l}) + B^{\alpha,LO}_{lm} \dot{u}^{\alpha,\sigma}_{l}(r^{\alpha}, E^{\alpha}_{1l}) + C^{\alpha,LO}_{lm} u^{\alpha,\sigma}_{l}(r^{\alpha}, E^{\alpha}_{2l})\right] Y^{l}_{m}(\hat{\mathbf{r}^{\alpha}}) & \text{if } \mathbf{r} \in S^{\alpha}_{MT} \end{cases} \tag{2.31}$$

These orbitals are defined for a particular l and m, and for a particular atom α. Moreover, they are zero in the interstitial region and in the muffin tin spheres of other atoms. That is why, they are called "*local orbitals*". *Local orbitals* are strictly speaking not connected to planewaves in the interstitial region, they have thus no $\mathbf{k}$ or $\mathbf{K}$-dependence.

The three expansion coefficients $A^{\alpha,LO}_{lm}$, $B^{\alpha,LO}_{lm}$ and $C^{\alpha,LO}_{lm}$ are determined by requiring the local orbital and its radial derivative to be zero at the muffin-tin sphere boundary. Through a third criterion, the local orbital can be associated to a fictitious planewave – $e^{i(\mathbf{k}+\mathbf{K}_{LO})\cdot\mathbf{r}}$ for instance – so that the orbital will behave just like the augmented planewave under inversion symmetry [149, 150]. However, we stress that local orbitals only exist inside the related muffin-tin sphere.

Adding local orbitals of course increases the LAPW basis set size. This slightly increases the computational time but is the price to pay for the much better accuracy that local orbitals offer to describe the semi-core states.

The "APW plus local orbitals" (APW+lo) basis

The prohibitive shortcoming of the APW method was the energy dependence of the basis set. This energy dependence have been removed in the LAPW(+LO) method, by increasing the size of the basis due to the linearization in energy and the introduction of local orbitals (LO). An alternative method in which the APW basis set may become energy independent but still have (almost) the same size as in the original APW method, was proposed in 2000 by Sjöstedt *et al.* [150, 151]. These two properties were obtained at the cost of adding a set of "*local orbitals*": the basis was then called "*APW plus local orbitals*"(APW+lo).

Two different types of functions compose the complete APW+lo basis set:

- the original APW basis functions described by (2.21) which are defined at chosen fixed linearization energies (E^{α}_{1l}):

$$\phi^k_{\mathbf{K}}(\mathbf{r}) = \begin{cases} \dfrac{1}{\sqrt{\Omega}} e^{i(\mathbf{k}+\mathbf{K})\cdot\mathbf{r}} & \text{if } \mathbf{r} \in I \\ \displaystyle\sum_{l}^{l_{max}} \sum_{m=-l}^{+l} A^{\alpha,\mathbf{k}+\mathbf{K}}_{lm} u^{\alpha,\sigma}_l(r^\alpha, E^\alpha_{1l}) Y^l_m(\hat{\mathbf{r}^\alpha}) & \text{if } \mathbf{r} \in S^\alpha_{MT} \end{cases} \tag{2.32}$$

$$\text{with} \qquad A^{\alpha,\mathbf{k}+\mathbf{K}}_{lm} = \frac{4\pi}{\sqrt{\Omega}} i^l \; Y^{m*}_l(\mathcal{R}_\alpha(\widehat{\mathbf{k}+\mathbf{K}})) \; \frac{j_l(\|\mathbf{k}+\mathbf{K}\|R^\alpha_{MT})}{u^{\alpha,\sigma}_l(R^\alpha_{MT}, E^\alpha_{1l})} \; e^{i(\mathbf{k}+\mathbf{K})\cdot\mathbf{r}_\alpha}$$

- the set of *local orbitals* (lo) to keep the flexibility of the basis set with respect to the reference energy:

$$\phi^{lo}_{lm,\alpha}(\mathbf{r}) = \begin{cases} 0 & \text{if } \mathbf{r} \in I \\ \left[A^{\alpha,lo}_{lm} u^{\alpha,\sigma}_l(r^\alpha, E^\alpha_{1l}) + B^{\alpha,lo}_{lm} \dot{u}^{\alpha,\sigma}_l(r^\alpha, E^\alpha_{1l})\right] Y^l_m(\hat{\mathbf{r}^\alpha}) & \text{if } \mathbf{r} \in S^\alpha_{MT} \end{cases} \tag{2.33}$$

These orbitals use the same linearization energies, although this is not strictly needed. The expansion coefficients $A^{\alpha,lo}_{lm}$ and $B^{\alpha,lo}_{lm}$ are calculated by imposing the function to be zero at the sphere boundary and by associating the local orbital to a fictitious planewave, as previously mentioned for the LO.

As in the LAPW method, a second set of local orbitals, labeled LO, can be introduced in order to treat semicore states:

$$\phi^{LO}_{lm,\alpha}(\mathbf{r}) = \begin{cases} 0 & \text{if } \mathbf{r} \in I \\ \left[A^{\alpha,LO}_{lm} u^{\alpha,\sigma}_l(r^\alpha, E^\alpha_{1l}) + C^{\alpha,LO}_{lm} u^{\alpha,\sigma}_l(r^\alpha, E^\alpha_{2l})\right] Y^l_m(\hat{\mathbf{r}^\alpha}) & \text{if } \mathbf{r} \in S^\alpha_{MT} \end{cases} \tag{2.34}$$

In contrast to the LO for LAPW, there is no derivative of $u^{\alpha,\sigma}_l(r^\alpha, E^\alpha_{1l})$ in the above expression. The expansion coefficients $A^{\alpha,LO}_{lm}$ and $C^{\alpha,LO}_{lm}$ are determined by matching the function to zero at the sphere boundary and by associating the local orbital to a fictitious planewave.

2.2.3 The LAPW basis with local orbitals or (L)APW+lo basis in Wien2k

We have previously introduced two types of basis set, namely the LAPW+LO and the APW+lo. Nowadays, the state-of-the-art method, like the Wien2k code, is a combination of these both approaches. The APW+lo basis is used for valence d and f states but also for states in atoms that have a muffin-tin sphere which is much smaller than the other spheres in the unit cell. For all the other states, the LAPW+LO basis is employed. This combination is known as the "*(L)APW+lo method*".

Whatever the choice for the basis, any eigenstate of the Kohn-Sham Hamiltonian $\psi^\sigma_{\mathbf{k}\nu}(\mathbf{r})$ can thus always be written as follows in Wien2k:

$$\psi^\sigma_{\mathbf{k}\nu}(\mathbf{r}) = \begin{cases} \dfrac{1}{\sqrt{\Omega}} \displaystyle\sum_{|\mathbf{K}|\le K_{max}} c^\sigma_{\mathbf{K}\nu}(\mathbf{k}) e^{i(\mathbf{k}+\mathbf{K})\mathbf{r}} & \text{if } \mathbf{r} \in I \\ \displaystyle\sum_{l=0}^{l_{max}} \sum_{m=-l}^{+l} \Big[A^{\nu\alpha}_{lm}(\mathbf{k},\sigma) u^{\alpha,\sigma}_l(r^\alpha, E^\alpha_{1l}) + B^{\nu\alpha}_{lm}(\mathbf{k},\sigma) \dot{u}^{\alpha,\sigma}_l(r^\alpha, E^\alpha_{1l}) \\ \qquad + C^{\nu\alpha}_{lm}(\mathbf{k},\sigma) u^{\alpha,\sigma}_l(r^\alpha, E^\alpha_{2l})\Big] Y^l_m(\hat{\mathbf{r}^\alpha}) & \text{if } \mathbf{r} \in S^\alpha_{MT} \end{cases} \tag{2.35}$$

More precisely, inside the muffin-tin spheres, the coefficients $A^{\nu\alpha}_{lm}(\mathbf{k},\sigma)$, $B^{\nu\alpha}_{lm}(\mathbf{k},\sigma)$ and $C^{\nu\alpha}_{lm}(\mathbf{k},\sigma)$ are given by:

- if the atom α is described in the LAPW(+LO) representation,

$$\begin{aligned} A_{lm}^{\nu\alpha}(\mathbf{k},\sigma) &= \sum_{|\mathbf{K}|\leq K_{max}} c_{\mathbf{K}\nu}^{\sigma}(\mathbf{k}) A_{lm}^{\alpha,\mathbf{k}+\mathbf{K}} + \sum_{nLO=0}^{LO_{MAX}(\alpha,l,m)} c_{LO}^{\nu,\sigma} A_{lm}^{\alpha,LO} \\ B_{lm}^{\nu\alpha}(\mathbf{k},\sigma) &= \sum_{|\mathbf{K}|\leq K_{max}} c_{\mathbf{K}\nu}^{\sigma}(\mathbf{k}) B_{lm}^{\alpha,\mathbf{k}+\mathbf{K}} + \sum_{nLO=0}^{LO_{MAX}(\alpha,l,m)} c_{LO}^{\nu,\sigma} B_{lm}^{\alpha,LO} \\ C_{lm}^{\nu\alpha}(\mathbf{k},\sigma) &= \sum_{nLO=0}^{LO_{MAX}(\alpha,l,m)} c_{LO}^{\nu,\sigma} C_{lm}^{\alpha,LO} \end{aligned} \tag{2.36}$$

- if the atom α is described in the APW+lo representation,

$$\begin{aligned} A_{lm}^{\nu\alpha}(\mathbf{k},\sigma) &= \sum_{|\mathbf{K}|\leq K_{max}} c_{\mathbf{K}\nu}^{\sigma}(\mathbf{k}) A_{lm}^{\alpha,\mathbf{k}+\mathbf{K}} + \sum_{nlo=1}^{lo_{max}} c_{lo}^{\nu,\sigma} A_{lm}^{\alpha,lo} + \sum_{nLO=0}^{LO_{MAX}(\alpha,l,m)} c_{LO}^{\nu,\sigma} A_{lm}^{\alpha,LO} \\ B_{lm}^{\nu\alpha}(\mathbf{k},\sigma) &= \sum_{nlo=1}^{lo_{max}} c_{lo}^{\nu,\sigma} B_{lm}^{\alpha,lo} \\ C_{lm}^{\nu\alpha}(\mathbf{k},\sigma) &= \sum_{nLO=0}^{LO_{MAX}(\alpha,l,m)} c_{LO}^{\nu,\sigma} C_{lm}^{\alpha,LO} \end{aligned} \tag{2.37}$$

where $LO_{MAX}(\alpha,l,m)$ can be 0, if no LO are needed, or the number of necessary LO.

The reader has certainly noticed that all the previous orbitals were defined in the unit cell. To extend their definition to the total crystal, it is enough to perform the following operation:

$$\phi_\mu(\mathbf{r}) = \frac{1}{\sqrt{\mathcal{N}}} \sum_{\mathbf{R}\in\mathcal{B}} e^{i\mathbf{k}\cdot\mathbf{R}} \phi_\mu(\mathbf{r}-\mathbf{R}) \quad \text{with} \quad \phi_\mu = \phi_{\mathbf{K}}^k,\ \phi_{lm,\alpha}^{lo} \text{ or } \phi_{lm,\alpha}^{LO} \tag{2.38}$$

where $\mathcal{N}$ is the number of unit cells in the volume of the crystal and $\mathbf{R}$ the translation vectors of the Bravais lattice. With this definition, the basis functions in the interstitial part are now $e^{i(\mathbf{k}+\mathbf{K})\cdot\mathbf{r}}/\sqrt{V}$, with $\mathbf{r}$ running in all the crystal volume V.

2.3 Projection onto Wannier orbitals

The implementation of LDA+DMFT [1] which has been extended to perform our calculation on Sr_2IrO_4 relies on the construction of *Wannier functions* from the previously described APW+lo basis. In this section, we first define more precisely the concept of "*Wannier functions*" which was briefly introduced in section 1.3. We then explain how the Wannier-function formalism based on the projection procedure developed by Anisimov *et al.* [10] was applied within the APW+lo framework.

2.3.1 Wannier functions: definition and calculations

As explained in section 1.3, Wannier functions are the Fourier transformation of the Bloch states:

$$\chi_{\nu\sigma}^{\mathbf{R}}(\mathbf{r}) = \frac{1}{\sqrt{\mathcal{N}}} \sum_{\mathbf{k}} e^{-i\mathbf{k}.\mathbf{R}} \psi_{\mathbf{k}\nu}^{\sigma}(\mathbf{r}) \tag{2.39}$$

where $\mathcal{N}$ is the number of $\mathbf{k}$-point in 1BZ (or the number of unit cells in the crystal), $\mathbf{R}$ a translation vector of the Bravais lattice, ν the band index[2] and σ the spin degree of freedom. The concept was first introduced in 1937 by Wannier [163], in order to get a basis set whose functions are centered on the atomic positions in the crystal lattice. However, in most cases – and in contrast to the simple example described in section 1.3 –, Wannier functions are not uniquely defined: if one considers a certain set of bands $\{\nu\}$, any orthogonal linear combination of Bloch functions $|\psi_{\mathbf{k}\nu}>$ can indeed be used in the definition (2.39):

$$\chi^{\mathbf{R}}_{\mu\sigma}(\mathbf{r}) = \frac{1}{\sqrt{\mathcal{N}}} \sum_{\mathbf{k}} e^{-i\mathbf{k}.\mathbf{R}} \sum_{\nu} U^{(\mathbf{k})}_{\mu\nu} \psi^{\sigma}_{\mathbf{k}\nu}(\mathbf{r}) \tag{2.40}$$

where $U^{\mathbf{k}}_{\mu\nu}$ is a unitary transformation matrix. To calculate in practice Wannier functions, one must thus introduce an additional restriction on the properties of Wannier functions, in order to fix this degree of freedom.

First methods

The first methods which were proposed were based on an iterative optimization of trial functions which have the same real and point group symmetry properties as the desired Wannier functions. Among these methods, one can cite the variational Koster-Parzen principle [95, 129] which was later generalized by Kohn [89, 92, 90, 91, 137], the general pseudopotential formalism proposed by Anderson [8] and the projection operator formalism introduced by Cloizeaux [45, 46, 47]. However, all these computational schemes were restricted to simple band structures.

The condition of "maximum localization"

In 1997, Marzari, Vanderbilt and Souza proposed the condition of "*maximum localization*" to calculate Wannier functions [111, 155]. In order to ensure a maximally localized Wannier-like basis, the unitary matrix $U^{(\mathbf{k})}_{\mu\nu}$ is obtained from a minimization of the sum Ω of the quadratic spreads of the Wannier probability distributions defined by:

$$\Omega = \sum_{\mu,\sigma} \left(\langle r^2 \rangle_{\mu\sigma} - \langle \mathbf{r} \rangle^2_{\mu\sigma} \right) \quad \text{where} \quad \langle \mathcal{O} \rangle_{\mu\sigma} = \int d^3\mathbf{r} \mathcal{O}(\mathbf{r}) |\chi^{\mathbf{0}}_{\mu\sigma}(\mathbf{r})|^2 \quad \text{with} \quad \mathcal{O} = \mathbf{r} \text{ or } r^2. \tag{2.41}$$

Therefore, the quantity Ω may be understood as a functional of the Wannier basis set. Starting from some initial guess for the Wannier basis, the formalism uses steepest-descent or conjugate-gradient methods to optimize $U^{(\mathbf{k}}_{\mu\nu}$. The resulting *maximally-localized Wannier functions* turn out to be real functions, although there is no available general proof for this property.

The projection procedure

A simpler alternative to this implementation was proposed in 2005 by Anisimov *et al.* [10]. The method roughly consists in using atomic orbitals which are promoted to Wannier functions by a truncated expansion over Bloch functions followed by an orthonormalization procedure.

More precisely, one needs first to define the site-centered atomic-like trial orbitals $\phi_{\mu\sigma}(\mathbf{r})$ in the unit cell and extend their definition to the total crystal by calculating:

$$\phi^{\mathbf{k}}_{\mu\sigma}(\mathbf{r}) = \frac{1}{\sqrt{\mathcal{N}}} \sum_{\mathbf{R}\in\mathcal{B}} e^{i\mathbf{k}\cdot\mathbf{R}} \phi_{\mu\sigma}(\mathbf{r} - \mathbf{R}) \tag{2.42}$$

[2] In order to keep our definition as general as possible, the Wannier functions $\chi^{\mathbf{R}}_{\nu\sigma}(\mathbf{r})$ will be now labelled directly by the band index ν, without any reference to a corresponding atomic character.

One must then find the set $\mathcal{W}$ of corresponding physically relevant Bloch states $|\psi^{\sigma}_{\mathbf{k}\nu}\rangle$ in the electronic band structure. These states – or bands – can be identified either by their band indices ν or by delimiting the energy interval $[\varepsilon_1, \varepsilon_2]$ in which they are located. The Wannier functions in the reciprocal space $\chi^{\mathbf{k}}_{\mu\sigma}(\mathbf{r})$ are then obtained by performing the following projection:

$$|\widetilde{\chi}^{\mathbf{k}}_{\mu\sigma}\rangle = \sum_{|\psi^{\sigma}_{\mathbf{k}\nu}\rangle \in \mathcal{W}} |\psi^{\sigma}_{\mathbf{k}\nu}\rangle\langle\psi^{\sigma}_{\mathbf{k}\nu}|\phi^{\mathbf{k}}_{\mu\sigma}\rangle \tag{2.43}$$

where the sum runs over the band indices ν only. A standard orthonormalization procedure is then performed, since in general only a subset of Bloch states are used in the previous expression.

With this definition, the obtained Wannier functions $\chi^{\mathbf{k}}_{\mu\sigma}(\mathbf{r})$ are not unique: they depend on the energy window $[\varepsilon_1, \varepsilon_2]$ covered by the Bloch functions: the larger this window, the more localized the Wannier functions. Despite this drawback, this procedure gives a quite straightforward scheme to construct Wannier functions. As a result, it was recently integrated in some LDA+DMFT implementations based on the projector augmented wave (PAW) and the mixed-basis pseudopotential framework [3] but also on the (L)APW+lo framework of Wien2k [1].

2.3.2 Projectors on Wannier functions within the (L)APW+lo basis of Wien2k

As explained in section 2.1, the main physical issue in LDA+DMFT is to construct the localized basis set $|\chi^{\alpha}_{L}\rangle$ which will span the correlated subspace $\mathcal{C}$. However, these basis functions are only involved through the projection operators $\mathbf{P}^{(\mathcal{C})}_{\alpha}$ in the equations (2.4), (2.6) and (2.8) of the DMFT self-consistent loop.Therefore, the program *interfacing* the DFT code and the DMFT part must merely determine the matrix elements of these projectors $\mathbf{P}^{(\mathcal{C})}_{\alpha}$ in the suitable bases.

This step is performed by the program "dmftproj" in the implementation we extended to perform our LDA+DMFT calculations on Sr_2IrO_4. We describe here the main structure of dmftproj as it was initially developed by M. Aichhorn, L. Pourovskii and V. Vildosola [1]. The more general implementation – in which the spin-orbit coupling may be taken into account – will be introduced in section 3.3.

Definition of the "*Wannier projectors*" $P^{\alpha,\sigma}_{lm,\nu}(\mathbf{k})$

As already mentionned in section 2.1, the DMFT self-consistent loop involves two different bases:

- the Bloch basis $|\psi^{\sigma}_{\mathbf{k}\nu}\rangle$, which is used to describe the lattice quantities,
- the Wannier functions $|\chi^{\alpha,\sigma}_{lm}\rangle$ which define a localized basis set, where α specifies an atom in the unit cell, (l, m) are the orbital indices and σ the spin degree of freedom.

We define the "*Wannier projectors*" $P^{\alpha,\sigma}_{lm,\nu}(\mathbf{k})$ as the matrix elements of the projectors $\mathbf{P}^{(\mathcal{C})}_{\alpha}$ between these two bases. They have the following expression:

$$P^{\alpha,\sigma}_{lm,\nu}(\mathbf{k}) = \langle\chi^{\alpha,\sigma}_{lm}|\psi^{\sigma}_{\mathbf{k}\nu}\rangle \tag{2.44}$$

and are explicitly calculated in the program dmftproj. With this definition, it is possible to specify the formulas (2.4), (2.6) and (2.8) which give respectively the expression of the initial dynamical mean-field $\mathcal{G}_0$:

$$[\mathcal{G}_0(i\omega_n)]^{\sigma}_{mm'} = \sum_{\mathbf{k},\nu\nu'} P^{\alpha,\sigma}_{lm,\nu}(\mathbf{k})\ [\mathbf{G}_{KS}(\mathbf{k}, i\omega_n)]^{\sigma}_{\nu\nu'}\ \left[P^{\alpha,\sigma}_{lm',\nu'}(\mathbf{k})\right]^{*} \tag{2.45}$$

of the lattice self-energy correction $\Sigma^{\sigma}_{\nu\nu'}(\mathbf{k}, i\omega_n)$:

$$\Sigma^{\sigma}_{\nu\nu'}(\mathbf{k}, i\omega_n) = \sum_{\alpha,mm'} \left[P^{\alpha,\sigma}_{lm,\nu}(\mathbf{k})\right]^* \; [\mathbf{\Delta}\Sigma^{\alpha}_{imp}(i\omega_n)]^{\sigma}_{mm'} \; P^{\alpha,\sigma}_{lm',\nu'}(\mathbf{k}) \tag{2.46}$$

and of the local Green's function $\mathbf{G}^{\alpha}_{loc}(i\omega_n)$:

$$[\mathbf{G}^{\alpha}_{loc}(i\omega_n)]^{\sigma}_{mm'} = \sum_{\mathbf{k},\nu\nu'} P^{\alpha,\sigma}_{lm,\nu}(\mathbf{k}) \; G^{\sigma}_{\nu\nu'}(\mathbf{k}, i\omega_n) \; \left[P^{\alpha,\sigma}_{lm',\nu'}(\mathbf{k})\right]^*. \tag{2.47}$$

Construction of the *Wannier projectors* within the (L)APW+lo basis

The calculation of the *Wannier projectors* in "dmftproj" follows the procedure introduced by Anisimov *et al.* [10]. For the interested reader, a brief tutorial to the program is provided in Appendix D.

If the orbital (l, m) of the atom α is considered as correlated, the solution of the Schrödinger equation within the corresponding muffin-tin sphere S^{α}_{MT} at the corresponding linearization energy E^{α}_{1l} is used as the trial orbital:

$$|\phi^{\alpha,\sigma}_{lm}\rangle = |u^{\alpha,\sigma}_{l}(E^{\alpha}_{1l})Y^{l}_{m}\rangle \tag{2.48}$$

Independently of this choice, the user must also choose himself the suitable energy window $\mathcal{W} = [\varepsilon_1, \varepsilon_2]$ in which lie the Bloch states $|\psi^{\sigma}_{\mathbf{k}\nu}\rangle$ used to perform the projection. From these definitions, the Wannier-like functions $|\tilde{\chi}^{\alpha,\sigma}_{lm}\rangle$ are given by:

$$|\tilde{\chi}^{\alpha,\sigma}_{lm}\rangle = \sum_{|\psi^{\sigma}_{\mathbf{k}\nu}\rangle \in \mathcal{W}} |\psi^{\sigma}_{\mathbf{k}\nu}\rangle\langle\psi^{\sigma}_{\mathbf{k}\nu}|u^{\alpha,\sigma}_{l}(E^{\alpha}_{1l})Y^{l}_{m}\rangle \tag{2.49}$$

where the sum runs both on the band indices ν and on the $\mathbf{k}$-points of 1BZ. The corresponding *temporary* projectors are:

$$\widetilde{P}^{\alpha,\sigma}_{lm,\nu}(\mathbf{k}) = \langle u^{\alpha,\sigma}_{l}(E^{\alpha}_{1l})Y^{l}_{m}|\psi^{\sigma}_{\mathbf{k}\nu}\rangle \qquad \forall\nu \in \mathcal{W} \quad \forall\mathbf{k} \in \text{1BZ}. \tag{2.50}$$

Since an energy window was chosen, the number of bands in the sum of (2.49) depends on $\mathbf{k}$ and σ. In practice, we define the temporary projection matrix $\widetilde{P}^{\alpha,\sigma}_{m\nu}(\mathbf{k})$ for all the bands ν such that $\nu_{min}(k,\sigma) \leq \nu \leq \nu_{max}(k,\sigma)$.

Using the decomposition of the Bloch states on the (L)APW+lo basis given by the general equation (2.35) and the following relations – which are deduced from the definition of the (L)APW+lo basis –:

$$\begin{aligned}
\langle u^{\alpha,\sigma}_{l}(E^{\alpha}_{1l})Y^{l}_{m}|u^{\alpha',\sigma'}_{l'}(E^{\alpha'}_{1l'})Y^{l'}_{m'}\rangle &= \delta_{\alpha\alpha'}\delta_{ll'mm'}\delta_{\sigma\sigma'} && \forall E^{\alpha}_{1l}, E^{\alpha'}_{1l'} \\
\langle u^{\alpha,\sigma}_{l}(E^{\alpha}_{1l})Y^{l}_{m}|\dot{u}^{\alpha,\sigma}_{l'}(E^{\alpha}_{1l})Y^{l'}_{m'}\rangle &= 0 && \forall E^{\alpha}_{1l} \\
\langle u^{\alpha,\sigma}_{l}(E^{\alpha}_{1l})Y^{l}_{m}|u^{\alpha',\sigma'}_{l'}(E^{\alpha'}_{2l'})Y^{l'}_{m'}\rangle &= \mathcal{O}^{\alpha,\sigma}_{lm,l'm'}\delta_{\alpha\alpha'}\delta_{\sigma\sigma'} \neq 0 && \forall E^{\alpha}_{1l}, E^{\alpha'}_{2l'}
\end{aligned} \tag{2.51}$$

the *temporary* projectors can be merely calculated by:

$$\widetilde{P}^{\alpha,\sigma}_{lm,\nu}(\mathbf{k}) = A^{\nu\alpha}_{lm}(\mathbf{k},\sigma) + \sum_{n_{LO}=1}^{LOMAX} c^{\nu,\sigma}_{LO} C^{\alpha,LO}_{lm} \mathcal{O}^{\alpha,\sigma}_{lm,l'm'} \tag{2.52}$$

Due to the truncation in the sum over the Bloch states, the Wannier-like orbitals $|\tilde{\chi}^{\alpha,\sigma}_{lm}\rangle$ should be orthonormalized in order to give the final set of Wannier functions. One thus needs to calculate the

overlap matrix:

$$\langle \tilde{\chi}^{\alpha,\sigma}_{lm} | \tilde{\chi}^{\alpha',\sigma'}_{lm'} \rangle = \sum_{\mathbf{k}\in 1\mathrm{BZ}} O^{\alpha,\alpha'}_{m,m'}(\mathbf{k},\sigma)\delta_{\sigma\sigma'} \tag{2.53}$$

$$\text{with} \quad O^{\alpha,\alpha'}_{m,m'}(\mathbf{k},\sigma) = \sum_{\nu=\nu_{min}(\mathbf{k},\sigma)}^{\nu_{max}(\mathbf{k},\sigma)} \widetilde{P}^{\alpha,\sigma}_{lm,\nu}(\mathbf{k}) \left[\widetilde{P}^{\alpha',\sigma}_{lm',\nu}(\mathbf{k})\right]^* . \tag{2.54}$$

However, for practical reasons, it is easier to remain in the reciprocal space to perform this orthonormalization. Indeed, in this case, it is enough to multiply each *temporary* projector by the inverse square root of $O^{\alpha,\alpha'}_{m,m'}(\mathbf{k},\sigma)$ and the "true" Wannier projectors $P^{\alpha,\sigma}_{lm,\nu}(\mathbf{k})$ finally reads:

$$P^{\alpha,\sigma}_{lm,\nu}(\mathbf{k}) = \sum_{\alpha' m'} \left\{ [O(\mathbf{k},\sigma)]^{-1/2} \right\}^{\alpha,\alpha'}_{m,m'} \widetilde{P}^{\alpha',\sigma}_{lm',\nu}(\mathbf{k}) \qquad \forall \nu \in \mathcal{W} \quad \forall \mathbf{k} \in 1\mathrm{BZ}. \tag{2.55}$$

As a result, the program dmftproj calculates roughly the Wannier projectors $P^{\alpha,\sigma}_{lm,\nu}(\mathbf{k})$ in two steps: a first subroutine produces the *temporary* projectors $\widetilde{P}^{\alpha,\sigma}_{lm,\nu}(\mathbf{k})$ using the equation (2.52) and a second subroutine performs the orthonormalization described in (2.55).

From this short description, it appears that the Wannier projectors $P^{\alpha,\sigma}_{lm,\nu}(\mathbf{k})$ are defined in the complex spherical harmonics basis. This does not imply that the program can only calculate the Wannier functions in this basis. It is possible to get the projectors to the correlated orbitals in cubic symmetry or in any desired basis $|\varphi^{(l)}_i\rangle$ by requiring it in the input file. For this, the program will read the corresponding unitary transformation $U^{(l)}_{i,m} = \langle \varphi^{(l)}_i | Y_{lm} \rangle$, which will be then used to transform the projectors:

$$P^{\alpha,\sigma}_{li,\nu}(\mathbf{k}) = \sum_{lm} U^{(l)}_{i,m} \; P^{\alpha,\sigma}_{lm,\nu}(\mathbf{k}) \tag{2.56}$$

The Brillouin zone integration

As observed (2.47), a sum over the $\mathbf{k}$-points in the first Brillouin-zone (1BZ) is necessary. However, in order to reduce the computational time, Wien2k code solves the Kohn-Sham equations for the $\mathbf{k}$-points in the irreducible Brillouin zone (IBZ). In order to evaluate $\mathbf{G}^{\alpha}_{loc}(i\omega_n)$, it is thus necessary to calculate first the unsymmetrized Green function in IBZ and then apply the symmetry operation $\mathcal{S}$ of the crystallographic space group $\mathcal{G}$ as follows:

$$[\mathbf{G}^{\alpha}_{loc}(i\omega_n)]^{\sigma}_{mm'} = \sum_{\mathbf{k}\in 1\mathrm{BZ}} G^{\alpha,\sigma}_{mm'}(\mathbf{k},i\omega_n) = \sum_{\mathcal{S}\in\mathcal{G}} \sum_{nn'} D^l(\mathcal{S})_{mn} \left[\sum_{\mathbf{k}'\in \mathrm{IBZ}} G^{\alpha,\sigma}_{nn'}(\mathbf{k}',i\omega_n)\; \omega(\mathbf{k}') \right] D^l(\mathcal{S}^{-1})_{n'm'}$$

$$\text{with} \qquad G^{\alpha,\sigma}_{mm'}(\mathbf{k},i\omega_n) = \sum_{\nu\nu'} P^{\alpha,\sigma}_{m\nu}(\mathbf{k})\; G^{\sigma}_{\nu\nu'}(\mathbf{k},i\omega_n)\; \left[P^{\alpha,\sigma}_{\nu' m'}(\mathbf{k})\right]^* \tag{2.57}$$

In this expression, $\mathbf{k}'$ samples a tetrahedral mesh and $\omega(\mathbf{k}')$ represents its corresponding weight. In principle, the tetrahedral weights $\omega_\nu(\mathbf{k}')$ depends also on the band index: its value is smaller for the bands which cross the Fermi level and it is 0 if the band is empty. In practice however, we take merely the simple geometrical factor of the tetrahedron $\omega(\mathbf{k}')$ as corresponding weight, since in the DMFT cycle the chemical potential μ will change.

A similar approach is also used to calculate the initial dynamical mean-field $\mathcal{G}_0$ since a sum over the $\mathbf{k}$-points appears also in (2.45). More generally, any local quantity – density matrix, spectral function,... – require such a treatment to be evaluated. For the interested reader, the formula (2.57) is explicitly derived in Appendix E.

Chapter 3

Taking into account the spin-orbit interaction in LDA+DMFT

In solid state physics, the spin-orbit interaction is commonly thought as a *weak* relativistic correction to the Schrödinger equation and is thus treated perturbatively. However, its effects on the band structure of solids can be quite dramatic, quantitatively and even qualitatively. This was originally highlighted in semiconductors with the well-known "*Dresselhaus splitting*" [49, 50] and more recently with the discovery of "*topological bands insulators*" [21, 94, 118]. Furthermore, by coupling the spin degree of freedom with the electronic angular momentum, the spin-orbit interaction seems to fulfill the expectations of "*spintronics*": to control the spin orientation in solid with an electric field.

The interplay between electronic correlations and the spin-orbit coupling is a very new field of interest in condensed matter physics [131, 164]. Recent works – on strontium rhodate [64, 107] or iridium-based transition metal oxides [84, 116] to only name a few – have also shown the significant rearrangements in the band structure which can arise by taking into account these both interactions. In this context, developing an LDA+DMFT implementation for which the spin-orbit corrections can be fully integrated in the definition of the correlated orbitals is of great interest.

In this section, the derivation of the spin-orbit interaction and its influence on an atomic level are first reminded. We then give a brief review of the effects induced by the spin-orbit coupling in solid state physics. We finally describe how this relativistic correction may be introduced in the LDA+DMFT implementation of Aichhorn *et al.* [1]. This improvement of the method is one of the major technical developments achieved during this thesis in order to perform the LDA+DMFT study of Sr_2IrO_4.

3.1 Basics on the spin-orbit interaction

In this section, we first derive the spin-orbit correction from the Dirac equation and then present the influence of this term at an atomic level by introducing the notion of "*fine structure multiplets*". Attention is particularly paid on the case of atomic d orbitals in cubic symmetry because of its importance in the case of Sr_2IrO_4. All these fundamental concepts on the spin-orbit interaction can be found in any reference book, but we specially recommend [154, 157].

3.1.1 Derivation of the spin-orbit coupling term

The "*spin-orbit interaction*" is a correction to the Schrödinger-Pauli equation in the limit where relativistic effects are assumed weak. It introduces a coupling between the spin $\mathbf{s}$ and the motion – or more precisely the orbital momentum $\mathbf{l}$ in the atomic case – of the electron.

Non-relativistic limit of Dirac's Hamiltonian

Dirac's Hamiltonian provides a description of an elementary spin-1/2 particles, such as electrons, consistent with both the principles of quantum mechanics and the theory of special relativity. An electron in an external potential $V(\mathbf{r})$ is thus described by the following equation:

$$H_{Dirac}\ \Psi = i\hbar\frac{\partial\Psi}{\partial t} \qquad \text{with} \qquad H_{Dirac} = c\ \boldsymbol{\alpha}\cdot\mathbf{p} + \beta m_0c^2 + V(\mathbf{r}) \tag{3.1}$$

where $\boldsymbol{\alpha}$ and β are the 4×4 matrices:

$$\boldsymbol{\alpha} = \begin{pmatrix} 0 & \boldsymbol{\sigma} \\ \boldsymbol{\sigma} & 0 \end{pmatrix} \qquad \text{and} \qquad \beta = \begin{pmatrix} \mathbf{Id} & 0 \\ 0 & -\mathbf{Id} \end{pmatrix} \tag{3.2}$$

and σ_x ,σ_y and σ_z are the Pauli-spin matrices. The stationary solutions of (3.1) are the four-component functions Ψ which can be written in terms of two 2-spinors Φ and χ as follows:

$$\Psi = e^{-iEt}\begin{pmatrix} \Phi \\ \chi \end{pmatrix} \quad \text{and} \quad \begin{cases} c\ [\boldsymbol{\sigma}\cdot\mathbf{p}]\ \chi &=& [E - V(\mathbf{r}) - m_0c^2]\ \Phi \\ c\ [\boldsymbol{\sigma}\cdot\mathbf{p}]\ \Phi &=& [E - V(\mathbf{r}) + m_0c^2]\ \chi \end{cases} \tag{3.3}$$

For electrons – which are positive energy solutions of (3.1) –, Φ describes the "*large component*" of the wave-function and χ the "*small*" one.

The "*spin-orbit coupling term*" appears when one develops the Hamiltonian (3.1) in the "*non-relativistic limit*" up to the order $(v/c)^2$. By shifting the energies reference by the rest energy m_0c^2 of the electron ($E = \varepsilon + m_0c^2$), the coupled equations (3.3) determine the order of magnitude of χ as (v/c) times smaller than Φ. As a result, the initial four-component problem can be reduced in the *non-relativistic limit* to the following equation where only the *large component* Φ appears:

$$\frac{1}{2m_0}[\boldsymbol{\sigma}\cdot\mathbf{p}]\left[1 + \frac{\varepsilon - V(\mathbf{r})}{2m_0c^2}\right]^{-1}[\boldsymbol{\sigma}\cdot\mathbf{p}]\ \Phi + V(\mathbf{r})\ \Phi = \varepsilon\ \Phi. \tag{3.4}$$

The expansion of the denominator of the first term gives:

$$\left[1 + \frac{\varepsilon - V(\mathbf{r})}{2m_0c^2}\right]^{-1} = 1 - \frac{\varepsilon - V(\mathbf{r})}{2m_0c^2} + O\left(\frac{1}{m_0^2c^4}\right). \tag{3.5}$$

By using then the following operator identities:

$$\begin{aligned} \mathbf{p}\ V(\mathbf{r}) &= V(\mathbf{r})\mathbf{p} - i\hbar\boldsymbol{\nabla}V(\mathbf{r}) \\ [\boldsymbol{\sigma}\cdot\boldsymbol{\nabla}V(\mathbf{r}])\,[\boldsymbol{\sigma}\cdot\mathbf{p}] &= \boldsymbol{\nabla}V(\mathbf{r})\cdot\mathbf{p} + i\sigma\cdot[\boldsymbol{\nabla}V(\mathbf{r})\times\mathbf{p}] \end{aligned} \tag{3.6}$$

the differential equation (3.4) becomes:

$$\begin{aligned} \left[\left(1 - \frac{\varepsilon - V(\mathbf{r})}{2m_0c^2}\right)\frac{\mathbf{p}^2}{2m_0} + V(\mathbf{r})\right]\Phi \quad -\frac{\hbar^2}{4m_0^2c^2}[\boldsymbol{\nabla}V(\mathbf{r})\cdot\boldsymbol{\nabla}\Phi] \quad +\frac{\hbar}{4m_0^2c^2}\boldsymbol{\sigma}\cdot[\boldsymbol{\nabla}V(\mathbf{r})\times\mathbf{p}]\ \Phi &= \varepsilon\ \Phi \\ \left[\frac{\mathbf{p}^2}{2m_0} + V(\mathbf{r})\right]\Phi \quad -\frac{\mathbf{p}^4}{8m_0^3c^2}\Phi \quad -\frac{\hbar^2}{4m_0^2c^2}[\boldsymbol{\nabla}V(\mathbf{r})\cdot\boldsymbol{\nabla}\Phi] \quad +\frac{\hbar}{4m_0^2c^2}\boldsymbol{\sigma}\cdot[\boldsymbol{\nabla}V(\mathbf{r})\times\mathbf{p}]\ \Phi &= \varepsilon\ \Phi. \end{aligned} \tag{3.7}$$

The first and the second term give the *usual* non-relativistic Schrödinger equation. The third and the fourth term are the *mass* and *Darwin correction* respectively. Finally, the last term corresponds to the *spin-orbit coupling* in its most general form:

$$H_{SO} = \frac{\hbar}{4m_0^2c^2}\boldsymbol{\sigma}\cdot[\boldsymbol{\nabla}V(\mathbf{r})\times\mathbf{p}]. \tag{3.8}$$

If the potential has the spherical symmetry – as, for instance, for a simple atomic nucleus –, we indeed obtain the more common expression:

$$H_{SO} = \frac{1}{2m_0^2c^2}\frac{1}{r}\frac{dV}{dr}(\mathbf{l}\cdot\mathbf{s}) \qquad \text{with} \qquad \mathbf{s} = \frac{1}{2}\hbar\boldsymbol{\sigma} \quad \text{and} \quad \mathbf{l} = \mathbf{r}\times\mathbf{p}. \tag{3.9}$$

"Intuitive" derivation in the atomic case

The spin-orbit interaction term H_{SO} can also be derived in the framework of classical electrodynamics if one considers a simple atom. Since there exits a magnetic moment of the electron, connected with the electron spin $\mathbf{s}$, this moment $\boldsymbol{\mu} = -2\mu_0\mathbf{s}/\hbar$, with $\mu_0 = e\hbar/2m_0$ the Bohr magneton, leads to an additional interaction $-\boldsymbol{\mu}\cdot\mathbf{B}$ between the electron and the nucleus.

In this expression, $\mathbf{B}$ is the magnetic field which is associated with the electron moving in the electric field $\mathbf{E}$ induced by the nucleus. Since $\mathbf{B} = -(\mathbf{v}\times\mathbf{E})/c^2$ in classical electromagnetism, the additional energy of the electron in the field can be rewritten as:

$$-\boldsymbol{\mu}\cdot\mathbf{B} = +\frac{e}{m_0}\mathbf{s}\cdot\mathbf{B} = +\frac{e}{m_0^2c^2}\mathbf{s}\cdot(\mathbf{E}\times\mathbf{p}). \tag{3.10}$$

This term in the Hamiltonian is essentially the spin-orbit term H_{SO}, except for a factor 2. This factor – the *Thomas precession factor* – is missing because the complete Lorentz transformation was not applied. Actually, while changing the frame of reference, a time transformation also occurs and consequently, the precession frequency of the electron spin in the magnetic field is modified by a factor $\frac{1}{2}$.

Since the electrical field induced by the nucleus is central symmetric, one can write:

$$\mathbf{E} = -\boldsymbol{\nabla}\left(-\frac{1}{e}V(\mathbf{r})\right) = \frac{1}{e}\frac{\partial V}{\partial r}\frac{\mathbf{r}}{r} \tag{3.11}$$

where $V(r)$ is the potential of the atomic nucleus. As a result, the previous energy term (3.10) becomes:

$$+\left(\frac{1}{2}\right)\frac{e}{m_0^2c^2}\mathbf{s}\cdot(\mathbf{E}\times\mathbf{p}) = \frac{e}{2m_0^2c^2}\mathbf{s}\cdot\left(\frac{1}{e}\frac{\partial V}{\partial r}\frac{\mathbf{r}}{r}\times\mathbf{p}\right) = \frac{1}{2m_0^2c^2}\frac{1}{r}\frac{\partial V}{\partial r}(\mathbf{l}\cdot\mathbf{s}) \tag{3.12}$$

which is exactly the *spin-orbit coupling term* (3.9).

3.1.2 Effects on atomic orbitals

According to the expression (3.9), the spin-orbit interaction depends on the value of the the angular momentum $\mathbf{l}$ of the electron – the spin has the same value $s = 1/2$ for all electrons – and the mutual orientation of the angular momentum $\mathbf{l}$ and the spin $\mathbf{s}$. In other words, the spin-orbit interaction depends on the value of the total angular momentum $\mathbf{j} = \mathbf{l} + \mathbf{s}$:

$$H_{SO} = \frac{1}{2m_0^2c^2}\left(\frac{1}{r}\frac{\partial V}{\partial r}\right)\frac{1}{2}(\mathbf{j}^2 - \mathbf{l}^2 - \mathbf{s}^2). \tag{3.13}$$

Energy splitting for an hydrogen-like ion

Because of the spin-orbit coupling, the energy of an electron in the states $j = l + \frac{1}{2}$ and $j = l - \frac{1}{2}$ is now different. To evaluate this energy splitting, one can calculate the mean value of the perturbation H_{SO} in the atomic state (n, l) for an hydrogen-like ion:

$$\langle H_{SO}\rangle_{n,l} = \frac{Ze^2}{4\pi\varepsilon_0}\frac{\hbar^2}{2m_0^2c^2}\,\langle\frac{1}{r^3}\rangle\,\frac{1}{2}\left[j(j+1) - l(l+1) - \frac{3}{4}\right] \quad \text{since} \quad V(r) = -\frac{Ze^2}{4\pi\varepsilon_0}\frac{1}{r}. \tag{3.14}$$

Consequently, the correction to the energy due to the spin-orbit coupling is:

$$(\Delta E_{SO})_{n,l} = \zeta_{SO}\frac{1}{2}\left[j(j+1) - l(l+1) - \frac{3}{4}\right] \tag{3.15}$$

$$\text{with} \quad \zeta_{SO} = \frac{e\hbar^2}{8\pi\varepsilon_0 m_0 c^2 a_0^3}\frac{1}{l(l+1)(l+\frac{1}{2})}\frac{Z^4}{n^3}\ \text{eV} = \frac{\alpha^2}{l(l+1)(l+\frac{1}{2})}\frac{Z^4}{n^3}\ \text{Ry}. \tag{3.16}$$

To obtain this expression, we have used[1] the following formula:

$$\langle\frac{1}{r^3}\rangle = \int \frac{1}{r^3}\ R_{nl}^2(r)\ r^2 dr = \frac{1}{n^3 l(l+1)(l+\frac{1}{2})}\frac{Z^3}{a_0^3}. \tag{3.18}$$

As a result, the spin-orbit corrections scale as Z^4 where Z is the atomic number. Heavy elements will thus undergo more important spin-orbit corrections than light ones, as shown in table 3.1.

Atom	Z	$\zeta_{SO}(3d)$
Iron (Fe)	26	0.050 eV
Copper (Cu)	29	0.103 eV

Atom	Z	$\zeta_{SO}(4d)$
Ruthenium (Ru)	44	0.161 eV
Rhodium (Rh)	45	0.191 eV

Atom	Z	$\zeta_{SO}(5d)$
Iridium (Ir)	77	0.4 eV
Gold (Au)	79	0.42 eV

Atom	Z	$\zeta_{SO}(6p)$
Bismuth (Bi)	83	1.5 eV

Table 3.1: Typical value of the spin-orbit constant ζ_{SO} for some elements of the periodic table. From [53] (5d), from [64] (4d), from Landolt-Börnstein database (3d) and from [71] (Bi)

Fine structure multiplets in multi-electronic atoms

Without spin-orbit interaction, the multi-electronic configuration of an atom is completely described by its total angular momentum **L** and its total spin **S**, which form the **LS** spectral term of the system. The $(2L+1)(2S+1)$ states – which differ by the value of the **z** component of the orbital and spin momenta M_L and M_S – have all the same energy. The spin-orbit interaction leads to a splitting of the standard **LS** spectral term into a number of components corresponding to different values of the total angular momentum **J** of the atom. This splitting is called "*fine*" or "*multiplet splitting*".

Multiplet splitting obeys a rule which is called "*Landé's interval rule*". According to this rule, the splitting of the levels J and $J-1$ is proportional to J:

$$\Delta E_{J,J-1} = \chi(LS).J \tag{3.19}$$

The multiplet splitting constant $\chi(LS)$ is different for different spectral terms and can be of either sign:

- When $\chi(LS) > 0$, the multiplet component with the smallest possible value $J = |L-S|$ has the lowest energy value. Such a multiplet is called "*normal*".
- When $\chi(LS) < 0$, the multiplet component with the greatest possible value $J = L+S$ has the lowest energy value. Such a multiplet is called "*inverted*".

[1] We remind that the Bohr radius a_0, the fine structure constant α and a Rydberg are defined by:

$$a_0 = \frac{4\pi\varepsilon_0\hbar^2}{m_0 e^2} \quad , \quad \alpha = \frac{e^2}{4\pi\varepsilon_0\hbar c} \quad \text{and} \quad 1\ \text{Ry} = \frac{\hbar^2}{2m_0 a_0^2}. \tag{3.17}$$

It has been empirically established that a configuration containing n equivalent electrons:

- corresponds to *normal* multiplets, when $n < 2l + 1$ (when shells are less than half-filled),
- corresponds to *inverted* multiplets, when $n > 2l + 1$ (when shells are more than half-filled),
- has no triplet splitting if $n = 2l + 1$.

Each spectral term, except for singlet terms and S terms, has a fine structure. In general however, the distance between the components of this structure is considerably less than the distance between different spectral terms. This grouping of levels is characteristic of the approximation which is called the "*Russel-Saunders coupling*" approximation. Since this is the most current case, the expression "**LS** *coupling*" or "*normal coupling*" is also used.

Analysis of experimental data have shown that the range of applicability of the **LS** *coupling* approximation is actually limited. It is therefore of interest to consider another limiting case: when the spin-orbit interaction considerably exceeds the electrostatic interaction. This case is called "jj-*coupling*". If the spin-orbit coupling is large, one can only speak of the total angular momentum of an electron **j**, as only this angular momentum is conserved. **jj** *coupling* is rarely found in pure form in atomic spectra. However, the structure of the spectra of the heavy elements very closely approaches the structure characteristic of **jj**-*coupling*. Generally speaking, in passing from the light to the heavy elements, a more or less continuous transition from **LS** to **jj** *coupling* is observed.

3.1.3 Atomic d orbitals in cubic symmetry and spin-orbit coupling

In many transition metal oxides – such as those which crystallize in the perovskyte or K_2NiF_4-type structure for instance –, the transition metal ion is at the center of an octahedron, typically made by six oxygen atoms. In this case, the local crystal field lifts the degeneracy of the d orbitals, which are then divided in:

- a three-fold group of states called "t_{2g}" (d_{xy},d_{xz} and d_{yz}) lower in energy,
- a doublet labelled "e_g" ($d_{x^2-y^2}$ and $d_{3z^2-r^2}$) higher in energy.[2]

If the transition metal ion is heavy enough, like an iridium atom or any other $5d$ element, the spin-orbit interaction must be taken into account. As a result, the symmetry of the system will be lowered and *fine multiplets* will appear. However, due to the cubic crystal field, the *fine structure* of the d orbitals will not be decomposed in a six-fold $j = 5/2$ group and a quartet $j = 3/2$ as for a single atom. Our aim is now to derive it in the framework of the "*TP-equivalence approximation*".

The matrix elements of the orbital angular momentum **l** in a cubic system with a single electron t_{2g} or e_g are the following:

$$l_x = \left(\begin{array}{ccc|cc} 0 & 0 & i & 0 & 0 \\ 0 & 0 & 0 & -i\sqrt{3} & -i \\ -i & 0 & 0 & 0 & 0 \\ \hline 0 & i\sqrt{3} & 0 & 0 & 0 \\ 0 & i & 0 & 0 & 0 \end{array}\right), \qquad l_y = \left(\begin{array}{ccc|cc} 0 & 0 & 0 & i\sqrt{3} & -i \\ 0 & 0 & -i & 0 & 0 \\ 0 & i & 0 & 0 & 0 \\ \hline -i\sqrt{3} & 0 & 0 & 0 & 0 \\ i & 0 & 0 & 0 & 0 \end{array}\right) \tag{3.20}$$

$$\text{and} \qquad l_z = \left(\begin{array}{ccc|cc} 0 & i & 0 & 0 & 0 \\ -i & 0 & 0 & 0 & 0 \\ 0 & 0 & 0 & 0 & 2i \\ \hline 0 & 0 & 0 & 0 & 0 \\ 0 & 0 & -2i & 0 & 0 \end{array}\right)$$

[2]For the interested reader, a brief reminder on the definition of atomic d states in an octahedral ligand field can be found in Appendix A.

where the matrices are given in the basis $\{d_{xz},\, d_{yz},\, d_{xy},\, d_{3z^2-r^2},\, d_{x^2-y^2}\}$. The calculation is straightforward by using the explicit forms of the t_{2g} and e_g orbitals and the well-known relations:

$$l_z|\varphi_{lm}\rangle = \hbar m|\varphi_{lm}\rangle \quad \text{and} \quad l_\pm|\varphi_{lm}\rangle = \hbar\sqrt{l(l+1)-m(m\pm1)}|\varphi_{lm\pm1}\rangle \quad \text{with} \quad l_\pm = l_x \pm i l_y. \tag{3.21}$$

The matrices (3.20) are hermitian and their elements are purely imaginary (the cubic basis is real). However, the matrix elements of $\mathbf{l}$ in the e_g subspace are zero. This means that the orbital angular momentum is "*completely quenched*" in the e_g states. As a result, there is *no* first-order spin-orbit interaction for these states.

On the contrary, in the t_{2g} subspace, the orbital angular momentum is not quenched. In addition, by comparing the matrix elements in the t_{2g} states with those in the p states of a free atom, it appears that:

$$\mathbf{l}(t_{2g}) = -\mathbf{l}(p). \tag{3.22}$$

This means that the expectation value of $\mathbf{l}^2 = l_x^2 + l_y^2 + l_z^2$ in the t_{2g} subspace is $l(l+1)$ not with $l=2$ but rather with $l=1$: the orbital angular momentum is thus "*partially quenched*" in the t_{2g} states. The relation (3.22) is called the "*TP-equivalence*".

The *TP-equivalence* is only formal as seen from the fact that $\mathbf{l}(t_{2g})$ does not satisfy the commutation relation which the angular momentum should satisfy. The non-diagonal matrix elements between e_g and t_{2g} states were indeed neglected. Nevertheless, if the cubic-field splitting between the e_g and t_{2g} states is large, neglecting these elements may be justified and the *TP-equivalence* can conveniently be used. In this case, the matrix of the spin-orbit interaction in the t_{2g} subspace can be decomposed in two submatrices:

$$\begin{pmatrix} 0 & -i & i \\ i & 0 & -1 \\ -i & -1 & 0 \end{pmatrix}.\frac{\zeta_{SO}}{2} \qquad \text{and} \qquad \begin{pmatrix} 0 & i & 1 \\ -i & 0 & i \\ -i & 1 & 0 \end{pmatrix}.\frac{\zeta_{SO}}{2} \tag{3.23}$$

in the bases $\{d_{xz}\uparrow,\, d_{yz}\uparrow,\, d_{xy}\downarrow\}$ and $\{d_{xz}\downarrow,\, d_{yz}\downarrow,\, d_{xy}\uparrow\}$ respectively, and with:

$$\zeta_{SO} = \frac{1}{2m_0^2c^2}\int_0^{+\infty}\frac{1}{r}\frac{\partial V}{\partial r}R_{nd}^2(r)\; r^2 dr. \tag{3.24}$$

Both these matrices can be partially diagonalized by using the following linear combination of d_{xz} and d_{yz}:

$$|t_+\rangle = -\frac{1}{\sqrt{2}}(|d_{yz}\rangle + i|d_{xz}\rangle) \quad \text{and} \quad |t_-\rangle = \frac{1}{\sqrt{2}}(|d_{yz}\rangle - i|d_{xz}\rangle). \tag{3.25}$$

As a result, in the bases $\{t_+\uparrow,\, t_-\uparrow,\, d_{xy}\downarrow\}$ and $\{t_+\downarrow,\, t_-\downarrow,\, d_{xy}\uparrow\}$, the matrices (3.23) become:

$$\begin{pmatrix} -1 & 0 & 0 \\ 0 & 1 & -\sqrt{2} \\ 0 & -\sqrt{2} & 0 \end{pmatrix}.\frac{\zeta_{SO}}{2} \qquad \text{and} \qquad \begin{pmatrix} 1 & 0 & -\sqrt{2} \\ 0 & -1 & 0 \\ -\sqrt{2} & 0 & 0 \end{pmatrix}.\frac{\zeta_{SO}}{2}. \tag{3.26}$$

By diagonalizing the last 2×2 block, one finally obtains:

- a doublet of eigenstates associated to the eigenvalue $\varepsilon^{SO}_{j_{\text{eff}}=\frac{1}{2}} = +\zeta_{SO}$:

$$\begin{cases} |j_{\text{eff}} = \frac{1}{2}, m_j = -\frac{1}{2}\rangle = \frac{1}{\sqrt{3}}|d_{yz}\uparrow\rangle - \frac{i}{\sqrt{3}}|d_{xz}\uparrow\rangle - \frac{1}{\sqrt{3}}|d_{xy}\downarrow\rangle \\ |j_{\text{eff}} = \frac{1}{2}, m_j = +\frac{1}{2}\rangle = \frac{1}{\sqrt{3}}|d_{yz}\downarrow\rangle + \frac{i}{\sqrt{3}}|d_{xz}\downarrow\rangle + \frac{1}{\sqrt{3}}|d_{xy}\uparrow\rangle \end{cases} \tag{3.27}$$

- a quartet of eigenstates with the same eigenvalue $\varepsilon^{SO}_{j_{\text{eff}}=\frac{3}{2}} = -\zeta_{SO}/2$:

$$\begin{cases} |j_{\text{eff}} = \frac{3}{2}, m_j = -\frac{3}{2}\rangle = \frac{1}{\sqrt{2}}|d_{yz}\downarrow\rangle - \frac{i}{\sqrt{2}}|d_{xz}\downarrow\rangle \\ |j_{\text{eff}} = \frac{3}{2}, m_j = +\frac{3}{2}\rangle = -\frac{1}{\sqrt{2}}|d_{yz}\uparrow\rangle - \frac{i}{\sqrt{2}}|d_{xz}\uparrow\rangle \\ |j_{\text{eff}} = \frac{3}{2}, m_j = -\frac{1}{2}\rangle = \frac{1}{\sqrt{6}}|d_{yz}\uparrow\rangle - \frac{i}{\sqrt{6}}|d_{xz}\uparrow\rangle + \sqrt{\frac{2}{3}}|d_{xy}\downarrow\rangle \\ |j_{\text{eff}} = \frac{3}{2}, m_j = +\frac{1}{2}\rangle = -\frac{1}{\sqrt{6}}|d_{yz}\downarrow\rangle - \frac{i}{\sqrt{6}}|d_{xz}\downarrow\rangle + \sqrt{\frac{2}{3}}|d_{xy}\uparrow\rangle \end{cases} . \tag{3.28}$$

In these expressions, the analogy with the $p_{\frac{1}{2}}$ and $p_{\frac{3}{2}}$ was used to label the states. Furthermore, the separation between the two multiplets is given by Landé's interval rule:

$$\varepsilon^{SO}_{j_{\text{eff}}=\frac{3}{2}} - \varepsilon^{SO}_{j_{\text{eff}}=\frac{1}{2}} = -\frac{3}{2}\zeta_{SO}. \tag{3.29}$$

As a result, by assuming that the cubic splitting between the e_g and t_{2g} orbitals is much larger than the spin-orbit splitting, the fine structure of the d atomic orbitals is given by:

- the e_g states on which the spin-orbit interaction is ineffective, because of their quenched angular momentum,
- the doublet $j_{\text{eff}} = 1/2$ (3.27) and the quartet of states $j_{\text{eff}} = 3/2$ (3.28), the former being higher in energy than the latter.

So far, we have neglected the non-diagonal matrix elements of the spin-orbit interaction, the complete calculation of the multiplets without the *TP-equivalence* is performed in the appendix A. In addition, a calculation within the *TP-equivalence* approximation but including a small tetragonal field between the t_{2g} states is also described in this appendix. Neverthelees, as we will see in section 5, this description of the atomic d orbitals within the "*TP-equivalence approximation*" is enough to study the effect of the spin-orbit coupling in Sr_2IrO_4.

3.2 Effects of the spin-orbit coupling in solids

In this section, a (very) general overview of the effects induced by the spin-orbit coupling in solid states physics is presented. Since many specific – and often new – branches are involved, we are not able to provide many details in each field. We present first the well-known effects induced by the spin-orbit coupling in semiconductor structures before merely listing the state-of-the-art discoveries which involve the spin-orbit interaction in modern condensed matter physics.

3.2.1 Dresselhaus and Rashba terms

In 1954, Elliot [51] and Dresselhaus *et al.* [50] emphasize that the spin-orbit interaction may have important consequences for the one electron energy levels in bulk semi-conductors. Subsequently, spin-orbit coupling effects in a bulk zinc blende structure were discussed in two classic papers by Parmenter [128] and Dresselhaus [49]. Unlike the diamond structure of silicon (Si) and germanium (Ge), the zinc blende structure does not have a center of inversion. As a result, a spin splitting of the electron and hole states occurs at non-zero $\mathbf{k}$-point even for a zero magnetic-field. This spin splitting was interpreted as a consequence of the spin-orbit coupling, because otherwise, the spin degree of freedom of the Bloch

electrons would not know whether it was moving in an inversion symmetric diamond structure or an inversion-antisymmetric zinc blende structure.

To understand better this last statement, it is necessary to consider the action of the time reversal operator Θ on the system defined by the Hamiltonian H:

$$H = \frac{\mathbf{p}^2}{2m_0} + V(\mathbf{r}) + \frac{\hbar^2}{4m_0^2c^2}\boldsymbol{\sigma} \cdot [\boldsymbol{\nabla} V(\mathbf{r}) \times \mathbf{p}] \tag{3.30}$$

where $V(\mathbf{r})$ is the lattice potential and the third term the spin-orbit correctionin its most general form (3.8). Since this Hamiltonian commutes with Θ, the Bloch function $\psi^{\sigma}_{\mathbf{k}}(\mathbf{r})$ and $\psi^{-\sigma *}_{-\mathbf{k}}(\mathbf{r})$ are associated to the same eigenvalue:

$$\varepsilon^{\sigma}(\mathbf{k}) = \varepsilon^{-\sigma}(-\mathbf{k}) \tag{3.31}$$

with $\mathbf{k}$ the momentum and σ the spin index (for the sake of simplicity, band indices were omitted).

If moreover the crystal has a center of inversion – that is to say, if the operation $I : \mathbf{r} \to -\mathbf{r}$ belongs to the crystallographic spacegroup – , the following relation also holds:

$$\varepsilon^{\sigma}(\mathbf{k}) = \varepsilon^{\sigma}(-\mathbf{k}) \tag{3.32}$$

By combining the equations (3.31) and (3.32), it becomes then clear that if both time reversal symmetry Θ and spatial inversion symmetry I are present in the system, the band structure should satisfy to the condition:

$$\varepsilon^{\sigma}(\mathbf{k}) = \varepsilon^{-\sigma}(\mathbf{k}) \tag{3.33}$$

In other words, each band will preserve its spin degeneracy, as illustrated in figure 3.1 (a). This is the case for the diamond structure of silicon and germanium. On the contrary, if a center of inversion symmetry is absent in the crystal, like in the zinc blende structure of the semiconductors InSb or GaAs, only the relation (3.31) remains and, as shown in figure 3.1 (b), the spin degeneracy is lifted by the spin-orbit term (3.8). This phenomenon is called the "*Dresselhaus splitting*".

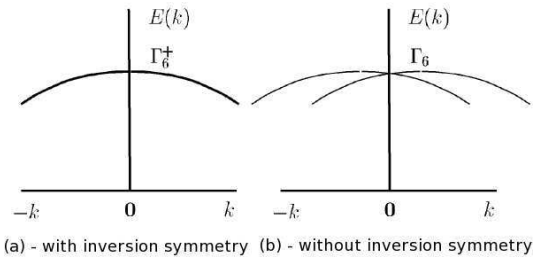

Figure 3.1: Schematic example of the "*Dresselhaus splitting*". In panel (a), the solid has a center of symmetry and the level is doubly degenerate. In panel (b), the solid has no center of inversion and the *Dresselhaus splitting* occurs.

Nevertheless, the spin degeneracy can not only be lifted because of a bulk inversion asymmetry of the underlying crystal structure but also because of a structure inversion asymmetry of the confining potential $V(\mathbf{r})$. Particularly, the termination of the crystal by a surface destroys the inversion symmetry in the direction of the normal. In this case, by performing a Taylor expansion of the potential $V(\mathbf{r})$:

$$V(\mathbf{r}) = V_0 + e\mathbf{r} \cdot \mathcal{E} + O(r^2) \tag{3.34}$$

the lowest order of the inversion asymmetry of the potential is characterized by an electric field $\mathcal{E}$. As a result, the corresponding spin-orbit correction can be rewritten as:

$$H_{Rashba} = \frac{\alpha_R}{\hbar}\boldsymbol{\sigma} \cdot (\mathbf{k} \times \mathcal{E}) \tag{3.35}$$

which is the "*Rashba Hamiltonian*" [29]. This term can induce significant effects in quasi-two-dimensional semiconductor structures, such as quantum wells and heterostructures [166]. Furthermore, exploiting this effect is at the root of "*semiconductor spintronics*", as we will see in the following.

3.2.2 New domains involving the spin-orbit coupling

As already mentioned in the introduction, the spin-orbit interaction has recently regained interest in condensed matter physics, especially through three different fields, which are briefly presented here.

Spintronics

"*Spintronics*" is a multidisciplinary field whose central theme is the active manipulation of spin degrees of freedom in solid state physics. The discovery of the giant magneto-resistance (GMR) in 1988 by Fert *et al.* [18] and Grünberg *et al.* [22] has marked the beginning of the development of this field.

Very recently, in the field of "*semiconductor spintronics*" a number of spin-electronic devices have been proposed, which explicitly make use of the Rashba effect (3.35), motivated by the proposal of a "*spin field-effect transistor*" by Datta and Das [44]. The basic idea is the control of the spin orientation by using this spin splitting due to the spin-orbit coupling in the presence of a structure inversion asymmetric potential. More details can be found in the review [162] for instance.

Topological band insulators

The discovery of "*topological band insulators*" in theory [21, 54, 82, 119] and experiment [71, 94] has opened a new field which is nowadays very active. In these remarkable materials, the strong spin-orbit interaction allows a non-trivial topology of the electron bands, resulting in protected "*helical edge*" and "*surface states*" in two and three dimensional systems. As a result, a *topological band insulator*, like an ordinary insulator, has a bulk energy gap separating the highest occupied electronic band from the lowest empty band but its surface – or edge in two dimensions – exhibits gapless electronic states that are protected by time reversal symmetry.

Many other interesting phenomena, including "*quantum number fractionalization*" and "*magneto-electric effects*" have been predicted to occur in these systems, and are currently the subject of a growing experimental effort.

Interplay between electronic correlations and the spin-orbit coupling

The interplay between the spin-orbit coupling and the electronic Coulomb correlations has recently become the subject of intense research in condensed matter physics [131, 164]. For instance, recent works on strontium rhodate (Sr_2RhO_4) have indeed shown that the spin-orbit coupling can be reinforced by the action of the Coulomb interaction [64, 86, 107], whereas the spin-orbit coupling is considered as the driving force for the Mott insulating state in strontium iridate (Sr_2IrO_4) [84].

In this field, the attention is particularly focused on the properties of iridium-based transition metal oxides – such as $Na_4Ir_3O_8$ [36, 127], Na_2IrO_3 [146], $Pr_2Ir_2O_7$ [125] and of course the Ruddlesden-Popper serie $Sr_{n+1}Ir_nO_{3n+1}$ [116] –, but other frustrated magnets [159] or Fe-spinel [37] are also studied a lot. In this context, developing an LDA+DMFT implementation for which the spin-orbit corrections can

be fully integrated in the definition of the correlated orbitals is of great interest. The subject of this thesis is therefore directly related to this very recent field of research.

3.3 Implementation of the spin-orbit coupling in LDA+DMFT

Theoretically, the spin-orbit interaction can easily be included inside the LDA+DMFT formalism. Indeed, the equations introduced in section 2.1 can still be used if any spin-index σ is forgotten[3]. In practice however, developing such an implementation of LDA+DMFT, which could be called an "*LDA+SO+DMFT implementation*", is highly dependent on how the spin-orbit coupling is already taken into account at the LDA level.

Since our aim during this thesis was to develop such an implementation based on the LAPW framework – extending then the LDA+DMFT implementation of Aichhorn *et al.* [1] –, we describe first in this section how the spin-orbit interaction is treated within the Wien2k code. The consequence on the definition of the Wannier projectors and on DMFT equations is then presented.

3.3.1 How the spin-orbit interaction is included in Wien2k

Wien2k provides the possibility of performing both non-relativistic and relativistic calculations. When running relativistic calculations, relativity is included in a way which differs for core and valence states. The core states are assumed to be fully occupied and a fully relativistic treatment is performed. On the contrary, the valence orbitals are only treated within the "*scalar relativistic approximation*", which actually consists in neglecting the spin-orbit interaction. The spin-orbit corrections can however be reintroduced later, via a second variational approach.

The *scalar relativistic approximation*

To introduce the *scalar relativistic approximation*, we have to consider the Hamiltonian obtained in (3.7) and assume that the potential $V(\mathbf{r})$ is spherically symmetric. We remind that Ψ is not an eigenfunction of spin s or orbital moment l within this description. Actually, the good quantum numbers are the total angular momentum j, its projection j_z and κ[4].

Despite, the four-component function Ψ can be written as:

$$\Psi = \begin{pmatrix} \Phi \\ \chi \end{pmatrix} = \begin{pmatrix} g(r)\mathcal{Y}^{j,l}_{j_z} \\ if(r)\mathcal{Y}^{j,l}_{j_z} \end{pmatrix} \tag{3.36}$$

where g and f are the radial function and $\mathcal{Y}^{j,l}_{j_z}$ is the r-independent eigenfunction of j^2, j_z, l^2 and $s^2 = \frac{3}{4}$ formed by the combination of the Pauli spinors $\varphi_\uparrow, \varphi_\downarrow$[5] with the spherical harmonics Y^l_m. One

[3] This implies of course to include the spin degree of freedom in the band index ν for all the quantities related to the Kohn-Sham basis and to consider that L stands now for the indices $\{j, j_z, \kappa\}$.

[4] This last quantum number is akin to the $\pm$ sign in $j = l \pm 1/2$ in the non-relativistic limit. It can be shown that $\kappa = \pm(j + \frac{1}{2})$. More precisely, $\hbar\kappa$ is the eigenvalue of the operator K such that:

$$K = \begin{pmatrix} \mathbf{l}\cdot\sigma + \hbar & 0 \\ 0 & -\mathbf{l}\cdot\sigma - \hbar \end{pmatrix}.$$

[5] We remind that $\varphi_\uparrow = \begin{pmatrix} 1 \\ 0 \end{pmatrix}$ and $\varphi_\downarrow = \begin{pmatrix} 0 \\ 1 \end{pmatrix}$.

can then derive the following coupled system of equations for f and g:

$$\left\{ \begin{array}{rcl} \hbar c \left[\dfrac{df}{dr} + \dfrac{1-\kappa}{r}\, f \right] & = & -[\varepsilon - V(r)]\, g \\ \hbar c \left[\dfrac{dg}{dr} + \dfrac{1+\kappa}{r}\, g \right] & = & \quad [\varepsilon - V(r) + 2m_0c^2]\, f. \end{array} \right. \tag{3.37}$$

By eliminating f, one gets:

$$-\frac{\hbar^2}{2Mr^2}\frac{d}{dr}\left(r^2\frac{dg}{dr}\right) + \left[V(r) + \frac{\hbar^2}{2M}\frac{l(l+1)}{r^2}\right] g - \frac{\hbar^2}{4M^2c^2}\frac{dV}{dr}\frac{dg}{dr} - \frac{\hbar^2}{4M^2c^2}\frac{dV}{dr}\frac{1+\kappa}{r}\, g = \varepsilon\, g \tag{3.38}$$

where we have used the "*relativistically enhanced mass*" $M = m_0 + (\varepsilon - V(r))/2c^2$ and the relation $\kappa(\kappa+1) = l(l+1)$. The function f is on the contrary given by

$$f = \frac{\hbar}{2Mc}\left(\frac{dg}{dr} + \frac{1+\kappa}{r} g\right). \tag{3.39}$$

The *scalar relativistic approximation* is obtained by omitting, in the previous equations (3.38) and (3.39), the terms which depend on κ. Clear advantage of this approximation is that l and s are now good quantum numbers.

Let $\widetilde{\Psi}$, $\widetilde{\Phi}$, $\widetilde{\chi}$, $\tilde{f}$ and $\tilde{g}$ be the *scalar relativistic approximation* of Ψ, Φ, χ, f and g. On the one hand, we have:

$$\widetilde{\Psi} = \begin{pmatrix} \widetilde{\Phi} \\ \widetilde{\chi} \end{pmatrix} \qquad \text{with} \qquad \widetilde{\Phi} = \tilde{g}\, Y_m^l\, \chi_s \qquad \forall\, s \in \{\uparrow, \downarrow\}. \tag{3.40}$$

since $\widetilde{\Phi}$ is a pure spin-state. On the contrary, $\widetilde{\chi}$ contains a mixture of up and down spin functions because it is obtained from equation (3.3):

$$\widetilde{\chi} = i\frac{\boldsymbol{\sigma}\cdot\mathbf{r}}{r}\left[-\tilde{f} + \frac{\tilde{g}}{2Mcr}\boldsymbol{\sigma}\cdot\mathbf{l}\right]\, Y_m^l\, \chi_s. \tag{3.41}$$

On the other hand, the radial functions satisfy the following equations:

$$\tilde{f} = \frac{\hbar}{2Mc}\,\frac{d\tilde{g}}{dr} \qquad \text{and} \qquad \tilde{g} = -\frac{\hbar c}{\varepsilon - V(r)}\,\frac{d\tilde{f}}{dr} \tag{3.42}$$

which lead to the following equation for $\tilde{g}$:

$$-\frac{\hbar^2}{2Mr^2}\frac{d}{dr}(r^2\frac{d\tilde{g}}{dr}) + [V(r) + \frac{\hbar^2}{2Mr^2}\frac{l(l+1)}{r^2}]\, \tilde{g} - \frac{\hbar^2}{4M^2c^2}\frac{dV}{dr}\frac{d\tilde{g}}{dr} = \varepsilon\, \tilde{g}. \tag{3.43}$$

From these definitions, the spin-orbit Hamiltonian H_{SO} is obtained by the following relation:

$$\widetilde{H_{Dirac}Psi} = \varepsilon\widetilde{\Psi} + H_{SO}\widetilde{\Psi}. \tag{3.44}$$

It can then be shown that in the scalar relativistic basis of function $\tilde{f}$ and $\tilde{g}$:

$$H_{SO} = \frac{\hbar}{2Mc^2}\frac{1}{r}\frac{dV}{dr}\begin{pmatrix} \sigma\cdot\mathbf{l} & 0 \\ 0 & 0 \end{pmatrix} \tag{3.45}$$

H_{SO} acts only on the large component of the wavefunction and can then be included perturbatively.

Second variational treatment of the spin-orbit interaction in Wien2k

In all the previously derived equations, the quantity $V(\mathbf{r})$ stands only for an *external* potential. However, equations (3.42) and (3.43) are solved in Wien2k to construct the (L)APW+lo basis set by using the effective Kohn-Sham potential $V_{KS}(\mathbf{r})$ which is defined in (1.18). The many-body effects induced by the Coulomb repulsion is thus included in this approach via the Hartree potential $V_H(\mathbf{r})$ and the exchange-correlation potential $V^{xc}(\mathbf{r})$. However, this does not imply that the initial many-body problem is rigorously treated within a *scalar relativistic approximation*. As explained in Appendix F, many-body spin-orbit interaction terms, called "*spin-same-orbit*" and "*spin-other-orbit*" interactions should also be taken into account when the *scalar relativistic approximation* is derived from the Dirac-Coulomb-Breit Hamiltonian [26]. Nevertheless, we will not discuss here the effects of these additional terms – the interested reader is invited to read Appendix F – and we will only focus our attention on the "standard" treatment of the spin-orbit interaction in Wien2k.

The scalar relativistic bands are first calculated by setting up and diagonalizing the secular equation derived from (3.42) and (3.43). As a result, one obtains the eigenvalues $\varepsilon^{\sigma}_{\mathbf{k}n}$ and their corresponding eigenfunctions $\varphi^{\sigma}_{\mathbf{k}n}(\mathbf{r})$:

$$H\varphi^{\sigma}_{\mathbf{k}n}(\mathbf{r}) = \varepsilon^{\sigma}_{n}(\mathbf{k})\ \varphi^{\sigma}_{\mathbf{k}n}(\mathbf{r}) \tag{3.46}$$

where $\mathbf{k}$ is the momentum, n the band index and σ the spin degree of freedom.[6] The spin-orbit coupling is then taken into account by using the method described hereafter: a *second variational* secular equation is set up with the scalar relativistic orbitals (for both spins) – $\varphi^{\uparrow}_{\mathbf{k}n}(\mathbf{r})$ and $\varphi^{\downarrow}_{\mathbf{k}n}(\mathbf{r})$ – as basis functions. This leads to a new secular equation where the Hamiltonian H_{SO} and the overlap matrices are given by:

$$\langle\varphi^{\sigma}_{\mathbf{k}n}|\varphi^{\tau}_{\mathbf{k}m}\rangle = \delta_{nm}\ \delta_{\sigma\tau} \tag{3.47}$$

$$\langle\varphi^{\sigma}_{\mathbf{k}n}|H_0|\varphi^{\tau}_{\mathbf{k}m}\rangle = \varepsilon^{\sigma}_{n}(\mathbf{k})\ \delta_{nm}\ \delta_{\sigma\tau} \tag{3.48}$$

$$\langle\varphi^{\sigma}_{\mathbf{k}n}|H_{SO}|\varphi^{\tau}_{\mathbf{k}m}\rangle = H^{SO}_{n\sigma,m\tau}(\mathbf{k}). \tag{3.49}$$

One thus obtains the following equation:

$$\forall n,\sigma \qquad \sum_{m,\tau}\left[\varepsilon^{\sigma}_{n}(\mathbf{k})\ \delta_{nm}\delta_{\sigma\tau} + H^{SO}_{n\sigma,m\tau}(\mathbf{k})\right] z^{\nu}_{m\tau} = \varepsilon_{\mathbf{k}\nu} z^{\nu}_{n\sigma} \tag{3.50}$$

where ν runs over both spin and orbital indices, $\nu = \nu(\{n,\sigma\})$ with ν bijective. By solving this matrix equation, one finally gets the eigenvalues $\tilde{\varepsilon}_{\nu\mathbf{k}}$ and the corresponding eigenvectors:

$$\psi_{\mathbf{k}\nu}(\mathbf{r}) = \sum_{n,\sigma} z^{\nu}_{n\sigma}\varphi^{\sigma}_{\mathbf{k}n}(\mathbf{r}). \tag{3.51}$$

Although the spin-orbit term couples the spin-up and spin-down wavefunctions, the wavefunctions $\psi_{\mathbf{k}\nu}(\mathbf{r})$ are still of the Bloch form:

$$\begin{aligned}\psi_{\mathbf{k}\nu}(\mathbf{r}) &= \sum_{n} z^{\nu}_{n\uparrow}\varphi^{\uparrow}_{\mathbf{k}n}(\mathbf{r}) + \sum_{n} z^{\nu}_{n\downarrow}\varphi^{\downarrow}_{\mathbf{k}n}(\mathbf{r}) = \psi^{+}_{\mathbf{k}\nu}(\mathbf{r}) + \psi^{-}_{\mathbf{k}\nu}(\mathbf{r}) \\ &= \left[u^{+}_{\mathbf{k}\nu}(\mathbf{r}) + u^{-}_{\mathbf{k}\nu}(\mathbf{r})\right] e^{i\mathbf{k}\cdot\mathbf{r}}.\end{aligned} \tag{3.52}$$

As a result, the charge density can also be decomposed as follows:

$$\rho(\mathbf{k}) = \sum_{\nu\ occ.}\langle\psi_{\mathbf{k}\nu}|\psi_{\mathbf{k}\nu}\rangle = \sum_{\nu\ occ.}\left[\langle\psi^{+}_{\mathbf{k}\nu}|\psi^{+}_{\mathbf{k}\nu}\rangle + \langle\psi^{-}_{\mathbf{k}\nu}|\psi^{-}_{\mathbf{k}\nu}\rangle\right] = \rho^{+}(\mathbf{k}) + \rho^{-}(\mathbf{k}) \tag{3.53}$$

and a calculation with spin-orbit coupling can thus be performed almost "*transparently*" as a usual calculation with spin densities, by just adding a routine which includes this second variational treatment. The cycle in Wien2k, in which the spin-orbit interaction may be included self-consistently, is described in Appendix C.

[6] As we have already said, the spin is a good quantum number within the *scalar relativistic approximation*.

3.3.2 Consequences on the definition of the Wannier projectors and on DMFT equations

According to equation (3.52), it is convenient to choose the basis $|\psi^+_{\nu\mathbf{k}}\rangle$, $|\psi^-_{\nu\mathbf{k}}\rangle$ to describe the lattice quantities in the LDA+DMFT implementation, since this is the natural output of the Wien2k code. A new set of index $i = \{+, -\}$ must thus be introduced to extend the formalism presented in section 2.3. The Wannier projectors can then be written as follows:

$$\left[P^{\alpha,\sigma}_{lm,\nu}\right]^+(\mathbf{k}) = \langle\chi^{\alpha,\sigma}_{lm}|\psi^+_{\mathbf{k}\nu}\rangle \qquad \text{and} \qquad \left[P^{\alpha,\sigma}_{lm,\nu}\right]^-(\mathbf{k}) = \langle\chi^{\alpha,\sigma}_{lm}|\psi^-_{\mathbf{k}\nu}\rangle \tag{3.54}$$

where we remind that ν runs over both spin and orbital indices. In addition, the Green's function and the self-energy of the solid are now related by:

$$\left\{[G(\mathbf{k}, i\omega_n)]^{-1}\right\}^{ij}_{\nu\nu'} = (i\omega_n + \mu - \varepsilon_{k\nu})\delta_{\nu\nu'}\delta_{ij} - \Sigma^{ij}_{\nu\nu'}(\mathbf{k}, i\omega_n) \qquad \text{with} \qquad i, j = \{+, -\}. \tag{3.55}$$

In the following, we will consider the Wannier projectors as "*spinors*" in the "initial" Bloch basis $|\psi_{\nu\mathbf{k}}\rangle$:

$$\mathbf{P}^{\alpha,\sigma}_{lm,\nu}(\mathbf{k}) = \begin{pmatrix} \left[P^{\alpha,\sigma}_{lm,\nu}\right]^+(\mathbf{k}) \\ \hline \left[P^{\alpha,\sigma}_{lm,\nu}\right]^-(\mathbf{k}) \end{pmatrix} \tag{3.56}$$

whereas the Green's function and the self-energy elements will be written as spin-matrices:

$$\begin{aligned} \mathbf{G}_{\nu\nu'}(\mathbf{k}, i\omega_n) &= \left(\begin{array}{c|c} G^{++}_{\nu\nu'}(\mathbf{k}, i\omega_n) & G^{+-}_{\nu\nu'}(\mathbf{k}, i\omega_n) \\ \hline G^{-+}_{\nu\nu'}(\mathbf{k}, i\omega_n) & G^{--}_{\nu\nu'}(\mathbf{k}, i\omega_n) \end{array}\right) \\ \text{and} \\ \mathbf{\Sigma}_{\nu\nu'}(\mathbf{k}, i\omega_n) &= \left(\begin{array}{c|c} \Sigma^{++}_{\nu\nu'}(\mathbf{k}, i\omega_n) & \Sigma^{+-}_{\nu\nu'}(\mathbf{k}, i\omega_n) \\ \hline \Sigma^{-+}_{\nu\nu'}(\mathbf{k}, i\omega_n) & \Sigma^{--}_{\nu\nu'}(\mathbf{k}, i\omega_n) \end{array}\right). \end{aligned} \tag{3.57}$$

With this convention of notations, the equation (2.4) which defines the intial dynamical mean-field becomes:

$$[\mathcal{G}_0(i\omega_n)]^{\sigma\sigma'}_{mm'} = \sum_{\mathbf{k},\nu\nu'} \left[\mathbf{P}^{\alpha,\sigma}_{lm,\nu}(\mathbf{k})\right]^T \; [\mathbf{G}_{KS}(\mathbf{k}, i\omega_n)]_{\nu\nu'} \; \left[\mathbf{P}^{\alpha,\sigma'}_{lm',\nu'}(\mathbf{k})\right]^*. \tag{3.58}$$

Similarly, the formula (2.8) which gives the expression of the local Green's function merely can be written as:

$$[\mathbf{G}^{\alpha}_{loc}(i\omega_n)]^{\sigma\sigma'}_{mm'} = \sum_{k,\nu\nu'} \left[\mathbf{P}^{\alpha,\sigma}_{lm,\nu}(\mathbf{k})\right]^T \mathbf{G}_{\nu\nu'}(k, i\omega_n) \left[\mathbf{P}^{\alpha,\sigma'}_{lm',\nu'}(\mathbf{k})\right]^* \tag{3.59}$$

and the expression (2.6) for the lattice self-energy correction is:

$$\mathbf{\Sigma}_{\nu\nu'}(\mathbf{k}, i\omega_n) = \sum_{\alpha,mm'} \left[\mathbf{P}^{\alpha,\sigma}_{lm,\nu}(\mathbf{k})\right]^* \left[\mathbf{\Delta}\Sigma^{\alpha}_{imp}(i\omega_n)\right]^{\sigma\sigma'}_{mm'} \left[\mathbf{P}^{\alpha,\sigma'}_{lm',\nu'}(\mathbf{k})\right]^T. \tag{3.60}$$

Consequently, the equations of the DMFT loop are formally the same as in the case without spin-orbit coupling (cf. expressions (2.45), (2.46) and (2.47)). However, the computations now involve matrices which are double in size.

The construction of the Wannier projectors is still done in two steps. The *temporary* Wannier projectors are first calculated – separately for the $|\psi^+_{\nu\mathbf{k}}\rangle$ and the $|\psi^-_{\nu\mathbf{k}}\rangle$ basis functions – with the following expression:

$$\left[\widetilde{P}^{\alpha,\sigma}_{lm,\nu}\right]^i(\mathbf{k}) = [A^{\nu\alpha}_{lm}(\mathbf{k}, \sigma)]^i + \sum_{n_{LO}=1}^{LOMAX} c^{\nu,\sigma}_{LO} \left[C^{\alpha,LO}_{lm}\mathcal{O}^{\alpha,\sigma}_{lm,l'm'}\right]^i \qquad \text{with} \qquad i = \{+, -\} \tag{3.61}$$

the coefficients $[A^{\nu\alpha}_{lm}(\mathbf{k},\sigma)]^i$ and $\left[C^{\alpha,LO}_{lm}\mathcal{O}^{\alpha,\sigma}_{lm,l'm'}\right]^i$ being direct outputs of the Wien2k program. They indeed are the analog of the coefficients $A^{\nu\alpha}_{lm}(\mathbf{k},\sigma)$ and $C^{\alpha,LO}_{lm}\mathcal{O}^{\alpha,\sigma}_{lm,l'm'}$ given in (2.35) for the $|\psi^{\sigma}_{\mathbf{k}\nu}\rangle$.

The orthogonalization is then performed in order to get the "true" Wannier projectors but this step cannot be done independently for the two parts of the Wannier projector, since the overlap matrix $O^{\alpha,\alpha'}_{m,m'}(\mathbf{k},\sigma)$ is defined by:

$$\langle\tilde{\chi}^{\alpha,\sigma}_{lm}|\tilde{\chi}^{\alpha',\sigma'}_{lm'}\rangle = \sum_{\mathbf{k}\in 1\mathrm{BZ}}\left[O^{\alpha,\alpha'}(\mathbf{k})\right]^{\sigma,\sigma'}_{m,m'} \tag{3.62}$$

$$\text{with}\quad \left[O^{\alpha,\alpha'}(\mathbf{k})\right]^{\sigma,\sigma'}_{m,m'} = \sum_{\nu=\nu_{min}(\mathbf{k})}^{\nu_{max}(\mathbf{k})}\langle\tilde{\chi}^{\alpha,\sigma}_{lm}|\psi_{\mathbf{k}\nu}\rangle\langle\psi_{\mathbf{k}\nu}|\tilde{\chi}^{\alpha',\sigma'}_{lm'}\rangle$$

$$= \sum_{\nu=\nu_{min}(\mathbf{k})}^{\nu_{max}(\mathbf{k})}\sum_{i,j=+,-}\left[\widetilde{P}^{\alpha,\sigma}_{lm,\nu}\right]^i(\mathbf{k})\left[\widetilde{P}^{\alpha',\sigma'}_{lm',\nu}\right]^{j*}(\mathbf{k}). \tag{3.63}$$

By requiring it in the input file, it is still possible to get the projectors of the correlated orbitals in cubic symmetry or in any desired basis. This option was also extended in order to define the Wannier projectors related to states which mix spin up and spin down complex spherical harmonics, such as the $j_{\text{eff}} = 1/2$ and $j_{\text{eff}} = 3/2$ states introduced at the end of section 3.1.

More details about the structure of the new implementation can be found in Appendix D and [110]. In addition, the interested reader can find in Appendix E how the Brillouin zone integration of equation (3.58) and (3.59) are performed[7].

3.4 Summary: Our "LDA+SO+DMFT" implementation within the LAPW framework

Our *LDA+SO+DMFT implementation* within the LAPW framework is summarized in figure 3.2. It extends the previous LDA+DMFT implementation of Aichhorn *et al.* [1] so that it may take into account the spin-orbit coupling in the construction of the Wannier orbitals which define the local impurity problem. We present here only the "*one-shot*" approach of the cycle, some developments are currently in progress to implement the complete *LDA+SO+DMFT* cycle.

i) The DFT calculation with *Wien2k*

The electronic structure calculations are performed using the Wien2k package, an *all-electron full-potential LAPW method* (cf. section 2.2). The spin-orbit interaction is introduced in the Kohn-Sham equations as explained in part 3.3.1.

ii) Calculating the *Wannier projectors* with *dmftproj*

The correlated orbitals are built from the (L)APW+lo basis in the interfacing program called dmftproj. This program calculates the *Wannier projectors* $\mathbf{P}^{\alpha,\sigma}_{lm,\nu}(\mathbf{k})$ by following the procedure introduced by Anisimov *et al.* [10], which is extended to take into account the spin-orbit interaction (cf. part 3.3.2).

[7] It is indeed possible to get an expression similar to (2.57) but one must then apply the symmetry operations of the *Shubnikov magnetic space group* of the compound on the unsymmetrized Green's function calculated in the irreducible Brillouin zone.

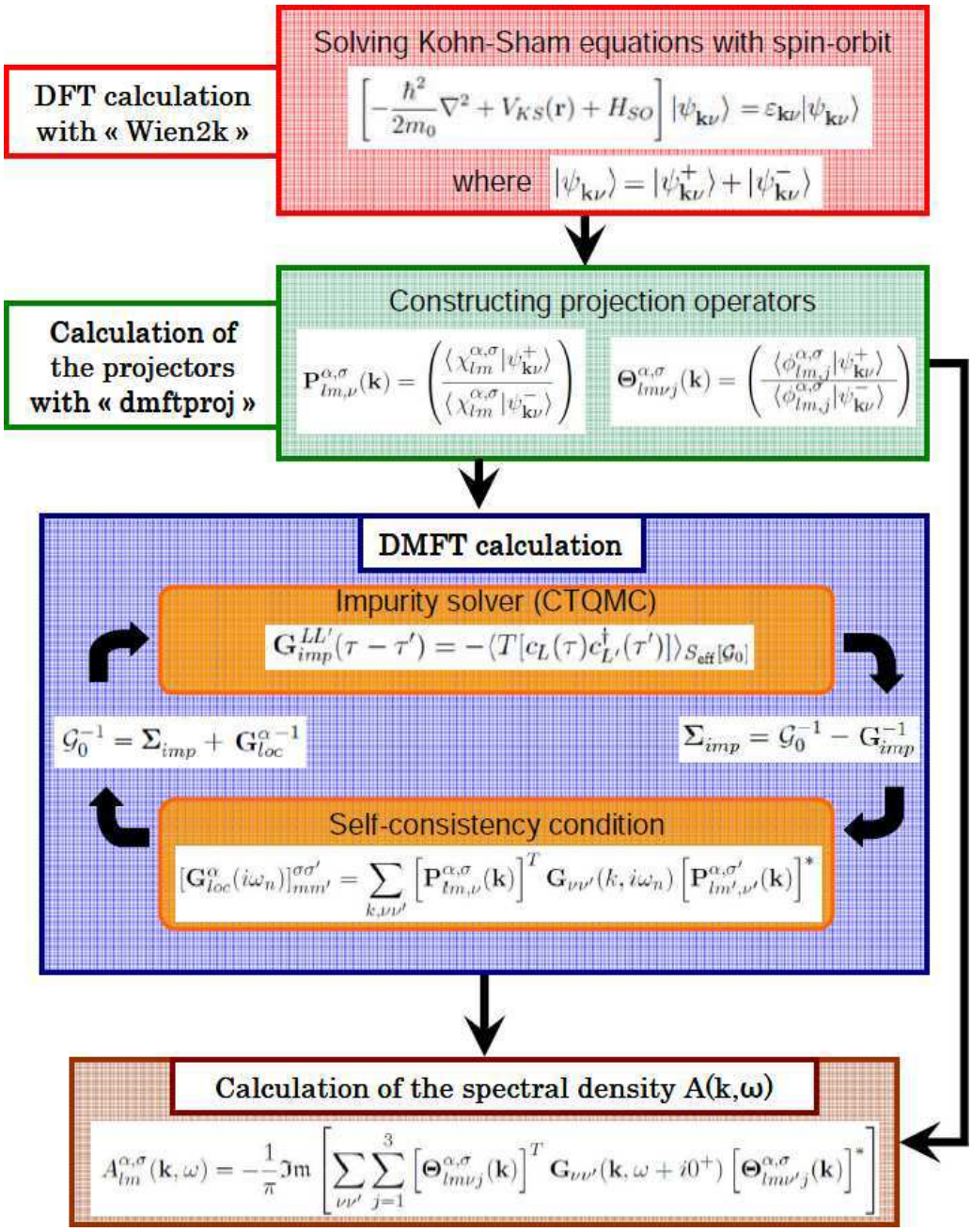

Figure 3.2: Our "one-shot" implementation of *LDA+SO+DMFT* withinn the LAPW framework:

The DFT-LDA+SO calculation is performed within Wien2k *[23]. The spin-orbit interaction is included in the Kohn-Sham equations with a second variational treatment. One then gets the eigenvalues* $\varepsilon_{\mathbf{k}\nu}$ *and the Bloch states* $|\psi^+_{\mathbf{k}\nu}\rangle$ *and* $|\psi^-_{\mathbf{k}\nu}\rangle$ ***(i)****.*
The correlated orbitals are then defined and the corresponding Wannier projectors $\mathbf{P}^{\alpha,\sigma}_{lm,\nu}(\mathbf{k})$ *are constructed in the interfacing program* dmftproj ***(ii)*** *in order to perform the DMFT loop. The latter* ***(iii)*** *consists in:*
- solving the effective impurity problem for the impurity Green's function $\mathbf{G}_{imp}$ *with a CTQMC solver [165], hence obtaining an impurity self-energy* $\mathbf{\Sigma}_{imp}$*;*
- combining the self-energy correction with the Green's function of the solid $\mathbf{G}(i\omega_n)$ *in order to calculate the local Green's function* $\mathbf{G}^{\alpha}_{loc}(i\omega_n)$ *– cf. equations* (3.55), (3.59) *and* (3.60) *–;*
- finally obtaining an updated dynamical mean-field $\mathcal{G}_0$ *for the impurity problem.*
Once the DMFT loop has converged, the chemical potential is updated and the spectral density $A(\mathbf{k},\omega)$ *can be calculated* ***(iv)*** *by using the projectors* $\mathbf{\Theta}^{\alpha}_{lm\nu j}(\mathbf{k})$*, which were also built while running* dmftproj*.*

iii) The DMFT self-consistent loop

The DMFT self-consistent loop relies on the same formalism as previously introduced in section 2.1. However, taking into account the spin-orbit coupling modifies slightly the equations (cf. expressions (3.55), (3.59) and (3.60)).

To solve the impurity problem, we use the strong-coupling version of the continuous-time quantum Monte Carlo (CTQMC) method [165]. This method is based on a hybridization expansion and has proved to be a very efficient solver for quantum impurity models in the weak and strong correlation regime. Moreover, this solver allows us to address room temperature (300 K) without any problems.

Sources of errors

The approximations performed by using the LDA+DMFT theory were previously presented in section 2.1. However, various other sources of errors were introduced with our choice of impurity solver. These numerical errors, which are rather hard to control, are the following:

Monte Carlo statistical errors: These are the statistical errors of the impurity solver itself. They are very well under control and can be checked by error estimations and extension of the runtime of the code. These errors are qualitatively very different from the errors of other impurity solvers commonly used. Whereas the iterated perturbation theory (IPT) – or Hubbard-I – solvers use additional approximations for the solution of the impurity problem, the only source of errors in our case is statistical Monte Carlo errors.

Numerical discretization errors: These stem from the fact that even within the continuous-time solvers, the dynamical mean field $\mathcal{G}_0(\tau)$ has to be discretized. The magnitude of these errors is however negligible, and Fourier transform errors are well under control with the techniques used [61].

Analytical continuation: As explained in part 1.4.3, CTQMC simulations are restricted to the imaginary time domain. In order to obtain quantities which are directly accessible to the experiment, like the spectral function $A(\mathbf{k},\omega)$, the imaginary time quantities have to be analytically continued to the real axis. This process involves the inversion of an ill-conditioned matrix. Maximum entropy methods determine the most probable spectral density by using the concept of Bayesian interference [78]. This induces errors which are hard to control and require careful analysis of covariance information.

iv) Post-processing: Calculating the spectral function $A(\mathbf{k},\omega)$

As just mentioned above, an analytic continuation is needed in order to obtain results such as the spectral function $A(\mathbf{k},\omega)$. In our implementatioin, we choose to perform the analytic continuation of the impurity self-energy using a stochastic version of the maximum entropy method [19]. Moreover, a new set of projectors has to be built.

Introduction of the Θ-*projectors*

In order to calculate quantities for a given atom α and a particular orbital (spin) character lm (σ) – such as the spectral functions $A^{\sigma\alpha}_{lm}(\mathbf{k},\omega)$ – , a set of projectors called "Θ-*projectors*" was built. Contrary to the previously introduced Wannier projectors $P^{\alpha,\sigma}_{lm,\nu}(\mathbf{k})$, their definition is not restricted to the correlated orbitals only. The formalism of these Θ-projectors was initially introduced by Aichhorn *et al.*. [1] We have also extended it so that they may take into account spin-orbit corrections.

As we have explained in section 2.2, inside the muffin-tin sphere S^{α}_{MT} associated to the atom α we can write $\psi^{\sigma}_{\mathbf{k}\nu}(\mathbf{r})$ as:

$$\begin{aligned}\psi^{\sigma}_{\mathbf{k}\nu}(\mathbf{r}) &= \sum_{l=0}^{l_{max}}\sum_{m=-l}^{+l}\Big[A^{\nu\alpha}_{lm}(\mathbf{k},\sigma)u^{\alpha,\sigma}_{l}(r^{\alpha},E^{\alpha}_{1l}) + B^{\nu\alpha}_{lm}(\mathbf{k},\sigma)\dot{u}^{\alpha,\sigma}_{l}(r^{\alpha},E^{\alpha}_{1l}) + C^{\nu\alpha}_{lm}(\mathbf{k},\sigma)u^{\alpha,\sigma}_{l}(r^{\alpha},E^{\alpha}_{2l})\Big]Y^{l}_{m}(\hat{\mathbf{r}^{\alpha}}) \\ &= \sum_{l=0}^{l_{max}}\sum_{m=-l}^{+l}\Big[A^{\nu\alpha}_{lm}(\mathbf{k},\sigma)\ u^{\alpha,\sigma}_{lm,1}(\mathbf{r}^{\alpha}) + B^{\nu\alpha}_{lm}(\mathbf{k},\sigma)\ u^{\alpha,\sigma}_{lm,2}(\mathbf{r}^{\alpha}) + C^{\nu\alpha}_{lm}(\mathbf{k},\sigma)\ u^{\alpha,\sigma}_{lm,3}(\mathbf{r}^{\alpha})\Big] \qquad (3.64)\end{aligned}$$

with the notation:

$$\begin{gathered}u^{\alpha,\sigma}_{lm,1}(\mathbf{r}^{\alpha}) = u^{\alpha,\sigma}_{l}(r^{\alpha},E^{\alpha}_{1l})Y^{l}_{m}(\hat{\mathbf{r}^{\alpha}}) \quad , \quad u^{\alpha,\sigma}_{lm,2}(\mathbf{r}^{\alpha}) = \dot{u}^{\alpha,\sigma}_{l}(r^{\alpha},E^{\alpha}_{1l})Y^{l}_{m}(\hat{\mathbf{r}^{\alpha}}) \\ \text{and} \quad u^{\alpha,\sigma}_{lm,3}(\mathbf{r}^{\alpha}) = u^{\alpha,\sigma}_{l}(r^{\alpha},E^{\alpha}_{2l})Y^{l}_{m}(\hat{\mathbf{r}^{\alpha}}).\end{gathered} \qquad (3.65)$$

The orbital character α,l,m,σ thus contributes in the eigenstates $\psi^{\sigma}_{\mathbf{k}\nu}(\mathbf{r})$ through three terms.

However, the basis $\{u^{\alpha,\sigma}_{lm,i}\}_{i=\{1,2,3\}}$ is not orthonormalized as already mentioned in 2.3. To make the calculations easier, we introduce an orthonormal basis set $\{\phi^{\alpha,\sigma}_{lm,j}\}_{j=1,2,3}$ for each atomic orbital (l,m). These orbitals are defined from the initial basis $\{u^{\alpha,\sigma}_{lmi}\}_{i=\{1,2,3\}}$ as follows:[8]

$$\forall i \quad u^{\alpha,\sigma}_{lm,i}(\mathbf{r}^{\alpha}) = \sum_{j=1}^{3} c_{ij}\phi^{\alpha,\sigma}_{lm,j} \quad \text{with} \quad \mathbf{C} = \begin{pmatrix} 1 & 0 & \langle u^{\alpha,\sigma}_{lm,1}|u^{\alpha,\sigma}_{lm,2}\rangle \\ 0 & \langle u^{\alpha,\sigma}_{lm,2}|u^{\alpha,\sigma}_{lm,2}\rangle & \langle u^{\alpha,\sigma}_{lm,2}|u^{\alpha,\sigma}_{lm,3}\rangle \\ \langle u^{\alpha,\sigma}_{lm,3}|u^{\alpha,\sigma}_{lm,1}\rangle & \langle u^{\alpha,\sigma}_{lm,3}|u^{\alpha,\sigma}_{lm,2}\rangle & 1 \end{pmatrix}^{\frac{1}{2}}. \qquad (3.66)$$

We can then rewrite (3.64) as:

$$\psi^{\sigma}_{\mathbf{k}\nu}(\mathbf{r}) = \sum_{l=0}^{l_{max}}\sum_{m=-l}^{+l}\sum_{j=1}^{3}\Theta^{\alpha,\sigma}_{lm\nu j}(\mathbf{k})\phi^{\alpha,\sigma}_{lm,j}(\mathbf{r}^{\alpha}). \qquad (3.67)$$

The matrix elements $\Theta^{\alpha,\sigma}_{lm\nu j}(\mathbf{k})$ are the "Θ-*projectors*", which are thus defined by:

$$\Theta^{\alpha,\sigma}_{lm\nu j}(\mathbf{k}) = \langle\phi^{\alpha,\sigma}_{lm,j}|\psi^{\sigma}_{\mathbf{k}\nu}\rangle = A^{\nu\alpha}_{lm}(\mathbf{k},\sigma)c_{1j} + B^{\nu\alpha}_{lm}(\mathbf{k},\sigma)c_{2j} + C^{\nu\alpha}_{lm}(\mathbf{k},\sigma)c_{3j}. \qquad (3.68)$$

When the spin-orbit interaction is introduced, the definition of the projectors $\Theta^{\alpha,\sigma}_{lm,\nu j}(\mathbf{k})$ must be extended to "spinor" projectors $\mathbf{\Theta}^{\alpha,\sigma}_{lm\nu j}(\mathbf{k})$, in a similar fashion as previously described for the Wannier projectors

$$\mathbf{\Theta}^{\alpha,\sigma}_{lm\nu j}(\mathbf{k}) = \begin{pmatrix} \langle\phi^{\alpha,\sigma}_{lm,j}|\psi^{+}_{\mathbf{k}\nu}\rangle \\ \hline \langle\phi^{\alpha,\sigma}_{lm,j}|\psi^{-}_{\mathbf{k}\nu}\rangle \end{pmatrix}. \qquad (3.69)$$

For the sake of simplicity, the Θ-projectors were introduced here in the complex spherical harmonics basis. As for the Wannier projectors, it is of course possible to get the Θ-projectors in any desired basis – even one which mixes spin up and spin down complex spherical harmonics, for a calculation including the spin-orbit coupling.

[8] We remind that the functions $u^{\alpha,\sigma}_{l}(r^{\alpha},E)Y^{l}_{m}(\hat{\mathbf{r}^{\alpha}})$ are normalized to 1 for each value of E by definition. As a result, $\langle u^{\alpha,\sigma}_{lm,1}|u^{\alpha,\sigma}_{lm,1}\rangle = \langle u^{\alpha,\sigma}_{lm,3}|u^{\alpha,\sigma}_{lm,3}\rangle = 1$ and $\langle u^{\alpha,\sigma}_{lm,1}|u^{\alpha,\sigma}_{lm,2}\rangle$=0.

Calculation of $A(\mathbf{k},\omega)$

By definition, the spectral function $A(\mathbf{k},\omega)$ is given by:

$$A(\mathbf{k},\omega) = -\frac{1}{\pi}\Im\mathfrak{m}\left[G(\mathbf{k},\omega)\right]. \tag{3.70}$$

As a result, the spectral function of a given atom α with orbital character (l,m) and spin σ, is finally obtained through the following formulas:

- in a calculation without spin-orbit interaction

$$A^{\alpha,\sigma}_{lm}(\mathbf{k},\omega) = -\frac{1}{\pi}\Im\mathfrak{m}\left[\sum_{\nu\nu'}\sum_{j=1}^{3}\Theta^{\alpha,\sigma}_{lm\nu j}(\mathbf{k})\; G^{\sigma}_{\nu\nu'}(\mathbf{k},\omega+i0^{+})\left[\Theta^{\alpha,\sigma}_{lm\nu' j}(\mathbf{k})\right]^{*}\right] \tag{3.71}$$

- in a calculation which includes the spin-orbit corrections

$$A^{\alpha,\sigma}_{lm}(\mathbf{k},\omega) = -\frac{1}{\pi}\Im\mathfrak{m}\left[\sum_{\nu\nu'}\sum_{j=1}^{3}\left[\mathbf{\Theta}^{\alpha,\sigma}_{lm\nu j}(\mathbf{k})\right]^{T}\mathbf{G}_{\nu\nu'}(\mathbf{k},\omega+i0^{+})\left[\mathbf{\Theta}^{\alpha,\sigma}_{lm\nu' j}(\mathbf{k})\right]^{*}\right]. \tag{3.72}$$

We have now developed a new set of tools which can be used within the LDA+DMFT scheme to study compounds with significant spin-orbit terms. The first application performed was on the paramagnetic insulating phase of strontium iridate (Sr_2IrO_4).

Part II

The paramagnetic insulating phase of Strontium Iridate Sr_2IrO_4

Chapter 4

Short review on strontium iridate Sr_2IrO_4

Although strontium iridate (Sr_2IrO_4) was first synthesized in 1956 by Randall *et al.* [136], it has taken almost 40 years for the scientific community to draw some attention to this compound. More precisely, this dates back to 1994 when superconductivity was discovered in strontium ruthenate (Sr_2RuO_4) [109]. Since both the ruthenate and iridate compounds have similar crystallographic structure, there was hope to shed light onto this unconventional state by studying also the iridate counterpart. Another reason for renewed interest was to better understand the magnetic properties of the isostructural cuprates, such as $La_{2-x}Ba_xCuO_4$, discovered in the late eighties [20].

Experimental studies based on different techniques have all come to two main conclusions:

- Sr_2IrO_4 is insulating at all temperatures, although it contains an odd number of electrons per formula unit.
- It exhibits a canted-antiferromagnetic order below 240 K with a ferromagnetic moment of 0.023 μ_B/Ir, which is very small in comparison to the expected value for such a compound (of about 1 μ_B/Ir).

This was to some extent puzzling, because the bandwidth of Sr_2IrO_4 is fairly large, and the Coulomb interaction for a $5d$ element is expected to be small, meaning that the Mott localization of electrons should be not very effective.

In 2008 Kim *et al.* [84] proposed a solution to this problem by emphasizing the role of the spin-orbit coupling in this compound : the insulating state of this material would indeed result from the cooperative interaction between the spin-orbit coupling and electronic correlations. This picture, called "*spin-orbit driven Mott insulator*", was quickly confirmed by resonant X-ray scattering [85] and has also given a framework to understand the canted-antiferromagnetic phase of Sr_2IrO_4 [79]. The purpose of this chapter is to review the existing experimental and theoretical works on Sr_2IrO_4, in order to put our calculations, which are presented in chapter 5, into context.

4.1 Crystal structure of Sr_2IrO_4

In 1956, $Sr_2IrO_4$was synthesized through a solid-state reaction "*between iridium metal powder and strontium oxide, carbonate, nitrate or hydroxide at 1200° C* " [136]. With this technique and its variations [34, 72], polycrystalline samples (or pellets) which are "*hard and black* " [135] are produced. Since 1998, another growth technique has also been developed with a flux method using strontium chloride $SrCl_2$ flux [31, 85]. With this new way of synthesis, one gets plate-like single crystals with typical dimension of $1 \times 1 \times (0.1 - 0.5)$ mm^3. The magnetic and transport properties of single crystals and polycrystalline samples are not entirely the same. In the following, we will explicitly specify the

nature of the samples used for the experiments, if a difference in their behavior was noticed.

The crystal structure of Sr_2IrO_4 was first described to be of K_2NiF_4-type, similar to Sr_2RuO_4 or the high-temperature superconductor $La_{2-x}Ba_xCuO_4$ [136]. This means that the compound is a layered perovskite with planes of Ir-O_2 and Sr-O. Moreover, it implies that iridium ions are surrounded by six oxygen atoms, forming then IrO_6 octahedra which are aligned along the crystal axes **a** and **b**.

However, electron diffraction measurements with Rietveld refinement [34] were carried out on the $Sr_2Ru_{1-x}Ir_xO_4$ system in 1994 and revealed weak super-lattice reflections, indicating that Sr_2IrO_4 has a lower symmetry. These results were corroborated by some further experiments (with powder X-ray diffraction or neutron diffraction) [41, 72, 88, 135, 156], which confirmed that crystallographic distortions take place in this material: the corner-shared IrO_6 octahedra are not well-aligned but are alternately rotated clockwise and anticlockwise around the **c**-axis of the crystal by about 11°. This tilting of the octahedra lowers the symmetry space group of Sr_2IrO_4 from $I4/mmm$ to $I4_1/acd$. Furthermore, DFT calculations performed by Cosio Castaneda *et al.* [39] have also confirmed that the $I4_1/acd$ symmetry is more stable than the $I4/mmm$ symmetry.

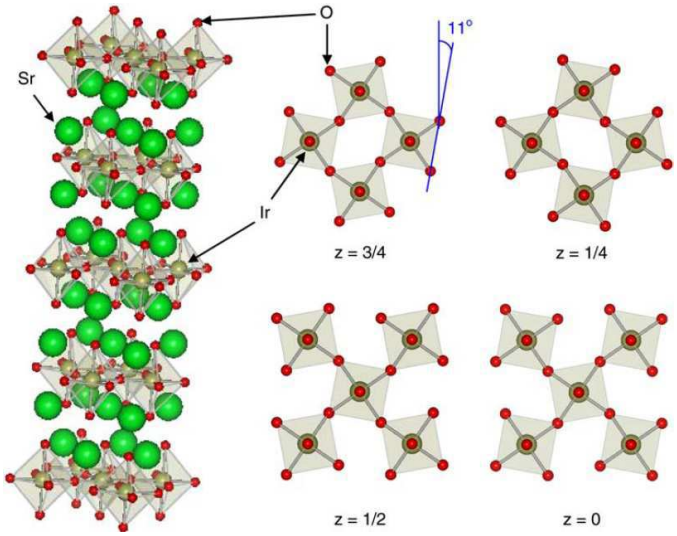

Figure 4.1: Conventional unit cell of Sr_2IrO_4. The green spheres stand for the strontium ions (Sr), the golden ones for iridium (Ir) and the red ones for oxygen (O). The corner-sharing IrO_6 octahedra are alternately rotated clockwise and anticlockwise around the **c**-axis by about 11°. From [88]

The conventional unit cell of Sr_2IrO_4 is depicted in figure 4.1. The structural parameters at 10 K and at room temperature can be found in [41, 72, 145]. The rotation of the IrO_6 octahedra decreases with temperature, from 11.72° at 10 K to 11.36° at room temperature according to Huang *et al.* [72]. The a and c axes have been reported many times with different values, ranging from 5.4921 to 5.4994 Å and from 25.766 to 25.798 Å respectively. This discrepancy in the lattice parameters has been explained by the oxygen non-stoichiometry in the different samples, since the control of this stoichiometry during the synthesis is difficult [88].

In figure 4.1, the IrO_6 octahedra are all rotated with respect to each other, consistently with the constraints imposed by the $I4_1/acd$ symmetry. However, each layer containing the IrO_6 octahedra is well separated from another by two Sr-O planes, which allow to consider Sr_2IrO_4 as a quasi-bidimensional compound. As a result, Huang *et al.* [72] proposed that the Ir-O_2 layers may be uncorrelated and the rotation of IrO_6 octahedra in a layer can be independent of the – clockwise or anticlockwise – configuration observed in its adjacent layers. Using neutron powder diffraction, they indeed confirmed that

disorder occurs quite significantly in the compound: about 83% of the oxygen ion position of a layer are generated from those of the adjacent layers by the operation of the 4_1 axis and about 17% of them are uncorrelated to the oxygen atoms of the adjacent layers by any symmetry operation of the space group. However, these results were obtained on polycrystalline sample, and no similar observations were reported in studies on single crystals.

4.2 Experimental evidence for an insulating state

As mentioned in the introduction it was surprising to find Sr_2IrO_4 to be an insulator, since this compound has an open $5d$ shell. Nevertheless, many different probes give evidence for its insulating behavior.

4.2.1 Transport measurements

As usual, the electric transport properties are highly sample-dependent, which is due to the different synthesis routes resulting in different sample qualities. However, all the experiments agree that Sr_2IrO_4 exhibits an insulating behavior and a significant anisotropy between the **a**/**b** and the **c** directions. Moreover, no anomaly at the magnetic transition, which occurs at $T_M = 240$ K, was reported. To illustrate these main features, figure 4.2 displays the temperature dependence of the electrical resistivity for the single crystal synthesized by Kim *et al.* [85].

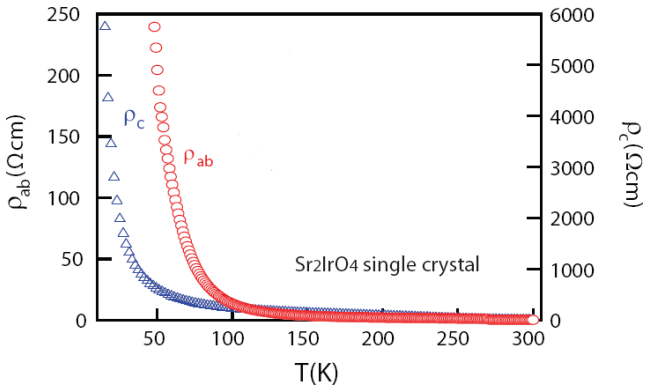

Figure 4.2: Temperature dependence of in-plane resistivity (ρ_{ab}) and out-of-plane resistivity (ρ_c). From [85].

At room temperature, the resistivity is estimated between 4 $\Omega.cm$ [87] and 10 $\Omega.cm$ [88]. The temperature dependence of the resistivity can not be fitted easily to a simple model. However, most authors assume an Arrhenius-type behavior $\rho(T) = \rho_0 \exp(E_a/k_BT)$, which is characteristic for semiconductor-like behavior. Since this model is not well-satisfied in the whole temperature range, some fittings to this model are reported by restriction to a certain range of temperatures:

- Shimura *et al.* [145] found $E_a = 0.06$ eV by considering only the temperature region below 200 K,
- Kini *et al.* [87] fitted the resistivity with $\rho_0 = 1.553$ $\Omega.cm$ and $E_a = 430.7k_B = 0.037$ eV in the middle temperature range [110 K;190 K],
- Kim *et al.* [85] reported an activation energy gap E_a of 0.070 eV,
- Fisher *et al.* [52] found a regime of constant activation energy with $E_a = 0.056$ eV between 54 and 205 K,

- Cosio Castaneda *et al.* [39] estimated the activation energy to be $E_a = 0.047$ eV in the temperature region [220 K;300 K].

All the results give the same order of magnitude but it is commonly accepted that the true gap in this compound is much larger than the soft gap estimated by these electrical resistivity measurements.

For the sake of completeness, we mention that a very detailed study of the temperature dependence of the electrical resistivity can be found in [87]. Particularly, for a low temperature range, a behavior of the type $\rho(T) = A\exp(T_0/T)^\nu$ with $\nu = 1/4$ is found for the compound. This can be associated to a three-dimensional various-range hopping of carriers between states localized by disorder. A similar behavior at low temperatures is mentioned in [31, 39].

4.2.2 Optical conductivity

The optical conductivity as reported in [84, 115, 116, 117] gives a more direct estimation of the gap than the analysis presented previously. For example, Moon *et al.*[117] measured the optical reflectivity $R(\omega)$ at 100 K and at room temperature between 5 meV and 30 eV, the conductivity $\sigma(\omega)$ being obtained by Kramers-Kronig transformation. Figure 4.3 displays the **ab**-plane optical conductivity of Sr_2IrO_4. Above 1.5 eV, the *p*-*d* charge transfer transitions observed are those from O $2p$ to d_{xy} (d_{xz}, d_{yz}) for peak A, to $d_{3z^2-r^2}$ for peak B and to $d_{x^2-y^2}$ for peak C.

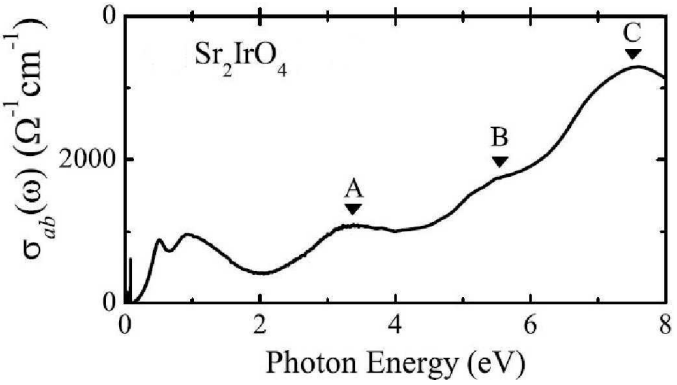

Figure 4.3: In-plane optical conductivity spectra $\sigma(\omega)$ of Sr_2IrO_4 at room temperature. Three peaks labeled A,B and C can be observed above 2.0 eV. From [117]

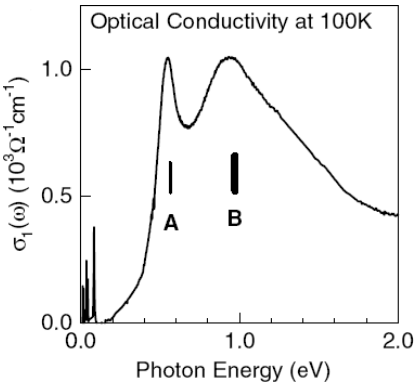

Figure 4.4: Zoom on the double peak structure, α and β, below 2 eV in the optical conductivity $\sigma(\omega)$ of Sr_2IrO_4at 100 K. From [84]

An optical gap of about 0.3 eV can be noticed at room temperature, the sharp spikes below 0.1 eV are due to optical phonon modes. The double peak structure, marked as α and β in figure 4.4 can not be explained by a simple model invoking the $5d$ orbitals of iridium. As we will show later, spin-orbit coupling is crucial for the explanation.

4.2.3 Spectroscopy measurements

With Angle Resolved Photo-Emission Spectroscopy (ARPES), one can investigates almost directly the electronic structure of a compound. Figure 4.5 presents the results obtained by performing ARPES on single crystals of Sr_2IrO_4. These spectra were obtained by Kim *et al.* [84] at 100 K from samples which were cleaved *in situ* under vacuum of 1×10^{-11} Torr. The energy distribution curves in panel (a) display the band features, whereas intensity maps at binding energies $E_B = 0.2$, 0.3, and 0.4 eV are shown panels (b)-(d).

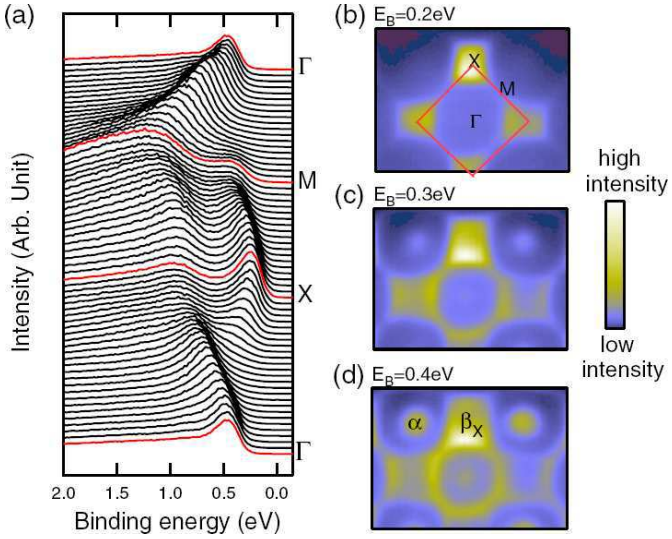

Figure 4.5: ARPES spectra along $\Gamma - M - X - \Gamma$ (panel a) and ARPES intensity maps at binding energies $E_B = 0.2$, 0.3, and 0.4 eV (panels b,c and d). From [84]

It is obvious that there is no band crossing the Fermi level (which would be an indication for a metallic state). The gap is roughly consistent with the optical gap estimation presented previously. For the sake of completeness, we also mention that ultraviolet photoelectron spectroscopy and X-ray photoelectron spectroscopy were also carried out on the material in [135]: the measurements confirmed that Sr_2IrO_4 is an insulator with a gaped density of states (DOS).

4.2.4 Heat properties

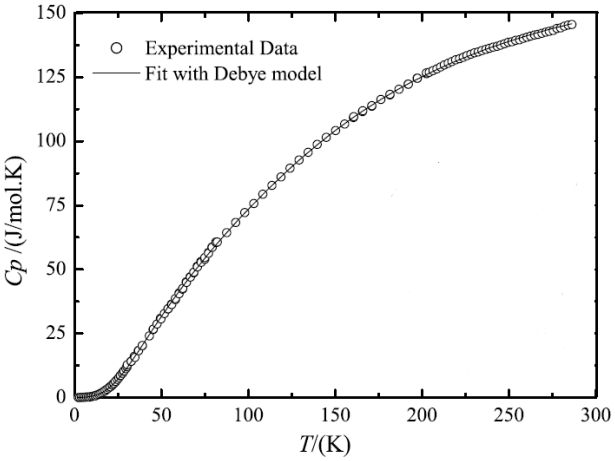

Figure 4.6: Temperature dependence of the specific heat (C_p) of Sr_2IrO_4. From [87]

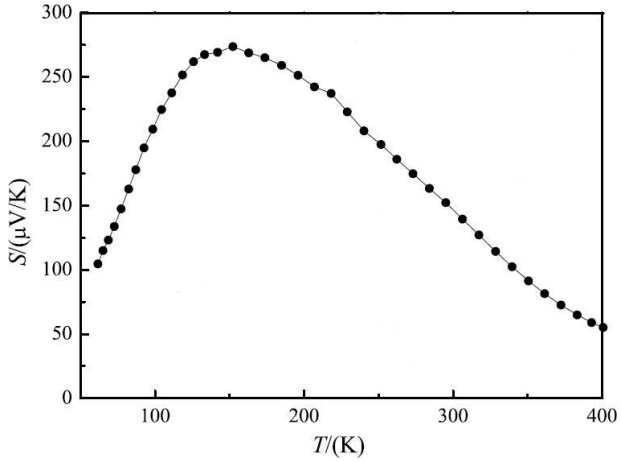

Figure 4.7: Temperature dependence of the Seebeck coefficient ($S(T)$) of Sr_2IrO_4. From [87]

Information about an energy gap can also be extracted from specific heat measurements. In figure 4.6 the specific heat $C_p(T)$ of Sr_2IrO_4 is displayed as a function of the temperature. The specific heat is completely dominated by Debye-phonon, that is to say by lattice excitations, and can be modeled by $C_p(T) = \gamma_0.T + \beta T^3$ with γ_0, the Sommerfeld contribution, being of the order of 1.8 $mJ.mol^{-1}.K^{-2}$ [33, 87]. Such a small value is in good agreement with the presence of a gap in Sr_2IrO_4.

[1]

A complete study about the Debye temperature can be found in [87]. Whereas it can not be observed on figure 4.6, recently Chikara *et al.* [38] measured a tiny specific heat anomaly ≈ 4 mJ.mol^{-1}.K^{-2} at $T_M = 240$ K, which was interpreted as a very small entropy change at the magnetic transition. The thermal conductivity $\kappa(T)$ was also studied by Kini *et al.*[87]. Their results confirm that heat conductivity in Sr_2IrO_4 is mainly due to lattice excitations.

The variation of the thermoelectric power – or Seebeck coefficient $S(T)$ – of Sr_2IrO_4 as function of temperature is displayed in figure 4.7 [38, 88, 52]. The value of $S(T)$ is positive, which is due to a hole conduction. A broad maximum, whose value ranges from 270 to 320μV.K^{-1} depending on the sample, is noticed around 100-150 K, before a decrease to a value of about 120 μV.K^{-1} at 300 K. No anomaly was ever reported at the magnetic transition temperature. Some attempts to estimate the gap of Sr_2IrO_4 from this curve was made but results do not agree with each other: Klein *et al.* [88] find an energy gap of 100 K – ≈ 0.01 eV – whereas Fisher *et al.*[52] estimate the gap to be of the order of 0.3 eV from a high-temperature range fitting.

4.3 Theoretical models for the insulating state

In 2000, Rama Rao *et al.* performed the first electronic band structure calculations for Sr_2IrO_4, by using the tight binding linear muffin-tin orbitals (TB-LMTO) within the atomic sphere approximation (ASA) [135]. The results incorrectly predicted Sr_2IrO_4 to be a metal with a finite DOSat the Fermi level. The failure of the LDA description indicates that electronic correlations are responsible for the insulating behavior of this compound. Mott physics based on the Hubbard Hamiltonian was then invoked to describe Sr_2IrO_4.

However, 4*d* and 5*d*-transition metal oxides are characterized by the larger spatial extent of their *d*-electron orbitals in comparison to their 3*d* counterparts – since the orthogonality to other orbitals can not be entirely assured by the angular part of the wavefunction. This feature enhances the *d-p* hybridization between the transition metal and the oxygen, which results in the formation of band structure with larger bandwidth in these compounds than in the 3*d*-transition metal oxides. The LDA calculations performed in [79] confirm that the band structure of Sr_2IrO_4 is almost identical to that of Sr_2RhO_4, with wide t_{2g} bands ranging from -2.5 to 0.5 eV.

In addition, since the 4*d* and – even more – the 5*d* states are delocalized, the electron correlations are commonly expected to play a smaller role in these compounds. As a result, to set the Hubbard Hamiltonian which will describe Sr_2IrO_4, the on-site Coulomb parameter U must be smaller than the typical values used for 3*d*-transition metal oxides– in which U typically ranges from 5 to 7 eV – and those used for 4*d*-transition metal oxides. Furthermore, a recent constrained-RPA calculation performed on Sr_2RuO_4 has estimated the value of U in this compound of about 2.3 eV [122]. In Sr_2IrO_4, the magnitude of the U parameter is thus expected to be of 2 eV maximum. Nevertheless, as it can be seen from the LDA+U calculations performed in [84], such a value for U cannot lead to an insulating state for Sr_2IrO_4.

[1] The Sommerfeld contribution γ_0 is rigorously defined only in the case of a metallic compound and is then proportional to the electronic density at the Fermi level. On the contrary, the expression of the specific heat for an insulator is rather $C_p(T) \sim T^{-1/2} \exp(-E_{gap}/2k_BT)$. However, it is still possible to fit this expression linearly at low temperature: in this case, one gets $\gamma_0 \sim \Delta T^{-1} \int_0^{\Delta T} \tau^{-3/2} \exp(-E_{gap}/2k_B\tau) d\tau$. The small value of γ_0 obtained for Sr_2IrO_4 implies that this last expression holds for this compound.

4.3.1 The "*spin-orbit driven Mott insulating*" model

The breakthrough in the understanding of the properties of Sr_2IrO_4 was done in 2008 by Kim *et al.* [84], where the picture of a "*spin-orbit driven Mott insulator*" in Sr_2IrO_4 was suggested. The spin-orbit coupling energy scale is indeed comparable to those of the other interactions in this $5d$ transition metal oxide: the spin-orbit coupling constant is estimated to be $\zeta_{SO} \approx 0.4$ eV for iridium according to [53, 43, 161].

As a result, by taking into account the spin-orbit coupling in the LDA calculations, the t_{2g} bands split into $j_{\text{eff}} = 1/2$ doublet and $j_{\text{eff}} = 3/2$ quartet bands, as we have explained in the chapter 3.1. Moreover, the latter are completely filled and one electron remains in the narrow $j_{\text{eff}} = 1/2$ bands. A U parameter of 2 eV is then enough to reach the Mott insulating state, as shown by the LDA+SO+U calculations performed in [84]. The cooperative interaction between electron correlation and the spin-orbit coupling thus explains the insulating state of Sr_2IrO_4. Furthermore, the electronic structures of the $5d$ Ruddlesden-Popper series $Sr_{n+1}Ir_nO_{3n+1}$ can also be understood by this phenomenon [116].

An experimental confirmation of this theoretical model was given by resonant X-ray scattering in 2009 [85]. This technique was indeed used to probe the relative phases of the electronic state, which corresponds to the *spin-orbit driven Mott insulating* state in Sr_2IrO_4. Results have shown that the ground state is very close to the $j_{\text{eff}} = 1/2$ limit, hence validating this theory.

In addition, the *spin-orbit driven Mott insulator* can also explain the double peak structure, marked as α and β in figure 4.4 as follows:

- Peak α is an optical transition from the lower Hubbard band to the upper Hubbard band of the $j_{\text{eff}} = 1/2$ states.
- Peak β is the optical transition from the $j_{\text{eff}} = 3/2$ bands to the upper Hubbard band of the $j_{\text{eff}} = 1/2$ states.

X-ray absorption spectra has confirmed this picture [84]. An orbital ratio $xy : yz : zx = 1 : 1 : 1$ within an estimation error $< 10\%$ for the unoccupied t_{2g} state was found, in good agreement with the ionic limit of the $j_{\text{eff}} = 1/2$ state (cf. equations (3.27)).

4.4 Magnetic properties

4.4.1 Experiments

Figure 4.8 displays the magnetic susceptibility $\chi(T) = M(T)/H$ of Sr_2IrO_4 at $H = 0.5$ T along the two principal crystallographic directions.[2] A clear ferromagnetic transition is observed at $T_M = 240$ K, as already mentioned in [34, 38, 88, 145]. The large anisotropy of the magnetic susceptibility indicates that the easy axis is aligned with the **a** axis.

Above T_M, the susceptibility can be fitted with a modified Curie-Weiss law $\chi(T) = \chi_0 + C/(T - \theta_{CW})$, where $C = N_A\mu_{\text{eff}}^2/3k_B$, with the following parameters [39, 87]:

- A Curie-Weiss temperature θ_{CW} between 236 and 251 K,
- A temperature independent susceptibility χ_0 of 1.5-8.8$\times 10^{-4}$ emu.mole^{-1},
- An effective magnetic moment μ_{eff} of about 0.3-0.5μ_B/Ir.

[2] The data have been corrected for core diamagnetism with the value 1.06×10^{-4}emu.mole^{-1}.

The discrepancy in the result is due to the fact that the ferromagnetism is very weak. Whereas θ_{CW} is comparable to the magnetic ordering temperature, the range of variations of μ_{eff} is significantly lower than the expected Hund's rule value of 1.73 μ_B/Ir for S=1/2. The temperature independent susceptibility χ_0 is likely due to a Van Vleck contribution [33], because of the insulating behavior of Sr_2IrO_4.

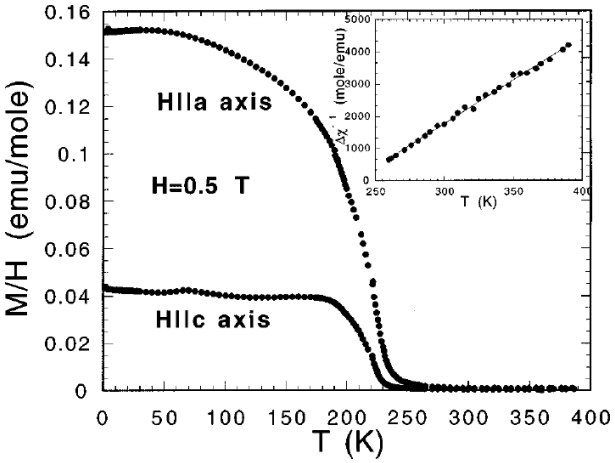

Figure 4.8: Magnetic susceptibility $\chi(T) = M(T)/H$ of Sr_2IrO_4 at $H = 0.5$ T along the two principal crystallographic directions. Inset: $\Delta\chi^{-1}$ in function of the temperature for $T > T_M$, with $\Delta\chi = \chi(T) - \chi_0$. From [31]

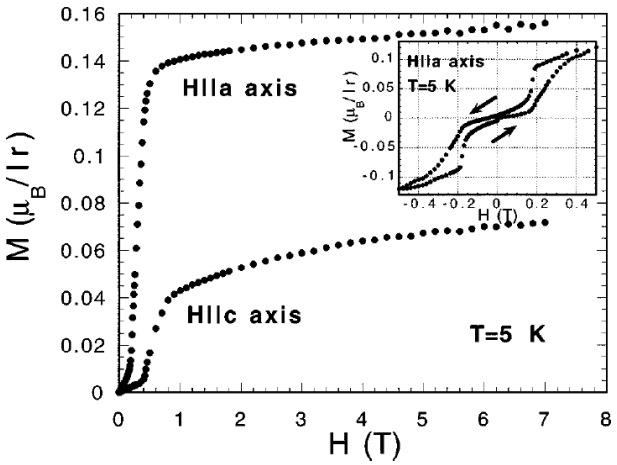

Figure 4.9: Isothermal magnetization M of Sr_2IrO_4 in function of the magnetic field H at $T = 5$ K. Inset: Isothermal magnetization along the **a**-axis for $-0.5 \leq H \leq 0.5$ T. From [31]

To be sure of the nature of the magnetic transition, magnetic hysteresis measurements (magnetization versus magnetic field) were performed at 5 K [31, 39, 41]. The observed hysteresis behavior, which can be seen on figure 4.9 is characteristic of a ferromagnetic compound. The saturation magnetic field was estimated more than 6.5 T and the magnitude for the ferromagnetic moment μ_{ferro} of about 0.023 μ_B/Ir. This value is far too small to attribute it to full ferromagnetically aligned spin 1/2 ions (corresponding to 1 μ_B). Moreover, the saturation moment μ_S is estimated of about 0.13-0.18 μ_B/Ir at low field ($H > 0.5$ T) [31, 38, 39] and of about 0.03-0.045 μ_B/Ir between 4 T and 5 T [41, 87]. In order to explain these low values of (saturation or effective) magnetic moment, the hypothesis of a canted antiferromagnetism was suggested in a early work by Crawford *et al.* [41].

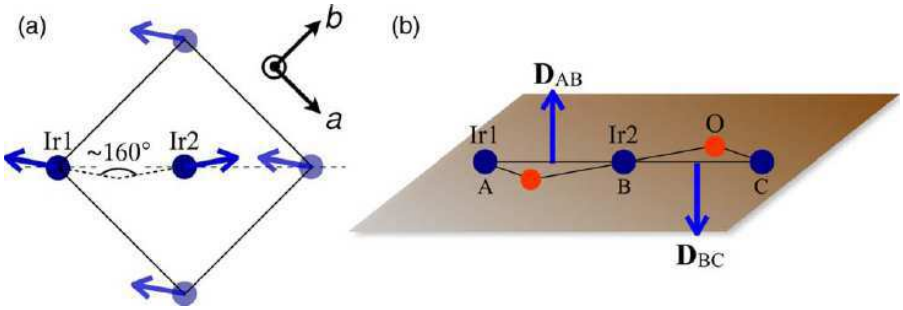

Figure 4.10: Magnetic configuration (panel a) and Dzyaloshinskii-Moriya vectors in Sr_2IrO_4 (panel b). The blue arrows in (a) represent the local iridium moments, consisting of both spin and orbital components, in a canted antiferromagnetic configuration. The Dzyaloshinskii-Moriya vectors in (b) are aligned along the **c**-axis. From [79]

4.4.2 Model for the canted-antiferromagnetism

In 2009, resonant X-ray scattering performed by Kim *et al.* [85] have confirmed that the magnetic structure of Sr_2IrO_4 is canted antiferromagnetic. In addition, based on the *spin-orbit driven Mott insulator* theory, a microscopic model was built to explain the magnetic state of Sr_2IrO_4 below $T_M = 240$ K [77, 79]. It is indeed possible to consider an effective Hamiltonian based on the $j_{\text{eff}} = 1/2$ single-band Hubbard model:

$$\mathcal{H} = \sum_{\langle ij \rangle} \sum_{m,m'} t^{ij}_{mm'} d^{\dagger}_{im} d_{jm'} + U \sum_{i} n_{i,+\frac{1}{2}} n_{i,-\frac{1}{2}} \tag{4.1}$$

where $d^{\dagger}_{im}$ stands for the $|\phi_{j_{\text{eff}}=\frac{1}{2},m}\rangle$ state (3.27) at the site i with $m = \pm 1/2$ and $n_{im} = d^{\dagger}_{im} d_{im}$. $t^{ij}_{mm'}$ and U are then the effective hopping and on-site Coulomb parameter. By taking into account the rotation of the IrO_6 octahedra, a spin dependent hopping term is generated and the following $j_{\text{eff}} = 1/2$-spin Hamiltonian can be derived:

$$\mathcal{H}_{spin} = \sum_{\langle ij \rangle} \left[I_0 \mathbf{J}_i \cdot \mathbf{J}_j + I_1 J_{zi} J_{zj} + \mathbf{D}_{ij} \cdot \mathbf{J}_i \times \mathbf{J}_j \right] \tag{4.2}$$

The first term is a conventional Heisenberg form of superexchange, the second and third terms are pseudodipolar and Dzyaloshinskii-Moriya antisymmetric exchange interactions. This last term explains the canted antiferromagnetism of Sr_2IrO_4 with the **ab** plane, as depicted on figure 4.10. Moreover, LDA+SO+U calculations [79] have confirmed that the magnetic configuration of Sr_2IrO_4 is a canted antiferromagnetic order with an angle close to the rotation angle of IrO_6 octahedra. This Dzyaloshinskii-Moriya type of magnetic interaction is thus the result of both the strong spin-orbit coupling and the distortions. Since $5d$ orbitals of iridium atoms are extended, exchange terms favoring parallel spin configurations are negligible. Moreover normal superexchange bonding contribution is more important than corresponding ferromagnetic exchange, hence favoring an antiferromagnetic arrangement. Because of the rotation of the IrO_6 octahedra, the center of inversion located on the oxygen is removed and a non collinear antiferromagnetic ordering is then allowed.

4.5 Still open questions about Sr_2IrO_4

Despite the success of the *spin-orbit driven Mott insulator* model, in particular to explain the characteristics of the phase below $T_M = 240$ K, some properties of Sr_2IrO_4 still remains out of the understanding.

4.5.1 Specificities of the electrical transport in single crystal

On the one hand, a non-trivial conducting behavior was reported for single crystal samples [31]: the current-voltage (I-V) characteristics exhibit a current controlled negative differential resistivity for both **a** and **c** directions, which occurs at very low voltage and decreases with increasing temperatures. I-V measurements were also carried out on polycrystalline samples [52]. Large deviations from linearity were found at high fields for the dc current density-electric field (J-E) characteristics, while the pulsed J-E characteristics have exhibited only weak non-linearity. Such a behavior seems to be attributed to an electrothermal effect – Joule heating – but more experimental works are necessary to draw a clear conclusion on this subject.

On the other hand, an unconventional giant magnetoelectric effect was recently observed in a single crystal of Sr_2IrO_4 [38]. It is characterized by a strongly peaked permittivity near an observed magnetic anomaly at about 100 K and a large magnetodielectric shift that occurs near a metamagnetic transition. Contrary to current models, this effect however depends on strong spin-orbit coupling rather than the magnitude and spatial dependence of magnetization. Further investigations on this phenomenon are expected in the future.

4.5.2 Temperature dependence of the optical gap

Figure 4.11 depicts the temperature-dependent optical conductivity $\sigma(\omega)$ of Sr_2IrO_4 [115]. As the temperature increases from 10 to 500 K, the optical gap is estimated to change from 0.41 to 0.08 eV. At room temperature (300 K), its value is about 0.26 eV. Moreover, the change in the optical gap is largest near the magnetic transition temperature. Looking more precisely to the evolution of the structure of the optical conductivity, the sharp peak α becomes broader and shifts to lower energy with increasing temperature. In addition, while the heights of the peaks α and β decrease, the spectral weight of the peak α increases and that of the peak β decreases as the temperature increases.

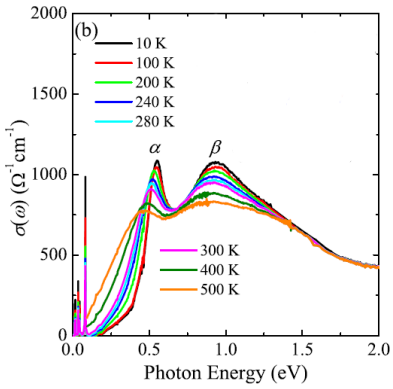

Figure 4.11: Temperature dependence of optical conductivity spectra $\sigma(\omega)$ of Sr_2IrO_4. As temperature increases, the peak α and β become broader and the optical gap decreases. From [115]

This decrease of the *spin-orbit driven Mott* gap has not been explained yet. The rate of decrease in the gap with temperature is about four to five times larger than those of the semiconductors. Therefore, it can not merely be associated to a thermal effect. Furthermore, the simple lattice distortions can not explain the large change in the bandwidth of Sr_2IrO_4 with temperature variation, according to LDA+SO+U calculations [115].

Summary

Sr_2IrO_4 is a 5*d*-transition metal oxide with a K_2NiF_4-type structure in which the corner-shared IrO_6 octahedra are not well-aligned but are alternately rotated clockwise and anticlockwise around the **c**-axis of the crystal. This compound is insulating and undergoes a magnetic transition at $T_M = 240$ K. Below $T_M = 240$ K, Sr_2IrO_4 indeed exhibits a unusual weak ferromagnetism with reduced iridium magnetic moments, which is attributed to a canted antiferromagnetic order.

These two surprising features can be explained by a cooperative interaction between electronic correlations and spin-orbit coupling: Sr_2IrO_4 can indeed be understood as a *spin-orbit driven Mott insulator* whose gap – of about 0.26 eV at 300 K – lies between the lower Hubbard band and the upper Hubbard band associated to its $j_{\text{eff}} = 1/2$ states. Below $T_M = 240$ K, the combined effect of the strong spin-orbit coupling and the distortions generates a Dzyaloshinskii-Moriya type of magnetic interaction, which results in the observed canted antiferromagnetism.

However, the *spin-orbit driven Mott insulating* model was only confirmed in the magnetic phase ($T < 240$ K) and is unable to explain the decrease of the optical gap with raising temperature. Before trying to explain this phenomenon, a band-structure calculation which includes both the spin-orbit coupling and the electronic correlations must be carried out in the paramagnetic phase of Sr_2IrO_4. Our work, which is described in the following chapter, presents the results obtained by studying Sr_2IrO_4 within LDA+DMFT. They highlight that the joint effort of the spin-orbit coupling and the structural distortions is essential to trigger the Mott transition in Sr_2IrO_4.

Chapter 5

The Sr_2IrO_4 Mott insulator: Role of the spin-orbit coupling and the lattice distortions

As described in the previous chapter, at room temperature Sr_2IrO_4 is a paramagnetic insulator with an optical gap of about 0.26 eV [115] However, DFT calculations give a metal as displayed in figure 5.1. Indeed, strontium and oxygen ions are respectively in the state Sr^{2+} and O^{2-}, which yields 5 electrons on the Ir $5d$ orbitals by formula unit, an odd number which is incompatible with an insulating state in the band picture. The insulating state must thus be caused by electronic correlations, which might seem surprising for a $5d$ element with strongly screened repulsion.

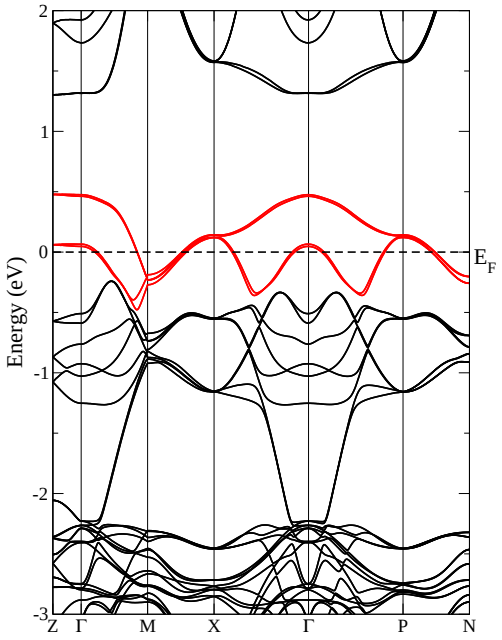

Figure 5.1: Kohn-Sham band structure of Sr_2IrO_4 in its realistic structure ($I4_1/acd$ symmetry). This calculation performed with Wien2k takes into account the spin-orbit coupling corrections. Four bands (in red) cross the Fermi level, which implies a metallic description of the compound.

In this chapter, we demonstrate that the following features collaborate to yield an insulator: (i) band narrowing due to the distortions in the material, (ii) spin-orbit coupling, and (iii) the Coulomb interaction with additional Hund's rule coupling. To achieve this goal, we use the LDA+DMFT toolbox as a numerical experiment in which we will subsequently turn on/off each of these features separately. This will enable us to understand why, in the real material, where all of these features are present, a moderate repulsion parameter $U = 1.3$ eV – as we will show – is sufficient to cause the transition to an insulator.

The scheme of our numerical experiment is presented on figure 5.2. There are thus four combinations we consider:

- an "*idealized*" description of Sr_2IrO_4, without distortions without spin-orbit coupling
- two "*intermediate*" states: an undistorted case with spin-orbit coupling and a distorted one without spin-orbit coupling
- a description which includes both the distortions and the spin-orbit coupling, which actually corresponds to the "*realistic*" Sr_2IrO_4.

The chapter is composed of two main parts:

- In the first section, the results of our DFT calculations are given. The reorganization of the band structure induced by taking into account the spin-orbit coupling and the distortions are considered, explaining the nature of the four narrow bands lying close to the Fermi level in the band structure of Sr_2IrO_4.
- In the second section, the results of our LDA+DMFT calculations are shown for each of the four cases, for several values for the Coulomb parameter U. The critical value at which the metal-insulator transition occurs is determined and used to characterize the fragility of the metallic state to correlations. In a nutshell, including the distortions reduces the bandwidth and induces an orbital polarization, while the spin-orbit coupling lifts some of the degeneracies of the metal-insulator transition. All these effects are necessary to explain the insulating nature of Sr_2IrO_4.

5.1 Influence of the spin-orbit coupling and the distortions on electronic correlations: Density functional study

5.1.1 Case 1: "*Undistorted*" Sr_2IrO_4 without spin-orbit coupling

We start by presenting the results of a DFT calculation performed on "*undistorted*" Sr_2IrO_4 in which the spin-orbit coupling is neglected. The structure of the compound is then of K_2NiF_4-type, and its band structure is similar to that of strontium ruthenate (Sr_2RuO_4) or the high-temperature superconductor lanthanum-baryum cuprate ($La_{2-x}Ba_xCuO_4$. This will enable us to present some general electronic characteristics of Sr_2IrO_4, such as its low-energy properties dominated by its t_{2g}*-bands*.

The unit cell and the chemical composition

According to X-ray and neutron diffraction studies [41, 72, 88, 135, 156], Sr_2IrO_4 has a tetragonal $I4_1/acd$ space group. It corresponds to the symmetry of a K_2NiF_4-type compound in which the corner-shared octahedra are not well-aligned along the crystallographic directions **a** and **b**, but are alternately rotated clockwise and anticlockwise around the **c**-axis. In the "*undistorted*" structure the tilting of the IrO_6 octahedra are neglected and thus the body-centered tetragonal unit cell of a

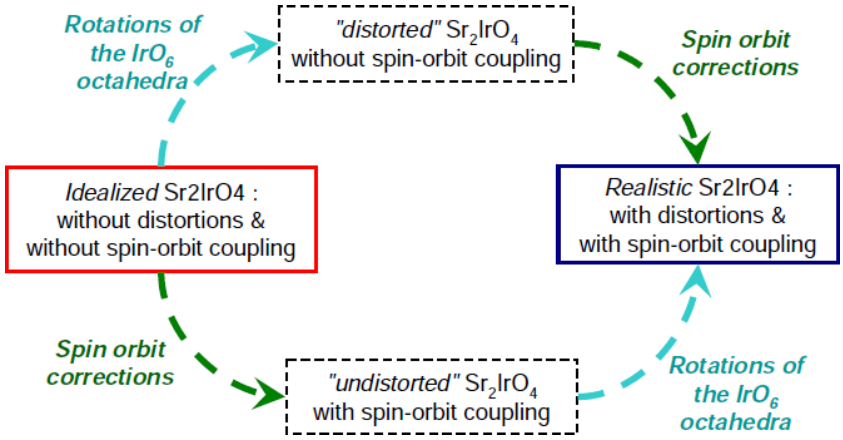

Figure 5.2: Scheme of our investigation. By following the blue arrow, the distortions are tuned up to their realistic level (a rotation of about 11° around the **c**-axis); by following the green arrow, the spin-orbit corrections are introduced.

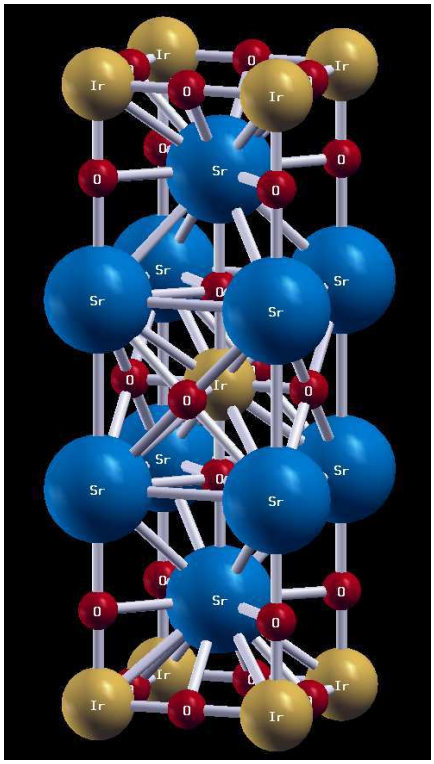

Figure 5.3: Conventional unit cell of Sr_2IrO_4 in the "*undistorted*" K_2NiF_4-type structure ($I4/mmm$ symmetry). The blue spheres stand for the strontium ions (Sr), the golden ones for Iridium (Ir) and the red ones for Oxygen (O). The covalent radius of each atomic species was used to set the size of the representing spheres. This picture was obtained with the software Xcrysden.

K_2NiF_4-type compound becomes suitable to describe of Sr_2IrO_4. The corresponding space-group is usually called $I4/mmm$ and the corresponding primitive unit cell contains only one formula unit.

The conventional representation of the unit cell of Sr_2IrO_4 in this *undistorted* symmetry is depicted in figure 5.3. The compound is a stacking of Ir-O_2 and Sr-O planes. Oxygen atoms which lie in the same plane as iridium (strontium) atoms will be refer to as O_1 (O_2) in the following. We use the original lattice parameters from [136]:[1] $a = b = 3.89$ Å and $c = 12.92$ Å. The crystallographic direction **a,b,c** corresponds to the usual **x,y,z** axis. The atomic positions are given in the first column of table 5.1. The ionization states of each atomic species in the crystal are Sr^{2+}, O^{2-} and Ir^{5+}. The iridium atoms thus accommodate 5 valence electrons (by formula unit) in their $5d$ orbitals. More details on the electronic configuration of each species can be found in table 5.2.

Each iridium atom is surrounded by four in-plane O_1 atoms and two apical O_2 atoms, forming then an octahedron (with $\widehat{O_1IrO_1} = \widehat{O_2IrO_1} = 90°$). These corner-shared IrO_6 octahedra are well-aligned along **a** and **b** direction ($\widehat{IrO_1Ir} = 180°$). Because of this local cubic crystal field, the $5d$ atomic orbitals of the iridium ions split into two e_g and three t_{2g} states. The octahedra are almost not elongated along the **c** axis: Ir-O_1=1.945 Å and Ir-O_2=1.951 Å. Consequently, the tetragonal crystal field induced by this distortion can be neglected in a first approach and no other splitting is thus expected in the $5d$ states[2]. The 5 valence electrons will thus occupy the three degenerate t_{2g} orbitals (d_{xy}, d_{xz} and d_{yz}) and the two degenerate e_g orbitals ($d_{3z^2-r^2}$ and $d_{x^2-y^2}$), with higher local energy, will be empty.

Technicalities of the DFT calculation

We have performed a DFT calculation on this *undistorted* description of Sr_2IrO_4 using the Wien2k package [23]. The main principles of this *all electron full potential LAPW method* have been presented in section 2.2. The calculations are done while using the LDA for the treatment of the exchange-correlation term. Standard parameters of Wien2k code are used: more precisely $R_{MT}.K_{max} = 7, l_{max} = 10$ and $l_{ns,max} = 4$. The irreducible Brillouin zone is sampled with 99 **k**-points with a tetrahedral mesh.

The muffin-tin radii chosen for each atomic species are presented in the second column of table 5.1. The energy threshold, which defines the boundary between the well-localized (*core*) and the delocalized (*semi-core* and *valence*) electronic states, is set at -7.5 Ry. This implies the categorization of the electronic states of each atomic species as described in table 5.2. The total semi-core and valence states considered during the calculation is then of 46+29=75 electrons by unit cell.

The band structure is plotted along the **k**-path depicted in figure 5.4. The conventional Brillouin zone is used. This **k**-path is chosen such that it contains the high-symmetry directions of the system. In the following, our attention will be focused on the $[Z\Gamma]$ direction – to investigate the k_z dispersion of the bands and then check the two-dimensional character of the compound – and the $[\Gamma MX\Gamma]$ path – to understand the k_x and k_y dispersion properties.

Kohn-Sham band structure of *undistorted* Sr_2IrO_4

Our LDA calculation without spin-orbit coupling predicts a metallic nature for Sr_2IrO_4 in the *undistorted* symmetry. As observed on figure 5.5, the total density of states (DOS) has indeed a finite value

[1] As mentioned in chapter 4, the distortions were indeed not detected by X-ray diffraction when Sr_2IrO_4 was synthesized for the first time in 1956. As a result, the compound was described in the *undistorted* symmetry, which makes the lattice parameters of this article particularly appropriate for our study.

[2] We will see that this approximation can not be used anymore in subsection 5.1.2. Indeed, despite its small value. this tetragonal crystal field must be taken into account to construct the local $j_{\text{eff}} = 1/2$ and $j_{\text{eff}} = 3/2$ basis out of the Kohn-Sham band structure of *undistorted* Sr_2IrO_4 with spin-orbit.

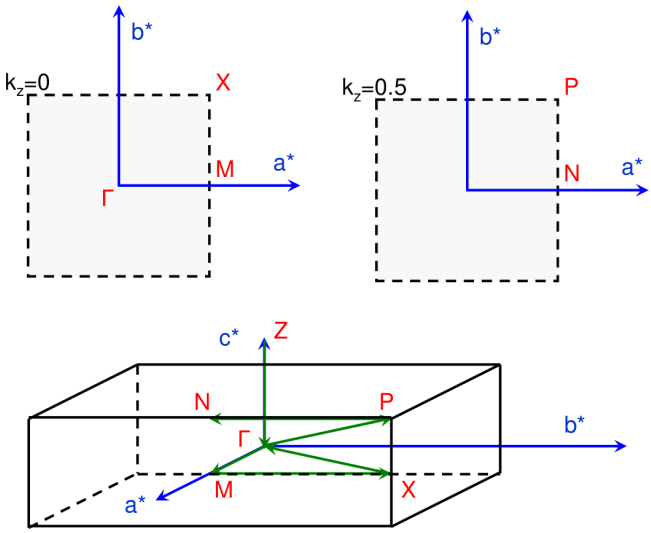

Figure 5.4: Conventional Brillouin zone for Sr_2IrO_4 in the *undistorted* symmetry. The high symmetry points are $\Gamma(0,0,0)$, $Z(0,0,1)$, $M(0.5,0,0)$, $X(0.5,0.5,0)$, $P(0.5,0.5,0.5)$ and $N(0.5,0,0.5)$. The green arrows depict the **k**-path along which bands are plotted in the following.

Atomic species	Position in reduced coordinates	Muffin-tin radius in Bohr radius $a_0 = 0.529$Å
Sr	(0,0,0.347)	2.38 a_0
Ir	(0,0,0)	1.94 a_0
O_1	(0,0.5,0)	1.72 a_0
O_2	(0,0,0.151)	1.72 a_0

Table 5.1: Description of the structural parameters used for our DFT calculation performed on Sr_2IrO_4 in the *undistorted* $I4/mmm$ symmetry.

Atomic species	Core states		Semi-core states		Valence states	
	description	electrons	description	electrons	description	electrons
Sr^{2+}	$[Ar]3d^{10}$	28 e^-	$4s^24p^6$	8 e^-	$5s^04d^05p^0$	0 e^-
Ir	$[Kr]4d^{10}$	46 e^-	$5s^25p^64f^{14}$	22 e^-	$6s^05d^56p$	5 e^-
O_1^{2-}, O_2^{2-}	$[He]=1s^2$	2 e^-	$2s^2$	2 e^-	$2p^6$	6 e^-
Total number of electrons		110 e^-		46 e^-		29 e^-

Table 5.2: Electronic configuration of the atoms in Sr_2IrO_4 and repartition between the core, semi-core and valence states as used during our DFT calculations.

at the Fermi level. To be more precise, in the Kohn-Sham band structure depicted on figure 5.6, four bands cross the Fermi level.

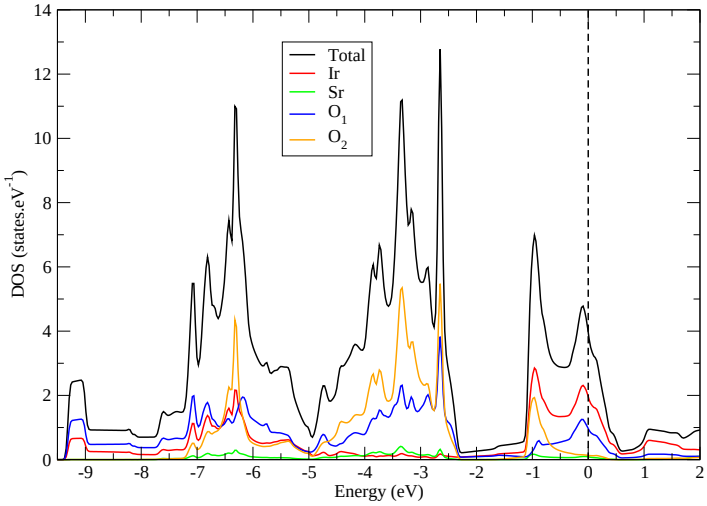

Figure 5.5: Total and partial desnity of states (DOS) of Sr_2IrO_4 in the *undistorted* symmetry without spin-orbit coupling. The Fermi level is materialized by the dotted vertical line.

As shown on figure 5.3, the structure of *undistorted* Sr_2IrO_4 is strongly anisotropic. Each layer containing the IrO_6 octahedra is indeed well separated from another by two Sr-O planes, corresponding to a distance of 2.56 Å. This implies a quasi-two dimensional character for the compound. By looking along the $[Z\ \Gamma]$ path on figure 5.6, the k_z dependence of the bands can be studied. Since almost no dispersion is observed in this direction, the main features of the Kohn-Sham band structure of *undistorted* Sr_2IrO_4 can be understood by considering only a single two-dimensional plane of IrO_6 octahedra.

On figures 5.5 and 5.6, only the valence bands – the bands which accommodate the 29 valence electrons – are displayed. They are exactly 17, as the number of atomic valence states in a formula unit (the 5 Ir $5d$ levels and the 4×3 O $2p$ levels). To give a general description of the "nature" of these bands, a simple tight-binding model can be developed: the IrO_6 plane is restricted to a two-dimensional square lattice with an effective atom in each node, whose "atomic levels" are the molecular orbitals of an IrO_6 octahedron. The pattern 5.7 summarizes the main structure of the molecular orbital diagram obtained for an IrO_6 octahedron. By drawing a parallel between this picture, the Kohn-Sham band structure of figure 5.6 and the partial DOS associated to the iridium and oxygen atomic characters – displayed on figure 5.5 –, it is then possible to give the following interpretation:

- Between -9.5 eV and about -5 eV, the bands come from the bonding $e_g(\sigma)$ and $t_{2g}(\pi)$ molecular orbital obtained from the Ir $5d$ and the O $2p$ states. They have mostly an O $2p$ character and for convenience, we will refer to them in the following as the "*oxygen-bands*".
- Between -5 eV and -2.5 eV, the bands come from the non-bonding O $2p$ states, which explains why the partial DOS associated to the iridium character is almost zero in this range. We will also refer to them in the following as "*oxygen-bands*".
- Above -2.5 eV, the 5 bands (the 3 blue and the 2 red ones on figure 5.6) come from the anti-bonding $e_g(\sigma^*)$ and $t_{2g}(\pi^*)$ molecular orbital built from the Ir $5d$ and the O $2p$ states. They are

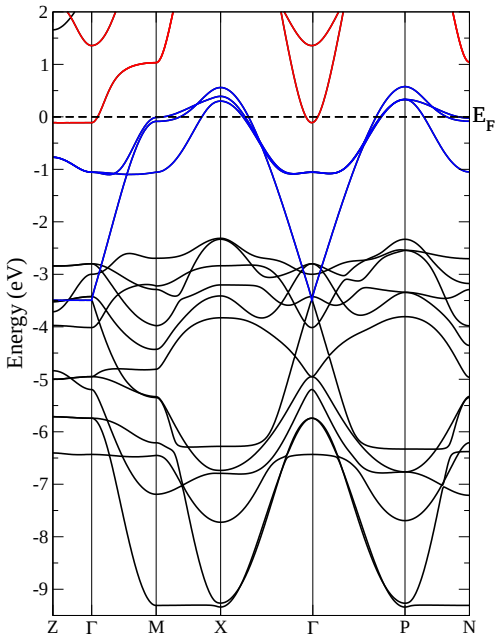

Figure 5.6: Kohn-Sham band structure of Sr_2IrO_4 in the *undistorted* symmetry without spin-orbit coupling. The lower boundary of the energy window is chosen such that the bands up to the Fermi level contain the 29 valence electrons. In blue the t_{2g} bands, in red the e_g and in black the O2p bands. On ΓZ there is almost no dispersion, confirming the two-dimensional nature of the material.

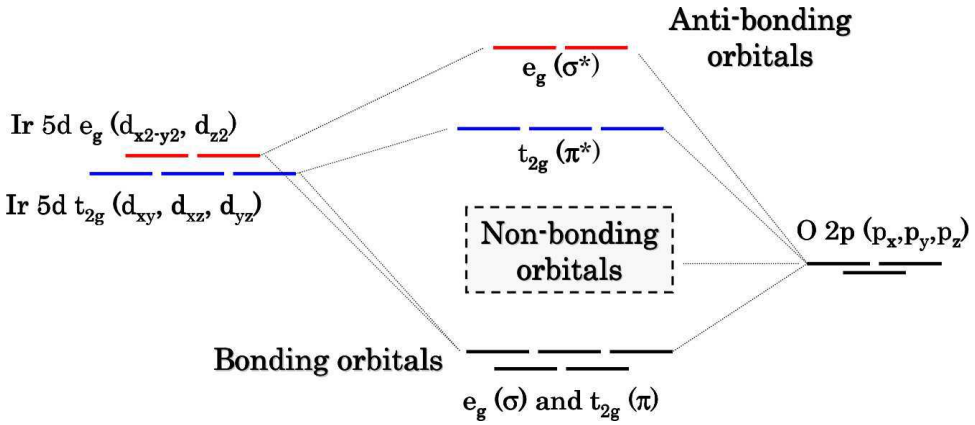

Figure 5.7: The molecular orbitals in an IrO_6 octahedron.

partially filled and have mainly an Ir $5d$ character. For convenience, we will refer to them as the "*e_g and t_{2g} bands*" in the following.

The atomic Ir $5d$ character from which each e_g or t_{2g} band derive has been plotted on figure 5.8. Each band has a pure character, which confirms that the cubic Ir $5d$ states are well-adapted to describe this band structure. The three bands which lie in the lower energy range – mostly below the Fermi level – are associated to the Ir $5d$ t_{2g} states and the two bands in the higher energy range – mainly above the Fermi level – to the Ir $5d$ e_g states. Because of this one-to-one correspondence, we will now call each band with the name of its corresponding atomic state.

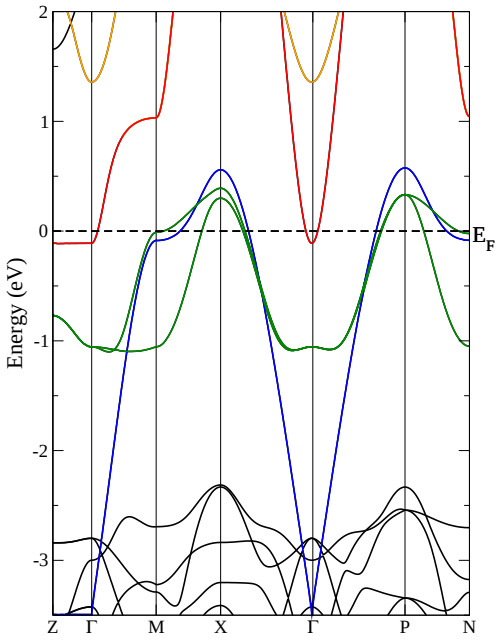

Figure 5.8: Kohn-Sham band structure of Sr_2IrO_4 in the *undistorted* symmetry without spin-orbit coupling. The d_{xy} band is represented in blue, the d_{xz} and d_{yz} in green, the $d_{x^2-y^2}$ in red and the $d_{3z^2-r^2}$ in yellow.

The shape of each t_{2g} band along the **k**-path can be understood with a tight-binding approach based on an effective model, in which iridium atomic orbitals are only involved. The cubic d_{xz} orbitals on each iridium site are perpendicular to the plane and form π bonds along the **x**-axis via the O_1 $2p_z$ orbitals. The hopping terms along the **y**-axis can be neglected, the model is thus composed of independent unidimensional chains of iridium along **x**. Within this framework, the electron dispersion of the d_{xz} band is of the following form:

$$\varepsilon^{\mathbf{k}}_{xz} = \varepsilon^{0}_{xz} - 2t_\pi \cos(k_x.a) \tag{5.1}$$

where ε^0_{xz} is the effective local energy associated to the atomic-like d_{xz} orbitals and t_π is the effective hopping amplitude between them. A similar model can be developed for the d_{yz} orbitals.

On the contrary, the d_{xy} orbitals which lie in the plane require a two-dimensional pattern. They indeed form π bondings along the **x**-axis and the **y**-axis. However, the hopping between next-nearest neighbors must also be included so as to get the following electron dispersion of the d_{xy} band:

$$\varepsilon^{\mathbf{k}}_{xy} = \varepsilon^{0}_{xy} - 2t\big[\cos(k_x.a) + \cos(k_y.a)\big] - 4t' \cos(k_x.a)\cos(k_y.a) \tag{5.2}$$

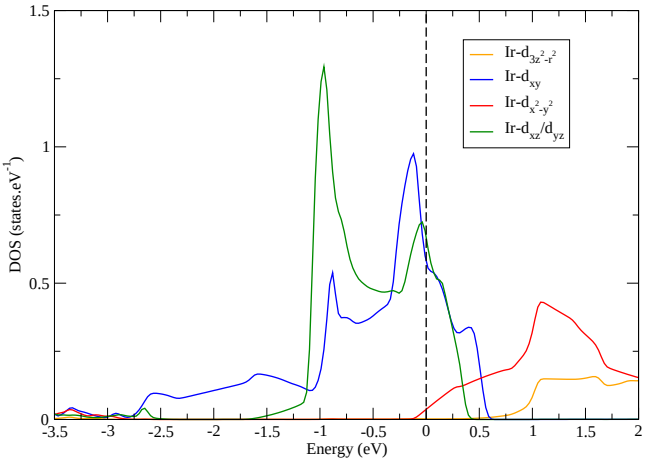

Figure 5.9: Partial DOS associated to the Ir $5d$ e_g and t_{2g} characters for Sr_2IrO_4 in the *"undistorted"* symmetry without spin-orbit coupling. The Fermi level is materialized by the dotted vertical line.

where ε^0_{xy} is the effective local energy associated to the atomic-like d_{xy} orbitals and t (t') the hopping amplitude between the nearest-neighbors (the next-nearest neighbors respectively). The larger bandwidth of the d_{xy} band – almost twice wider than the one for the d_{xz} and the d_{yz} bands – thus comes from its two-dimensional character.

Similar effective models can also be developed to explain the shape of the two e_g bands. This tight-binding approach is in good agreement with the structure of the partial DOS associated to each Ir $5d$ character and represented in figure 5.9. The peak located at -0.1 eV in the partial DOS associated to the d_{xy} character can be identified as the Van Hove singularity of a two-dimensional band. Similarly, the two peaks, at -1 eV and at the Fermi level respectively, of the band d_{xz} (or d_{yz}) can be linked to the two Van Hove singularities which can be found in a one-dimensional band.

Construction of a localized e_g-t_{2g} Wannier-type basis set for *undistorted* Sr_2IrO_4

In Sr_2IrO_4, the Ir-$5d$ orbitals are considered to span the correlated subspace of the system. Since electronic correlations play a more significant role on partially filled bands than on completely filled or empty ones, we construct the effective local impurity model used for the DMFT treatment from the Wannier orbitals related to the five e_g and t_{2g} bands. To perform this, we use the scheme to build Wannier projectors which was described in the section 2.3. By choosing an energy window ranging from -3.5 eV to 0.6 eV, it is possible to associate a Wannier function to each band (in a similar picture as in figure 5.8).

Their respective charges, which correspond to the filling of the band, are presented in the second column of table 5.3. The t_{2g} bands are almost equally filled and accommodate 5 electrons per formula unit. Furthermore, the e_g bands of the system are almost empty, although the $d_{x^2-y^2}$ band cross the Fermi level.

Consequently, in the following we consider a "t_{2g} bands" system with 5 electrons (by formula unit) in 3 t_{2g} *bands*. Besides, in a calculation where electronic correlations will be better taken into account – such as a LDA+DMFT calculation –, the $d_{3z^2-r^2}$ and $d_{x^2-y^2}$ are expected to be shifted above the Fermi

Charge	calculated from the partial DOS	of the Wannier functions of the energy window [-3.5;0.6] eV
Ir 5d $d_{3z^2-r^2}$	0.005	0.005
Ir 5d $d_{x^2-y^2}$	0.016	0.017
Ir 5d d_{xy}	0.731	1.612
Ir 5d d_{xz}/d_{yz}	0.752	1.696

Table 5.3: Charge repartition between the e_g and t_{2g} atomic states (first column) and the e_g and t_{2g} bands (second column), between -3.5 eV and the Fermi level. The results of the first column were calculated by integrating the partial DOS calculated in Wien2k for the corresponding Ir 5d state from -3.5 eV to the Fermi level. The results of the second column were evaluated similarly but by considering the Wannier orbitals built in the energy window $[-3.5; 0.6]$ eV. The Wannier orbitals are clearly "more than" just the Ir 5d orbitals.

level, which will remove completely the charge in them. *Undistorted* Sr_2IrO_4 has a large bandwidth of the d_{xy} band (about 4.1 eV). As a result, an insulating state would emerge only if unphysically large interaction was introduced. For realistic values of the Coulomb parameter U (below 2 eV for a 5d-transition metal oxide), only moderately correlated metallic state, such as that of the Sr_2RuO_4, will emerge. More quantitative results are presented in section 5.2.

5.1.2 Case 2: Modifications in the Kohn-Sham band structure induced by the spin-orbit interaction

The second-variational method used in Wien2k to take into account the spin-orbit coupling was described in section 3.3. In our calculation, the spin-orbit corrections have been introduced only for the iridium atoms. Since the system is not spin-polarized, its symmetry is unchanged[3] and the Kohn-Sham band structure can therefore be plotted along the same **k**-path (in the same Brillouin zone) as previously.

Kohn-Sham band structure of the *undistorted* Sr_2IrO_4 including the spin-orbit coupling

Our LDA calculation predicts also a metallic nature for *undistorted* Sr_2IrO_4 when the spin-orbit coupling is taken into account. To ease the comparison, the total DOS of the compound with and without spin-orbit coupling are both represented on figure 5.10. The major rearrangements of the structure occur mostly between -2.5 eV and 1 eV, which corresponds to the energy range where e_g and t_{2g} bands previously lay. However, since Ir 5d states are also involved – but are in minority – in the formation of the *oxygen bands* which lay between -9.5 and -5 eV, some little changes can be noticed in this energy range too, but they will not be discussed in the following.

The Kohn-Sham band structure depicted on figure 5.11 reveals that still four bands cross the Fermi level. Although the spin quantum number is not well-adapted to describe a system in which the spin-orbit coupling is taken into account, each band on figure 5.11 is still twice degenerate, because the spatial inversion is included in the *undistorted* symmetry ($I4/mmm$) and the system is paramagnetic[4]. As a result, each band still accommodates up to 2 electrons. The main changes have mostly affected the t_{2g} bands, whereas the e_g bands have essentially been shifted up by about 0.1 eV. By plotting the atomic Ir 5d character from which each e_g and t_{2g} bands derive, this first impression is confirmed:

[3] Taking into account the spin-orbit coupling does not modify the magnetic Shubnikov space group of the compound, as explained in Appendix E.

[4] This property was demonstrated in section 3.1.

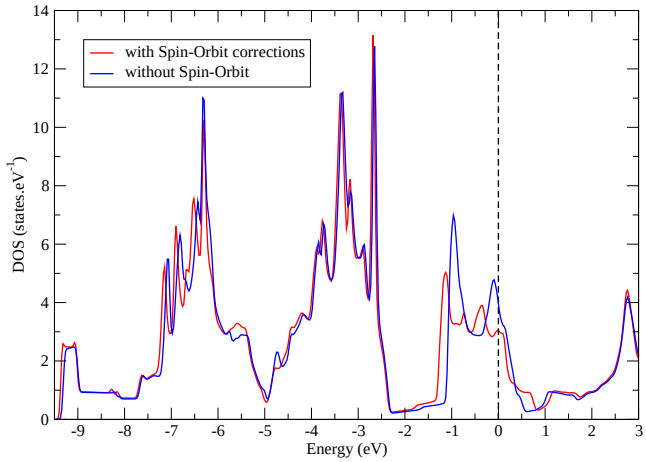

Figure 5.10: Total DOS for Sr_2IrO_4 in the *undistorted* symmetry. The red curve includes the corrections induced by taking into account the spin-orbit coupling. The Fermi level is materialized by the dotted vertical line. The major change in the overall structure occurs close to the Fermi level between -2.5 eV and 1 eV.

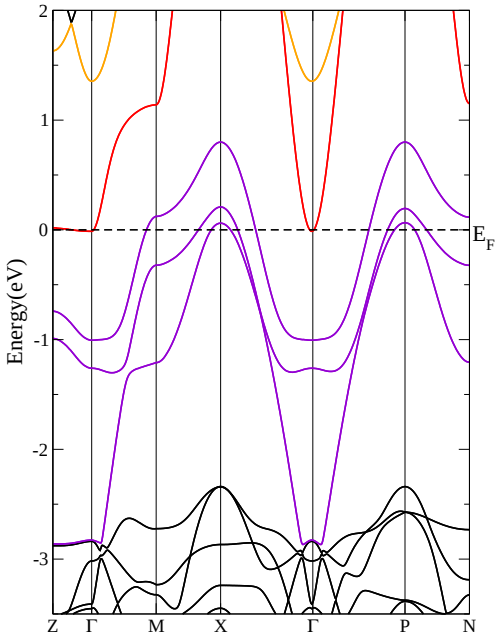

Figure 5.11: Kohn-Sham band structure of Sr_2IrO_4 in the *undistorted* symmetry including the spin-orbit coupling. The e_g bands ($d_{3z^2-r^2}$ in yellow and $d_{x^2-y^2}$ in red) are almost not affected by the corrections and their atomic character is preserved. On the contrary, the t_{2g} bands (in purple) are deeply modified and mix from now on the d_{xy}, d_{xz} and d_{yz} atomic characters along the **k**-path.

- Each e_g band has indeed kept its own atomic Ir $5d$ character ($d_{3z^2-r^2}$ and $d_{x^2-y^2}$ – in yellow and red respectively on figure 5.11 –). The spin-orbit coupling has thus not affected them and the observed energy shift is actually the consequence of the new charge repartition between the t_{2g} bands.

- The t_{2g} bands are not in one-to-one correspondence with one Ir-$5d$ t_{2g} character anymore. A mixing of the three cubic states (d_{xy}, d_{xz} and d_{yz}) can indeed be found in each band, which implies that the t_{2g} cubic basis is not well-suited anymore to describe this new band structure.

Although figure 5.11 does not display the repartition of the d_{xy}, d_{xz} and d_{yz} character along the t_{2g} bands (in purple on the figure), the partial DOS associated to these atomic characters – and presented in figure 5.12 – can confirm this last statement. First, the energy range of the d_{xz} (or d_{yz}) character has increased: for instance, its partial DOS has almost the same significant weight as that of d_{xy} state between 0.2 eV and 0.75 eV, where only the "upper" t_{2g} band lie. Furthermore, the Van Hove singularities associated to the t_{2g} states have reduced significantly, which implies strong deviations with the tight-binding model based on the Ir $5d$ t2g orbitals we have previously developed.

The spin-orbit coupling plays an important role in Sr_2IrO_4. From our Kohn-Sham band structure, we estimate the value of the spin-orbit coupling constant ζ_{SO} as in the same order of magnitude as [43, 53, 161]: $\zeta_{SO} \approx 0.4$ eV. For the interested reader, the details of this calculation can be found in Appendix A. Since our previous effective model is from now on irrelevant to describe the t_{2g} bands, a tight-binging approach in which iridium atomic levels are described in the the strong-spin-orbit-coupling limit is seducing.

In section 3.1, the impact of the corrections induced by the spin-orbit coupling on the e_g and t_{2g} states was thoroughly described and the *TP-equivalence approximation* was introduced. In this approach, the cubic crystal field is assumed large enough to treat the e_g and t_{2g} states still separately even if the spin-orbit coupling is taken into account. As a result, the spin-orbit corrections in the t_{2g} subspace imply to use a new basis which is composed of what we have called in section 3.1 the "$j_{\text{eff}} = 1/2$" and the two "$j_{\text{eff}} = 3/2$" states, whereas the spin-orbit interaction is ineffective on $d_{3z^2-r^2}$ and $d_{x^2-y^2}$ states, since their orbital angular momentum is completely quenched. The *TP-equivalence approximation* appears particularly adapted to describe the formation of the electronic band structure of *undistorted* Sr_2IrO_4 with the spin-orbit coupling. Consequently, the t_{2g} bands would come from the $j_{\text{eff}} = 1/2$ and $j_{\text{eff}} = 3/2$ atomic states.

Some details on the determination of the local $j_{\text{eff}} = 1/2$ and $j_{\text{eff}} = 3/2$ basis

The $j_{\text{eff}} = 1/2$ and $j_{\text{eff}} = 3/2$ states were introduced in section3.1 to describe the eigenstates of a cubic system in which the spin-orbit coupling is taken into account within the framework of the *TP-equivalence* approximation. We remind here that their forms are the following:

$$\begin{cases} |j_{\text{eff}} = \frac{1}{2}, m_j = -\frac{1}{2}\rangle = \frac{1}{\sqrt{3}}|d_{yz}\uparrow\rangle - \frac{i}{\sqrt{3}}|d_{xz}\uparrow\rangle - \frac{1}{\sqrt{3}}|d_{xy}\downarrow\rangle \\ |j_{\text{eff}} = \frac{1}{2}, m_j = +\frac{1}{2}\rangle = \frac{1}{\sqrt{3}}|d_{yz}\downarrow\rangle + \frac{i}{\sqrt{3}}|d_{xz}\downarrow\rangle + \frac{1}{\sqrt{3}}|d_{xy}\uparrow\rangle \end{cases} \tag{3.27}$$

and:

$$\begin{cases} |j_{\text{eff}} = \frac{3}{2}, m_j = -\frac{3}{2}\rangle = \frac{1}{\sqrt{2}}|d_{yz}\downarrow\rangle - \frac{i}{\sqrt{2}}|d_{xz}\downarrow\rangle \\ |j_{\text{eff}} = \frac{3}{2}, m_j = +\frac{3}{2}\rangle = -\frac{1}{\sqrt{2}}|d_{yz}\uparrow\rangle - \frac{i}{\sqrt{2}}|d_{xz}\uparrow\rangle \\ |j_{\text{eff}} = \frac{3}{2}, m_j = -\frac{1}{2}\rangle = \frac{1}{\sqrt{6}}|d_{yz}\uparrow\rangle - \frac{i}{\sqrt{6}}|d_{xz}\uparrow\rangle + \sqrt{\frac{2}{3}}|d_{xy}\downarrow\rangle \\ |j_{\text{eff}} = \frac{3}{2}, m_j = +\frac{1}{2}\rangle = -\frac{1}{\sqrt{6}}|d_{yz}\downarrow\rangle - \frac{i}{\sqrt{6}}|d_{xz}\downarrow\rangle + \sqrt{\frac{2}{3}}|d_{xy}\uparrow\rangle \end{cases} . \tag{3.28}$$

Following our previous discussion, the local basis composed of $|d_{3z^2-r^2}\rangle$, $|d_{x^2-y^2}\rangle$, $|j_{\text{eff}} = 1/2\rangle$, $|j_{\text{eff}} = 3/2, |m_j| = 3/2\rangle$, $|j_{\text{eff}} = 3/2, |m_j| = 1/2\rangle$ appears to be a natural choice to perform the calculation of the Wannier orbitals. Besides, this basis has a great advantage: the coefficients of each eigenstate is independent of the values taken by the spin-orbit coupling constant ζ_{SO} and the cubic crystal field.

The program dmftproj was thus used with this local basis to describe the Ir $5d$ states in the system. Unfortunately, contrary to what have been expected, this basis does not diagonalize the local Hamiltonian and leads to the appearance of several hybridization terms between these eigenstates. This occurs because the calculation performed in section 3.1 was made with two approximations:

- the *TP-equivalence approximation*, of course, which is not rigorously verified here.
- the degeneracy of the three t_{2g} states.[5]

The calculation of the eigenstates of a system which takes into account the spin-orbit coupling and a tetragonal splitting in the framework of the *TP-equivalence approximation* is presented in Appendix A.

[5]This last assumption does hold for our problem too. The small elongation of the IrO_6 octahedra induces a tetragonal splitting which puts the d_{xy} higher in energy than the d_{xz} and d_{yz}. This is also the origin of the charge difference shown in table 5.3.

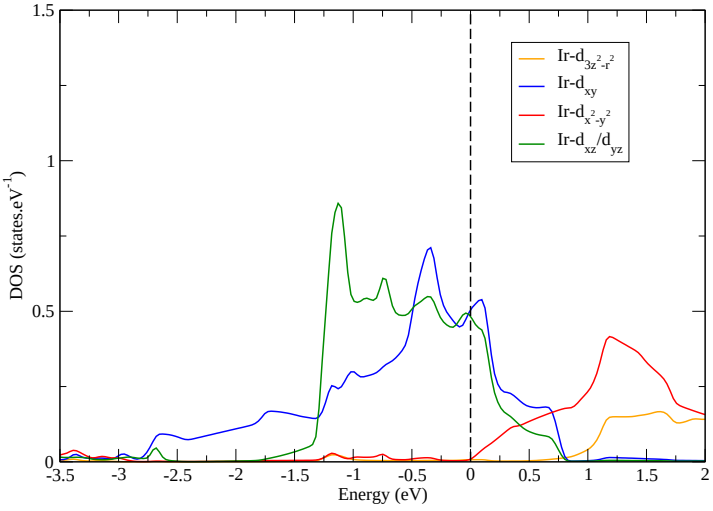

Atomic state	Charge
Ir $5d$ $d_{3z^2-r^2}$	0.013
Ir $5d$ $d_{x^2-y^2}$	0.033
Ir $5d$ d_{xy}	0.687
Ir $5d$ d_{xz}/d_{yz}	0.737

Figure 5.12: Partial DOS associated to the Ir $5d$ e_g and t_{2g} characters for Sr_2IrO_4 in the *undistorted* symmetry with spin-orbit coupling. The Fermi level is materialized by the dotted vertical line. The charge of each atomic state was calculated by integrating the corresponding DOS between -3.5 eV and the Fermi level.

It shows that the eigenvalues and the coefficients of the eigenvectors $|j_{\text{eff}} = 1/2\rangle$, $|j_{\text{eff}} = 3/2, |m_j| = 3/2\rangle$ and $|j_{\text{eff}} = 3/2, |m_j| = 1/2\rangle$ will explicitly depend in this case of the ratio $\eta = 2Q_1/\zeta_{SO}$. Since no estimation of this ratio can easily be calculated, another approach was used to find the local basis which described at best our local problem: it consists in evaluating numerically the basis which diagonalizes the density matrix in the considered energy window for calculating the Wannier projectors.

More precisely, the method consists in calculating a first time the Wannier orbitals based on the standard (complex or cubic) basis in order to obtain the density matrix associated to them. And then, the basis which diagonalizes this density matrix is found and used in a second run to calculate directly the Wannier orbitals. In this approach one must use a large energy window which contains all the complex (or cubic) orbitals initially. In the case of *undistorted* Sr_2IrO_4 in which the spin-orbit coupling is included, the energy window is $[-3.5; 6.5]$ eV. The Wannier orbitals finally obtained with this method diagonalizes the density matrix at the end of the program dmftproj, which is also of practical advantage for a CTQMC calculation because the sign problem in CTQMC arises mostly because of off-diagonal terms in the local Hamiltonian.

Our approach can of course be improved further. In the current framework, the integration over the Brillouin zone used in dmftproj and in the CTQMC calculations are not the same (a tetragonal integration for the former and a point integration for the latter). Because of this difference, even if the Wannier projectors diagonalize the density matrix at the end of dmftproj, some small off-diagonal terms (of maximal order of magnitude 0.001 eV) will appear in the local Hamiltonian used in the CTQMC calculations. They can easily be neglected during the calculations but we have no control on these terms yet. Another improvement would be achieved by restricting the size of the energy window or restrict the projection to a subspace of orbitals (only the t_{2g} for instance).

Introduction of the "$j_{\text{eff}} = 1/2$" and "$j_{\text{eff}} = 3/2$ *bands*"

With the previously described method, the best basis for our local problem was evaluated to be the following vectors[6]:

$$
\begin{array}{lllll}
|\psi_1\rangle = & +0.99429\ |d_{3z^2-r^2}\downarrow\rangle & & +0.07543\ |d_{xz}\uparrow\rangle & +i0.07543\ |d_{yz}\uparrow\rangle \\
|\psi_1\rangle \approx & |d_{3z^2-r^2}\downarrow\rangle & & & \\
 & & & & \\
|\psi_2\rangle = & +0.99018\ |d_{x^2-y^2}\downarrow\rangle & -i0.10487\ |d_{xy}\downarrow\rangle & -0.06536\ |d_{xz}\uparrow\rangle & -i0.06536\ |d_{yz}\uparrow\rangle \\
|\psi_2\rangle \approx & |d_{x^2-y^2}\downarrow\rangle & & &
\end{array}
\tag{5.3}
$$

The deviations of this two first states from $d_{3z^2-r^2}$ and $d_{x^2-y^2}$ respectively can be understood as a measure of the validity of the *TP-equivalence approximation*. The numerical method used does indeed take into account the off-diagonal terms due to the spin-orbit coupling corrections, which are neglected by using this approximation. Looking at the value of the coefficients, a tight-binding model based on iridium described in the *TP-equivalence approximation* framework is thus a very good approach.

[6] We display here only half of the basis. The results are similar for the states $|d_{3z^2-r^2}\uparrow\rangle$, $|d_{x^2-y^2}\uparrow\rangle$, $|j_{\text{eff}} = 1/2, m_j = +1/2\rangle$, $|j_{\text{eff}} = 3/2, m_j = +1/2\rangle$ and $|j_{\text{eff}} = 3/2, m_j = -3/2\rangle$.

$$
\begin{array}{lllll}
|\psi_3\rangle = & -i0.00588\ |d_{x^2-y^2}\downarrow\rangle & -0.62942\ |d_{xy}\downarrow\rangle & -i0.54945\ |d_{xz}\uparrow\rangle & +0.54945\ |d_{yz}\uparrow\rangle \\
|\psi_3\rangle = & |j_{\text{eff}}=\tfrac{1}{2}, m_j=-\tfrac{1}{2}\rangle & & & \\
 & & & & \\
|\psi_4\rangle = & -i0.13967\ |d_{x^2-y^2}\downarrow\rangle & +0.76996\ |d_{xy}\downarrow\rangle & -i0.44026\ |d_{xz}\uparrow\rangle & +0.44026\ |d_{yz}\uparrow\rangle \\
|\psi_4\rangle = & |j_{\text{eff}}=\tfrac{3}{2}, m_j=-\tfrac{1}{2}\rangle & & & \\
 & & & & \\
|\psi_5\rangle = & +i0.10668\ |d_{3z^2-r^2}\downarrow\rangle & & -i0.70307\ |d_{xz}\uparrow\rangle & -0.70307\ |d_{yz}\uparrow\rangle \\
|\psi_5\rangle = & |j_{\text{eff}}=\tfrac{3}{2}, m_j=+\tfrac{3}{2}\rangle & & &
\end{array}
\tag{5.4}
$$

The three vectors $|\psi_3\rangle$, $|\psi_4\rangle$ and $|\psi_5\rangle$ are thus associated to the t_{2g} states. The first column of coefficients comes from the deviations from the *TP-equivalence approximation* and can thus be neglected. The three last column of coefficients of these vectors are really close to the "idealized" case of the expressions (3.27) and (3.28).[7]

The state $|\psi_5\rangle$ is thus the state $|j_{\text{eff}}=3/2, m_j=+3/2\rangle$. The discrepancy of the value of the coefficients of $|\psi_3\rangle$ and $|\psi_4\rangle$ from the theoretical "idealized" case comes from the non-degeneracy of the t_{2g} orbitals because of the tetragonal crystal-field splitting Q_1. Using the expressions calculated in Appendix A, the value of the ratio $\eta = 2Q_1/\zeta_{SO}$ is positive and estimated to be about 0.400. This implies that the local d_{xy} states has an higher energy than the local d_{xz} and d_{yz} states, which is in good agreement with an elongation of the IrO_6 octahedron along the **z**-axis. By using the value of the spin-orbit coupling in the compound – $\zeta_{SO} \approx 0.4$ eV–, the tetragonal splitting is found to be $Q_1 = 0.08$ eV. The fitting between the numerical coefficients and the theory confirms that we can label these states as $|j_{\text{eff}}=1/2, m_j=-1/2\rangle$ and $|j_{\text{eff}}=3/2, m_j=-1/2\rangle$.

As a result, the Kohn-Sham band structure of *undistorted* Sr_2IrO_4 with the spin-orbit coupling seems to be explained by a tight-binding approach in which only iridium sites are considered and with on-site atomic levels described by the local basis made of the states $d_{3z^2-r^2}$ $d_{x^2-y^2}$ $j_{\text{eff}}=1/2$ and $j_{\text{eff}}=3/2$. At the beginning of this study, it was highlighted that each band is twice degenerated. Whereas for $d_{3z^2-r^2}$ and $d_{x^2-y^2}$ the spin is still a good quantum number, this degeneracy can be associated to the m_j number associated to $j_{\text{eff}}=1/2$ states – $m_j=\pm1/2$ – and $j_{\text{eff}}=3/2$ states – $m_j=\pm1/2$ and $m_j=\pm3/2$.

To confirm the validity of our approach, the magnitude of each character along the Kohn-Sham band structure is plotted in figures 5.13 and 5.14. Whereas the $j_{\text{eff}}=1/2$ state is mainly associated to only one band (the "upper" t_{2g} band), the two $j_{\text{eff}}=3/2$ states are mixed along the two other bands. Moreover close to the Γ point, the $j_{\text{eff}}=1/2$ and the $j_{\text{eff}}=3/2$ $|m_j|=1/2$ characters are mixed. This mixing of several characters along each band was not expected since the local basis is orthonormal and diagonalizes the density matrix. That is why we assume that these mixings might come from some numerical errors: the subprogram we use to plot thes characters indeed performs a point integration instead of the integration based on the tetragonal weight as in dmftproj. This might introduce some hybridization between the local states. A more detailed study must be carried out to confirm this idea.

Consequently, in a first approach, we will consider that a one-to-one correspondence between the bands and the $j_{\text{eff}}=1/2$ and $j_{\text{eff}}=3/2$ states is possible:

- The "upper" t_{2g} band (in light green on the left picture of figure 5.13) which crosses the Fermi level can be understood as the "$j_{\text{eff}}=1/2$ *band*".

[7] We remind to the reader the following numerical values: $\sqrt{1/6}$ ≈0.40824, $\sqrt{1/3}$ ≈0.57735, $\sqrt{1/2}$ ≈0.70710 and $\sqrt{2/3}$ ≈0.81649.

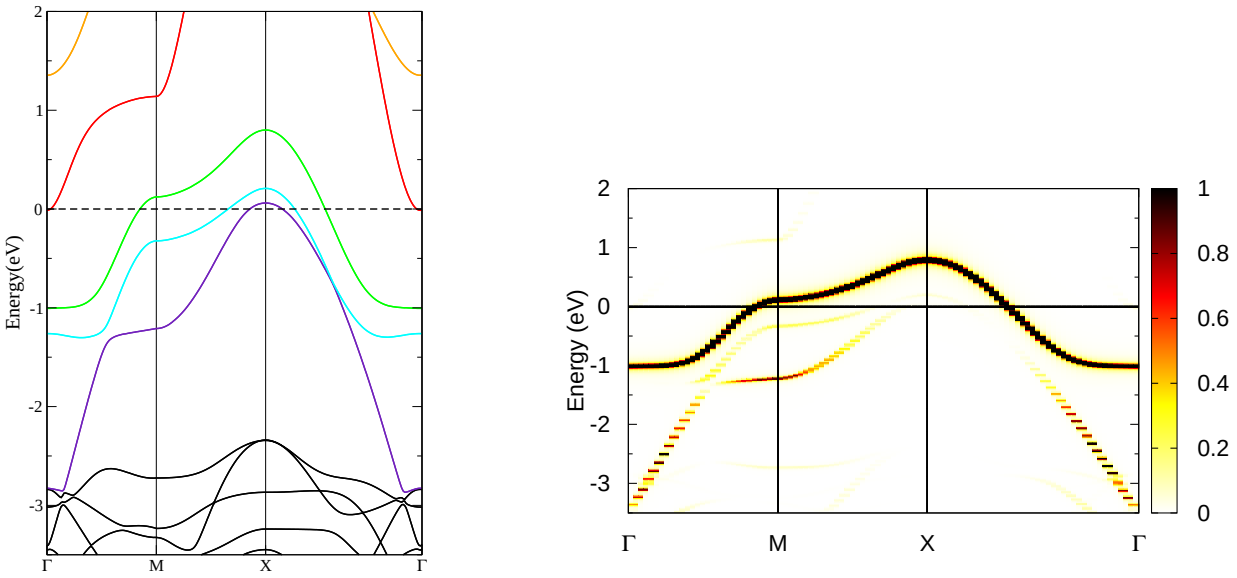

Figure 5.13: Magnitude of the Wannier character named $j_{\text{eff}} = 1/2$ along the bands in the energy window $[-3.5; 2]$ eV. The scale in renormalized arbitrary unit gives the weight of the Wannier character in the band. The band structure of *undistorted* Sr_2IrO_4 with the spin-orbit coupling is reminded on the left picture.

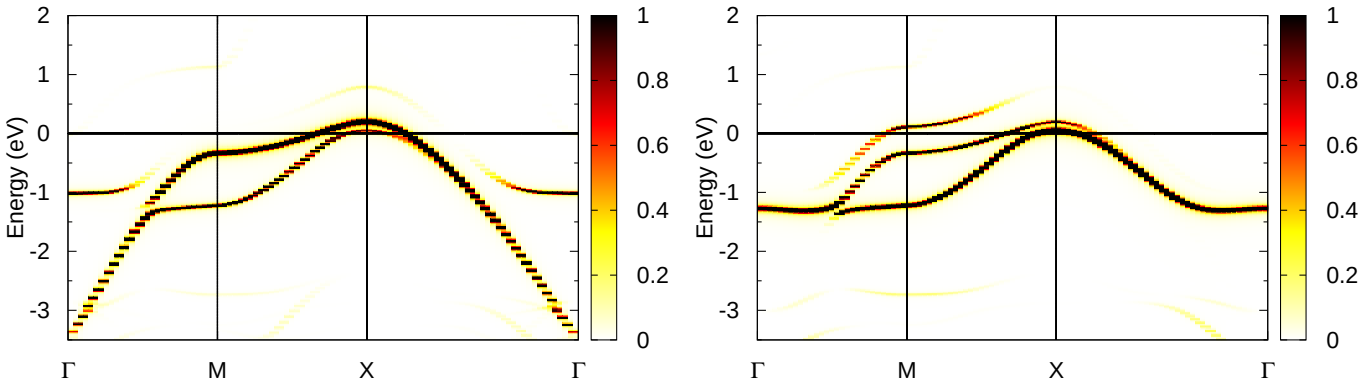

Figure 5.14: Same as the right picture above. Left picture corresponds to the character $j_{\text{eff}} = 3/2$ $|m_j| = 1/2$, right picture to the character $j_{\text{eff}} = 3/2$ $|m_j| = 3/2$

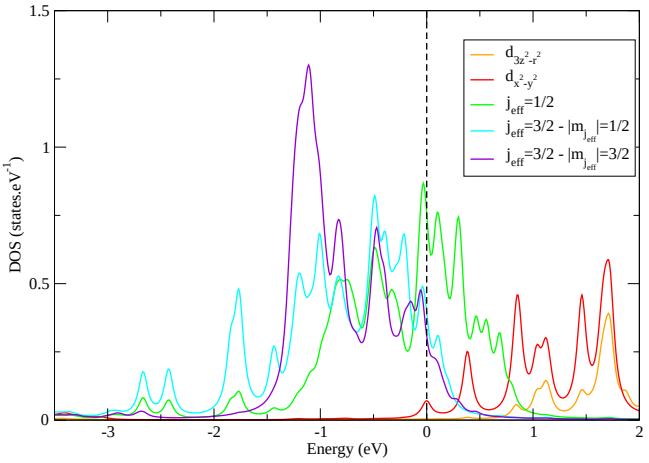

Wannier orbital	Charge
$d_{3z^2-r^2}$	0.010
$d_{x^2-y^2}$	0.030
$j_{\text{eff}} = 1/2$	1.147
$j_{\text{eff}} = 3/2$ $\lvert m_j\rvert = 1/2$	1.820
$j_{\text{eff}} = 3/2$ $\lvert m_j\rvert = 3/2$	1.826

Figure 5.15: Partial DOS associated to each Wannier character for Sr_2IrO_4 in the *undistorted* symmetry with spin-orbit coupling. The table on the right presents the charge repartition between the Wannier states.

- the "middle" t_{2g} band (in light blue) is associated to the $j_{\text{eff}} = 3/2$ $|m_j| = 3/2$ state.

- the "lower" t_{2g} band (in purple) can be understood as the "$j_{eff} = 3/2$ $|m_j| = 1/2$ *band*".

The filling of each band can thus be deduced from the integration of the DOS of the corresponding Wannier states up to the Fermi level. The partial DOS associated to each Wannier orbital is displayed on the left part of figure 5.15 and the corresponding table presents the results of the integration: the $j_{\text{eff}} = 1/2$ band is a little more than half-filled, whereas the two $j_{\text{eff}} = 3/2$ bands are almost filled and moreover equally filled.

To conclude, this study has highlighted that the band structure of *undistorted* Sr_2IrO_4 with the spin-orbit coupling can be easily understood if the $j_{\text{eff}} = 1/2$ and $j_{\text{eff}} = 3/2$ states local basis is used: the $j_{\text{eff}} = 1/2$ band is then confined almost alone close to the Fermi level and is almost half-filled, whereas the $j_{\text{eff}} = 3/2$ are almost completely filled.

This new distribution of the bands will change also drastically the influence of the correlations on the system. In a LDA+DMFT calculation, it is expected that the $j_{\text{eff}} = 3/2$ bands will be firstly completely full, reducing then the problem to the metal-insulator transition of one half-filled band. The effective dimensionality of the system is then reduced, which eases a lot the impact of the correlations.

However, the bandwidth of the $j_{\text{eff}} = 1/2$ band is of about 1.8 eV, which implies that the critical value for the Coulomb repulsion parameter U would lie between 2.2 and 2.7 eV in a pure one-band model. Since some charge redistribution between the $j_{\text{eff}} = 1/2$ and $j_{\text{eff}} = 3/2$ bands is expected, these values must be increased again. A Coulomb parameter U of 2 eV maximum will thus lead to a correlated metallic state only, although the metal-insulator transition is not so far. As a result, the spin-orbit coupling helps to reinforce the power of the electronic correlations by reducing the effective dimensionality of the problem and we will see in the following that the distortions will enhance even more this phenomenon.

5.1.3 Case 3: Modifications in the electronic band structure induced by the distortions

Structural properties

As we have already explained, according to X-ray and neutron diffraction studies [41, 72, 88, 135, 156], Sr_2IrO_4 is assigned the tetragonal $I4_1/acd$ space group. It corresponds to the symmetry of a K_2NiF_4-type compound in which the corner-shared octahedra are not well-aligned along the crystallographic direction **a** and **b**, but are alternately rotated clockwise and anticlockwise around the **c**-axis by about 11°. The corresponding space-group is usually called $I4_1/acd$ but for the sake of simplicity, we will refer to it as the "*distorted*" symmetry in the following. It results in the formation of a superstructure of size $\sqrt{2}a_t \times \sqrt{2}a_t \times 2c_t$ – where a_t and c_t are the parameter of the corresponding tetragonal K_2NiF_4 structure – and which contains four formula units.

The conventional representation of the unit cell of Sr_2IrO_4 in this *distorted* symmetry is depicted in figure 5.16. The compound is still a stacking of Ir-O_2 and Sr-O planes. The lattice constants we used were: $a = 5.497$ Å ($a_t = 3.887$ Å) and $c = 25.798$ Å ($c_t = 12.899$ Å) (taken from the values obtained at 295 K by Crawford *et al.* [41]). In the following, the **c**-axis and the **z**-axis are the same, but the **x**-axis and **y**-axis are turned of 45° from the crystallographic directions **a** and **b**, so that they would still point to the corner of the IrO_6 octahedra if they were no distortions. The detail of the atomic positions can be found in the first column of table 5.4.

Atomic species	Position in reduced coordinates	Muffin-tin radius in Bohr radius $a_0 = 0.529$Å
Sr	(0,0.25,0.550)	2.31 a_0
Ir	(0,0.25,0.375)	1.97 a_0
O_1	(0.201,0.451,0.125)	1.75 a_0
O_2	(0,0.25,0.45475)	1.75 a_0

Table 5.4: Description of the structural parameters used for our DFT calculation on Sr_2IrO_4 in the *distorted* $I4_1/acd$ symmetry.

The distortions do not change the electronic state of each atomic species in the crystal which still are Sr^{2+}, O^{2-} and Ir^{5+}. Iridium atoms still accommodate 5 valence electrons in their $5d$ orbitals. The corner-shared IrO_6 octahedra are not well-aligned along **x** and **y** directions ($\widehat{IrO_1Ir} = 157.8°$). Moreover the octahedra are elongated along the **c** axis: Ir-O_1=1.980 Å and Ir-O_2=2.057 Å (+3.8%). It induces an additional tetragonal field, which leads to a destabilization in energy of the d_{xy} orbital in comparison to the d_{xz} and d_{yz} states. Thus the chemical picture predicts that 1 electron remains in the d_{xy} level. However, we will see that the distortions will introduce another effect which cancels this phenomenon and leads to a configuration different from this molecular picture. Be it as it may, the 5 valence electrons will thus occupy the three degenerate t_{2g} orbitals (d_{xy}, d_{xz} and d_{yz}) and the two degenerate e_g orbitals ($d_{3z^2-r^2}$ and $d_{x^2-y^2}$), with higher local energy, will be empty. From this result, the band theory predicts a metallic description for *distorted* Sr_2IrO_4.

Technicalities of the DFT calculation

We have performed our DFT calculation on this *distorted* description of Sr_2IrO_4 with the same parameters as for the *undistorted* case: $R_{MT}.K_{max} = 7, l_{max} = 10$ and $l_{ns,max} = 4$. The local density approximation (LDA) was used for the treatment of the exchange-correlation term, and the irreducible Brillouin zone was sampled with 99 **k**-points (using a tetrahedral mesh).

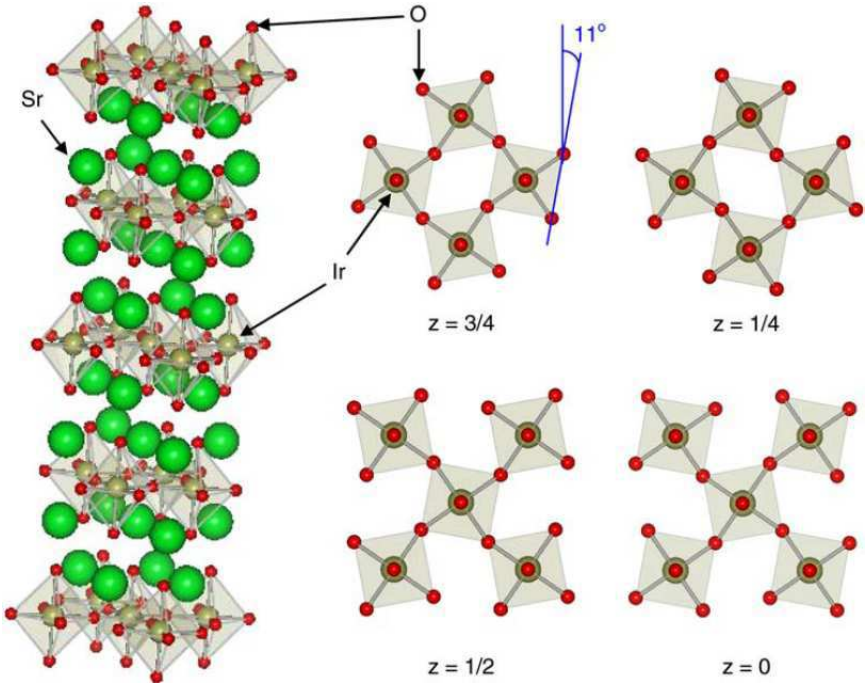

Figure 5.16: Conventional unit cell of Sr_2IrO_4 in the "*distorted*" structure ($I4_1/acd$ symmetry). The green spheres stand for the strontium ions (Sr), the golden ones for Iridium (Ir) and the red ones for Oxygen (O). The corner-shared IrO_6 octahedra are alternately rotated clockwise and anticlockwise around the **c**-axis by about 11°. From [88]

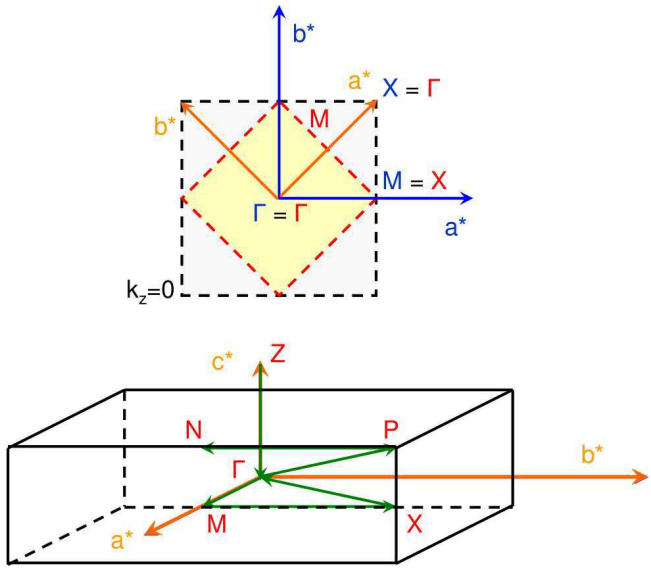

Figure 5.17: Conventional Brillouin zone for Sr_2IrO_4 in the *distorted* symmetry. The high symmetry points are $\Gamma(0,0,0)$, $Z(0,0,1)$, $M(0.5,0,0)$, $X(0.5,0.5,0)$, $P(0.5,0.5,0.5)$ and $N(0.5,0,0.5)$. The green arrows depict the **k**-path which will be used to represent the electronic band structure in the following. The upper part depicts the correspondence between the *distorted* Brillouin zone (in red with orange axes) and the *undistorted* Brillouin zone (in black with blue axes).

The muffin-tin radii chosen for each atomic species are presented in the second column of table 5.4. They are different from the previously used values of table 5.1 because the lattice parameters (a_t and c_t) are not exactly the same as those of the *undistorted* structure studied in the previous sections. This will create some little changes in the calculation of the partial DOS or in the bandwidth of the bands, but the main physical phenomena will not depend on this.

The energy threshold was set at -7.5 Ry. The categorization of the electronic states of each atomic species described in table 5.2 still holds. The total semi-core and valence states considered during the calculation was then of 46+29=75 electrons times 4 – because there are now 4 formula units in the unit cell–, that is to say 300 electrons.

The Kohn-Sham band structure was plotted along the **k**-path depicted in figure 5.17. In fact, the conventional Brillouin zone for the *distorted* structure has the same shape than the *undistorted* one but since the unit cell was quadrupled in the *distorted* symmetry, the Brillouin zone is in fact four times smaller than previously. It is however possible to find a correspondence between these two Brillouin zones, as depicted on figure 5.17. For instance in the $k_z = 0$ plane, because of the $\sqrt{2}\times\sqrt{2}$ superlattice:

- the X and Γ points of the *undistorted* Brillouin zone become equivalent in the *distorted* symmetry,
- the M point of the *undistorted* Brillouin zone corresponds to the X point of the *distorted* Brillouin zone,
- the M point of the *distorted* Brillouin zone is located in the middle of the segment $[\Gamma X]$ of the *undistorted* Brillouin zone.

These relations will enable us to compare more easily the Kohn-Sham band structure obtained for *distorted* Sr_2IrO_4 with its *undistorted* counterpart, and thus to shed the light on the effects induced by the structural distortions.

Kohn-Sham band structure of *distorted* Sr_2IrO_4

As expected, our LDA calculation without spin-orbit coupling predicts a metallic nature for Sr_2IrO_4 in the *distorted* symmetry. As observed on figure 5.18, the total DOS has indeed a finite value at the Fermi level but a separation in energy is obvious between 0.4 and 1.3 eV. The set of bands spreads less low in energy. However the same coarse band ordering can be found when a study relying on a tight binding approach is performed:

- Between -8.5 eV and about -4.5 eV, lie the *oxygen bands* which come from the bonding e_g (σ) and t_{2g} (π) molecular orbital between the Ir $5d$ and the O $2p$ states and have mostly an O $2p$ character.
- Between -4.5 eV and -2 eV, one finds the *oxygen bands* which come from the non-bonding oxygen molecular orbitals.
- From -2 eV, lie the e_g and t_{2g} *bands*.

In the following, we will again focus our attention to the e_g and t_{2g} *bands* only, since they still dominate the physical properties of the material.

In the Kohn-Sham band structure depicted on figure 5.19, the number of bands is four times bigger than in the previous *undistorted* case, because there are now four formula units in the unit cell. As a result, 12 t_{2g} bands can be counted (4 blue and 8 green) between -2 and 0.4 eV. Up to 6 bands cross the Fermi level: on the $[\Gamma M]$ segment, four green bands and two blue bands cross indeed it.

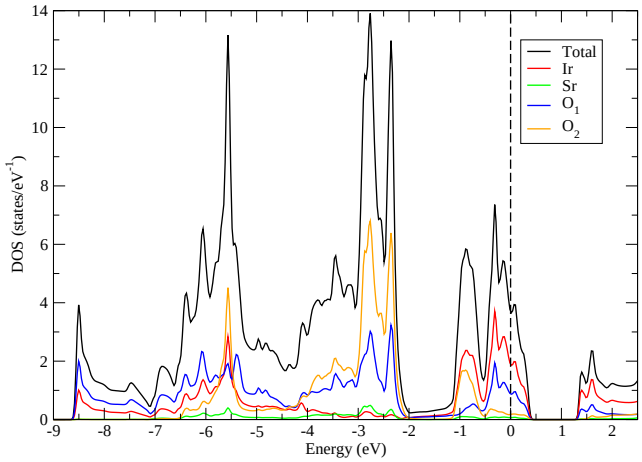

Figure 5.18: Total and partial DOS of Sr_2IrO_4 in the *distorted* symmetry without spin-orbit coupling. The Fermi level is materialized by the dotted vertical line. Each curve was divided by four (thus describing only one formula unit) in order to ease the comparison with the *undistorted* case.

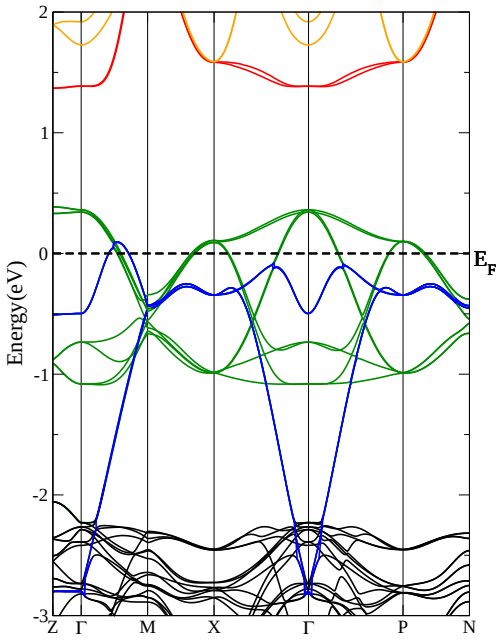

Figure 5.19: Kohn-Sham band structure of Sr_2IrO_4 in the *distorted* symmetry without the spin-orbit coupling. The e_g bands ($d_{3z^2-r^2}$ in yellow and $d_{x^2-y^2}$ in red) are well-separated from the t_{2g} bands (in blue and green on the figure). The size of the unit cell was quadrupled, implying a multiplication by 4 of the number of bands in comparison with the *undistorted* case. There is a mirror effect for the d_{xz} and d_{yz} bands.

The partial DOS associated to the Ir $5d$ characters are depicted on figure 5.20. The separation in energy lies between a lower set of bands whose characters are essentially of t_{2g}-type and an upper set of bands whose characters are mainly of e_g-type. By plotting the Ir $5d$ character along the Kohn-Sham band structure, the green and yellow bands in figure 5.19 has a pure character: d_{xz} and d_{yz} for the former and $d_{3z^2-r^2}$ for the latter. On the contrary, d_{xy} and $d_{x^2-y^2}$ characters are mixed along the blue and red bands. However, the d_{xy} contribution is more important along the blue one and $d_{x^2-y^2}$ character is the most present along the red one. The structure of the partial DOS associated to these states in figure 5.20 confirms also this picture. As a result, we will refer to the blue (red) band as the "d_{xy} *band*" ("$d_{x^2-y^2}$ *band*" respectively) in the following.

In order to compare the Kohn-Sham band structures of *undistorted* and *distorted* Sr_2IrO_4, a similar supercell of size $\sqrt{2}a \times \sqrt{2}a \times 2c$ was constructed for *undistorted* Sr_2IrO_4 and the corresponding Kohn-Sham band structure is depicted in figure 5.21-(b) along the same **k**-path we used for the *distorted* case. The correspondence between the *undistorted* and the *distorted* Brillouin zones was explained previously and enables to understand how the figure 5.21-(b) can be obtained from figure 5.8:

- By "*folding along M*" in figure 5.8, the bands along the $[\Gamma\ M]$ segment and those along the $[M\ X]$ segment are superimposed, which gives the band structure observed along the $[\Gamma\ X]$ segment in figure 5.21-(b).
- Similarly, by "*folding along the middle of the* $[\Gamma\ X]$ *segment*" in figure 5.8, the Kohn-Sham band structure observed along the $[\Gamma\ M]$ segment in figure 5.21-b is found.
- Each band of the obtained band structures must of course be "*twice drawn*" to take into account the doubling of the size along the **c**-axis in the supercell.

As a result, the folding of the bands result in a "*mirror effect*" for the d_{xz} and d_{yz} (green) bands and the d_{xy} (blue) band. Moreover, the $d_{x^2-y^2}$ (red) bands has now an overlap with the t_{2g} bands, as it can be seen at the Γ point of figure 5.21-(b). When the distortions are taken into account, the symmetry of the system is lowered and the d_{xy} and $d_{x^2-y^2}$ bands are no longer orthogonal. The hybridization between the two leads then to the formation of a gap between a bonding and an antibonding bands, which corresponds actually to the red and the blue bands observed on figure 5.21-(a). The same phenomenon does not occur between the $d_{x^2-y^2}$ band and the d_{xz}, d_{yz} bands because their orthogonality is preserved despite the distortions. As a result, the d_{xz}, d_{yz} and $d_{3z^2-r^2}$ bands are not affected much by the distortions, as shown by comparing figures 5.21-(a) and (b).

By comparing the two pictures, a narrowing of the d_{xz} and d_{yz} bands can be also noticed (from $[-1.35; 0.27]$ eV to $[-1.09; 0.36]$ eV). Because of the rotations of the IrO_6 octahedra, the hopping between Ir and O_1 sites decreases, which leads to this reduction of the bandwidth. However, this effect is strongly increased between figures 5.21-(a) and (b) because of a small default in our modelization[8]. The bandwidth of the d_{xz} and d_{yz} bands measured in figure 5.8 is indeed $[-1.11; 0.39]$ eV. The reduction of the bandwidth due to the distortions is thus more of an order of a few percent.

By creating the bonding and the antibonding bands with the $d_{x^2-y^2}$ band, the d_{xy} *band* was effectively pushed lower in energy and thus more filled. By calculating the charge associated to the Ir $5d$ states – obtained by integrating the corresponding partial DOS up to the Fermi level – in table 5.5, this effect appears clearly: whereas in table 5.3, the d_{xy} state has slightly less charge than the d_{xz} and d_{yz} states, the former is now more filled than the latter, although the elongation of the IrO_6 octahedra along the **c**-axis is more pronounced in the *undistorted* structure we used.

[8] While creating the *undistorted* supercell, we have reduced the size of the IrO_6 octahedra by accident. The hybridization between Ir and O_1 was then overestimated during the calculation, hence the wider bands.

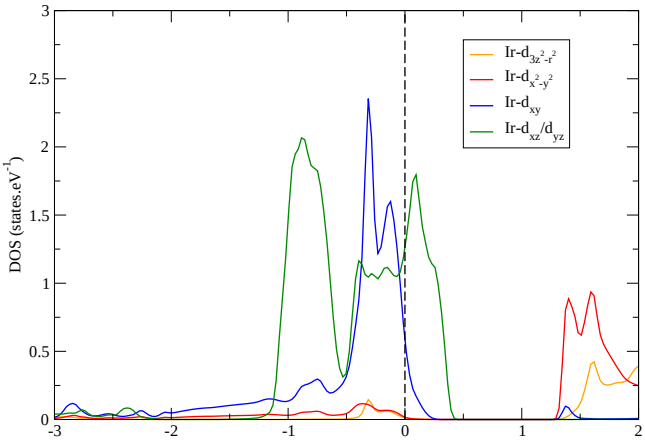

Figure 5.20: Partial DOS of the Iridium e_g and t_{2g} characters for Sr_2IrO_4 in the "*undistorted*" symmetry without spin-orbit coupling. The energy are given with respect to the Fermi level, materialized by the dotted vertical line.

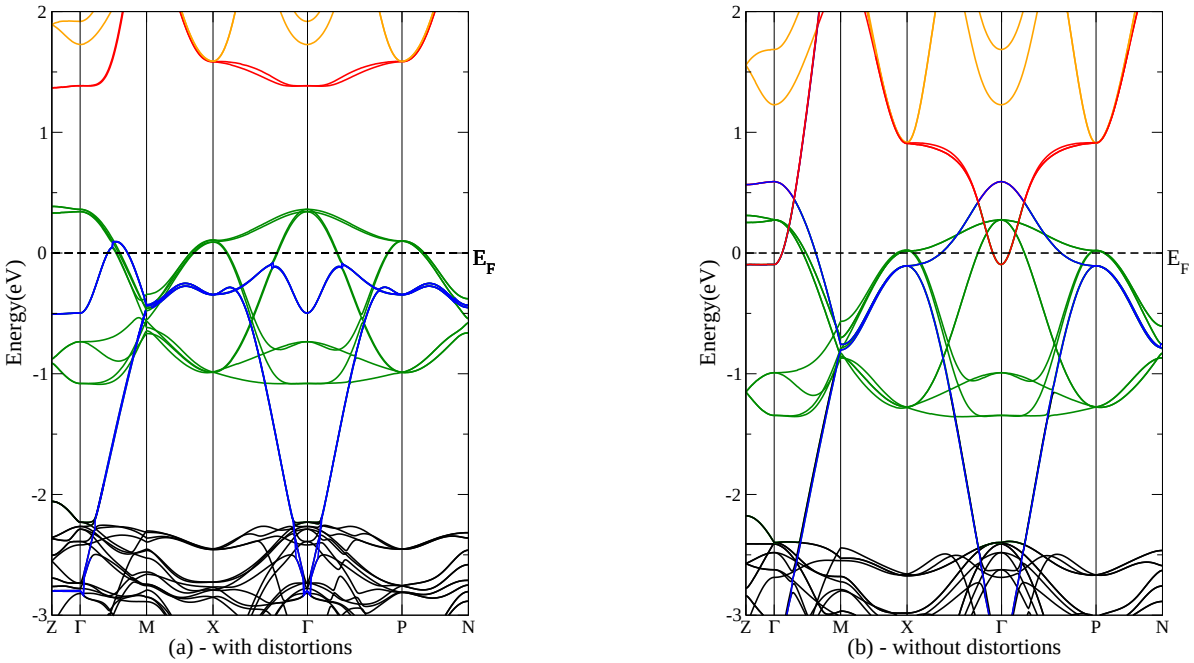

Figure 5.21: Comparison of the Kohn-Sham band structures between *distorted* Sr_2IrO_4 (panel a) and *undistorted* Sr_2IrO_4 (panel b) without the spin-orbit coupling. Both band structures are represented along the same **k**-path (in the *distorted* $I4_1/acd$ symmetry). The hybridization between the $d_{x^2-y^2}$ and d_{xy} bands (in red and blue respectively) leads to a the formation of the energy gap between 0.4 eV and 1.3 eV.

Construction of a localized e_g-t_{2g} basis set Wannier-type basis set for *distorted* Sr_2IrO_4

In order to get a better idea of the filling of the t_{2g} *bands*, the Wannier orbitals associated to these bands have been calculated. We have built the Wannier projectors from the cubic basis in the energy window $[-2.8; 0.4]$ eV. The e_g states were omitted on purpose in our approach, since their charge is almost zero in the considered energy range. The hybridization between d_{xy} and $d_{x^2-y^2}$ bands were considered also small enough to be neglected (0.146 eV in the chosen energy window).

The obtained results are in good agreement with figure 5.19: the Wannier functions built from the d_{xz} and d_{yz} states indeed correspond to the green bands and the Wannier function built from the d_{xy} states describes exactly the blue band. In fact, no information in the description of the antibonding d_{xy} *band* was lost in the calculation, thanks to the orthogonalization process of the Wannier functions. The filling of each band is presented in the second column of table 5.5. The d_{xy} *band* is almost completely filled, as expected. It thus remains almost three electrons in the d_{xz} and d_{yz}bands.

Charge	calculated from the partial DOS	of the Wannier functions of the energy window $[-2.8; 0.4]$ eV
Ir 5d $d_{3z^2-r^2}$	0.027	0.027
Ir 5d $d_{x^2-y^2}$	0.096	0.097
Ir 5d d_{xy}	0.841	1.936
Ir 5d d_{xz} /d_{yz}	0.672	1.540

Table 5.5: Charge repartition between the e_g and t_{2g} atomic states (first column) and the e_g and t_{2g} bands (second column), between -2.8 eV and the Fermi level. The Wannier orbitals were obtained from a calculation based on the energy window $[-2.8; 0.4]$ eV.

To conclude, by taking into account the rotations of the IrO_6 octahedra around the **c**-axis, the description of Sr_2IrO_4 requires to use four formula units in the less symmetric unit cell. It implies that each *undistorted* band is folded four times in the obtained Kohn-Sham band structure, which introduces an hybridization between the d_{xy} and the $d_{x^2-y^2}$ bands. As a result, an antibonding and a bonding bands are formed and a gap is opened between 0.4 and 1.3 eV. Besides, the bonding band can be considered as completely filled.

The electronic correlations will thus mostly affect the d_{xz} and d_{yz} bands only. In an LDA+DMFT approach, the Hubbard model used for the calculation will reduce to two 3/4-filled bands. It is thus expected that an insulating state will be more easily reached than in the *undistorted* case since the dimensionality of the problem has decreased and also because the bandwidth of the d_{xz} and d_{yz} bands – about 1.45 eV – is much narrower than the one of the d_{xy} band in the *undistorted* case. However, with a Coulomb parameter of 2 eV maximum, it seems difficult to obtain an insulating state for this system.

5.1.4 Influence of the spin-orbit coupling and the distortions together

As we have already mentioned in the introduction, LDA calculations predict a metallic state for Sr_2IrO_4 and four bands cross the Fermi level (cf. figure 5.1). In this part, we use the previous studies – on the spin-orbit coupling and the distortions – to understand the Kohn-Sham band structure of Sr_2IrO_4 and above all explain the nature of these four bands.

To obtain the DFT description of Sr_2IrO_4, the spin-orbit corrections were introduced on the iridium atoms of the previous *distorted* structure. Since the calculation is not spin-polarized, the Kohn-Sham

band structure can be plotted along the same **k**-path (in the same Brillouin zone) as in part 5.1.3, and the correspondence between the *distorted* and the *undistorted* Brillouin zone can be used again.

The Kohn-Sham band structure of Sr_2IrO_4

The method used for the calculation suggests first to draw a comparison between the Kohn-Sham band structures of *distorted* Sr_2IrO_4 with and without spin-orbit coupling. Both of them are depicted in figure 5.22. It appears clearly that the spin-orbit corrections do not affect the e_g bands (the $d_{3z^2-r^2}$ band represented in red and the $d_{x^2-y^2}$ *band* in yellow on both pictures), whereas deep modifications occur in the set of t_{2g} bands. The comparison of the corresponding total DOS – both represented in figure 5.23 – confirms of course this conclusion. Moreover, it highlights that the energy separation between the e_g and the t_{2g} bands has a little decreased: from $[0.4; 1.3]$ eV to $[0.5; 1.27]$ eV.

Consequently, a similar approach based on the *TP-equivalence approximation* appears to be valid also in the *distorted* case. However, as explained in part 5.1.3, the red and blue bands in figure 5.22 (b), are the bonding and antibonding bands which results from the hybridization of the initial d_{xy} and $d_{x^2-y^2}$ bands and thus mix these two Ir $5d$ characters. As a result, a modified version of the *TP-equivalence approxmation* introduced in section 3.1 must be considered strictly speaking. We will call it in the following the "*distorted TP equivalence approximation*". This version must consider the two linear combinations of d_{xy} and $d_{x^2-y^2}$ respectively associated to the antibonding and the bonding states. The former will be unaffected by the spin-orbit coupling as the $d_{3z^2-r^2}$ state, and the latter will be involved in the formation of the $j_{\text{eff}} = 1/2$ and the $j_{\text{eff}} = 3/2$ states. It can therefore be expected that the corresponding $j_{\text{eff}} = 1/2$ and the $j_{\text{eff}} = 3/2$ bands will differ from the previous $j_{\text{eff}} = 1/2$ and the $j_{\text{eff}} = 3/2$ bands introduced in the *undistorted* case with spin-orbit coupling.

To better understand the impact of the distortions on the $j_{\text{eff}} = 1/2$ and $j_{\text{eff}} = 3/2$ bands, it is also possible to imagine that the distortions were introduced in the *undistorted* structure "once" the spin-orbit coupling was already included. In this case, the supercell of size $\sqrt{2}a \times \sqrt{2}a \times 2c$ can be considered again for *undistorted* Sr_2IrO_4 in order to make the comparison easier between the two band structures. The result is displayed in figure 5.24 (b). The color code used for the bands is the same as in the section 5.1.2:

- the light green bands are the $j_{\text{eff}} = 1/2$ bands and their replicas,
- the light blue bands are the $j_{\text{eff}} = 3/2$ $|m_j| = 3/2$ bands,
- the purple bands are the $j_{\text{eff}} = 3/2$ $|m_j| = 1/2$ bands.

The folding method – described in part 5.1.3 – can also be applied to understand how the figure 5.24-(b) can be obtained from the figure 5.11. The main consequence of these foldings is the overlap between the $d_{x^2-y^2}$ (red) bands and the $j_{\text{eff}} = 1/2$ and $j_{\text{eff}} = 3/2$ bands, as it can be seen at the Γ point of figure 5.24-(b). As we have explained in the previous subsection, the d_{xy} and $d_{x^2-y^2}$ bands are no longer orthogonal when the structural distortions are introduced. In a picture where the spin-orbit coupling are taken into account, this implies that both the $j_{\text{eff}} = 1/2$ and $j_{\text{eff}} = 3/2$ $|m_j| = 1/2$ bands are not orthogonal anymore with the $d_{x^2-y^2}$ bands. Therefore, the formation of bonding and antibonding bands involves now these three types of band. It is however expected that the $j_{\text{eff}} = 1/2$ and $j_{\text{eff}} = 3/2$ $|m_j| = 1/2$ states are not mixed during this process since they still are orthogonal. Moreover, the $j_{\text{eff}} = 3/2$ $|m_j| = 3/2$ band must not be modified much by the distortions.

By comparing this analysis with the electronic band structure of figure 5.24-(a), more changes have happened than expected, but the main features previously described allow us to say that:

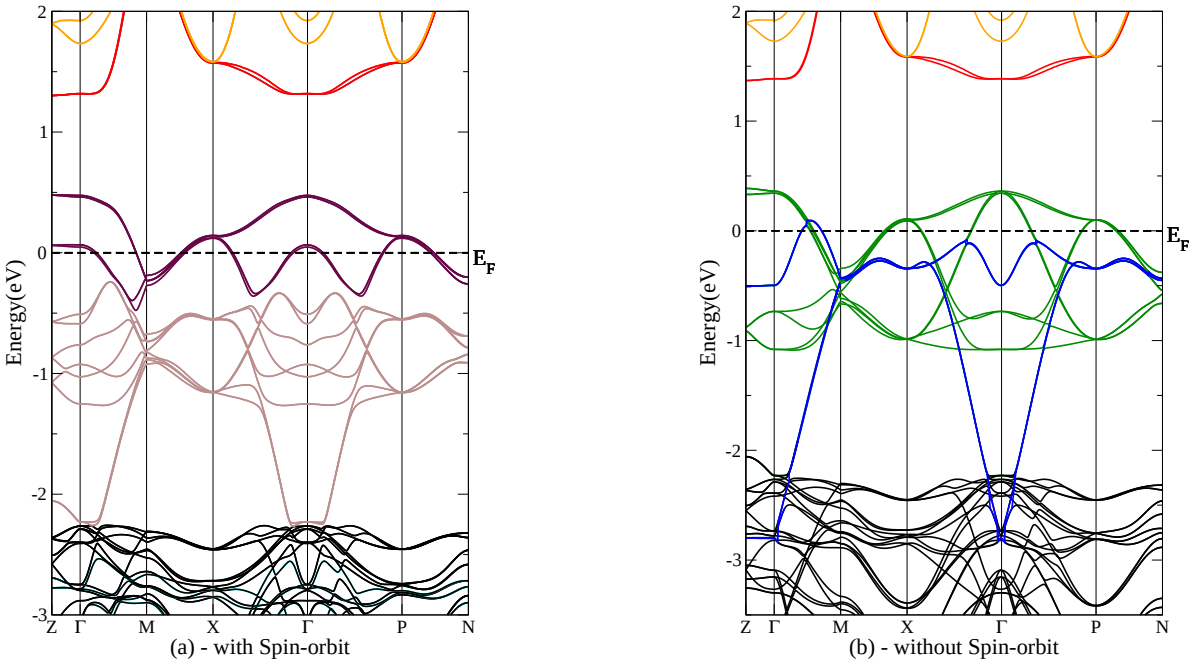

Figure 5.22: Comparison of the Kohn-Sham band structure of *distorted* Sr_2IrO_4, with (panel a) and without (panel b) the spin-orbit coupling. The $d_{3z^2-r^2}$ band (in yellow) and the $d_{x^2-y^2}$ *band* (in red) are not affected by the spin-orbit corrections. On the contrary, the t_{2g} bands are modified a lot.

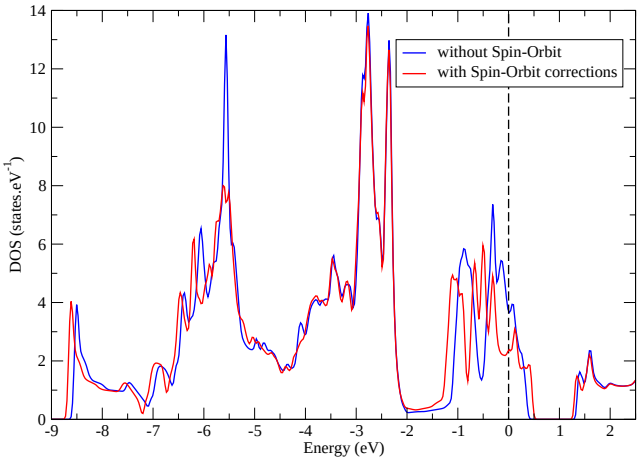

Figure 5.23: Total DOS for Sr_2IrO_4 in the *distorted* symmetry. The red curve includes the corrections induced by taking into account the spin-orbit coupling. The Fermi level is materialized by the dotted vertical line.

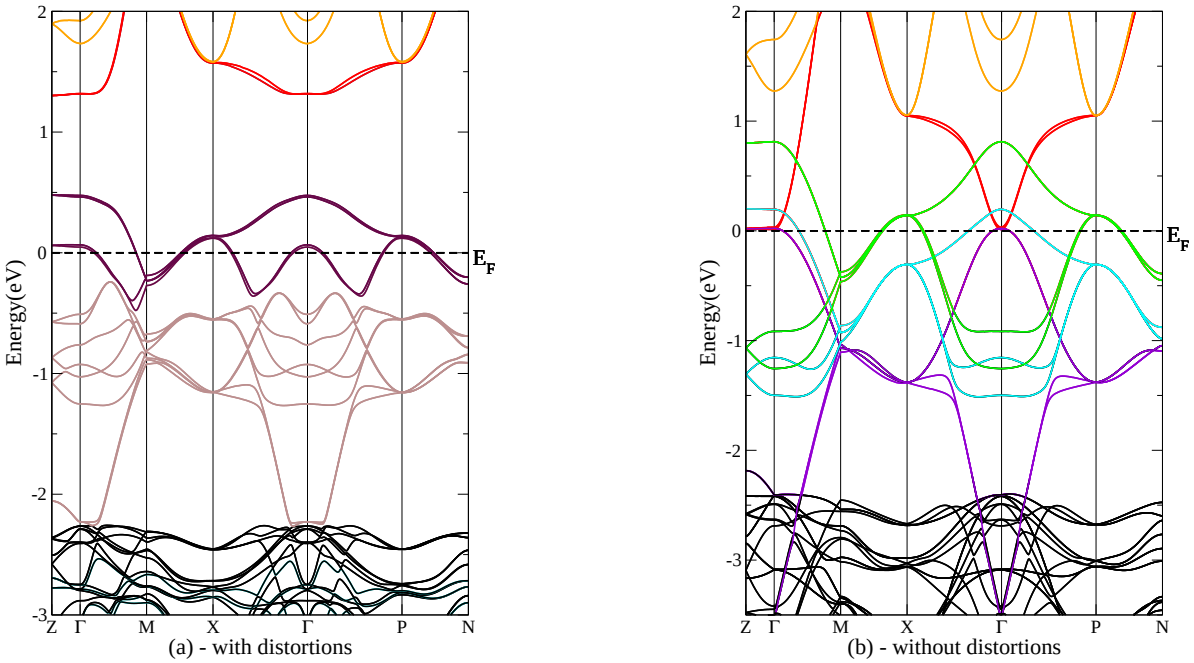

Figure 5.24: Comparison of the Kohn-Sham band structure between *distorted* Sr_2IrO_4 (panel a) and *undistorted* Sr_2IrO_4 (panel b) with the spin-orbit coupling. Both band structures are represented along the same **k**-path (in the *distorted* $I4_1/acd$ symmetry). The hybridization between the $d_{x^2-y^2}$ and d_{xy} bands (in red and blue respectively) leads to a the formation of the energy gap between 0.4 eV and 1.3 eV.

- at the Γ point, the "upper" (light brown) band must derive from the hybridization between the $d_{x^2-y^2}$ and the $j_{\text{eff}} = 3/2$ $|m_j| = 1/2$ bands.

- the four bands close to the Fermi level (in dark brown on the figure) certainly derive only from the $j_{\text{eff}} = 1/2$ and $j_{\text{eff}} = 3/2$ $|m_j| = 3/2$ bands: the upper intersection at the Γ point clearly comes from the previous $j_{\text{eff}} = 1/2$ bands, whereas the lower intersection can be understood as the one from the $j_{\text{eff}} = 3/2$ $|m_j| = 3/2$ band.

However, in order to confirm these statements, a study based on the Wannier functions was carried out. Its results are discussed in the next paragraph.

Nature of the four bands crossing the Fermi level in Sr_2IrO_4

As explained previously, the local Ir 5*d* basis which describes at best Sr_2IrO_4 must rely on a modified *TP equivalence approximation* framework, where the hybridization between the d_{xy} and the $d_{x^2-y^2}$ states induced by the structural distortions is taken into account. For the sake of simplicity, we decided to evaluate it numerically by using the same approach which was presented in part 5.1.2. We used the energy window $[-4.0; 6.8]$ eV in order to have a rather complete description of the antibonding and bonding bands which come from the d_{xy} and $d_{x^2-y^2}$ bands. The obtained basis vectors were the following:[9]

[9] Here again, we will study only half of the basis. The results are similar for the other half.

	$\|d_{3z^2-r^2}\downarrow\rangle$	$\|d_{x^2-y^2}\downarrow\rangle$	$\|d_{xy}\downarrow\rangle$	$\|d_{xz}\uparrow\rangle$	$\|d_{yz}\uparrow\rangle$
$\|\psi_1\rangle$	0.9926	0	0	0.0862	0.0862
$\|\psi_2\rangle$	0	0.9525	0.2865	0.0724	0.0724
$\|\psi_3\rangle$	0	0.18303	0.46377	0.61295	0.61295
$\|\psi_4\rangle$	0	0.24310	0.83833	0.34503	0.34503
$\|\psi_5\rangle$	0.12196	0	0	0.70183	0.70183

Table 5.6: Modulus of the coefficients of each states $(|\psi_i\rangle)_{i=1,5}$ on the cubic orbitals.

$$\begin{aligned}
|\psi_1\rangle = &\ +0.9571 + i0.2629\ |\phi_{d_{3z^2-r^2}\downarrow}\rangle \quad +0.0853 + i0.0125\ |\phi_{d_{xz}\uparrow}\rangle \quad +0.0125 - i0.0853\ |\phi_{d_{yz}\uparrow}\rangle \\
|\psi_2\rangle = &\ +0.9085 + i0.2863\ |\phi_{d_{x^2-y^2}\downarrow}\rangle \quad -0.2863 + i0.0121\ |\phi_{d_{xy}\downarrow}\rangle \\
&\qquad\qquad +0.0397 + i0.0605\ |\phi_{d_{xz}\uparrow}\rangle \quad -0.0605 + i0.0397\ |\phi_{d_{yz}\uparrow}\rangle
\end{aligned} \tag{5.5}$$

These two states have most of their weight on the e_g orbitals. On the contrary, the three others are mainly decomposed on the t_{2g} levels:

$$\begin{aligned}
|\psi_3\rangle = &\ -0.04023 + i0.17855\ |\phi_{d_{x^2-y^2}\downarrow}\rangle \quad -0.17855 + i0.42802\ |\phi_{d_{xy}\downarrow}\rangle \\
&\qquad\qquad +0.03950 - i0.61168\ |\phi_{d_{xz}\uparrow}\rangle \quad +0.61168 + i0.03950\ |\phi_{d_{yz}\uparrow}\rangle \\
|\psi_4\rangle = &\ +0.16869 - i0.17504\ |\phi_{d_{x^2-y^2}\downarrow}\rangle \quad +0.17504 - i0.81985\ |\phi_{d_{xy}\downarrow}\rangle \\
&\qquad\qquad -0.01730 - i0.34460\ |\phi_{d_{xz}\uparrow}\rangle \quad +0.34460 - i0.01730\ |\phi_{d_{yz}\uparrow}\rangle \\
|\psi_5\rangle = &\ -0.00874 + i0.12165\ |\phi_{d_{3z^2-r^2}\downarrow}\rangle \quad -0.03558 - i0.70093\ |\phi_{d_{xz}\uparrow}\rangle \quad -0.70093 + i0.03558\ |\phi_{d_{yz}\uparrow}\rangle
\end{aligned} \tag{5.6}$$

Contrary to the results obtained in part 5.1.2, the coefficients of these vectors in the cubic basis are complex – with real and imaginary parts –. In order to go further in the study, we will focus our attention on the modulus associated to each coefficient[10] and support our analysis by a comparison between the values of table 5.6 with the theoretical coefficients of the states obtained in the true *TP equivalence approximation* framework (cf. expressions (3.27) and (3.28)).

The contribution of the d_{xz} and the d_{yz} states in the vectors $|\psi_1\rangle$ and $|\psi_2\rangle$ can be easily neglected. In this case, $|\psi_1\rangle$ obviously corresponds to the $d_{3z^2-r^2}$ state and $|\psi_2\rangle$ is the linear combination of the states $d_{x^2-y^2}$ and d_{xy} with a major weight on the $d_{x^2-y^2}$ orbital. This vector can then be seen as describing the antibonding level associated to the (red) $d_{x^2-y^2}$ *band* on figure 5.22 (a).

Moreover, by neglecting the contribution of the $d_{3z^2-r^2}$ orbital in $|\psi_5\rangle$, the decomposition of this basis vector becomes really close to the state $|j_{\text{eff}} = 3/2, m_j = +3/2\rangle$ (whose coefficients are equal to $\sqrt{1/2} \approx 0.70710$). As discussed previously, no great change was expected for this level and we will then consider in the following that $|\psi_5\rangle$ describes the $|j_{\text{eff}} = \frac{3}{2}, m_j = +3/2\rangle$ state in the local basis.

The last vectors $|\psi_3\rangle$, $|\psi_4\rangle$ must then be linked to the "modified" $|j_{\text{eff}} = 1/2, m_j = -1/2\rangle$ and $|j_{\text{eff}} = 3/2, m_j = -1/2\rangle$ states, which involve the bonding linear combination between $d_{x^2-y^2}$ and d_{xy}. If we deliberately omit the coefficient before the $d_{x^2-y^2}$ orbital, the decomposition in modulus of $|\psi_3\rangle$

[10]Some works are in progress to understand whether the phase factors have a physical meaning or whether they arise from pure numerical reasons.

reminds the expression of $|j_{\text{eff}} = 1/2, m_j = -1/2\rangle$, whereas the decomposition of $|\psi_4\rangle$ seems quite close of the expression of $|j_{\text{eff}} = 3/2, m_j = 1/2\rangle$. [11] This argument tends to show that $|\psi_3\rangle$ ($|\psi_4\rangle$) can be understood as $|j_{\text{eff}} = 1/2, m_j = -12\rangle$ ($|j_{\text{eff}} = 3/2, m_j = -1/2\rangle$ respectively).

To confirm this idea, the magnitude of the Wannier characters $|\psi_3\rangle$, $|\psi_4\rangle$ and $|\psi_5\rangle$ were plotted along the Kohn-Sham band structure. The results are displayed in figures 5.25 and 5.26. As it can be seen on the right picture of figure 5.25, the upper intersection with the Γ point at 0.5 eV can be attributed to the $|\psi_3\rangle$ character. Furthermore, the two "legs" on the segment [Γ X] and [Γ M] between -1.5 and -3 eV have mostly a $|\psi_4\rangle$ character on the left picture of figure 5.26. These two features respectively belong to the $j_{\text{eff}} = 1/2$ and the $j_{\text{eff}} = 3/2$ $m_j = -1/2$ bands, as discussed previously. With this last argument, we thus state that:

- the $|\psi_3\rangle$ Wannier character is the "*modified*" $|j_{\text{eff}} = 1/2, m_j = -1/2\rangle$ of the model which described the local problem in the "*distorted TP equivalence approximation*" framework.
- the $|\psi_4\rangle$ Wannier character is the "*modified*" $|j_{\text{eff}} = 3/2, m_j = -1/2\rangle$ of the same model.

With these results in mind, the four bands crossing the Fermi level in Sr_2IrO_4 are mainly described by the "*modified*" $j_{\text{eff}} = 1/2$ states but also by the $j_{\text{eff}} = 3/2$ $|m_j| = 3/2$ states, as expected from our previous discussion. The intersection with the Γ point at 0.05 eV is doubtless of character $|\psi_5\rangle$.

However, the energy window we used to find this local basis and the corresponding Wannier functions is obviously too large. Consequently, the basis is too localized in the real space and that is why the bands mixes several character along the considered **k**-path. A new calculation with a smaller energy-range – which typically contains only the four bands crossing the Fermi level – must be performed to find the Wannier functions associated to them. It is strongly expected that only one Wannier character is necessary to describe them: these four bands can indeed be seen as the foldings of only one band whose character is a linear combination of the "*modified*" $j_{\text{eff}} = 1/2$ and the $j_{\text{eff}} = 3/2$ $|m_j| = 3/2$ states. Nevertheless, this requires to improve the method used to find the local basis on which the Wannier functions are built. This work is still currently in progress but this study already shows that the four band crossing the Fermi level cannot be understood as "*pure* $j_{\text{eff}} = 1/2$ *states*", contrary to what is commonly taught in the literature [84].

Although the true Wannier function which describes these four bands is not known yet, it is possible to anticipate the effect of the electronic correlations in Sr_2IrO_4. The four bands close to the Fermi level are indeed the foldings of a band whose width can be estimated as about 1 eV. Moreover, this band is half-filled as can be confirmed by integrating the total DOS between the Fermi level and -0.5 eV. Consequently, in an LDA+DMFT framework, Sr_2IrO_4 can be fully described by a half-filled one-band Hubbard model. The critical value for the Coulomb parameter U is then expected to be between 1.25 and 1.5 eV. The metal-insulator transition will appear already at moderate values of the Coulomb repulsion $U \sim 2$ eV.

Conclusion of this density functional study

In conclusion, the spin-orbit coupling and the distortions in Sr_2IrO_4 both induce complementary effects in the electronic band structure of Sr_2IrO_4. Whereas the former modifies strongly the distribution of the t_{2g} bands so that almost one band remains close to the Fermi level – the "$j_{\text{eff}} = 1/2$ band" – , the latter induces an hybridization between the d_{xy} and the $d_{x^2-y^2}$ band which leads to a separation

[11] We remind again to the reader the following numerical values: $\sqrt{1/6} \approx 0.40824$, $\sqrt{1/3} \approx 0.57735$ and $\sqrt{2/3} \approx 0.81649$.

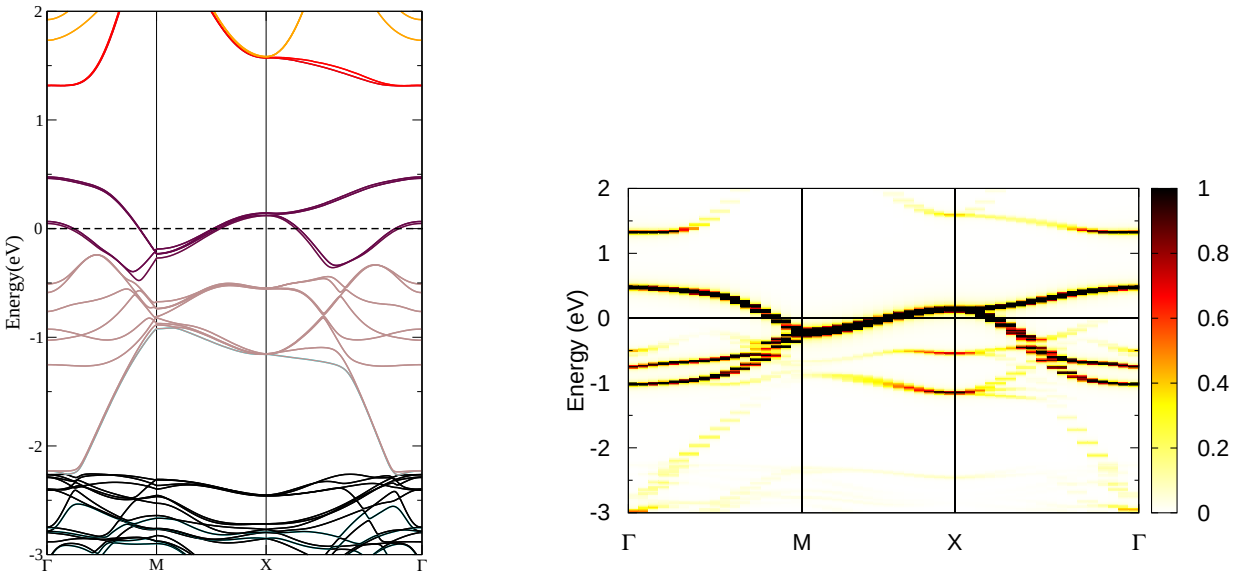

Figure 5.25: Magnitude of the Wannier character $|\psi_3\rangle$ along the Kohn-Sham band structure of Sr_2IrO_4 in the energy window $[-3; 2]$ eV. The scale in renormalized arbitrary unit gives the weight of the Wannier character in the band. This Wannier character can be associated to the "*modified*" $j_{\text{eff}} = 1/2$ state. The band structure of Sr_2IrO_4– with distortions and the spin-orbit coupling – is reminded on the left picture.

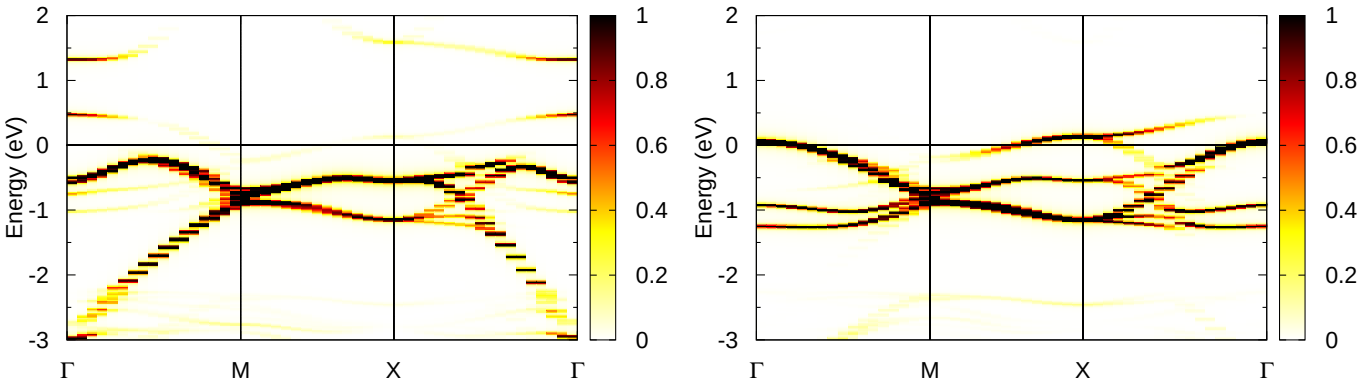

Figure 5.26: Same as the right picture above for the Wannier characters $|\psi_4\rangle$ (left picture) and $|\psi_5\rangle$ (right picture). While $|\psi_4\rangle$ can be considered as the "*modified*" $j_{\text{eff}} = 3/2$ $m_j = -1/2$ character, the character $j_{\text{eff}} = 3/2$ $m_j = +3/2$ can be associated to $|\psi_5\rangle$.

in energy between e_g and t_{2g} bands and to an orbital polarization – the bonding "*dxy* band" becomes completely filled –.

These two effects alone are not efficient enough to reach a Mott insulating state, when the electronic correlations are also taken into account. However, when these two phenomena are applied together – like in the *realistic* compound Sr_2IrO_4 –, they enable to isolate one band – or more precisely, four bands because of the foldings – close to the Fermi level whose bandwidth is about 1 eV. A Mott insulating state then emerges due to electronic correlations: Sr_2IrO_4 can thus be understood as a Mott insulator, driven by the joint effort of the spin-orbit interaction and the distortions.

To confirm this picture and quantify more precisely the help given by the spin-orbit coupling and the distortions to the electronic correlations, an LDA+DMFT calculation was carried out in each of the four cases we have previously studied. The results are presented and discussed in the following section.

5.2 Influence of the spin-orbit coupling and the distortions on electronic correlations: LDA+DMFT study

In the previous section on LDA calculations, we have already highlighted the effect of the spin-orbit coupling and the structural distortions on the Kohn-Sham band structure of Sr_2IrO_4. These effects give us some ideas on how the spin-orbit coupling and the distortions will make the electronic correlations more efficient, but so far we did not quantify this. In this part, we determine the impact of electronic correlations by performing LDA+DMFT calculations for all the cases shown in the schematic plot 5.2. Doing the calculations separately for spin-orbit coupling and distortions, similar to the previous section, we can distinguish clearly between their influence, and in a final step, we analyze the correlations for the realistic situation, where both spin-orbit and distortions are present.

When performing DMFT calculations, a problem that arises is the proper determination of the interaction parameters: the Coulomb intra-orbital repulsion U, the Coulomb inter-orbital repulsion U' and Hund's rule exchange coupling J (cf. equation (1.36)). So far, there is no estimate from theory for these parameters – which could in principle be done within constrained-RPA or similar methods – that is why we have chosen to use U and J as parameters, assuming that a lattice model restricted only to t_{2g} orbitals still holds for all the considered cases.

In the following, we thus perform LDA+DMFT calculations for several values of the parameter U, ranging from about 1 eV to 6 eV, in order to study the metal-insulator transition. By doing this, we are able to get some information on the critical U, when the transition occurs. This is a way to "quantify" the efficiency of spin-orbit coupling and distortions to drive the system into an insulating state. Moreover, we can analyze in details, how the transition occurs. In particular, we are interested in how the orbital polarization, the degeneracy of the atomic multiplet, or the narrowing of the effective bandwidth influence the metal-insulator transition, and how these properties change with spin-orbit coupling and the presence of distortions.

With this idea in mind, our purpose will be to treat all the cases introduced in the previous section (undistorted without spin-orbit coupling, distorted without spin-orbit coupling, undistorted with spin-orbit coupling, distorted with spin-orbit coupling) at roughly the same conditions, and to look for the critical value of U. Remember that the goal is to find a situation, where a realistic value of $U \approx 2$ eV is sufficient to get an insulating state. As for all multiband systems, the Hund's rule exchange J must not be neglected (cf. equation (1.37)). For a $5d$ transition metal oxide, it is expected that J is not larger than 0.2 eV. That is why we fix J to this value, keeping only U as a parameter. This is

also justified because J is not affected too much by electronic screening, so the material dependence of this parameter should be weak. To speed up the calculations, we do calculations using density-density interactions only, and neglect off-diagonal components of the interaction matrix like spin-flip and pair-hopping terms. Moreover, all calculations in this section have been done at room temperature T=300 K (which corresponds to $\beta = 1/k_B T = 40$ eV^{-1}).

5.2.1 Case 1: "*Undistorted*" Sr_2IrO_4 without spin-orbit coupling

General description of the metal-insulator transition

In part 5.1.1, the LDA study of *undistorted* Sr_2IrO_4 has shown that this idealized compound can be described as a simple t_{2g} system. Within this picture, the three t_{2g} bands of the system accommodate 5 electrons (by formula unit) and the two e_g bands are considered as completely empty. This approximation relies on the two following arguments:

- The charge of the two e_g bands is negligible (less than 0.02 electrons according to table 5.3) in comparison to the charge of the t_{2g} bands.
- Electronic correlations will push the e_g bands up and leave them completely empty. Since their bottom is close the the Fermi level, even a small Coulomb repulsion parameter U will be sufficient.

In order to justify these assumptions, we also performed calculations for the full five-band model, including both t_{2g} and e_g states, and the validity of above arguments was indeed confirmed.

In the following, we use only the t_{2g} bands to build the local Hamiltonian of our problem. A technical reason for this simplification is that reducing the number of orbitals from 5 to 3 makes the calculations one order of magnitude faster, since the dimensionality of the local problem scales exponentially with the number of orbitals. In order to carry out the LDA+DMFT calculations, we use the *standard* implementation of LDA+DMFT within the FP-LAPW framework of Aichhorn *et al.* [1], which was described in chapter 2. Moreover, since the spin-orbit coupling is not included, the corresponding impurity problem can be solved by the CTQMC method without any problems. As explained in section 3.4, an analytical continuation is needed in order to obtain results on the real-frequency axis. The details to finally get the lattice spectral function have been presented in section 3.4.

Since only the t_{2g} bands are considered, the Wannier functions were constructed from the energy window $[-3.5; 0.6]$ eV, as introduced in part 5.1.1. According to their charge given in table 5.3, the total charge of the impurity model is 5.004 electrons. Moreover, since there is no hybridization term between the Wannier functions, the CTQMC calculation is free of any sign-problem. We carried out LDA+DMFT calculations for this system for Coulomb repulsion U ranging from 2 to 6 eV.

The total spectral density obtained for U=2, 3, 3.8 and 4 eV are shown in figure 5.27. In all the plots that will be shown in the remainder of this thesis, the Fermi level is set to 0 eV. Our calculations show that the metal-insulator transition occurs between 3.8 and 4.0 eV. This value confirms that *undistorted* Sr_2IrO_4 would be a rather *weak correlated metal* for a realistic value of U of the order of 2 eV. In the present case, a Coulomb parameter of slightly below 4 eV is necessary to reproduce the measured gap of about 0.3 eV.

An insulating state with 2 bands 3/4-filled

To go further in the understanding of this metal-insulator transition, the spectral density obtained for the different orbitals are depicted in figures 5.28 and 5.29. Since the orbital d_{xz} and d_{yz} are degenerate, only the results for the d_{xy} and the d_{xz} Wannier functions are plotted. The left panels of

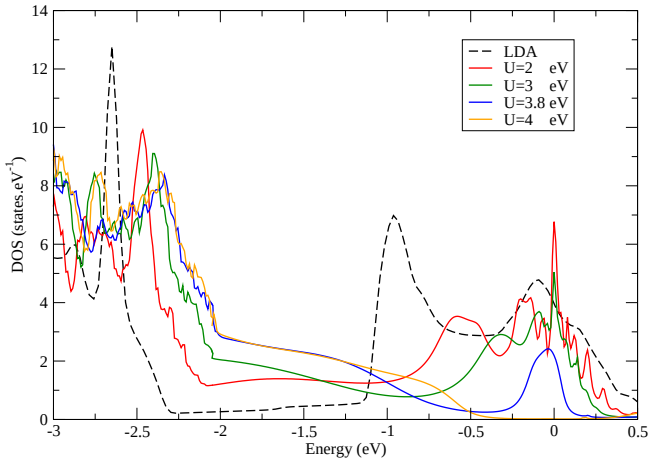

Figure 5.27: Total LDA+DMFT spectral functions of *undistorted* Sr_2IrO_4 without spin-orbit coupling for U=2, 3, 3.8 and 4 eV. The LDA DOS is shown as dashed line, and the Fermi level is set to 0 eV.

figures 5.28 and 5.29 show the spectral function in the metallic regime (U$\leq$ 3.8 eV), whereas the right panels display the results in the insulating regime. Both orbitals (d_{xy} and d_{xz}) undergo their metal-insulator transition simultaneously – between 3.8 eV and 4.0 eV.

On the left panels, the well-known *three-peak structure* can be easily recognized: the quasi-particle peak is located close to the Fermi level, surrounded by the incoherent part of the spectrum which corresponds to the two Hubbard bands. As the value of the Coulomb parameter U increases, the quasi-particle peak becomes narrower and the corresponding spectral weight is transferred over large energy scales to the Hubbard bands. Moreover, the internal structure of the quasi-particle peak is less pronounced as the metal-insulator transition approaches: the same structure as the original DOS of the Wannier orbital appears to be rescaled for U=2 eV, whereas for U=3 eV, only peaks which remind the Van-Hove singularities remain, before merging for higher values.

This behavior of the spectral functions are directly related to the properties of the associated self-energies by the relations established in chapter 2. However, in this present case, they can be simplified, as shown in Appendix B. As a result, the spectral density associated to each t_{2g} character m ($m = d_{xy}, d_{xz}, d_{yz}$) can be written as:

$$A_m^{\alpha,\sigma}(\omega) \quad = \quad -\frac{1}{\pi} \sum_{\mathbf{k} \in BZ} \mathfrak{Im} \left[\frac{\mathcal{D}_m^{\alpha,\sigma}(\mathbf{k})}{\omega + i0^+ + \mu - \varepsilon^{\sigma}_{\mathbf{k}\nu_m} - \Delta\Sigma_m^{\alpha,\sigma}(\omega)} \right] \tag{5.7}$$

where $\mathcal{D}_m^{\alpha,\sigma}(\mathbf{k})$ is the LDA partial DOS associated to the spin σ and the m character along the "m t_{2g} band" and $\Delta\Sigma_m^{\alpha,\sigma}(\omega)$ is the local self-energy associated to the m Wannier orbital. The spectral functions can thus be considered as independent one-band spectral function with respect to their corresponding character and the physical interpretation already presented in chapter 1 for the one-band model can be applied here for each orbital separately.

The imaginary parts of the self-energies are displayed on figures 5.30. From their linear regime at small Matsubara frequencies, the quasi-particle weight Z can be estimated, and the results are given in table 5.7. The width of the quasi-particle peak is then ZW, where W is the initial bandwidth of

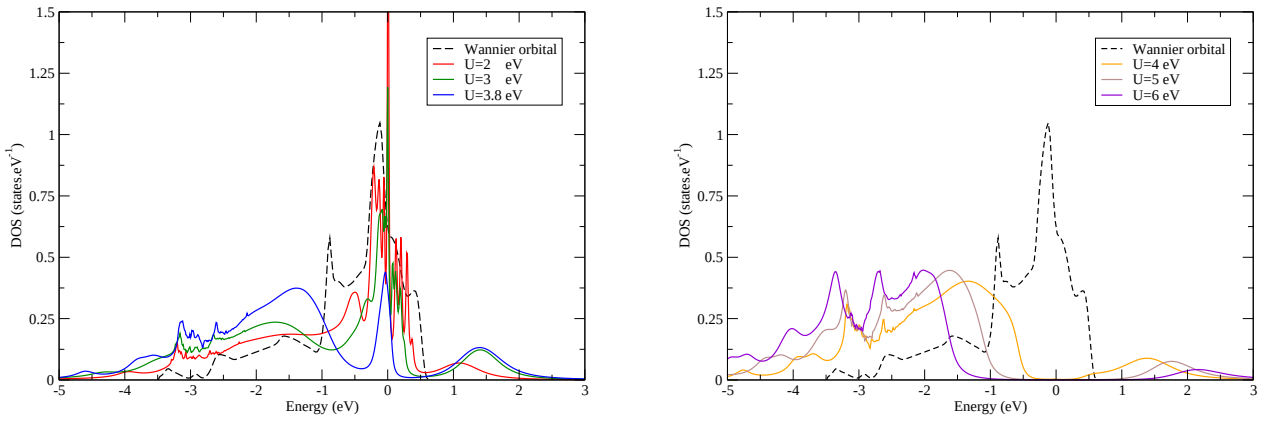

Figure 5.28: LDA+DMFT spectral functions of the d_{xy} Wannier orbital in *undistorted* Sr_2IrO_4 without spin-orbit coupling for U=2, 3, and 3.8 eV (left panel) and U=4, 5 and 6 eV (right panel). The calculations were performed at T=300 K ($\beta = 40$ eV^{-1}) and with J=0.2 eV. The LDA DOS is shown as dashed line.

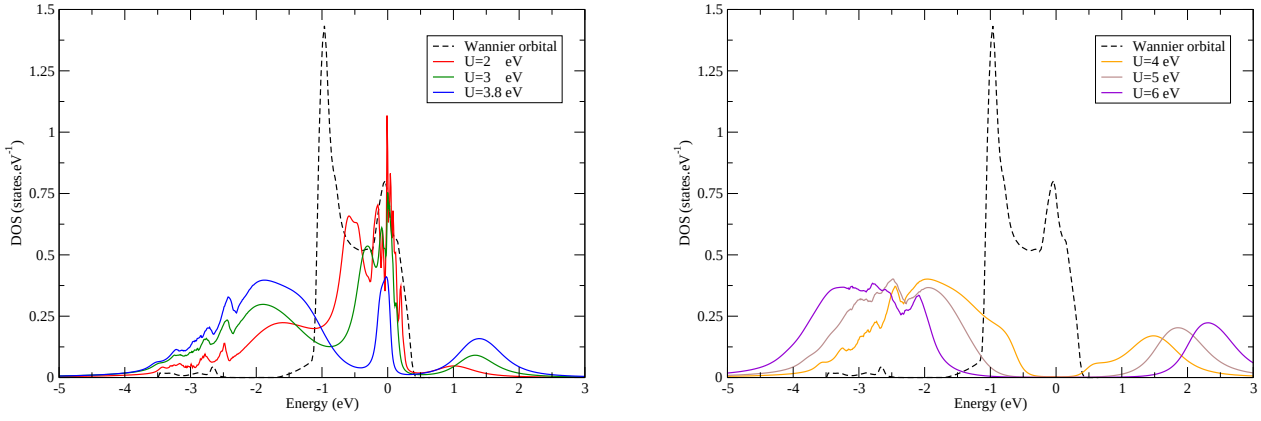

Figure 5.29: Same as figure 5.28, but for the d_{xz} orbital.

the Wannier function.[12]

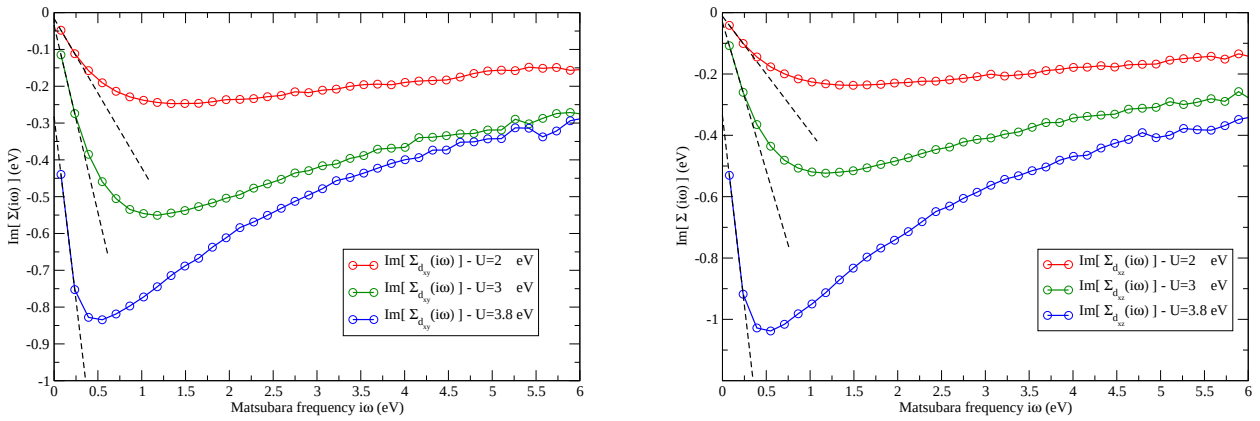

Figure 5.30: Imaginary parts of the LDA+DMFT self-energy on the Matsubara axis associated to the d_{xy} (left panel) and the d_{xz} (right panel) Wannier orbitals for U=2, 3, and 3.8 eV. Parameters as in fig. 5.28. The dashed lines are the linear extrapolations of the self-energy to $i\omega = 0$, their slope α is related to the quasi-particle weight Z by the relation $Z = (1 - \alpha)^{-1}$.

Besides, there is no pinning of the spectral function to its non-interacting value at 0 eV. Actually, the value of the spectral function at the new Fermi level depends on the value of the initial DOS at $Re[\Sigma(0)] - \mu$. In a half-filled one-band model, this quantity is zero because of particle-hole symmetry, hence the pinning at the non-interacting value at 0 eV. In a three-band model with 5 electrons, this symmetry argument does not hold anymore. Consequently, the different values of $Re[\Sigma(0)] - \mu$ as U increases, will induce some shift. It implies a modification of the spectral function at the new Fermi level. However, the numerical noise close to the Fermi level in figures 5.28 and 5.29 prevent from any thorough analysis.

	d_{xy} orbital	d_{xz} / d_{yz} orbital
U=2 eV	0.711	0.726
U=3 eV	0.496	0.508
U=3.8 eV	0.334	0.288

Table 5.7: Quasi-particle weight Z of the d_{xy} and d_{xz} Wannier orbitals. The values were calculated from the linearization of the imaginary part of the corresponding self-energy close to 0.

	d_{xy} orbital	d_{xz} / d_{yz} orbital
U=4 eV	[-0.28;0.30] eV	[-0.26;0.25] eV
U=5 eV	[-0.63;0.98] eV	[-0.67;0.77] eV
U=6 eV	[-0.99;1.41] eV	[-0.98;1.27] eV

Table 5.8: Gap between the upper and the lower Hubbard band of each orbital.

Above the metal-insulator transition only the two Hubbard bands remain, as observed on the right panel of figures 5.28 and 5.29. The lower Hubbard band exhibits an internal structure which is certainly a reminiscence of the Van-Hove singularities of the initial DOS. The gap between the two Hubbard bands becomes wider as the Coulomb parameter U is further increased. The boundaries of the gap for each value of the parameter U are presented in table 5.8.

[12] For the d_{xy} orbital, the significant energy scale to use as W is not the total bandwidth – 4.1 eV –but rather the part between -1 eV and 0.6 eV.

By comparing the right panel of figures 5.28 and 5.29, the spectral weight of the upper Hubbard band of the d_{xy} orbital is smaller than its d_{xz} counterpart, which implies that their respective charges are different in the insulating state. The charge of each Wannier orbital as function of U is presented in table 5.9.

Value of U (eV)	0.0	2.0	3.0	3.5	3.7	3.8	4.0	5.0	6.0
Charge of the d_{xy} orbital	0.806	0.806	0.810	0.821	0.831	0.853	0.899	0.927	0.950
Charge of the d_{xz} / d_{yz} orbital	0.848	0.848	0.847	0.842	0.836	0.825	0.801	0.787	0.776

Table 5.9: Evolution of the charge of each Wannier orbital as function of U. By definition, the value $U = 0$ eV corresponds to the charge of the Wannier orbital in LDA.

The displayed values confirm that there is a charge transfer from the d_{xz} and d_{yz} to the d_{xy} orbital, as the strength of the correlations increases. As a result, in the insulating state of *undistorted* Sr_2IrO_4 without the spin-orbit coupling, the d_{xz} and d_{yz} orbitals are nearly 3/4-filled, while the d_{xy} band is almost full. The self-energy of a system composed of two 3/4-filled bands in the atomic limit was calculated in Appendix B: the self-energy associated to the d_{xz} and d_{yz} orbitals was then fitted with the obtained expression and the quality of the fitting increases as U becomes larger. This allows to conclude that the insulating state of *undistorted* Sr_2IrO_4 without the spin-orbit coupling can be described by this 3/4-filled two-band model as soon as U=4 eV.

As a consequence, *undistorted* Sr_2IrO_4 without spin-orbit coupling behaves like an effective two-band system, once the metal-insulator transition has occurred. This result is surprising, since our LDA calculations have shown that the d_{xy} band is initially less occupied than the d_{xz} and d_{yz} bands, because of the small tetragonal field in the IrO_6 octahedra. One could have imagined that electronic correlations could increase this crystal field up to a critical value, where the d_{xz} and d_{yz} orbitals are completely filled, leaving only one electron in the d_{xy} band. In this hypothetical situation, the critical value for the Coulomb parameter U of this half-filled one-band model lies then between 5.12 and 6.15 eV, since the bandwidth of the d_{xy} band is about 4.1 eV.

On the contrary, our numerical simulations show that the metal-insulator transition of the system occurs for U between 3.8 and 4 eV. This means that the system thus favors the configuration which "minimizes" the critical value of the Coulomb parameter U, or, in other words, the insulating state which involves the least energy given by the electronic correlations. Similar orbital polarization was found in lanthanum titanate ($LaTiO_3$) and yttrium titanate ($YTiO_3$) [130].

To sum up, this LDA+DMFT study has shown that electronic correlations induce an orbital polarization in *undistorted* Sr_2IrO_4 so that charge is transferred to the d_{xy} orbital, which gets finally completely filled in the insulating state. Please note that in part 5.1.3, we have seen on the level of the LDA that the structural distortions in Sr_2IrO_4 already induce a *similar* orbital polarization. This is already a hint that distortions indeed reduce the critical value of U.

5.2.2 Case 2: Distortions leading to orbital polarization

In part 5.1.3, it was shown that a unit cell which contains four formula-units must be used to describe the structure of *distorted* Sr_2IrO_4. However, since the four Ir sites are equivalent – there exists at least one symmetry operation which transforms one site into another one in the unit cell –, it is sufficient to solve the local impurity problem for one of them only. Consequently, the complexity of the impurity problem is not increased and performing an LDA+DMFT calculation will be only slightly

more time-consuming than previously.

Wannier orbitals with distortions

In the Kohn-Sham band structure of *distorted* Sr_2IrO_4, the energy gap between the e_g and t_{2g} *bands* between 0.4 and 1.3 eV suggests to consider only the t_{2g} *bands* for the description of the system. The electronic correlations will indeed merely shift the empty e_g *bands* even more above the Fermi level. The d_{xy} *band*, however, must be kept in the local problem: although it is almost full, its density at the Fermi level is actually of the same order of magnitude as those of the d_{xz} and d_{yz} bands, as it can be seen in figure 5.20. *Distorted* Sr_2IrO_4 can thus be described as an effective three-band system.

However, there is one important complication as compared to the *undistorted* case. In part 5.1.3 it was shown that the band structure of *distorted* Sr_2IrO_4 mainly results from the hybridization between the d_{xy} and the $d_{x^2-y^2}$ states (a t_{2g} and an e_g state). It is thus not possible to consider this compound as a *"pure" t_{2g}-band* system and the Wannier functions should be constructed from an atomic basis consisting of the orbitals d_{xz}, $d_{yz}$and the bonding linear combination of $d_{x^2-y^2}$ and d_{xy} states. Since we want to avoid to calculate this bonding orbital, we describe this orbital by projecting to the d_{xy} character only. This thus allows to construct the Wannier functions from the t_{2g} atomic basis but it is still not possible to consider the t_{2g} block as an irreducible representation of the $5d$ group: the cubic basis is well-adapted to describe the local problem on Ir site, only if the hybridization term between the d_{xy} and $d_{x^2-y^2}$ states can be neglected.

The approach we used to create the Wannier orbitals relies on this last assumption: the energy window $[-2.8; 0.4]$ eV was considered and the Wannier functions were constructed from the t_{2g} atomic basis (d_{xy}, d_{xz} and d_{yz}) only. According to their charge displayed in table 5.5, the total charge of the considered impurity model is 5.01 electrons and since no hybridization term exist betwen these three Wannier functions, the CTQMC calculation is free of any sign-problem during the convergence process[13].

The metal-insulator transition in *distorted* Sr_2IrO_4

The total spectral density obtained for U=2, 3, 3.2 and 3.4 eV are displayed in figure 5.31. Our calculations show that the metal-insulator transition occurs between 3.2 and 3.4 eV. As expected, this value is smaller than the critical value of U in the *undistorted* case. A Coulomb parameter of 3.4 eV is necessary to get a Mott gap of about 0.3 eV.

In figures 5.32 and 5.33 the orbitally resolved spectral densities are shown (d_{xz} and d_{yz} are degenerate). The left panels of figures 5.32 and 5.33 depict the spectral functions in the metallic regime (U$\leq$ 3.2 eV), whereas the right panels display the results in the insulating regime. Both orbitals (d_{xy} and d_{xz}) undergo their metal-insulator transition simultaneously between 3.2 eV and 3.4 eV.

As the value of U increases, the evolution of the d_{xz} orbital is qualitatively similar to what we have observed in the previous section. The well-known *three-peak structure* can be easily recognized in the left panel of figure 5.33, whereas only the two Hubbard bands can be seen in the right panel.

On the contrary, the upper Hubbard band of the d_{xy} orbital is hardly visible, whatever the value for the Coulomb parameter U is. This results from the filling of the d_{xy} *band*: Already at the LDA level, the band is almost completely filled, with 0.96 eletrons by unit cell according to table 5.5. Nevertheless,

[13]Including both d_{xy} and $d_{x^2-y^2}$ and their hybridization into the local Hamiltonian was tried but is actually not possible, because the hybridization introduces a severe sign-problem, making calculations at the temperatures of interest impossible.

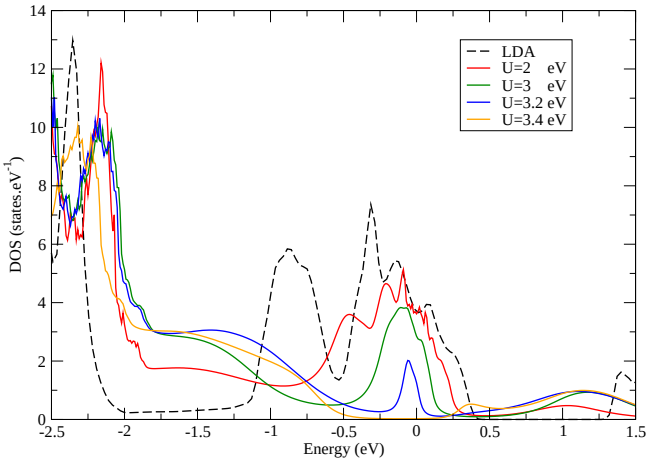

Figure 5.31: Total LDA+DMFT spectral functions of *distorted* Sr_2IrO_4 without spin-orbit coupling for U=2, 3, 3.2 and 3.4 eV. The LDA DOS is plotted as dashed line.

a sharp quasi-particle peak is observed in the metallic regime (U$\leq$ 3.2 eV) and its spectral weight is transferred to the lower Hubbard band as the value of U increases.

As in the *undistorted* case, the spectral functions of each Wannier orbital can be considered as independent one-band spectral function with respect to their corresponding character – the proof of Appendix B still holds. The width of the quasi-particle peak is then ZW, where W is the initial bandwidth of the Wannier function[14] and Z the quasi-particle weight. For U=2 and 3 eV, the values of Z for both orbitals are given in table 5.10. Contrary to the values displayed in table 5.7, the quasi-particle weight Z of the two orbitals are not equal anymore. Further studies must be carried out to understand whether these differences can be linked to their different filling.

In the insulating regime (U$\geq$ 3.4 eV), the upper Hubbard band of the d_{xy} orbital can be neglected. Moreover, the upper limits of the lower d_{xy} and lower d_{xz} Hubbard bands are nearly the same. As a result, the gap of *distorted* Sr_2IrO_4 corresponds to the gap between the two d_{xz} Hubbard bands. Its value as function of U are presented in table 5.11.

	d_{xy} orbital	d_{xz} / d_{yz} orbital
U=2 eV	0.719	0.657
U=3 eV	0.474	0.353

Table 5.10: Quasi-particle weight Z of the d_{xy} and d_{xz} orbitals. The values were calculated from the linear regime of the imaginary part of the corresponding self-energy close to 0.

	Gap in *distorted* Sr_2IrO_4
U=3.4 eV	[-0.37;0.15] eV
U=4 eV	[-0.69;0.12] eV
U=5 eV	[-1.10;0.58] eV

Table 5.11: Gap between the upper and the lower Hubbard band of the d_{xz} (d_{yz}) orbital, which determines the gap in "*distorted*" Sr_2IrO_4

Similar to the previous section, we studied the evolution of the charge of each Wannier orbital as function of the value of U. In the metallic regime, they remain constant to their respective initial

[14]For the d_{xy} orbital, the significant energy scale to use as W is not the total bandwidth – 3.2 eV – but rather the part between -0.5 eV and 0.25 eV.

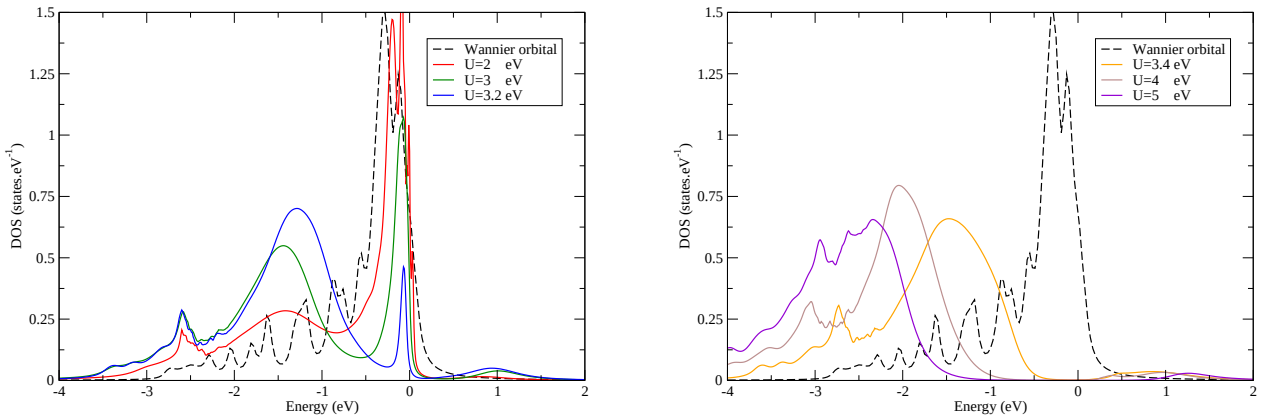

Figure 5.32: LDA+DMFT spectral functions of the d_{xy} Wannier orbital in *distorted* Sr_2IrO_4 without spin-orbit coupling for U=2, 3, and 3.2 eV (left picture) and U=3.4, 4 and 5 eV (right picture).

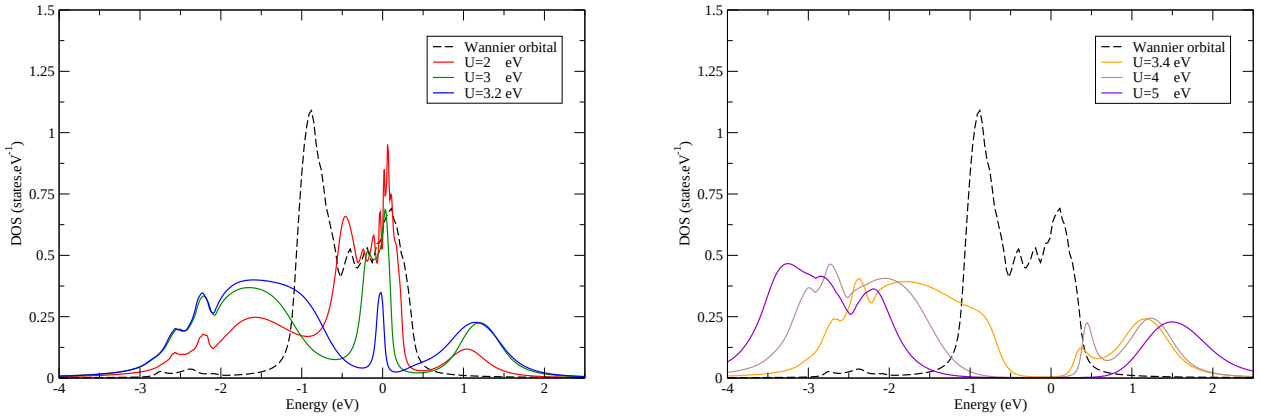

Figure 5.33: Same as fig. 5.32, but for the d_{xz} orbital.

LDA value, which is 0.968 for the d_{xy} orbital and 0.770 for the d_{xz} (d_{yz}) orbital. Above the the metal-insulator transition the charge of the d_{xy} orbital increases slowly with the value of U, whereas the charge of the d_{xz} (and d_{yz}) orbital slowly decreases. Therefore, in the insulating regime, the system can be described by a d_{xy} band completely filled and two 3/4-filled orbitals (d_{xz} and d_{yz}), this picture becoming more and more exact as the value of U is further increases.

This result is in good agreement with our expectations: the insulating state in *undistorted* and *distorted* Sr_2IrO_4 are similar but the metal-insulator transition occurs earlier when the distortions are taken into account. However, the narrowing of the d_{xz} andd_{yz} bands from 1.45 to 1.40 eV is *not* enough to explain this decrease of the critical value from 3.8-4.0 eV to 3.2-3.4 eV. It is the orbital polarization induced by the structural distortions which plays the major role. In *undistorted* Sr_2IrO_4, the three t_{2g} bands are initially almost equally filled at $U = 0$ eV. Before being able to open an insulating gap, correlations have to polarize the system first. In *distorted* Sr_2IrO_4, since the d_{xy} *band* is nearly full even at $U = 0$ eV, the electronic correlations need not introduce an additional polarization and are only used to open the gap, hence a smaller critical value of U. The values of the charge in the table 5.9 confirm that between 3.0 and 4.0 eV, the charge transfer is the most important. As a result, the orbital polarization can be seen as a "*physical requirement*" in the compound to achieve its insulating state.

In addition, in both *undistorted* and *distorted* Sr_2IrO_4, the insulating state with two 3/4-filled bands corresponds to the physical state obtained with the minimal critical value for U. Because of the larger bandwidth of the d_{xy} band, opening a Mott gap for the half-filled d_{xy} orbital would require a larger Coulomb parameter U. Nevertheless, for the sake of completeness, we want to note that the behavior of the self energy of *undistorted* and *distorted* Sr_2IrO_4 are different in the insulating regime. The imaginary part of the self-energy of the d_{xz} (and d_{yz}) orbital appears to diverge at low frequencies for U$\geq$ 3.4 eV in *distorted* Sr_2IrO_4. It is thus not possible to fit them with the expression obtained for the 3/4-filled two-band model at the atomic limit. This behavior is still unexplained and further analyzes are currently in progress to understand it.

5.2.3 Case 3: Spin-orbit coupling and the reduction of the effective degeneracy

Following part 5.1.2, the local basis at each Ir site in the presence of spin-orbit coupling is given by the e_g orbitals ($d_{3z^2-r^2}$ and $d_{x^2-y^2}$), the $j_{\text{eff}} = 1/2$ and the $j_{\text{eff}} = 3/2$ states. Applying the same arguments as for Case 1, we neglect the e_g sates in the local Hamiltonian and work in the t_{2g} subset only.

Wannier function and local Hamiltonian in the presence of spin-orbit coupling

The method used to numerically find the local basis which describes at best the local problem on an Ir site was explained in details in part 5.1.2. It imposes to use a large energy-window – $[-3.5; 6.5]$ eV in this case – and to construct the Wannier functions from the obtained atomic states in this same energy-window. The resulting Wannier orbitals were found in one-to-one correspondence with the five Ir 5d bands. If one wants to use these Wannier projectors directly in the LDA+DMFT approach, one has to face the following problem. Since we change our basis from cubic harmonics to the $j_{\text{eff}} = 1/2$ and $j_{\text{eff}} = 3/2$ basis, off-diagonal *complex* hybridizations are introduced to the local Hamiltonian. However,

the current CTQMC impurity solver can not deal with complex numbers yet.[15]

Nevertheless, in order to perform the LDA+DMFT calculations in the presence of spin-orbit coupling, we decided to use a simplified approach. Since there still exits a one-to-one correspondence between the bands and the Wannier projectors, the density of the Wannier orbitals corresponds also to the DOS of the corresponding band. As a result, it is possible to make the calculation by using this DOS in the self-consistency loop. What we are neglecting here are off-diagonal elements of the self-energy, which are of course not captured.

The main difference between this approach and the former implementation we used is that the self-energy is not "*upgraded*". However, since the local self-energy of our local problem is diagonal, this is not a problem: each band can be seen as treated independently. This method was frequently used in the past and it was shown that these numerical simulations delay the metal-insulator transition in comparison to the scheme we have up to now used. In other words, it overestimates the critical value of U [10, 158].

With this other LDA+DMFT implementation, it is now possible to perform the calculation. As already explained, the compound can be seen as a one-band model. It is thus tempting to consider only the $j_{\text{eff}} = 1/2$ Wannier orbital. However, by doing such a calculation, it will not be possible to make a clear comparison with the three band calculations done in the previous sections. Moreover, the value of the DOS at the Fermi level of the $j_{\text{eff}} = 3/2$ bands is of the same order of magnitude as the one of the $j_{\text{eff}} = 1/2$ band. We thus decided to consider the corresponding three band model with the three Wannier orbitals: $j_{\text{eff}} = 1/2$ and $j_{\text{eff}} = 3/2$.

We remind that there was some problem when calculating the DOS of the Wannier orbital, due to the integration scheme used in the program. In order to minimize these effects, the DOS were slightly renormalized: the tail between -4 and -2 eV of the $j_{\text{eff}} = 1/2$ and the $j_{\text{eff}} = 3/2$ $|m_j| = 1/2$ orbitals was suppressed, their charge then renormalized: 0.592 instead of 0.573 for the former and 0.929 instead of 0.910 for the latter. The charge of the $j_{\text{eff}} = 3/2$ $|m_j| = 3/2$ is still the same (0.913), which leads to a total local charge of 4.87. The total charge of the impurity model was nevertheless set at 5.0 electrons during the calculation. In this case, we chose to perform an analytic continuation of the local Green-function using a stochastic version of the maximum entropy method [19].

The metal-insulator transition in "*undistorted*" Sr_2IrO_4 with spin-orbit coupling

The LDA+DMFT spectral densities obtained for each orbital are depicted in figures 5.34 and 5.35 (a) and (b). As expected, the insulating state of the *undistorted* Sr_2IrO_4 with spin-orbit coupling corresponds to the Mott insulating state of the half-filled $j_{\text{eff}} = 1/2$ Wannier orbital, the two $j_{\text{eff}} = 3/2$ Wannier orbitals being completely filled. However, by studying more thoroughly the properties of each Wannier orbital, it appears that three main steps must be considered during the overall metal-insulator transition in the compound.

[15] We remind that the Lehmann representation of the Green function $G_{ij}(\tau)$ is:

$$G_{ij}(\tau) = -\langle c_i(\tau) c_j^\dagger(0)\rangle = \sum_m \langle 0|c_i|m\rangle\langle m|c_j^\dagger|0\rangle \exp(-\beta E_m) \tag{5.8}$$

If the local Hamiltonian is symmetric and real, its eigenvalues are real and it is possible to find a basis of real eigenvectors. As a result, the Green function $G_{ij}(\tau)$ where i and j belong to this real basis is also real according to the previous expression. If the Hamiltonian is a complex hermitian operator, the eigenvalues are still real, but the eigenvectors will have complex coefficients. Consequently, the Green function $G_{ij}(\tau)$ where i and j belong to an eigenbasis of the Hamiltonian is a complex number in general, except of the case $i = j$, where it is real.

First of all, for the small values of the Coulomb parameter – up to a value U_1 between 2 and 3 eV –, the $j_{\text{eff}} = 3/2$ Wannier orbitals are not completely filled yet. As observed on the figures 5.35 (a) and (b), they thus have some weight at the Fermi level. Besides, their respective self-energy on the Matsubara axis have a small but non-zero imaginary part. The electronic correlations thus have a *weak* impact on these states, hence the two features in their spectral functions which remind of a lower Hubbard band and a quasi-particle peak. The $j_{\text{eff}} = 1/2$ Wannier orbital is in a *weak correlated metallic state* and as the value of U increases, its charge decreases until one electron remains in the orbital.

For intermediate values – between U_1 and the critical value U_c which lies between 3.2 and 3.7 eV –, the final charge repartition is achieved: the two $j_{\text{eff}} = 3/2$ Wannier orbitals are filled and there remains only one electron in the $j_{\text{eff}} = 1/2$ Wannier orbital. As observed in the figures 5.35-(a) and (b), the $j_{\text{eff}} = 3/2$ Wannier orbitals are merely shifted above the Fermi level. Their self-energy can be considered as pure real constants and the electronic correlations act only on the $j_{\text{eff}} = 1/2$ Wannier orbital which undergoes its metal-insulator transition at U_c.

For $U \geq U_c$, the insulating state is reached. As the Coulomb parameter is further increased, the two $j_{\text{eff}} = 3/2$ Wannier orbitals are shifted lower in energy and the gap between the two Hubbard bands of the $j_{\text{eff}} = 1/2$ Wannier orbital becomes larger. The self energy of the $j_{\text{eff}} = 1/2$ Wannier orbital diverges in zero frequency, as expected.

Consequently, the metal-insulator transition of *undistorted* Sr_2IrO_4 with the spin-orbit coupling is directly the metal-insulator transition of the $j_{\text{eff}} = 1/2$ Wannier orbital which occurs between 3.2 and 3.7 eV. However, we would like to point out that the gap corresponds to the gap between the upper $j_{\text{eff}} = 1/2$ Hubbard band and the two filled $j_{\text{eff}} = 3/2$ orbitals, as shown in figure 5.36.

In part 5.1.2 the bandwidth of the $j_{\text{eff}} = 1/2$ orbital was estimated to be of the order of 1.8 eV. Consequently, the critical value for an half-filled one-band model with the same bandwidth is expected to lie between 2.25 and 2.7 eV. Our numerical simulations seem thus to overestimate the critical value of U, but note that the calculations were performed on a three-band model. Taking into account the $j_{\text{eff}} = 3/2$ orbitals has delayed the metal-insulator transition, because electronic correlations have also driven the filling of these bands in addition of the metal-insulator transition of the $j_{\text{eff}} = 1/2$ orbital.

To emphasize this effect, a half-filled one-band Hubbard model with a DOS of the $j_{\text{eff}} = 1/2$ Wannier state was studied as function of the Coulomb parameter U. The LDA+DMFT spectral densities obtained are depicted in figure 5.37. As expected, the metal-insulator transition occurs for $U = 3$ eV, since the bandwidth of the considered Wannier orbital is about 2.0 eV. The delay in the metal-insulator transition of the three-band model induced by the filling of the $j_{\text{eff}} = 3/2$ bands is then of the order of 0.2-0.7 eV.

To sum up, our calculations show that the critical value for the Coulomb parameter U is smaller in *undistorted* Sr_2IrO_4 with spin-orbit coupling than in the one without the spin-orbit coupling.[16]. The spin-orbit coupling thus enhances the effect of electronic correlations by reducing the effective degeneracy of the impurity problem. Besides, the metal-insulator transition occurs almost in the same energy-range as in *distorted* Sr_2IrO_4 without spin-orbit coupling. The $j_{\text{eff}} = 1/2$ Wannier orbital is actually broader by a factor of about $\sqrt{2}$ than the d_{xz} and d_{yz} bands. This must compensate for the increase of the critical value of U when a two-band model is used rather than a one-band model.

[16]The comparison is not rigorously exact since two different LDA+DMFT methods was used. As explained at the beginning of this subsection, the critical value we have found are slightly overestimated in comparison to the one we would have obtained if the same LDA+DMFT implementation as in the case without spin-orbit coupling were used. Fortunately, this precision does not change the conclusion.

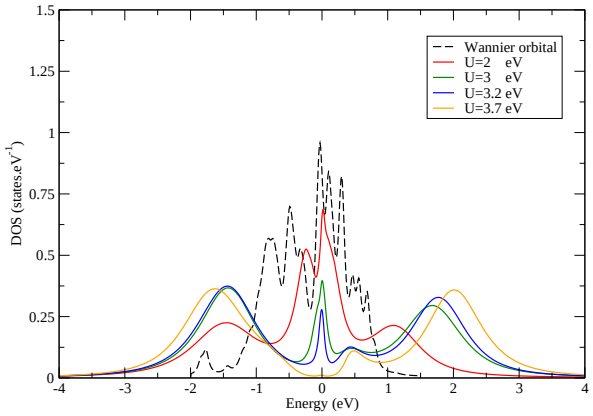

Value of U (eV)	2.0	3.0	3.2
Quasi-particle weight Z	0.552	0.227	0.204

Value of U (eV)	3.7	4.0
Gap width (eV)	[-0.20;0.15]	[-0.29;0.27]

Figure 5.34: LDA+DMFT spectral functions of the $j_{\text{eff}} = 1/2$ Wannier orbital in *undistorted* Sr_2IrO_4 with spin-orbit coupling for U=2, 3, 3.2 and 3.7 eV. The quasi-particle weight and the gap of the $j_{\text{eff}} = 1/2$ Wannier orbital are displayed on the right hand side.

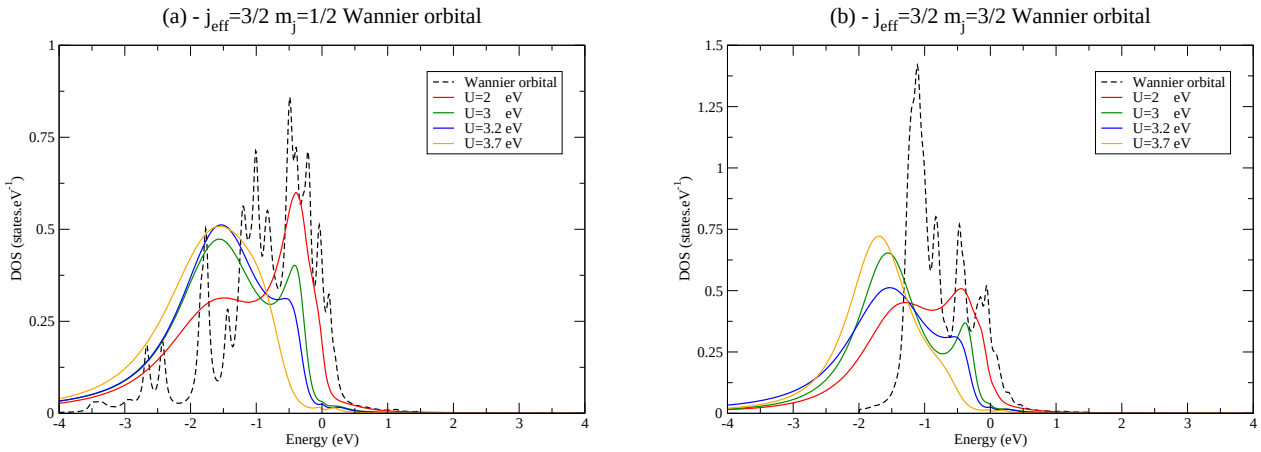

Figure 5.35: Same as fig. 5.34, but for the $j_{\text{eff}} = 3/2$ Wannier orbitals.

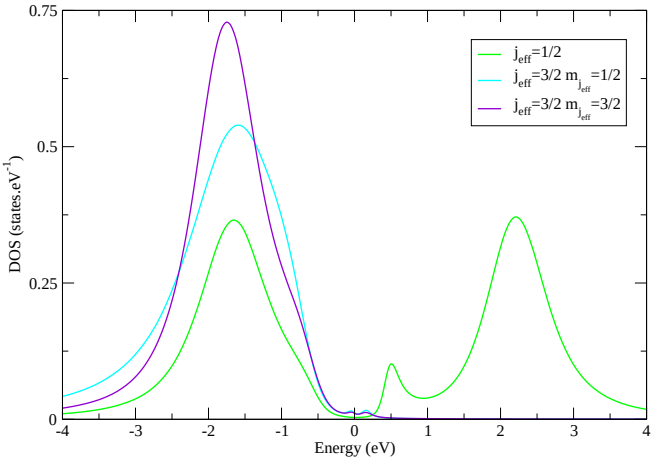

Figure 5.36: LDA+DMFT spectral functions of each Wannier orbital in the *undistorted* Sr_2IrO_4 with the spin-orbit coupling for U=4 eV. The gap lies between the filled $j_{\text{eff}} = 3/2$ orbitals and the upper $j_{\text{eff}} = 1/2$ Hubbard band.

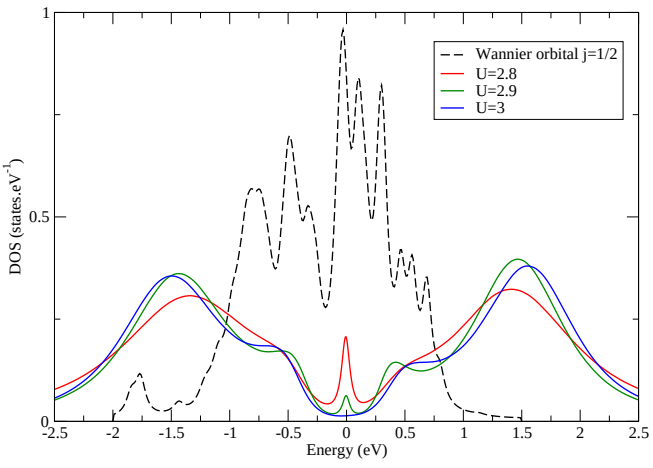

Figure 5.37: LDA+DMFT spectral density of a half-filled one-band Hubbard model whose DOS is the one of the $j_{\text{eff}} = 1/2$ Wannier state. The calculations were performed for U=2.8, 2.9 and 3.0 eV.

5.2.4 The Mott insulating state in Sr_2IrO_4

According to its Kohn-Sham band structure (cf. figure 5.1), Sr_2IrO_4 with both the structural distortions and the spin-orbit coupling, has only four partially filled bands crossing the Fermi level. As a result, in an LDA+DMFT approach, these four bands will be strongly modified by the electronic correlations, whereas all the other bands will be merely shifted, further above or below the Fermi level. In what follows, we restrict ourselves to these four bands and perform an LDA+DMFT calculation only on them.

Introduction to the model used

In part 5.1.4, it was shown that the four bands which cross the Fermi level in Sr_2IrO_4 can be understood as the foldings of one half-filled band only, whose character is a linear combination of the "*modified*" $j_{\text{eff}} = 1/2$ and the $j_{\text{eff}} = 3/2$ $|m_j| = 3/2$ states. However, we were not able to find the expression of this atomic orbital and the Wannier function which is associated to these four bands is consequently not known.

As a result, it is not possible to perform an LDA+DMFT calculation for Sr_2IrO_4 in the same way as in subsections 5.2.1 and 5.2.2. In addition, even if this Wannier function was known, the implementation of LDA+DMFT based on the Wannier projectors and the CTQMC impurity solver could not have been used for the same reasons as part 5.2.3.

However, as it can be seen on the kohn-Sham band structure, these four bands are well-separated from the other bands at each **k**-point and it is then possible to find an energy window around the Fermi level which contains only them. As a result, the total DOS in this energy range corresponds exactly to the DOS associated to these bands. By using this part of the total DOS, we can thus perform an LDA+DMFT calculation with the same method as described in part 5.2.3. In other words, since the four bands are the replicas of the same band, the problem is finally to solve a half-filled one-band Hubbard model with a particular DOS.

The energy window we have chosen is displayed on figure 5.38. The upper boundary was set to 0.56 eV, as given by the Kohn-Sham band structure. The lower boundary was set to -0.35 eV such that the obtained DOS is half-filled. As can be seen in the left panel of figure 5.38, with this choice, the four bands are completely included in the energy window all along the **k**-path, except for the segment $[\Gamma\ M]$. Moreover, the upper part of two other bands are slightly included in this energy-range, mostly in the segment $[\Gamma\ M]$. The contribution of these two extra bands between -0.25 and -0.35 eV is assumed to be small in the obtained DOS – hatched in purple on the right panel of figure 5.38.

The metal-insulator transition in Sr_2IrO_4

The LDA+DMFT spectral density obtained for the half-filled one-band model used to describe Sr_2IrO_4 are displayed in figure 5.39. Since the bandwidth of the initial DOS is about 0.91 eV, a critical value of the Coulomb parameter between 1.14 and 1.36 eV was expected. Our calculations show that the metal-insulator transition indeed occurs between 1.1 and 1.3 eV.

The evolution of the self-energy and the spectral density as U increases follows the general pattern described in section 1.4 with the DOS of a Bethe lattice. The only difference comes from the inner structure of the quasi-particle peak for U=0.75 eV and of the Hubbard bands for U=1.3 and 1.5 eV. One can see some features of the initial DOS, especially the two peaks at -1 and 0.25 eV. The Mott gap is about 0.2 eV (0.4 and 1.5 eV) for U=1.3 eV (1.5 and 2 eV respectively).

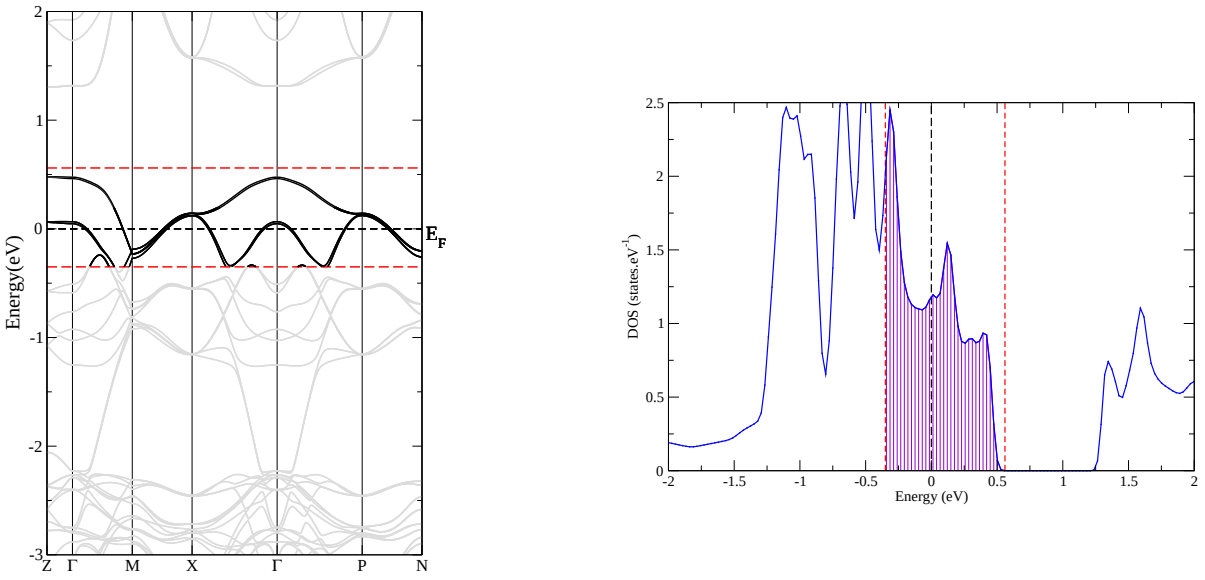

Figure 5.38: Kohn-Sham band structure (on the left) and total LDA DOS (on the right) of Sr_2IrO_4. The dashed red lines – at -0.35 and 0.56 eV– define the energy window used to describe Sr_2IrO_4in an LDA+DMFT approach. It contains essentially the four bands which cross the Fermi level. The corresponding part of the total DOS (hatched in purple) is exactly half-filled.

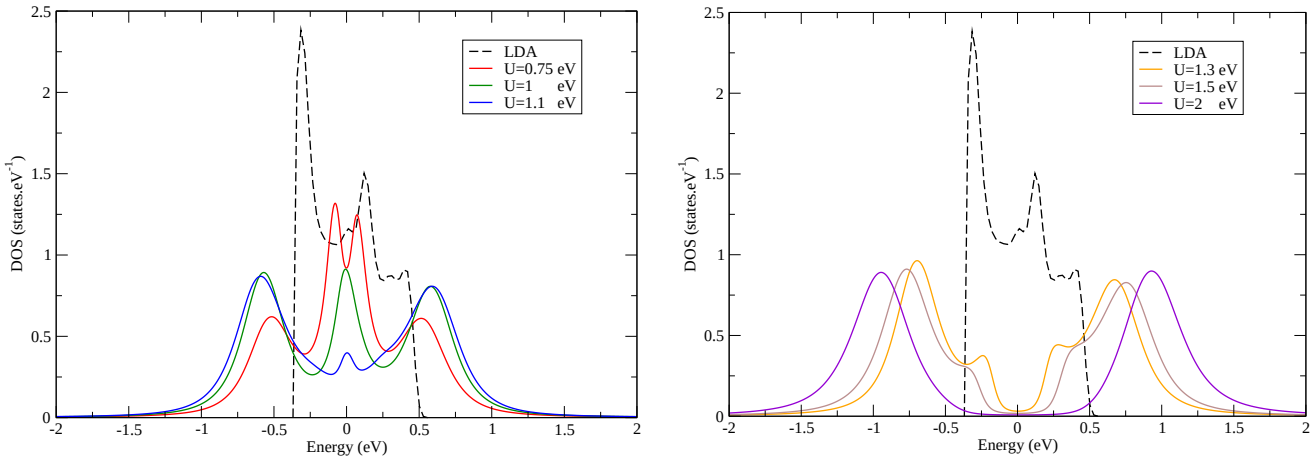

Figure 5.39: LDA+DMFT spectral density of the half-filled one-band Hubbard model used to describe Sr_2IrO_4 – with distortions and spin-orbit coupling. The calculations were performed for U=0.75, 1.0 and 1.1 eV (left panel) and U=1.3, 1.5 and 2.0 eV (right panel). The truncation of the total LDA DOS used has been plotted in dashed line.

As explained previously, all the other bands are either completely empty or filled. It can thus be expected that in a more precise calculation that includes more bands, the same quantitative results will be obtained. With this last argument, it is then possible to draw a comparison between these results and those obtained in the previous sections. Although the impact of the spin-orbit coupling and of the structural distortions taken separately on the critical value U_c is weak, the metal-insulator transition occurs dramatically earlier when both of these two effects are considered.

By adding the spin-orbit corrections to *distorted* Sr_2IrO_4, the 3/4-filled two-band impurity problem is transformed in a half-filled one-band problem. This reduction of the effective degeneracy induces a first decrease in the value of U_c, but the reduction of the bandwidth considered in the model – from 1.4 eV to 0.91 eV – plays also a key role in this decrease.

Similarly, by adding the structural distortions to *undistorted* Sr_2IrO_4 already described with the spin-orbit coupling, a significant reduction of the bandwidth can be noticed: that is why the metal-insulator transition occurs around 3 eV on figure 5.37 and about three times earlier on figure 5.39. Moreover, the orbital polarization induced by the distortions avoid the delay in the metal-insulator transition due to the filling of the other bands, which exists in the *undistorted* case.

To conclude, a Coulomb parameter between 1.3 and 1.5 eV is thus sufficient to get a Mott gap of about 0.3 eV, as experimentally found in [115]. Such a value for the Coulomb parameter is physically possible in a $5d$ transition metal oxide, like Sr_2IrO_4. Therefore, this LDA+DMFT study confirms that Sr_2IrO_4 is a Mott insulator at room temperature, thanks to the joint effort of the spin-orbit coupling and the structural distortions in the compound.

Conclusion

In this thesis, we have studied the transition metal oxide Sr_2IrO_4. Although being a $5d$ material, it exhibits insulating behavior, which is unexpected for an iridium-based compound. In particular, we have studied how structural distortions and spin-orbit coupling modify the electronic structure of this compound, and how they make it possible to open an insulating gap for moderate values of the interaction. According to our calculations, a Coulomb parameter between 1.3 and 1.5 eV is enough to produce a Mott gap of about 0.3 eV.

These works have also highlighted the importance of taking into account *both* the spin-orbit coupling and the structural distortions. Moreover, the underlying effects induced by these two parameters, separately and also together, were understood and quantified:

- The structural distortions (the rotations of the IrO_6 octahedra of about 11° around the **c**-axis) introduce an hybridization between the $d_{x^2-y^2}$ and the d_{xy} bands, which leads to the formation of a filled bonding and an empty antibonding band and an energy separation between the e_g and t_{2g} bands. The "*distorted*" compound can then be described as a system with two 3/4-filled bands, instead of a complete t_{2g} system. This orbital polarization induced by the distortions makes the electronic correlations slightly more efficient than in the corresponding "*undistorted*" compound.

- The spin-orbit coupling (of about 0.4 eV on each Ir site) causes a deep change in the "nature" of the t_{2g} bands. They must indeed be seen as the result of the hybridization between the O-$2p$ states and the orbitals of Ir-$5d$ in the limit of strong spin-orbit coupling. As a result, one "$j_{\text{eff}} = 1/2$ band" lies almost alone close to the Fermi level, whereas the two "$j_{\text{eff}} = 3/2$ bands" are almost completely filled. This reduction of the effective degeneracy in the t_{2g} bands could have made the electronic correlations more efficient, if the bandwidth of the "$j_{\text{eff}} = 1/2$ band" was not bigger than those of the previous d_{xz} and d_{yz} bands.

- By introducing *both* the structural distortions and the spin-orbit corrections in the description of Sr_2IrO_4, one half-filled band – four times folded – remains well separated from all the other bands. Its bandwidth is narrow enough to get an insulating state with a Coulomb parameter physically possible for Sr_2IrO_4. Therefore, the orbital polarization (from the distortions) and the reduction of the effective degeneracy (from the spin-orbit coupling) are not the underlying effects which occur but there is also a reduction of the bandwidth which comes from the joint-effort of these two parameters. These three effects explain the insulating state in Sr_2IrO_4.

Furthermore, contrary to what can be found in the litterature, our work has revealed that the "$j_{\text{eff}} = 1/2$ bands" and "$j_{\text{eff}} = 3/2$ bands" are not well separated in the LDA band structure of Sr_2IrO_4. The structural distortions indeed induce a mixing of these two characters in the four half-filled bands which will form the upper and lower Hubbard bands in the material. This finding was recently confirmed by Watanabe *et al.* [164] who have calculated the one-particle spectrum of Sr_2IrO_4 by using a variational cluster approximation (VCA) and explored the internal electronic structure in the insulating state. This new understanding of the internal electronic structure of Sr_2IrO_4 could explain the

decrease of the optical gap with increasing temperature, which was recently observed in Sr_2IrO_4 by Moon *et al.* [115]. In this sense, our LDA+DMFT calculations can be considered as the first step of a more general LDA+DMFT study of this material within temperature.

In order to describe Sr_2IrO_4 within LDA+DMFT, it was necessary to take into account the spin-orbit corrections both in the LDA band structure and in the definition of the correlated orbitals. Consequently, we have extended the implementation of LDA+DMFT developed in the LAPW framework by Aichhorn *et al.* [1] such that the Wannier orbitals, which are used to define the impurity problem, may be constructed when the spin-orbit interaction is included. The interest for such an approach goes beyond the present case of Sr_2IrO_4 since it could be applied in the future to take into account electronic correlations in the description of other $5d$-transition metal oxides or even topological band insulators. In this sense, some further developments of this "*LDA+SO+DMFT implementation*" are already under way. In particular, the CTQMC impurity solver must be extended to deal with a complex hermitian Hamiltonian, a necessary improvement to be able to perform a complete LDA+DMFT treatment of a compound including the spin-orbit interaction.

As mentioned above, our work has emphasized the key-role played by the spin-orbit coupling and the structural distortions to reach the Mott insulating state in Sr_2IrO_4. However, looking at the recent study on Sr_2RhO_4, it appears that the spin-orbit interaction can be strongly modified – almost doubled – by electronic correlations [107]. In this case, the question arises to what extent the Coulomb parameters U and J *themselves* depend on the strength of the spin-orbit interaction. The interplay between the spin-orbit interaction and the electronic correlations can thus be much more complex and require the development of new models to be investigated in the future.

Part III

Appendices

Appendix A

Atomic d orbitals and spin-orbit coupling: Complements

In Sr_2IrO_4 and many other transition metal oxides[1] the transition metal ion M is surrounded by six oxygen atoms O, forming then an MO_6 octahedron. As a result, the system is locally of cubic – or even lower – symmetry and the $d_{x^2-y^2}$, $d_{3z^2-r^2}$, d_{xy}, d_{xz} and d_{yz} orbitals are usually introduced to describe the atomic states. Moreover, because of this octahedral environment, the fine structure of the d orbitals is not the same as in the case of a single atom. This was particularly highlighted in section 3.1 where the $j_{\text{eff}} = 1/2$ and $j_{\text{eff}} = 3/2$ states were introduced.

In this appendix, we first briefly remind the definitions of the $d_{x^2-y^2}$, $d_{3z^2-r^2}$, d_{xy}, d_{xz} and d_{yz} orbitals and then investigate further the fine structure of the d orbitals in two cases:

- **in an octahedron with *perfect* cubic symmetry:** In this case, we calculate the atomic d states without any *TP-equivalence* approximation, in order to emphasize the impact of the non-diagonal terms neglected in section 3.1.

- **in an elongated or compressed octahedron:** Within the *TP-equivalence* approximation, we show the influence of the additional tetragonal splitting Q_1 on the definition of the $j_{\text{eff}} = 1/2$ and $j_{\text{eff}} = 3/2$ states.

The results of this latter study are finally used to estimate the value of the spin-orbit coupling constant ζ_{SO} and the energy splitting Q_1 in "*undistorted*" Sr_2IrO_4.

A.1 Atomic d states of a metal in an octahedral ligand field

We consider an atom M surrounded by six point charges $-Ze$ with $Z < 0$ (for oxygen atoms, $Z = -2$). The M atom is at the center of the coordinate system, whereas the point charges have the following positions $(a_1, 0, 0)$, $(-a_4, 0, 0)$, $(0, a_2, 0)$, $(0. - a_5, 0)$, $(0, 0, a_3)$ and $(0, 0, -a_6)$, forming then an octahedron.

Case of an octahedron with "*perfect*" cubic symmetry

If all the point charges are at the same distance a of the center ion M ($\forall\ i \quad a_i = a$), the symmetry of the system is "*cubic*". The degeneracy of the five d atomic orbitals of the metal is lifted and two multiplets are created:

[1] For instance, the transition metal oxides which crystallize in the perovskyte or K_2NiF_4-type structure

- **the three t_{2g} states** d_{xy},d_{xz} and d_{yz}:

$$\begin{aligned}
\varphi_{nd_{xy}}(\mathbf{r}) &= -\frac{i}{\sqrt{2}}\left[Y_2^2(\hat{\mathbf{r}}) - Y_{-2}^2(\hat{\mathbf{r}})\right] R_{nd}(r) &= \left(\frac{15}{4\pi}\right)^{\frac{1}{2}}\left(\frac{xy}{r^2}\right) R_{nd}(r) \\
\varphi_{nd_{yz}}(\mathbf{r}) &= \frac{i}{\sqrt{2}}\left[Y_1^2(\hat{\mathbf{r}}) + Y_{-1}^2(\hat{\mathbf{r}})\right] R_{nd}(r) &= \left(\frac{15}{4\pi}\right)^{\frac{1}{2}}\left(\frac{yz}{r^2}\right) R_{nd}(r) \\
\varphi_{nd_{xz}}(\mathbf{r}) &= -\frac{1}{\sqrt{2}}\left[Y_1^2(\hat{\mathbf{r}}) - Y_{-1}^2(\hat{\mathbf{r}})\right] R_{nd}(r) &= \left(\frac{15}{4\pi}\right)^{\frac{1}{2}}\left(\frac{xz}{r^2}\right) R_{nd}(r)
\end{aligned} \tag{A.1}$$

- **the two e_g states** $d_{3z^2-r^2}$ and $d_{x^2-y^2}$:

$$\begin{aligned}
\varphi_{nd_{3z^2-r^2}}(\mathbf{r}) &= Y_0^2(\hat{\mathbf{r}})\ R_{nd}(r) &= \left(\frac{15}{16\pi}\right)^{\frac{1}{2}}\left(\frac{3z^2-r^2}{r^2}\right) R_{nd}(r) \\
\varphi_{ndx^2-y^2}(\mathbf{r}) &= \frac{1}{\sqrt{2}}\left[Y_2^2(\hat{\mathbf{r}}) + Y_{-2}^2(\hat{\mathbf{r}})\right] R_{nd}(r) &= \left(\frac{15}{16\pi}\right)^{\frac{1}{2}}\left(\frac{x^2-y^2}{r^2}\right) R_{nd}(r)
\end{aligned} \tag{A.2}$$

where r denotes the length of the vector $\mathbf{r}$ and the angles, θ and ϕ, specifying the direction of the vector in spherical coordinates, are indicated as $\hat{\mathbf{r}}$. n is the principal quantum number (typically $n = 3, 4$ or 5).

As observed on figure A.1, the t_{2g} orbitals do not point towards the point charges – or the ligand atoms –, in contrast to the e_g ones. As a result, the latter are destabilized by an higher Coulomb repulsion energy. More precisely, it can be shown [157] that:

$$\varepsilon_{t_{2g}} = \varepsilon_0 + \frac{6Ze^2}{a} - 4Dq \quad \text{and} \quad \varepsilon_{e_g} = \varepsilon_0 + \frac{6Ze^2}{a} + 6Dq \tag{A.3}$$

where ε_0 is the energy of the d states of the original M atom and the parameters D, q are defined as follows:

$$D = \frac{35Ze^2}{4a^5} \quad \text{and} \quad q = \frac{2}{105}\int r^4 |R_{nd}(r)|^2\ r^2 dr \tag{A.4}$$

A.1.1 Case of an elongated or compressed octahedron

As mentioned in section 5.1, the IrO_6 octahedra are slightly elongated along the **z**-axis in Sr_2IrO_4. Consequently, the site symmetry of the metal ion is lower than *cubic* and the degeneracies between the two e_g and the three t_{2g} states are lifted.

More generally, we will consider here the case of an elongation – or a compression – of the octahedron along the **z**-axis. In other words, the MO_6 octahedron is now defined by $a_1 = a_2 = a_4 = a_5 = a$ and $a_3 = a_6 = b$, with $b \neq a$. The symmetry of the system is now "*tetragonal*": the $d_{3z^2-r^2}$, $d_{x^2-y^2}$, d_{xy}, d_{xz} and d_{yz}orbitals are still eigenstates of the problem but some additional energy splittings occur between them, as depicted on figure A.2.

When $b < a$, the MO_6 octahedron is *compressed*. As a result, the d_{xz}, d_{yz} and $d_{3z^2-r^2}$ orbitals "feel" a slightly higher Coulomb repulsion energy than their d_{xy} and $d_{x^2-y^2}$ counterparts. Conversely, when $b > a$, the octahedron is *elongated* and the latter are now higher in energy than the former. The energy splitting induced by the tetragonal field between the two e_g (three t_{2g}) states is noted Q_2 (Q_1 respectively). Their expression in function of the ligand-field can be found in [157]. Moreover, since the symmetry of the system is now "*tetragonal*", the d atomic orbitals can not be referred to as the e_g and t_{2g} states anymore:

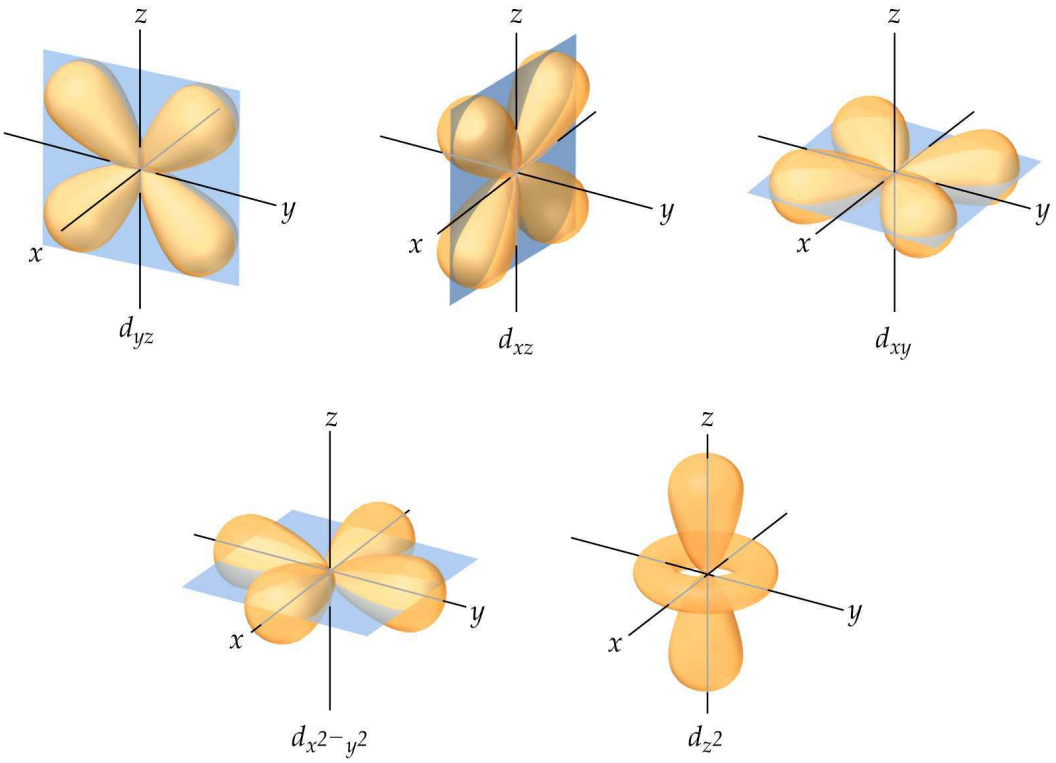

Figure A.1: Angular behaviors of the d atomic orbitals d_{xz}, d_{yz}, d_{xy} (first line) and $d_{x^2-y^2}$, $d_{3z^2-r^2}$ (second line).

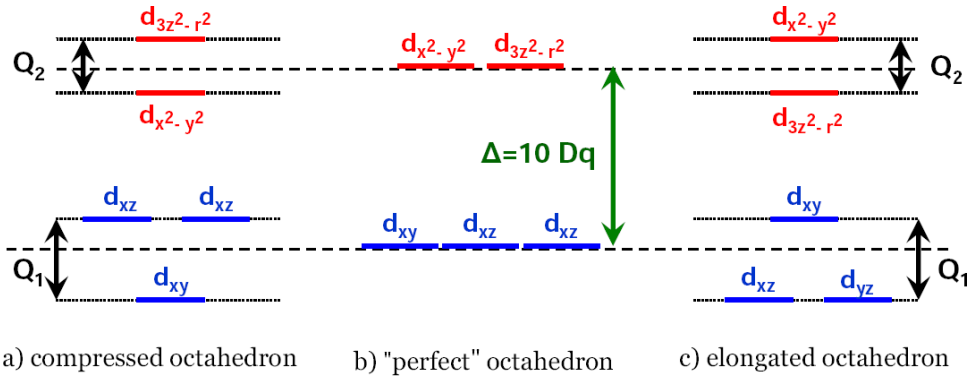

Figure A.2: Energy splitting between the d atomic orbitals in a compressed (panel a), a "perfect" (panel b) and an elongated (panel c) octahedron.

- $d_{3z^2-r^2}$ must be called the a_{1g} state and $d_{x^2-y^2}$ the b_{1g} state,
- d_{xz} and d_{yz} are now the e_g states and d_{xy} the b_{2g} state.

As a result, the Ir-5d d_{xy} orbital must be higher in energy – and thus slightly less populated – than its d_{xz} and d_{yz} counterparts in Sr_2IrO_4. This effect is actually observed in table 5.3, when neither the spin-orbit interaction nor the distortions are taken into account.

A.2 Cubic symmetry and spin-orbit coupling

In section 3.1, we have calculated the impact of the spin-orbit interaction on the d atomic states in cubic symmetry within the *TP-equivalence approximation*. For the sake of completeness, we present here the complete calculation of the fine structure of the d atomic states in cubic symmetry. In addition, we study the influence of a tetragonal energy splitting Q_1 on the definition of the $j_{\text{eff}} = 1/2$ and $j_{\text{eff}} = 3/2$ states.

A.2.1 Effect of the spin-orbit interaction beyond the *TP-equivalence approximation*

Using the expression of the orbital angular momentum $\mathbf{l}$ in the basis $\{d_{xz},\, d_{yz},\, d_{xy},\, d_{3z^2-r^2},\, d_{x^2-y^2}\}$ – presented in (3.20) –, the complete matrix of the spin-orbit interaction can be reduced to two five-dimensional submatrices:

$$\left(\begin{array}{ccc|cc} 0 & -i & i & \sqrt{3} & -1 \\ i & 0 & -1 & -i\sqrt{3} & -i \\ -i & -1 & 0 & 0 & -2i \\ \hline \sqrt{3} & i\sqrt{3} & 0 & 0 & 0 \\ -1 & i & 2i & 0 & 0 \end{array}\right).\frac{\zeta_{SO}}{2} \qquad \text{and} \qquad \left(\begin{array}{ccc|cc} 0 & i & i & -\sqrt{3} & 1 \\ -i & 0 & 1 & -i\sqrt{3} & -i \\ -i & 1 & 0 & 0 & 2i \\ \hline -\sqrt{3} & i\sqrt{3} & 0 & 0 & 0 \\ 1 & i & -2i & 0 & 0 \end{array}\right).\frac{\zeta_{SO}}{2} \quad \text{(A.5)}$$

in the basis:

$\{d_{xz}\uparrow, d_{yz}\uparrow, d_{xy}\downarrow, d_{3z^2-r^2}\downarrow, d_{x^2-y^2}\downarrow\}$ and $\{d_{xz}\downarrow, d_{yz}\downarrow, d_{xy}\uparrow, d_{3z^2-r^2}\uparrow, d_{x^2-y^2}\uparrow\}$ respectively.

When we used the "*TP-equivalence*" approximation in section 3.1, the cubic crystal field $\Delta = 10Dq$ was assumed much larger than the spin-orbit coupling constant ζ_{SO}. As a result, the e_g and t_{2g} orbitals were considered as decoupled and:

- the e_g states were not affected by the spin-orbit coupling ($\varepsilon_{e_g} = \varepsilon_{t_{2g}} + \Delta$)
- the t_{2g} states were split into a doublet of eigenstates of energy: $\varepsilon_{j_{\text{eff}}=\frac{1}{2}} = \varepsilon_{t_{2g}} + \zeta_{SO}$

$$\left\{\begin{array}{rcccl} |\frac{1}{2},-\frac{1}{2}\rangle & = & |j_{\text{eff}}=\frac{1}{2}, m_j=-\frac{1}{2}\rangle & = & \frac{1}{\sqrt{3}}|d_{yz}\uparrow\rangle - \frac{i}{\sqrt{3}}|d_{xz}\uparrow\rangle - \frac{1}{\sqrt{3}}|d_{xy}\downarrow\rangle \\ |\frac{1}{2},+\frac{1}{2}\rangle & = & |j_{\text{eff}}=\frac{1}{2}, m_j=+\frac{1}{2}\rangle & = & \frac{1}{\sqrt{3}}|d_{yz}\downarrow\rangle + \frac{i}{\sqrt{3}}|d_{xz}\downarrow\rangle + \frac{1}{\sqrt{3}}|d_{xy}\uparrow\rangle \end{array}\right. \quad (3.27)$$

and a quartet of eigenstates of energy: $\varepsilon_{j_{\text{eff}}=\frac{3}{2}} = \varepsilon_{t_{2g}} - \zeta_{SO}/2$

$$\left\{\begin{array}{rcccl} |\frac{3}{2},-\frac{3}{2}\rangle & = & |j_{\text{eff}}=\frac{3}{2}, m_j=-\frac{3}{2}\rangle & = & \frac{1}{\sqrt{2}}|d_{yz}\downarrow\rangle - \frac{i}{\sqrt{2}}|d_{xz}\downarrow\rangle \\ |\frac{3}{2},+\frac{3}{2}\rangle & = & |j_{\text{eff}}=\frac{3}{2}, m_j=+\frac{3}{2}\rangle & = & -\frac{1}{\sqrt{2}}|d_{yz}\uparrow\rangle - \frac{i}{\sqrt{2}}|d_{xz}\uparrow\rangle \\ |\frac{3}{2},-\frac{1}{2}\rangle & = & |j_{\text{eff}}=\frac{3}{2}, m_j=-\frac{1}{2}\rangle & = & \frac{1}{\sqrt{6}}|d_{yz}\uparrow\rangle - \frac{i}{\sqrt{6}}|d_{xz}\uparrow\rangle + \sqrt{\frac{2}{3}}|d_{xy}\downarrow\rangle \\ |\frac{3}{2},+\frac{1}{2}\rangle & = & |j_{\text{eff}}=\frac{3}{2}, m_j=+\frac{1}{2}\rangle & = & -\frac{1}{\sqrt{6}}|d_{yz}\downarrow\rangle - \frac{i}{\sqrt{6}}|d_{xz}\downarrow\rangle + \sqrt{\frac{2}{3}}|d_{xy}\uparrow\rangle \end{array}\right. \quad (3.28)$$

In order to calculate the complete fine structure of the d atomic states in cubic symmetry, we will use these states to partially diagonalize the complete Hamiltonian H of the system. Indeed, with $\xi = 2\Delta/\zeta_{SO}$, one can write:

$$H = \varepsilon_{t_{2g}}.Id + \left(\begin{array}{ccccc|ccccc} 2 & 0 & 0 & 0 & 0 & & & & & \\ \hline 0 & -1 & i\sqrt{6} & 0 & 0 & & & & & \\ 0 & -i\sqrt{6} & \xi & 0 & 0 & & & \mathbb{O} & & \\ \hline 0 & 0 & 0 & -1 & -i\sqrt{6} & & & & & \\ 0 & 0 & 0 & i\sqrt{6} & \xi & & & & & \\ \hline & & & & & 2 & 0 & 0 & 0 & 0 \\ \hline & & & & & 0 & -1 & -i\sqrt{6} & 0 & 0 \\ & & \mathbb{O} & & & 0 & i\sqrt{6} & \xi & 0 & 0 \\ \hline & & & & & 0 & 0 & 0 & -1 & i\sqrt{6} \\ & & & & & 0 & 0 & 0 & -i\sqrt{6} & \xi \end{array}\right).\frac{\zeta_{SO}}{2} \tag{A.6}$$

in the basis

$$\{|\frac{1}{2},-\frac{1}{2}\rangle, |\frac{3}{2},+\frac{3}{2}\rangle, |d_{3z^2-r^2}\downarrow\rangle, |\frac{3}{2},-\frac{1}{2}\rangle, |d_{x^2-y^2}\downarrow\rangle, |\frac{1}{2},+\frac{1}{2}\rangle, |\frac{3}{2},-\frac{3}{2}\rangle, |d_{3z^2-r^2}\uparrow\rangle, |\frac{3}{2},+\frac{1}{2}\rangle, |d_{x^2-y^2}\uparrow\rangle\}$$

Finally, the fine structure of the d atomic states in cubic symmetry is then composed of:

- a first quartet of eigenstates associated to the energy

$$\varepsilon_+ = \varepsilon_{t_{2g}} + \frac{\zeta_{SO}}{2}\left(\frac{\xi-1}{2} + \sqrt{6}\sqrt{1+\frac{(1+\xi)^2}{24}}\right) \tag{A.7}$$

$$\left\{\begin{array}{l} x\ |\frac{3}{2},-\frac{1}{2}\rangle + y\ |d_{x^2-y^2}\downarrow\rangle \\ \\ x\ |\frac{3}{2},+\frac{3}{2}\rangle - y\ |d_{3z^2-r^2}\downarrow\rangle \end{array}\right. \quad \text{and} \quad \left\{\begin{array}{l} x\ |\frac{3}{2},-\frac{3}{2}\rangle + y\ |d_{3z^2-r^2}\uparrow\rangle \\ \\ x\ |\frac{3}{2},+\frac{1}{2}\rangle - y\ |d_{x^2-y^2}\uparrow\rangle \end{array}\right. \tag{A.8}$$

- a doublet of eigenstates of energy $\varepsilon_{j_{\text{eff}}=\frac{1}{2}} = \varepsilon_{t_{2g}} + \zeta_{SO}$

$$|\frac{1}{2},-\frac{1}{2}\rangle \quad \text{and} \quad |\frac{1}{2},+\frac{1}{2}\rangle \tag{A.9}$$

- a second quartet of eigenstates associated to the energy

$$\varepsilon_- = \varepsilon_{t_{2g}} + \frac{\zeta_{SO}}{2}\left(\frac{\xi-1}{2} - \sqrt{6}\sqrt{1+\frac{(1+\xi)^2}{24}}\right) \tag{A.10}$$

$$\left\{\begin{array}{l} -y\ |\frac{3}{2},-\frac{1}{2}\rangle + x\ |d_{x^2-y^2}\downarrow\rangle \\ \\ -y\ |\frac{3}{2},-\frac{3}{2}\rangle + x\ |d_{3z^2-r^2}\uparrow\rangle \end{array}\right. \quad \text{and} \quad \left\{\begin{array}{l} y\ |\frac{3}{2},+\frac{1}{2}\rangle + x\ |d_{x^2-y^2}\uparrow\rangle \\ \\ y\ |\frac{3}{2},+\frac{3}{2}\rangle + x\ |d_{3z^2-r^2}\downarrow\rangle \end{array}\right. \tag{A.11}$$

In the previous expressions, we have used the following quantities :

$$\xi = \frac{2\Delta}{\zeta_{SO}}\ , \quad h = \frac{\xi+1}{2\sqrt{6}}\ , \quad x = \frac{1}{\sqrt{2}}\sqrt{1-\frac{h}{\sqrt{1+h^2}}} \quad \text{and} \quad y = \frac{i}{\sqrt{2}}\sqrt{1+\frac{h}{\sqrt{1+h^2}}} \tag{A.12}$$

If $\Delta > 0$, it can be shown that $\varepsilon_+ > \varepsilon_{j=\frac{1}{2}} > \varepsilon_-$, and when $\xi \to +\infty$, the multiplets obtained within the *TP-equivalence* approximation are of course found.

As a result, no other splitting is introduced by going beyond the *TP-equivalence* approximation: the d orbitals are still split into two quartets and one doublet. Moreover, the $j_{\text{eff}} = 1/2$ states are still eigenstates of the complete Hamiltonian H, whereas the $j_{\text{eff}} = 3/2$ and e_g states are mixed.

A.2.2 Effect of a tetragonal splitting within the *TP-equivalence* approximation

We consider now that the six ligands surrounding the metal ion form a slightly elongated – or compressed – octahedron. Moreover, we assume that the cubic crystal field is still much larger than the spin-orbit couping constant ($\Delta = 10Dq \gg \zeta_{SO}$).

As previously explained, the $d_{3z^2-r^2}$, $d_{x^2-y^2}$, d_{xy}, d_{xz} and d_{yz} orbitals are still suitable to describe the atomic d states in tetragonal symmetry. The spin-orbit interaction matrix is thus the same as in the *cubic* case and the "*TP-equivalence*" approximation still holds for this system: the $d_{3z^2-r^2}$ and $d_{x^2-y^2}$ states can be studied independently of the d_{xy}, d_{xz} and d_{yz} states.

As in the *cubic* symmetry, the spin-orbit interaction is ineffective on the $d_{3z^2-r^2}$ and $d_{x^2-y^2}$ orbitals because of their quenched angular momentum. On the contrary, the tetragonal splitting Q_1 – between the d_{xy} and d_{xz},d_{yz} states – modifies the structure of the multiplets $j_{\text{eff}} = 1/2$ and $j_{\text{eff}} = 3/2$. In the "t_{2g}" subspace, the Hamiltonian H of the system can indeed be written as follows:

$$H = \varepsilon_{t_{2g}}.Id + \left(\begin{array}{ccc|ccc} 0 & -i & i & & & \\ i & 0 & -1 & & \mathbb{O} & \\ -i & -1 & \eta & & & \\ \hline & & & 0 & -i & i \\ & \mathbb{O} & & i & 0 & -1 \\ & & & -i & -1 & \eta \end{array}\right).\frac{\zeta_{SO}}{2}$$

in the basis $\{d_{xz}\uparrow, d_{yz}\uparrow, d_{xy}\downarrow, d_{xz}\downarrow, d_{yz}\downarrow, d_{xy}\uparrow\}$ with $\eta = 2Q_1/\zeta_{SO}$.

Using the same approach as in section 3.1 to diagonalize this matrix, one obtains three doublets of eigenstates:

- a first doublet of eigenstates associated to the energy

$$\varepsilon_{j_{\text{eff}}=\frac{1}{2}} = \varepsilon_{t_{2g}} + \frac{\zeta_{SO}}{2}\left(\frac{1+\eta}{2} + \sqrt{2}\sqrt{1+\frac{(\eta-1)^2}{8}}\right) \tag{A.13}$$

$$\left\{\begin{array}{l} |j_{\text{eff}} = \frac{1}{2}, m_j = -\frac{1}{2}\rangle = \frac{x}{\sqrt{2}}\,|d_{yz}\uparrow\rangle - \frac{ix}{\sqrt{2}}\,|d_{xz}\uparrow\rangle + y\,|d_{xy}\downarrow\rangle \\ |j_{\text{eff}} = \frac{1}{2}, m_j = +\frac{1}{2}\rangle = \frac{x}{\sqrt{2}}\,|d_{yz}\downarrow\rangle + \frac{ix}{\sqrt{2}}\,|d_{xz}\downarrow\rangle - y|d_{xy}\uparrow\rangle \end{array}\right. \tag{A.14}$$

- a second doublet of eigenstates associated to the energy

$$\varepsilon_{j_{\text{eff}}=\frac{3}{2},|m_j|=\frac{3}{2}} = \varepsilon_{t_{2g}} - \frac{\zeta_{SO}}{2} \tag{A.15}$$

$$\left\{\begin{array}{l} |j_{\text{eff}} = \frac{3}{2}, m_j = -\frac{3}{2}\rangle = \frac{1}{\sqrt{2}}|d_{yz}\downarrow\rangle - \frac{i}{\sqrt{2}}|d_{xz}\downarrow\rangle \\ |j_{\text{eff}} = \frac{3}{2}, m_j = +\frac{3}{2}\rangle = -\frac{1}{\sqrt{2}}|d_{yz}\uparrow\rangle - \frac{i}{\sqrt{2}}|d_{xz}\uparrow\rangle \end{array}\right. \tag{A.16}$$

- a third doublet with energy

$$\varepsilon_{j_{\text{eff}}=\frac{3}{2},|m_j|=\frac{1}{2}} = \varepsilon_{t_{2g}} + \frac{\zeta_{SO}}{2}\left(\frac{1+\eta}{2} - \sqrt{2}\sqrt{1+\frac{(\eta-1)^2}{8}}\right) \tag{A.17}$$

$$\left\{\begin{array}{l} |j_{\text{eff}} = \frac{3}{2}, m_j = -\frac{1}{2}\rangle = -\frac{y}{\sqrt{2}}\,|d_{yz}\uparrow\rangle + \frac{iy}{\sqrt{2}}\,|d_{xz}\uparrow\rangle + x\,|d_{xy}\downarrow\rangle \\ |j_{\text{eff}} = \frac{3}{2}, m_j = +\frac{1}{2}\rangle = \frac{y}{\sqrt{2}}\,|d_{yz}\downarrow\rangle + \frac{iy}{\sqrt{2}}\,|d_{xz}\downarrow\rangle + x\,|d_{xy}\uparrow\rangle \end{array}\right. \tag{A.18}$$

In these expressions, we have used the following quantities :

$$\eta = \frac{2Q_1}{\zeta_{SO}} \ , \quad h = \frac{\eta - 1}{2\sqrt{2}} \ , \quad x = \frac{1}{\sqrt{2}}\sqrt{1 - \frac{h}{\sqrt{1+h^2}}} \quad \text{and} \quad y = -\frac{1}{\sqrt{2}}\sqrt{1 + \frac{h}{\sqrt{1+h^2}}} \tag{A.19}$$

The states were labeled with the effective quantum number j_{eff}, m_j which can be associated to them in the "*perfect*" cubic symmetry ($Q_1 = 0$).

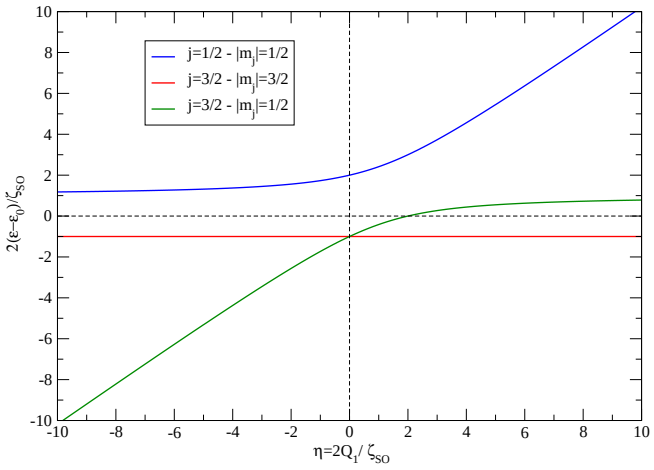

Figure A.3: Evolution of the eigenvalues of the system with the amplitude of the tetragonal splitting Q_1. The eigenvalues are given with respect to the local energy of the t_{2g} states ε_0. All the values are adimensionalized with respect to the value $\zeta_{SO}/2$.

The evolution of the energy of each doublet with respect to the parameter η is presented on figure A.3. Although the $j_{\text{eff}} = 1/2$ states are always the highest in energy, the order of the two $j_{\text{eff}} = 3/2$ doublets depends on the sign of the tetragonal splitting Q_1:

- for an elongated octahedron ($Q_1 > 0$), the $j_{\text{eff}} = 3/2$ $|m_j| = 1/2$ states are higher in energy than the $j_{\text{eff}} = 3/2$ $|m_j| = 3/2$;
- for a compressed octahedron ($Q_1 < 0$), the $j_{\text{eff}} = 3/2$ $|m_j| = 3/2$ states are higher in energy than the $j_{\text{eff}} = 3/2$ $|m_j| = 1/2$;
- for $Q_1 = 0$, they form a degenerate quartet of eigenstates, since the symmetry is merely cubic.

A.3 Evaluation of the spin-orbit coupling constant and the tetragonal splitting in "*undistorted*" Sr_2IrO_4

As mentioned in section 5.1.2, we have estimated the value of the spin-orbit coupling constant ζ_{SO} and the tetragonal splitting Q_1 in "*undistorted*" Sr_2IrO_4. To perform these calculations, we have used the previously obtained expressions of the $j_{\text{eff}} = 1/2$ and $j_{\text{eff}} = 3/2$ states when the tetragonal splitting Q_1 is taken into account.

Estimation of the spin-orbit coupling constant ζ_{SO}

Let λ be the energy splitting between the $j_{\text{eff}} = 1/2$ and $j_{\text{eff}} = 3/2$ $|m_j| = 3/2$ bands:

$$\lambda = \varepsilon_{j_{\text{eff}}=\frac{1}{2}} - \varepsilon_{j_{\text{eff}}=\frac{3}{2},|m_j|=\frac{3}{2}} \tag{A.20}$$

From the expressions (A.13) and (A.15), one obtains:

$$\frac{2\lambda}{\zeta_{SO}} = \frac{1+\eta}{2} + \sqrt{2}\sqrt{1+\frac{(\eta-1)^2}{8}} + 1 \qquad \Leftrightarrow \qquad \eta = \frac{Q_1(3\lambda - Q_1)}{\lambda(\lambda - Q_1)} \tag{A.21}$$

As a result, if Q_1 is known, it is possible to evaluate the value of ζ_{SO}, since $\eta = 2Q_1/\zeta_{SO}$.

We first applied the formula (A.21) by using the values taken by the bands at the Γ point in *undistorted* Sr_2IrO_4. From figure 5.8, we measured $Q_1 = -2.45$ eV and from figure 5.11, $\lambda = 0.26$ eV. As a result, we found $\zeta_{SO} = 0.436$ eV.

We also performed the same calculation by using the mean-energy associated to the corresponding bands. The mean-energy was obtained from:

$$E = \frac{\int \varepsilon D(\varepsilon) d\varepsilon}{\int D(\varepsilon) d\varepsilon} \tag{A.22}$$

where the integration of the partial DOS was performed between -3.5 and 6.5 eV.[2] From the partial DOS of d_{xy}, d_{xz} and d_{yz}displayed in figure 5.9, we estimated $Q_1 = -0.216$ eV. From the partial DOS associated to the $j_{\text{eff}} = 1/2$ and $j_{\text{eff}} = 3/2$ $m_j = 3/2$ states – depicted in figure 5.15– , we obtained $\lambda = 0.476$ eV. This led to $\zeta_{SO} = 0.401$ eV. Both these results are in good agreement with the standard estimation of ζ_{SO} for iridium [53, 43, 161].

Evaluation of the tetragonal splitting Q_1

The previous estimations of Q_1 merely are effective tetragonal splittings between the d_{xy} and the d_{xz},d_{yz} bands. It is however possible to find the "real" value of Q_1 by using the expressions of the $j_{\text{eff}} = 1/2$ and $j_{\text{eff}} = 3/2$ $|m_j| = 1/2$ states numerically found in section 5.1.2:

$$\begin{aligned}
|\phi_{j_{eff}=\frac{1}{2},m_j=-\frac{1}{2}}\rangle = &\ -i0.00588\ |\phi_{d_{x^2-y^2}\downarrow}\rangle\ \ -0.62942\ |\phi_{d_{xy}\downarrow}\rangle\ \ -i0.54945\ |\phi_{d_{xz}\uparrow}\rangle\ \ +0.54945\ |\phi_{d_{yz}\uparrow}\rangle \\
|\phi_{j_{eff}=\frac{3}{2},m_j=-\frac{1}{2}}\rangle = &\ -i0.13967\ |\phi_{d_{x^2-y^2}\downarrow}\rangle\ \ +0.76996\ |\phi_{d_{xy}\downarrow}\rangle\ \ -i0.44026\ |\phi_{d_{xz}\uparrow}\rangle\ \ +0.44026\ |\phi_{d_{yz}\uparrow}\rangle
\end{aligned} \tag{A.23}$$

By neglecting the term in $|\phi_{d_{x^2-y^2}\downarrow}\rangle$, we can map this to the expressions (A.14) and (A.18) and then determine the value of the ratio η. The following relation can indeed be found from (A.19),

$$\eta = \sqrt{2}\left(\frac{x}{y} - \frac{y}{x}\right) + 1 \tag{A.24}$$

By applying this formula for the $j_{\text{eff}} = 1/2$ states, we found $\eta = 0.400$ and for the $j_{\text{eff}} = 3/2$ $|m_j| = 1/2$ states, we obtained $\eta = 0.395$. Using then the value of the spin-orbit coupling constant found previously, we get that $Q_1 = 0.08$ eV.

This value has the same order of magnitude than the one used by Jin *et al.* [79] to fit the LDA band structure with a tight-binding model. However, their estimation ($Q_1 = 0.15$ eV) is twice bigger than ours, certainly because we do not use the same crystallographic data.

[2] This is the energy window in which the Wannier orbitals were calculated.

Appendix B

The self-energy of Sr_2IrO_4

In this appendix, some properties of the self-energies of Sr_2IrO_4 are presented. Our study is restricted to the easier case where both the spin-orbit coupling and the structural distortion are not taken into account. First, we establish the relation (5.7) which relates the momentum-resolved spectral function $A_m^{\alpha,\sigma}(\mathbf{k},\omega)$ and the local self-energy $\Delta\Sigma_m^{\alpha,\sigma}(\omega)$ in the particular case when there is a one-to-one correspondence between the Wannier characters (α, lm, σ) and the bands. We then calculate the self-energy of a 3/4-filled two-bands Hubbard model in the atomic limit and show the good agreement between the self-energies of *undistorted* Sr_2IrO_4 without the spin-orbit coupling with the obtained expressions when the Coulomb parameter U is large enough.

B.1 Relation between the spectral function and the self-energy

In a general LDA+DMFT scheme[1], the spectral functions $A_{m,m'}^{\alpha,\sigma}(\mathbf{k},\omega)$ is linked to the behavior of the self-energies of the impurity model $\mathbf{\Delta}\Sigma_m^{\alpha,\sigma}(\omega)$ by the following relations introduced in section 3.4:

$$\begin{aligned} A_{m,m'}^{\alpha,\sigma}(\mathbf{k},\omega) &= -\frac{1}{\pi}\mathfrak{Im}\left[\sum_{\nu,\nu'}\sum_{j=1}^{3}\Theta_{lm\nu j}^{\alpha,\sigma}(\mathbf{k})G_{\nu\nu'}^{\sigma}(\mathbf{k},\omega+i0^+)\left[\Theta_{lm'\nu' j}^{\alpha,\sigma}(\mathbf{k})\right]^*\right] \\ &= -\frac{1}{\pi}\sum_{\nu,\nu'}\sum_{j=1}^{3}\mathfrak{Im}\left[\frac{\Theta_{lm\nu j}^{\alpha,\sigma}(\mathbf{k})\ \left[\Theta_{lm'\nu' j}^{\alpha,\sigma}(\mathbf{k})\right]^*}{(\omega+i0^+ +\mu-\varepsilon_{\mathbf{k}\nu}^{\sigma})\delta_{\nu\nu'}-\Sigma_{\nu\nu'}^{\sigma}(\mathbf{k},\omega)}\right] \\ \text{where}\quad & \Sigma_{\nu\nu'}^{\sigma}(\mathbf{k},\omega)=\sum_{\alpha,mm'}\left[P_{lm,\nu}^{\alpha,\sigma}(\mathbf{k})\right]^*\ [\mathbf{\Delta}\Sigma_{imp}^{\alpha}(\omega)]_{mm'}^{\sigma}\ P_{lm',\nu'}^{\alpha,\sigma}(\mathbf{k}) \\ \text{and}\quad & [\mathbf{\Delta}\Sigma_{imp}^{\alpha}(\omega)]_{mm'}^{\sigma}=[\mathbf{\Sigma}_{imp}^{\alpha}(\omega)]_{mm'}^{\sigma}-[\mathbf{\Sigma}_{dc}^{\alpha}(\omega)]_{mm'}^{\sigma}. \end{aligned} \tag{B.1}$$

In the case of *undistorted* Sr_2IrO_4 without the spin-orbit coupling, we have highlighted in part 5.1.1 that there is a one-to-one correspondence between the Wannier functions and the t_{2g} bands. In addition, the impurity Green function $\mathbf{G}_{loc}^{\alpha}(i\omega_n)$ of the t_{2g} block has the same structure as the density matrix : it is diagonal and degenerate in spin (cf. part 5.2.1). As a result, so are the impurity and double-counting self-energies ($\mathbf{\Sigma}_{imp}^{\alpha}(i\omega_n)$ and $\mathbf{\Sigma}_{dc}^{\alpha}(i\omega_n)$). Consequently, if ν_p refers to the band associated to the p^{th} Wannier orbital, we can write[2] that:

$$\Sigma_{\nu\nu'}^{\sigma}(\mathbf{k},\omega)=\left[\left[\Sigma_{imp}^{\alpha,\sigma}\right]_{pp}(\omega)-\left[\Sigma_{dc}^{\alpha,\sigma}\right]_{pp}(\omega)\right]\delta(\nu-\nu_p)\delta_{\nu\nu'}=\Delta\Sigma_p^{\alpha,\sigma}(\omega)\delta(\nu-\nu_p)\delta_{\nu\nu'} \tag{B.2}$$

[1] We do not take into account the spin-orbit coupling in the following study.

[2] We remind to the reader that there is only one Ir atom in the unit cell, so $\alpha = 1$ in (B.1).

This implies that $A^{\alpha,\sigma}_{m,m'}(\mathbf{k},\omega) = A^{\alpha,\sigma}_{m}(\mathbf{k},\omega)\delta_{mm'}$ and:

$$\begin{aligned} A^{\alpha,\sigma}_{m}(\mathbf{k},\omega) &= -\frac{1}{\pi}\sum_{\nu,\nu'}\sum_{j=1}^{3}\Im\mathfrak{m}\left[\Theta^{\alpha,\sigma}_{lm\nu j}(\mathbf{k})\frac{\delta(\nu-\nu_p)\delta_{\nu\nu'}}{\omega+i0^+ +\mu-\varepsilon^{\sigma}_{\mathbf{k}\nu_p}-\Delta\Sigma^{\alpha,\sigma}_{p}(\omega)}\left[\Theta^{\alpha,\sigma}_{lm\nu' j}(\mathbf{k})\right]^*\right] \\ &= -\frac{1}{\pi}\Im\mathfrak{m}\left[\frac{1}{\omega+i0^+ +\mu-\varepsilon^{\sigma}_{\mathbf{k}\nu_p}-\Delta\Sigma^{\alpha,\sigma}_{p}(\omega)}\left(\sum_{j=1}^{3}\Theta^{\alpha,\sigma}_{lm\nu_p j}(\mathbf{k})\left[\Theta^{\alpha,\sigma}_{lm\nu_p j}(\mathbf{k})\right]^*\right)\right]. \end{aligned} \tag{B.3}$$

If the character m corresponds to an Ir $5d$ t_{2g} orbital, this expression can be even more simplified. The Wannier functions were indeed constructed from the promoting of the Ir $5d$ t_{2g} orbital-part $u^{\alpha,\sigma}_{lm,1}(\mathbf{r}^{\alpha})$: in the considered energy-window, the one-to-one correspondence between bands and Wannier functions can then be extended to the *total* Ir $5d$ t_{2g} states. However, since the t_{2g} bands have both Ir $5d$ and O $2p$ characters,

$$\sum_{j=1}^{3}\Theta^{\alpha,\sigma}_{lm\nu_p j}(\mathbf{k})\left[\Theta^{\alpha,\sigma}_{lm\nu_p j}(\mathbf{k})\right]^* = \mathcal{D}^{\alpha,\sigma}_{m}(\mathbf{k})\delta_{mp} \tag{B.4}$$

where $\mathcal{D}^{\alpha,\sigma}_{m}(\mathbf{k})$ is the LDA partial DOS associated to ths pin σ and the m character along the band ν_p.

As a result, in the energy-window where the t_{2g} Wannier projectors were defined, the spectral density $A^{\alpha,\sigma}_{m}(\omega)$ associated to an Ir $5d$ t_{2g} orbital m can finally be estimated from the following formula:

$$A^{\alpha,\sigma}_{m}(\omega) = -\frac{1}{\pi}\sum_{\mathbf{k}\in BZ}\Im\mathfrak{m}\left[\frac{\mathcal{D}^{\alpha,\sigma}_{m}(\mathbf{k})}{\omega+i0^+ +\mu-\varepsilon^{\sigma}_{\mathbf{k}\nu_m}-\Delta\Sigma^{\alpha,\sigma}_{m}(\omega)}\right] \tag{5.7}$$

which is similar to the expression of the spectral function of a one-band model.

B.2 The self energy of a 3/4-filled two-band Hubbard model in the atomic limit

We consider the following two-band Hubbard model with only density-density terms:

$$\mathbf{H} = \sum_{i=1,2;\sigma=\uparrow,\downarrow}\varepsilon_i c^{\dagger}_{i\sigma}c_{i\sigma} + \sum_{i=1,2}Un_{i\uparrow}n_{i\downarrow} + (U-2J)(n_{1\uparrow}n_{2\downarrow}+n_{2\uparrow}n_{1\downarrow}) + (U-3J)(n_{1\uparrow}n_{2\uparrow}+n_{1\downarrow}n_{2\downarrow}) \tag{B.5}$$

We will assume that the two bands are degenerate ($\varepsilon_1 = \varepsilon_2 = \varepsilon_0$) and that $J \ll U$. As a result, the expression can be simplified as follows:

$$\mathbf{H} = \sum_{i=1,2;\sigma=\uparrow,\downarrow}\varepsilon_0 c^{\dagger}_{i\sigma}c_{i\sigma} + \sum_{i=1,2}Un_{i\uparrow}n_{i\downarrow} + U(n_{1\uparrow}n_{2\downarrow}+n_{2\uparrow}n_{1\downarrow}) + U(n_{1\uparrow}n_{2\uparrow}+n_{1\downarrow}n_{2\downarrow}) \tag{B.6}$$

The states of the system are:

- 1 state $|0\rangle$ of energy 0,
- 4 one-particle states $|i,\sigma\rangle$ $(i=1,2;\sigma=\uparrow,\downarrow)$ of energy ε_0,
- 6 two-particle states of energy $2\varepsilon_0+U$, which we denote $|2_j\rangle$ with $j=1,..,6$,
- 4 three-particle states $|3_j\rangle$ with $j=1,...,4$ of energy $3\varepsilon_0+3U$,

- 1 four-particle state $|4\rangle$ of energy $4\varepsilon_0 + 6U$

Our aim is to find the expression of the self-energy of this system when it is 3/4-filled: that is to say, when it accomodates 3 electrons. We perform the calculation at $T = 0$ K. Because of the degeneracy, the ground-state with three particle is:

$$|\Psi_0\rangle = \frac{1}{4}\sum_{j=1}^{4}|3_j\rangle \tag{B.7}$$

The spectral density of the system is the following:

$$\begin{aligned} A(\omega) &= \sum_{i=1,2}\sum_{\sigma}|\langle\Psi_0|c_{i\sigma}|4\rangle|^2\delta(\omega+\mu+(3\varepsilon_0+3U)-(4\varepsilon_0+6U)) \qquad \text{(B.8)}\\ &\quad+\sum_{i=1,2}\sum_{\sigma}\sum_{j=1}^{6}|\langle\Psi_0|c^{\dagger}_{i\sigma}|2_j\rangle|^2\delta(\omega+\mu+(2\varepsilon_0+U)-(3\varepsilon_0+3U))\\ &= \frac{3}{4}\delta(\omega+\mu-\varepsilon_0-2U)+\frac{1}{4}\delta(\omega+\mu-\varepsilon_0-3U) \qquad \text{(B.9)}\end{aligned}$$

As a result, the Green function of the system can be written as:

$$\begin{aligned} G(\omega) &= \frac{3}{4}\frac{1}{\omega+i\eta+\mu-\varepsilon_0-2U}+\frac{1}{4}\frac{1}{\omega-i\eta+\mu-\varepsilon_0-3U}\\ &= \frac{\omega+\mu-\varepsilon_0-\frac{11}{4}U}{(\omega+i\eta+\mu-\varepsilon_0-2U)(\omega-i\eta+\mu-\varepsilon_0-3U)} \qquad \text{(B.10)}\end{aligned}$$

And finally, the associated self-energy is:

$$\begin{aligned} \Sigma(\omega) &= G_0^{-1}(\omega)-G^{-1}(\omega)\\ &= (\omega+i\eta+\mu-\varepsilon_0)-\frac{(\omega+i\eta+\mu-\varepsilon_0-2U)(\omega-i\eta+\mu-\varepsilon_0-3U)}{\omega+\mu-\varepsilon_0-\frac{11}{4}U}\\ &= (\omega+i\eta+\mu-\varepsilon_0)-(\omega+i\eta+\mu-\varepsilon_0-2U)(1+\frac{\frac{U}{4}-i\eta}{\omega+\mu-\varepsilon_0-\frac{11}{4}U})\\ &= 2U+\frac{U}{4}\frac{\omega+i\eta+\mu-\varepsilon_0-2U}{\omega+\mu-\varepsilon_0-\frac{11}{4}U}\\ &= 2U+\frac{U}{4}\left(1+\frac{\frac{3}{4}U}{\omega+\mu-\varepsilon_0-\frac{11}{4}U}\right)\\ &= 3\left(\frac{3}{4}U\right)+\frac{\frac{3U^2}{16}}{\omega+\mu-\varepsilon_0-\frac{11}{4}U} \qquad \text{(B.11)}\end{aligned}$$

The chemical potential at T=0 K must lie between ε_0+2U and ε_0+3U. We take the value $\varepsilon_0+\frac{5}{2}U$ to be more symmetric, which allows to write the following expression for the self-energy:

$$\Sigma(\omega) = 3\left(\frac{3}{4}U\right)+\frac{3U^2}{16}\frac{1}{\omega-\frac{U}{4}} \tag{B.12}$$

Consequently, on the Matsubara axis, the self-energy is:

$$\begin{aligned} \Sigma(i\omega) &= \frac{9}{4}U+\frac{3U^2}{16}\frac{1}{i\omega-\frac{U}{4}}\\ &= 3\left(\frac{3}{4}U\right)-\frac{3U^3}{64}\frac{1}{\omega^2+\frac{U^2}{16}}-i\frac{3U^2}{16}\frac{\omega}{\omega^2+\frac{U^2}{16}} \qquad \text{(B.13)}\end{aligned}$$

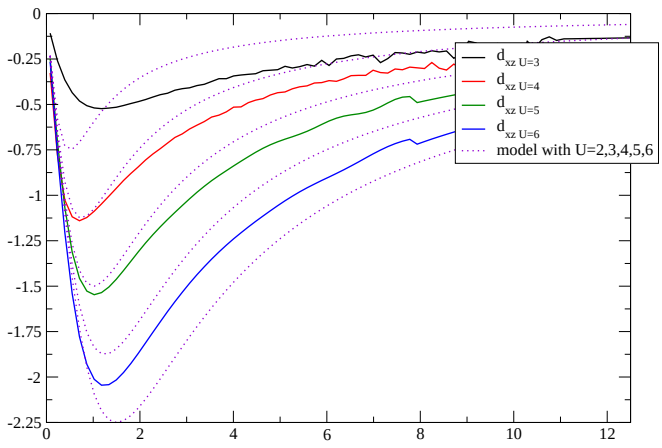

Figure B.1: Imaginary part of $\Sigma_{d_{xz}}(i\omega)$ for *undistorted* Sr_2IrO_4 without spin-orbit coupling T=300 K ($\beta = 40$ eV^{-1}) and with J=0.2 eV. The purple curves are the modelized behavior of the imaginary part of the self-energy for a 3/4 filled band in the atomic limit. For U$\geq$ 4 eV $\Sigma_{d_{xz}}(i\omega)$ behaves quite similarly as that of the model.

We have used this last expression to fit the self-energy associated to the d_{xz} – or equivalently d_{yz} – orbital for *undistorted* Sr_2IrO_4 without the spin-orbit coupling. As observed on figure B.1, the quality of the fitting increases as U becomes larger, namely when the atomic limit approximation becomes more and more valid.

To concude, we suggest that the expression (B.13) can be used as a general fitting expression for the imaginary and real parts of the self-energy each time the system can be considered as a 3/4-filled two-band problem.

Appendix C

Structure and conventions in *Wien2k*

In this appendix, we first describe the structure of a Wien2k calculation in order to complete the general introduction to this program which was begun in section 2.2. The second part of this appendix then focus on the conventions used in the auxiliary program lapw2 to calculate the coefficients $A_{lm}^{\nu\alpha}(\mathbf{k},\sigma)$, $B_{lm}^{\nu\alpha}(\mathbf{k},\sigma)$ and $C_{lm}^{\nu\alpha}(\mathbf{k},\sigma)$ of equation (2.35). Understanding these conventions was indeed an essential step in order to develop the interfacing program dmftproj.

C.1 General structure of the Wien2k package

The Wien2k package actually consists of several independent programs. We will give here only a general description of those which are used when a DFT-LDA calculation is performed. More technicalities on the overall structure of the Wien2k package and on the input and output files can be found in [23].

The initialization

The *initialization* consists of running a series of small auxiliary programs, which generates the inputs for the main programs. One first defines the structure of the studied compound – in a file called case.struct – and the initialization procedure is then performed by executing the script init_lapw. It consists in:

- calculating the muffin-tin radii R_{MT}^{α} for each atom α,
- generating all the symmetry operations of the *space group* of the compound,
- defining the *core*, *valence* and *semi-core* states,
- generating the **k**-mesh in the irreducible Brillouin zone,
- calculating finally a starting density $\rho(\mathbf{r})$ for the compound from the superposition of the free atomic densities.

The self-consistent cycle

The *self-consistent cycle* is initiated by executing the script run_lapw and is composed of the following steps:

- **lapw0** which generates the effective Kohn-Sham potential $V_{KS}(\mathbf{r})$ from the density $\rho(\mathbf{r})$ by using Poisson's equation to get $V_{ext}(\mathbf{r})$ and the LDA to get $V^{xc}(\mathbf{r})$,
- **lapw1** which calculates the eigenvalues $\varepsilon_{\mathbf{k}\nu}^{\sigma}$ and eigenvectors $|\psi_{\mathbf{k}\nu}^{\sigma}\rangle$ for the valence electrons,

- **lapw2** which computes the semi-core and valence densities $\rho_{valence}(\mathbf{r})$ from the eigenvectors,
- **lcore** which computes core states and their corresponding densities $\rho_{core}(\mathbf{r})$ within a fully relativistic treatment,
- **mixer** which calculates the total density $\rho(\mathbf{r}) = \rho_{core}(\mathbf{r}) + \rho_{valence}(\mathbf{r})$ and mixes input and output densities

The cycle is repeated until the convergence criterion is met. Usually, the calculation is considered as *converged* when the difference in energy between the two last iterations is less than 0.0001 Ry.

Taking into account the spin-orbit coupling

In order to perform a DFT calculation which includes the spin-orbit interaction, the standard procedure consists in running a regular self-consistent cycle calculation first and then initializing the spin-orbit coupling parameters for the compound to perform a second self-consistent cycle.

This specific *initialization step* is done by executing the script initso_lapw. Whereas for a non-spin-polarized case, the generation of the necessary input files is straightforward, care must be taken for spin-polarized cases: the spin-orbit interaction may indeed lower the symmetry of the system depending on how the direction of magnetization is chosen, as explained in [126].

The self-consistent cycle which includes the spin-orbit coupling is then performed by executing the script run_lapw -so. As described in section 3.3, a second variational approach is used to add the spin-orbit corrections to the scalar-relativistic orbitals calculated in lapw1. As a result, the general structure of the self-consistent loop is only slightly modified:

- the program lapwso is called directly after lapw1 to introduce the spin-orbit corrections in the total Hamiltonian,
- the basis $|\psi^+_{\nu\mathbf{k}}\rangle$, $|\psi^-_{\nu\mathbf{k}}\rangle$ must be considered (cf. equation (3.52)), which implies that the size of the matrix diagonalized in lapw1 is multiplied by two and the complex version of lapw2 is used .

C.2 Conventions for the symmetry operations in Wien2k

In this section, we introduce how the symmetry operations are stored and calculated in Wien2k. As we will see in Appendix E, understanding these technicalities are essential to define the projectors from the coefficients $A^{\nu\alpha}_{lm}(\mathbf{k},\sigma)$, $B^{\nu\alpha}_{lm}(\mathbf{k},\sigma)$ and $C^{\nu\alpha}_{lm}(\mathbf{k},\sigma)$ of (2.35) and perform the Brillouin zone integration.

C.2.1 Symmetry operations $\mathcal{T}$ and local rotations R_{loc}

As explained in Appendix E, the symmetry operations of the "*crystallographic space group*" of a compound have the general following form:

$$\forall\ \mathbf{r} \in \mathbb{R}^3 \qquad \mathcal{T}(\mathbf{r}) = \mathcal{R}(\mathbf{r}) + \mathbf{v} \tag{C.1}$$

where $\mathbf{v}$ is a translation vector which belongs to the Bravais lattice or is a rational fraction of such a vector and $\mathcal{R}$ is an operator of the *crystallographic point group* of the compound. In Wien2k, the symmetry operations $\mathcal{T}$ of the studied compound are calculated during the *initialization step* and described at the end of the case.struct file within the following form of a 3×4 matrix :

$$\begin{array}{cccc} r_{xx} & r_{xy} & r_{xz} & t_x \\ r_{yx} & r_{yy} & r_{yz} & t_y \\ r_{zx} & r_{zy} & r_{zz} & t_z \end{array} \iff \forall \quad \mathbf{u} \in \mathbb{R}^3 \quad \mathcal{T}(\mathbf{u}) = \begin{pmatrix} r_{xx} & r_{xy} & r_{xz} \\ r_{yx} & r_{yy} & r_{yz} \\ r_{zx} & r_{zy} & r_{zz} \end{pmatrix} \begin{pmatrix} u_x \\ u_y \\ u_z \end{pmatrix} + \begin{pmatrix} t_x \\ t_y \\ t_z \end{pmatrix}. \tag{C.2}$$

Each matrix is then read in the subroutine init_struct and stored under the following form :

$$\mathsf{iz(iord)} = {}^t\mathcal{R} \qquad \text{and} \qquad \mathsf{tau(iord)} = \mathbf{t} \tag{C.3}$$

where iord is the number of the symmetry operation. Although iz seems to describe $\mathcal{R}^{-1}$ – we remind the reader that the matrices $\mathcal{R}$ are orthogonal, so that ${}^t\mathcal{R} = \mathcal{R}^{-1}$ –, it should be kept in mind that this is just a way of storing the information : ^{t}iz(iord) will be actually used in most of the programs called during the calculation.

The previous symmetry operations are defined in the "*global coordinate system*". On the contrary, the local orbitals of each atom α of the unit cell are defined in the "*local coordinate system*" associated to this atom α. We insist that this *local frame* may be different for each atom α, even if they are of the same atomic species A. This *local frame* is defined in two steps:

- First, the symmetry operation $\mathcal{T}$ which transforms the first representant of the atomic species A into the atom α is applied. This transformation is computed in the subroutine permop of the Wien2k package.
- Then, the specific local rotation R^A_{loc} associated to the atomic species A and defined in the case.struct file is applied.

As a result, the transformation from the global coordinate system to the local frame of an atom α is:

$$R^\alpha_{loc} = R^A_{loc}.\mathcal{T}. \tag{C.4}$$

The matrices R^A_{loc} are also read in the subroutine init_struct and as previously, ${}^tR^A_{loc}$ are actually stored. In the following, only the operator part $\mathcal{R}$ of $\mathcal{T}$ will be considered. The translation vector $\mathbf{t}$ of $\mathcal{T}$ introduce only phase factor in the definition of the coefficients and can thus be neglected for calculating local quantities.

C.2.2 Representation of the symmetry operations by Euler angles

The symmetry operations $\mathcal{T}$ and the local rotation R^A_{loc} are described as matrices in real space $\mathbb{R}^3$ in the case.struct file. However, when applied to the coefficient, one must use the corresponding transformation matrices $\mathcal{D}^{\frac{1}{2}}(S)$ in spin-space or $\mathcal{D}^l(S)$ in the space spanned by the spherical harmonics Y^l_m, with $S = \mathcal{T}$ or R^A_{loc}.

In order to generate these matrices, it is necessary to determine if the transformation S is proper (its determinant is 1) or improper (its determinant is -1). In the first case, S can be completely described by three Euler angles α, β and γ. In the second case, S can always be written as the product of an inversion $I = -Id$ and a proper transformation. As a result $I.S$ can be completely described by three Euler angles α, β and γ.

The three Euler angles associated to a proper transformation S are calculated in the program euler of the Wien2k package. The convention used is the following:

$$S = R[\mathbf{z}](\gamma).R[\mathbf{y}](\beta).R[\mathbf{z}](\alpha) \tag{C.5}$$

where $R[\mathbf{z}](\gamma)$ stands for the rotation of angle $\gamma \in [0; 2\pi[$ around the $\mathbf{z}$-axis, $R[\mathbf{y}](\beta)$ is the rotation of angle $\beta \in [0; \pi]$ around the $\mathbf{y}$-axis and $R[\mathbf{z}](\alpha)$ the rotation of angle $\alpha \in [0; 2\pi[$ around the $\mathbf{z}$-axis.

This corresponds in $\mathbb{R}^3$ to:

$$\begin{aligned} D^{\mathbb{R}^3}(S) &= \begin{pmatrix} \cos\gamma & -\sin\gamma & 0 \\ \sin\gamma & \cos\gamma & 0 \\ 0 & 0 & 1 \end{pmatrix} \begin{pmatrix} \cos\beta & 0 & \sin\beta \\ 0 & 1 & 0 \\ -\sin\beta & 0 & \cos\beta \end{pmatrix} \begin{pmatrix} \cos\alpha & -\sin\alpha & 0 \\ \sin\alpha & \cos\alpha & 0 \\ 0 & 0 & 1 \end{pmatrix} \\ &= \begin{pmatrix} \cos\gamma\cos\beta\cos\alpha - \sin\gamma\sin\alpha & -\sin\gamma\cos\alpha - \cos\gamma\cos\beta\sin\alpha & \cos\gamma\sin\beta \\ \sin\gamma\cos\beta\cos\alpha + \cos\gamma\sin\alpha & \cos\gamma\cos\alpha - \sin\gamma\cos\beta\sin\alpha & \sin\gamma\sin\beta \\ -\sin\beta\cos\alpha & \sin\beta\sin\alpha & \cos\beta \end{pmatrix} \end{aligned} \tag{C.6}$$

However, the program euler does not calculate the Euler angles, it rather gives three parameters a, b and c which are linked to α, β and γ as follows:

- if $\beta = 0$, then b= 0, c= 0 and a= $2\pi - \alpha$ for $\alpha \in]0; 2\pi[$ and a= 0 when $\alpha = 0$,
- if $\beta = \pi$, then b= 0, a= 0 and c= $2\pi - \gamma$ for $\gamma \in]0; 2\pi[$ and c= 0 when $\gamma = 0$,
- if $\beta \in]0; \pi[$, then b= β, a= $\pi - \alpha$ for $\alpha \in [0; \pi]$ and a= $3\pi - \alpha$ for $\alpha \in]\pi; 2\pi[$ and similarly for c and γ.[1]

C.2.3 Standard computation of the rotation matrices

We remind briefly here how the rotation matrices $\mathcal{D}^{\frac{1}{2}}(S)$ or $\mathcal{D}^{l}(S)$ are usually calculated for a proper rotation, in order to ease the comparison with the matrices computed in Wien2k.

The proper rotations form the $\mathcal{O}^+(3)$ group which is a compact Lie group with 3 parameters. Let α_1, α_2 and α_3 be these parameters. Then, there exist 3 infinitesimal matrices I_1, I_2 and I_3 such that each element of this group can be written:

$$R(\alpha_1, \alpha_2, \alpha_3) = \exp I_1\alpha_1 + I_2\alpha_2 + I_3\alpha_3. \tag{C.7}$$

In particular, for a physical system if $\{1, 2, 3\}$ stands for $\{x, y, z\}$, it can be shown that:

$$R(\alpha_x, \alpha_y, \alpha_z) = \exp -\frac{i}{\hbar}(l_x\alpha_x + l_y\alpha_y + l_z\alpha_z) \tag{C.8}$$

where $\mathbf{l}$ is the angular momentum of the system. Using the convention used in Wien2k for the Euler angles (C.5) and the usual relations:

$$l_z|l, m\rangle = \hbar m|l, m\rangle \quad \text{and} \quad l_\pm|l, m\rangle = \hbar\sqrt{l(l+1) - m(m \pm 1)}|l, m \pm 1\rangle \quad \text{with} \quad l_+ = l_x \pm il_y \tag{C.9}$$

it is possible to get an explicit form for the irreducible representation associated to the rotation matrix $\mathcal{D}^l(R)$.

Case of $l = 0$

For $l = 0$, the representation is the trivial one :

$$\forall\alpha, \beta, \gamma \quad \mathcal{D}^0(R) = (1). \tag{C.10}$$

[1] These relations hold if the matrix used as an input of euler is directly iz(iord).

Case of the spin-space $l = \frac{1}{2}$

For $l = \frac{1}{2}$, we have the following matrices for the spin moment operators in the basis $\{|\uparrow\rangle, |\downarrow\rangle\}$:

$$s_x = \frac{\hbar}{2}\begin{pmatrix} 0 & 1 \\ 1 & 0 \end{pmatrix} \qquad s_y = \frac{\hbar}{2}\begin{pmatrix} 0 & -i \\ i & 0 \end{pmatrix} \qquad s_z = \frac{\hbar}{2}\begin{pmatrix} 1 & 0 \\ 0 & -1 \end{pmatrix}. \tag{C.11}$$

It is therefore quite simple to get the representation of a rotation around the **z**-axis:

$$\mathcal{D}^{\frac{1}{2}}(R[\mathbf{z}](\alpha)) = \begin{pmatrix} e^{-\frac{i\alpha}{2}} & 0 \\ 0 & e^{\frac{i\alpha}{2}} \end{pmatrix} \qquad \mathcal{D}^{\frac{1}{2}}(R[\mathbf{z}](\gamma)) = \begin{pmatrix} e^{-\frac{i\gamma}{2}} & 0 \\ 0 & e^{\frac{i\gamma}{2}} \end{pmatrix} \tag{C.12}$$

whereas the expression for a rotation around the **y**-axis is:

$$\mathcal{D}^{\frac{1}{2}}(R[\mathbf{y}](\beta)) = \sum_{n=0}^{\infty} \frac{(-1)^n}{(2n)!}\frac{\beta^{2n}}{2^{2n}}\begin{pmatrix} 1 & 0 \\ 0 & 1 \end{pmatrix} - i\frac{(-1)^n}{(2n+1)!}\frac{\beta^{2n+1}}{2^{2n+1}}\begin{pmatrix} 0 & -i \\ i & 0 \end{pmatrix} = \begin{pmatrix} \cos\frac{\beta}{2} & -\sin\frac{\beta}{2} \\ \sin\frac{\beta}{2} & \cos\frac{\beta}{2} \end{pmatrix} \tag{C.13}$$

Finally, we got the following general expression:

$$\mathcal{D}^{\frac{1}{2}}(R) = \begin{pmatrix} \cos\frac{\beta}{2}e^{-i\frac{\alpha+\gamma}{2}} & -\sin\frac{\beta}{2}e^{i\frac{\alpha-\gamma}{2}} \\ \sin\frac{\beta}{2}e^{-i\frac{\alpha-\gamma}{2}} & \cos\frac{\beta}{2}e^{i\frac{\alpha+\gamma}{2}} \end{pmatrix} \tag{C.14}$$

when R is defined by the Euler angles α, β and γ.

Case of orbital-spaces with $l \geq 1$

For integer values of $l \geq 1$, the representation needs of course more computational effort. We will only perform the calculation in the case $l = 1$. We have the following matrices for the kinetic operators in the basis $\{|1,-1\rangle, |1,0\rangle, |1,1\rangle\}$:

$$l_x = \frac{\hbar}{\sqrt{2}}\begin{pmatrix} 0 & 1 & 0 \\ 1 & 0 & 1 \\ 0 & 1 & 0 \end{pmatrix} \qquad l_y = \frac{i\hbar}{\sqrt{2}}\begin{pmatrix} 0 & 1 & 0 \\ -1 & 0 & 1 \\ 0 & -1 & 0 \end{pmatrix} \qquad l_z = \hbar\begin{pmatrix} -1 & 0 & 0 \\ 0 & 0 & 0 \\ 0 & 0 & 1 \end{pmatrix}. \tag{C.15}$$

The representation of a rotation around the **z**-axis are thus:

$$\mathcal{D}^{l}(R[\mathbf{z}](\alpha)) = \begin{pmatrix} e^{i\alpha} & 0 & 0 \\ 0 & 1 & 0 \\ 0 & 0 & e^{-i\alpha} \end{pmatrix} \qquad \mathcal{D}^{l}(R[\mathbf{z}](\gamma)) = \begin{pmatrix} e^{i\gamma} & 0 & 0 \\ 0 & 1 & 0 \\ 0 & 0 & e^{-i\gamma} \end{pmatrix} \tag{C.16}$$

whereas the expression for a rotation around the **y**-axis is:

$$\begin{aligned} \mathcal{D}^{l}(R[\mathbf{y}](\beta)) &= \mathcal{I}_3 + \sum_{n=1}^{\infty}\frac{1}{(2n)!}\frac{\beta^{2n}}{2^n}\begin{pmatrix} -(-2)^{n-1} & 0 & (-2)^{n-1} \\ 0 & (-2)^n & 0 \\ (-2)^{n-1} & 0 & -(-2)^{n-1} \end{pmatrix} \\ &\quad + \sum_{n=0}^{\infty}\frac{1}{(2n+1)!}\frac{\beta^{2n+1}}{2^n\sqrt{2}}\begin{pmatrix} 0 & (-2)^n & 0 \\ -(-2)^n & 0 & (-2)^n \\ 0 & -(-2)^n & 0 \end{pmatrix} \\ &= \begin{pmatrix} \frac{1+\cos\beta}{2} & \frac{\sin\beta}{\sqrt{2}} & \frac{1-\cos\beta}{2} \\ -\frac{\sin\beta}{\sqrt{2}} & \cos\beta & \frac{\sin\beta}{\sqrt{2}} \\ \frac{1-\cos\beta}{2} & -\frac{\sin\beta}{\sqrt{2}} & \frac{1+\cos\beta}{2} \end{pmatrix}. \end{aligned} \tag{C.17}$$

Finally, the general expression of a rotation matrix is:

$$\mathcal{D}^1(R) = \begin{pmatrix} \frac{1+\cos\beta}{2}e^{i(\alpha+\gamma)} & \frac{\sin\beta}{\sqrt{2}}e^{i\gamma} & \frac{1-\cos\beta}{2}e^{-i(\alpha-\gamma)} \\ -\frac{\sin\beta}{\sqrt{2}}e^{i\alpha} & \cos\beta & \frac{\sin\beta}{\sqrt{2}}e^{-i\alpha} \\ \frac{1-\cos\beta}{2}e^{i(\alpha-\gamma)} & -\frac{\sin\beta}{\sqrt{2}}e^{-i\gamma} & \frac{1+\cos\beta}{2}e^{-i(\alpha+\gamma)} \end{pmatrix} \tag{C.18}$$

when R is defined by the Euler angles α, β and γ.

C.2.4 Computation of the rotation matrices in Wien2k

A spinor rotation $\mathcal{D}^{\frac{1}{2}}(S)$ is defined by the following matrix in the basis $\{|\uparrow\rangle, |\downarrow\rangle\}$:

$$\forall\alpha,\beta,\gamma \quad \mathcal{D}^{\frac{1}{2}}(\mathsf{a},\mathsf{b},\mathsf{c}) = \begin{pmatrix} \cos\frac{\mathsf{b}}{2}e^{i\frac{\mathsf{a}+\mathsf{c}}{2}} & \sin\frac{\mathsf{b}}{2}e^{-i\frac{\mathsf{a}-\mathsf{c}}{2}} \\ -\sin\frac{\mathsf{b}}{2}e^{i\frac{\mathsf{a}-\mathsf{c}}{2}} & \cos\frac{\mathsf{b}}{2}e^{-i\frac{\mathsf{a}+\mathsf{c}}{2}} \end{pmatrix}. \tag{C.19}$$

The rotation matrices $\mathcal{D}^l(S)$ are calculated by the program dmat which creates the matrix whose coefficients are in the basis $\{|l,-l\rangle,\ldots,|l,l\rangle\}$:

$$\begin{aligned} \left(\mathcal{D}^l(\mathsf{a},\mathsf{b},\mathsf{c})\right)_{m,n} &= e^{i(n\mathsf{a}+m\mathsf{c})}\sqrt{\frac{(l+m)!(l-m)!}{(l+n)!(l-n)!}}\cdot\sum_{k=0}^{2l}(-1)^{l-m-k}C_{m,n}^{l,k}(\sin\frac{\mathsf{b}}{2})^{2l-m-n-2k}(\cos\frac{\mathsf{b}}{2})^{2k+m+n} \\ \text{with} \qquad C_{m,n}^{l,k} &= \frac{(l+n)!(l-n)!}{(l-m-k)!(m+n+k)!(l-n-k)!k!} \quad \text{and} \quad m,n\in[-l;l] \end{aligned} \tag{C.20}$$

For each $\left(\mathcal{D}^l(\mathsf{a},\mathsf{b},\mathsf{c})\right)_{m,n}$, the value of k considered in the sum are only those for which :

$$l-m-k\geq 0 \quad \text{and} \quad l-n-k\geq 0 \quad \text{and} \quad m+n+k\geq 0. \tag{C.21}$$

To understand better this expression, we compute explicitly the rotation matrix in the subspace $l=1$. The basis considered is thus $\{|1,-1\rangle,|1,0\rangle,|1,1\rangle\}$ and we get:

$$\begin{aligned} \mathcal{D}^1(\mathsf{a},\mathsf{b},\mathsf{c}) &= \begin{pmatrix} (\cos\frac{\mathsf{b}}{2})^2e^{-i(\mathsf{a}+\mathsf{c})} & -\sqrt{2}\sin\frac{\mathsf{b}}{2}\cos\frac{\mathsf{b}}{2}e^{-i\mathsf{c}} & (\sin\frac{\mathsf{b}}{2})^2e^{i(\mathsf{a}-\mathsf{c})} \\ \sqrt{2}\sin\frac{\mathsf{b}}{2}\cos\frac{\mathsf{b}}{2}e^{-i\mathsf{a}} & (\cos\frac{\mathsf{b}}{2})^2-(\sin\frac{\mathsf{b}}{2})^2 & -\sqrt{2}\sin\frac{\mathsf{b}}{2}\cos\frac{\mathsf{b}}{2}e^{i\mathsf{a}} \\ (\sin\frac{\mathsf{b}}{2})^2e^{-i(\mathsf{a}-\mathsf{c})} & \sqrt{2}\sin\frac{\mathsf{b}}{2}\cos\frac{\mathsf{b}}{2}e^{i\mathsf{c}} & (\cos\frac{\mathsf{b}}{2})^2e^{i(\mathsf{a}+\mathsf{c})} \end{pmatrix} \\ &= \begin{pmatrix} \frac{1+\cos\mathsf{b}}{2}e^{-i(\mathsf{a}+\mathsf{c})} & -\frac{\sin\mathsf{b}}{\sqrt{2}}e^{-i\mathsf{c}} & \frac{1-\cos\mathsf{b}}{2}e^{i(\mathsf{a}-\mathsf{c})} \\ \frac{\sin\mathsf{b}}{\sqrt{2}}e^{-i\mathsf{a}} & \cos\mathsf{b} & -\frac{\sin\mathsf{b}}{\sqrt{2}}e^{i\mathsf{a}} \\ \frac{1-\cos\mathsf{b}}{2}e^{-i(\mathsf{a}-\mathsf{c})} & \frac{\sin\mathsf{b}}{\sqrt{2}}e^{i\mathsf{c}} & \frac{1+\cos\mathsf{b}}{2}e^{i(\mathsf{a}+\mathsf{c})} \end{pmatrix} \end{aligned} \tag{C.22}$$

By comparing this expression with (C.18) and by taking into account the definition of the parameters a, b and c, it appears that $\mathcal{D}^1(\mathsf{a},\mathsf{b},\mathsf{c})$ corresponds to $\mathcal{D}^l(R)$. In spin-space however, some phase factors need to be compensated because of factor $\frac{1}{2}$.

We have only discussed here the proper transformation. As we mentioned previously, a transformation can also be improper and can thus be written as the product of a proper rotation and a spatial inversion $I=-Id$. However, inversion I acts only on the **r**-space and doesn't affect the spin-space. As a result, taking into account this transformation consists merely in adding a factor $(-1)^l$ in $\mathcal{D}^l(R)$ – and $\mathcal{D}^l(\mathsf{a},\mathsf{b},\mathsf{c})$ – for integer values of l, whereas no change in $\mathcal{D}^{\frac{1}{2}}(R)$ – and $\mathcal{D}^{\frac{1}{2}}(\mathsf{a},\mathsf{b},\mathsf{c})$ – occurs.

C.3 Conventions for the coefficients $A_{lm}^{\nu\alpha}(\mathbf{k},\sigma)$, $B_{lm}^{\nu\alpha}(\mathbf{k},\sigma)$ and $C_{lm}^{\nu\alpha}(\mathbf{k},\sigma)$

The charge density $\rho(\mathbf{r})$ is calculated in lapw2 in the *global coordinate system* of the compound. However, the coefficients $A_{lm}^{\nu\alpha}(\mathbf{k},\sigma)$, $B_{lm}^{\nu\alpha}(\mathbf{k},\sigma)$ and $C_{lm}^{\nu\alpha}(\mathbf{k},\sigma)$ of (2.35) are defined in the *local coordinate system* associated to the atom α. A multiplication by a transformation from the *global* frame to the *local* frame of the atom α is then applied in the program lapw2.

However, contrary to what we would have expected, we noticed that this transformation is applied *without taking into account the spinor rotation matrix* and even when the calculation explicitly includes the spin-orbit coupling. In order to remain consistent in our implementation of dmftproj, we thus had to introduce this lacking coefficients in the definition of the coefficients $A_{lm}^{\nu\alpha}(\mathbf{k},\sigma)$, $B_{lm}^{\nu\alpha}(\mathbf{k},\sigma)$ and $C_{lm}^{\nu\alpha}(\mathbf{k},\sigma)$. This is done in the program set_projections.

Appendix D

Description of dmftproj

In this appendix, we present the general structure of the interfacing program dmftproj and give a brief tutorial to its use. More information are available in [110].

D.1 General structure of dmftproj

The dmftproj program is structured as follows:

- the input file case.indmftpr is first read in order to define which projectors $P^{\alpha\sigma}_{lm,\nu}(\mathbf{k})$ and $\Theta^{\alpha,\sigma}_{lm\nu j}(\mathbf{k})$ will be calculated during the execution.
- the $\Theta^{\alpha}_{lm\nu j}(\mathbf{k})$ projectors are then built without any restriction in the energy window, in order to evaluate the density matrices of each orbital character. The results obtained are the same as obtained with the program lapwdm of the Wien2k package.
- the projectors $P^{\alpha\sigma}_{lm,\nu}(\mathbf{k})$ are then constructed for the chosen orbitals – the "correlated" ones – and the density matrix associated to the obtained Wannier orbitals is finally displayed.

The dmftproj program is composed of the following auxiliary subroutines:

set_ang_trans: it sets the transformation from the complex basis to the desired one.

setsym: it sets the symmetry matrices of the system after reading the case.dmftsym file.

set_rotloc: it sets the local rotation matrices R^{α}_{loc} for each atom of the system (cf. Appendix C).

set_projections: it computes the projectors $\widetilde{P}^{\alpha\sigma}_{lm,\nu}(\mathbf{k})$ and $\Theta^{\alpha}_{lm\nu j}(\mathbf{k})$, as explained in sections 2.3, 3.3 and 3.4.

orthogonal_wannier : it performs the orthogonalization for the projectors $\widetilde{P}^{\alpha\sigma}_{lm,\nu}(\mathbf{k})$ in order to get the final $P^{\alpha\sigma}_{lm,\nu}(\mathbf{k})$ projectors.

density: it calculates the local density matrix associated to each atom.

symmetrize_mat: it performs the symmetrization in order to get the integration over the whole Brillouin zone when the density matrices are calculated. (cf. discussion in section 2.3 and Appendix E)

To allow the interfacing, some changes were also introduced in the program lapw2 in order to get the coefficients $A^{\nu\alpha}_{lm}(\mathbf{k},\sigma)$, $B^{\nu\alpha}_{lm}(\mathbf{k},\sigma)$ and $C^{\nu\alpha}_{lm}(\mathbf{k},\sigma)$ of (2.35) in the file case.almblm and the description of the symmetry operations in the file case.dmftsym. However, we will not describe the technicalities of these modifications here.

D.2 Description of the master input file case.indmftpr

The master input file case.indmftpr of dmftproj has the following structure. We give an example of such a file in the case of Sr_2IrO_4.

a)	3	! nsort
	1 2 2 2	! mult(isrt)
	3	! lmax
b-1)	fromfile	! basis
	file_name	
	1 1 2 0	! lsort(l)
	0 0 2 0	! nb_irep(l)
	01	
	0	! ifSO
b-2)	complex	! basis
	1 0 0 0	! lsort(l)
	0 0 0 0	! nb_irep(l)
b-3)	cubic	! basis
	1 1 2 0	! lsort(l)
	0 0 1 0	! nb_irep(l)
	0	! ifSO
c)	-0.26 0.48	! e_bot and e_top
	0.65650	! e_Fermi

Part a) is the general description for the considered material:

nsort: number (integer) of inequivalent atomic sort in the system,

mult(isrt): nsort integers equal to the multiplicity of each sort in the unit cell,

lmax: maximal l number (integer) considered in the system.

Part b) describes the chosen "treatment" for each atomic sort (it must then be repeated nsort time). Moreover, the order for the description must be the same as in the case.struct file.

basis: name associated to the description of the basis (for the projector). It can be:

- *complex* for complex spherical harmonics,
- *cubic* for cubic spherical harmonics.
- *fromfile* for a basis described in an added file. In this last case, the complete name of the file must be written the line after. In the example, the file is thus called "file_name". This file must be in the directory where the computation is performed. It must contain the description of the basis for all the included orbital. No newline for the separation of the basis description is needed. The s-orbital does not need a basis description in this file, if it is included.

lsort(l): (lmax+1) integers to describe the "treatment" of each orbital:

- 0 means that the corresponding orbital is not included,
- 1 means that the orbital is included but no projector $P^{\alpha\sigma}_{lm,\nu}(\mathbf{k})$ will be calculated for it. (this corresponds to an orbital "significantly present" in the considered energy window but which do not require a DMFT calculation to treat its correlation level),

- 2 means that the orbital is included and a projector $P^{\alpha\sigma}_{lm,\nu}(\mathbf{k})$ will be calculated for it. (this typically corresponds to an orbital "significantly present" in the considered energy window and *correlated*.)

nb_irep(l): (lmax+1) integers to describe the number of irreducible representation (irep) to consider for each orbital l. This description is read (and used) only if the corresponding lsort(l)=2. only *one* particular irep can be "*correlated*". If the number of irep is more than 2 for one orbital, the line after must describe the treatment of each irep (nb_irep(l) number in this line) with a flag (0/1) (cf. case b-1):

- 0 means that the orbital is not *correlated* ; no projector $P^{\alpha\sigma}_{lm,\nu}(\mathbf{k})$ will be calculated for it,
- 1 means that the orbital is *correlated* and a projector $P^{\alpha\sigma}_{lm,\nu}(\mathbf{k})$ will be calculated for it.

ifSO: flag (0/1) which states if the spin-orbit coupling is taken into account for this atomic sort. This flag is necessary only if one of the orbital of the sort is *correlated*. That is why this line does not appear in the section b-2.

Part c) finally precises the last options for the computation:

e_bot and **e_top** define the size of the energy window (given in Rydberg and relatively to the Fermi level),

e_Fermi is the Fermi level obtained at the end of the DFT calculation. This line is read only when one wants to calculate the momentum-resolved spectral function for the system.

Remark : The number of irreducible representation depends on the chosen basis description.

For the complex basis, none is possible. (irep=0).

For the cubic basis, they are implemented only in the case without any spin-orbit coupling (for instance : e_g-t_{2g} for $l = 2$).

When one uses the option fromfile, several irep could be considered even with spin-orbit coupling but it depends of course on the chosen basis. In the added file, the irep are indicated by a star (*) at the beginning of a line.

D.3 Execution of the program

D.3.1 In order to perform a DMFT calculation

Before running dmftproj, the coefficients $A^{\nu\alpha}_{lm}(\mathbf{k},\sigma)$, $B^{\nu\alpha}_{lm}(\mathbf{k},\sigma)$ and $C^{\nu\alpha}_{lm}(\mathbf{k},\sigma)$ of (2.35) and some other general informations on the system (symmetry operations and local rotations) must be calculated. The lapw2 program has thus to be executed in the following way:

```
x lapw2 -almd [-up/-dn -c -so]
```

The new flag "-almd" is written in the first line of case.in2(c) so that the input files (case.almdblm(up/dn) and case.dmftsym) for dmftproj are produced. The master input file required by dmftproj is called case.indmftpr and was described previously. The program should be executed as follows:

```
dmftproj [-sp] [-so]
```

The options stand for spin-polarized (-sp) calculations and for calculation which takes into account the spin-orbit interaction (-so). For technical reasons, the spin-orbit coupling is however implemented for the spin-polarized case only.

We remind that up to now the dmftproj program can be used only with a Continuous-Time Quantum Monte Carlo (CTQMC) impurity solver and an Hubbard-I solver.

D.3.2 In order to calculate a momentum-resolved spectral function

To produce the output needed to calculate the momentum-resolved spectral function after a DMFT calculation was performed, one must first prepare the desired **k**-point path for $A(k,\omega)$ in a case.klist_band file. Then, the same procedure as used in Wien2k to calculate Kohn-Sham band structure must be applied:

```
x lapw1 [-up/-dn-so] -band
x lapw2 -alm [-up/-dn-so] -band
```

After putting the Fermi energy of the system in the last line of the file case.indmftpr, it is then enough to execute the following command in the same directory:

```
dmftproj [-sp] [-so] -band
```

D.4 Description of the output files

D.4.1 Output to perform a DMFT calculation

The subroutine outputqmc.f of dmftproj produces the following four data files required to perform a DMFT calculation and some simple post-processing of the results:

i) case.ctqmcout and case.symqmc: these files contain all the main data to perform the DMFT self-consistent loop.

   More precisely, case.ctqmcout describes the number of k-points in IBZ, the total number of orbitals, and correlated orbitals, the multiplicity of each sort of atoms, the rotation matrices, the projectors $P^{\alpha\sigma}_{lm,\nu}(\mathbf{k})$ to correlated orbitals, the **k**-point weights, the eigenvalues of the Hamiltonian in Kohn-Sham basis. case.symqmc contains the number of symmetry operations for the symmetrization, the corresponding permutation matrices, the rotations matrices $\mathcal{D}^{l}_{mm'}(R)$, and additional transformation if symmetry-adapted basis is required

ii) case.parproj and case.sympar: thes files contain the same informations as the previous ones but are used to recalculate partial quantities (for example the spectral density) after the DMFT calculation. Instead of describing the Wannier projectors, they give the projectors $\Theta^{\alpha,\sigma}_{lm\nu j}(\mathbf{k})$.

D.4.2 Output for calculating a momentum-resolved spectral function

The flag -band allows to produce the file case.outband which contains: the projectors of the correlated orbitals, $P^{\alpha\sigma}_{lm,\nu}(\mathbf{k})$ for the new k-points, the corresponding eigenvalues, the projectors $\Theta^{\alpha}_{lm\nu j}(\mathbf{k})$, if some fatband character plotting are desired, information on the new **k**-list (especially, the labels for special **k**-points).

It is then possible to plot the momentum-resolved spectral function, to compare the result of the LDA+DMFT calculation with the experimental curves obtained with Angle-Resolved Photo-Emission Spectroscopy (ARPES).

More precise description of these files can be found in the tutorial of the programm [110].

Appendix E

Symmetry operations and projectors

In this appendix, we explain the formula to integrate over the all Brillouin zone (for local quantities like G_{loc}, the density matrix or the spectral density $A(\omega)$). As we have highlighted at the end of the section XXX, we have to go from the irreducible BZ to the full BZ and then use symmetry operation of the space group of the compound. However, in Wien2k and dmftproj, this is not the ordinary "*crystallographic space group*" which is considered in this sum but the "*Shubnikov (magnetic) group*" of the compound.

In a first part, we give an introduction to the "*Shubnikov (magnetic) group*" which introduce the time-operator Θ. we then remind the unusual properties of an anti-symmetry operators, before determining the modification of the projectors when they are applied any symmetry operations. We conclude by deriving the equations...

E.1 Space groups and time reversal operator

As mentioned in section 1.1, to describe a crystal – in which the atomic nuclei are arranged in an orderly periodic pattern in the three spatial dimensions –, it is convenient to define the "*Bravais lattice*" $\mathcal{B}$ and the "*crystallographic point group*" of the compound. More generally, one introduces the "*crystallographic space group*" of a crystal as the set of all the symmetry operations $\mathcal{T}$ which leave the system invariant after applying any of them to it. These operations have the following form:

$$\forall\ \mathbf{r} \in \mathbb{R}^3 \qquad \mathcal{T}(\mathbf{r}) = \mathcal{R}(\mathbf{r}) + \mathbf{v} \tag{E.1}$$

where $\mathbf{v}$ is a translation vector which belongs to the Bravais lattice or is a rational fraction of such a vector and $\mathcal{R}$ is an operator of the *crystallographic point group*: a rotation through integral multiple of $\frac{2\pi}{n}$ about some axis, a rotation-reflection, a rotation-inversion, a reflection or an inversion.

By combining the 32 *crystallographic point group* with the 14 *Bravais lattices*, there turn out to be 230 different *space groups* in three dimensions. More details can be found in [16, 25]. These groups were regarded as the ultimate development in the study of the symmetry of a crystal until Shubnikov introduced the idea of operations of *anti-symmetry* in 1951 [147].

Brief introduction to Shubnikov magnetic groups

By considering an extra coordinate, with only two possible values, in addition to the ordinary position coordinates – for instance, the direction of a local magnetic moment, parallel or anti-parallel to a given direction –, it is possible to define the operation of *anti-symmetry* as the operation which changes the value of this coordinate. If we call this operation Θ, it is then possible to have compound operations of anti-symmetry corresponding to the performance of both an ordinary *space group* operation $\mathcal{T}$ – or *point group* operation – together with the operation Θ.

As a result, many more point groups and space groups can be defined. They are respectively 122 and 1651 of them and they are referred to the "*Shubnikov (magnetic) groups*".

The *Shubnikov groups* are of great use to describe the symmetry of magnetic crystals. In this case, Θ is the operation which reverses the magnetic moment and corresponds to the *time reversal* operation. A change of magnetic moment can indeed be thought as caused by a reversal of the direction of the electric current which gives rise to it and this reversal of the direction is equivalent to a reversal of the sense of the direction of the time variable (since $i = \frac{dq}{dt}$).

Classification of Shubnikov point groups

In the following, we will only consider *Shubnikov magnetic point groups*. If $\mathcal{G}$ denotes one of the ordinary *crystallographic point groups*, there are three types of Shubnikov group corresponding to it:

type I: the "*uncolored*" or standard point group $\mathcal{G}$;

type II: the "*grey*" point group defined as $\mathcal{G} + \Theta\mathcal{G}$

type III: the "*black and white*" point group which is given by: $\mathcal{H} + \Theta\,(\mathcal{G} \setminus \mathcal{H})$, where $\mathcal{H}$ is a halving subgroup of $\mathcal{G}$.

Type II or *grey* point groups possess the operation of time inversion Θ itself as a symmetry operation. As a result, no spontaneous magnetic field can exist anywhere in the crystal. Therefore, either the individual atoms within the crystal have no magnetic moments – the compound can only exhibit diamagnetism –, or they do possess spontaneous magnetic moments but randomly oriented – the compound is paramagnetic –.

On the contrary, the operation of antisymmetry is absent in type I groups or is only present in combination with a symmetry operation $\mathcal{R}$ in type III groups. Consequently, it may be possible for a crystal described by these groups to possess a net magnetic moment – ferromagnetic or ferrimagnetic crystal – or to be antiferromagnetic.

We will not going further in the theoretical description of *Shubnikov magnetic point groups* and their properties. The interested reader can find a detailled presentation in [25].

In Wien2k, a "*grey*" (type II) point group is always used when performing a *paramagnetic* computation and a "*black and white*" (type III) point group is always considered when the calculation is *spin-polarized*. The same conventions were applied when implementing the interfacing program dmftproj.

E.2 Properties of an antilinear operator

Any *anti-symmetry* – and among them the *time reversal* operation – is described by an *antilinear* operator Θ:

$$\forall \lambda, \mu \in \mathbb{C} \quad \forall \mathbf{u}, \mathbf{v} \qquad \Theta(\lambda \mathbf{u} + \mu \mathbf{v}) = \lambda^* \Theta(\mathbf{u}) + \mu^* \Theta(\mathbf{v}) \tag{E.2}$$

and more precisely an *antiunitary* operator – with the property $\Theta^\dagger = \Theta^{-1}$. In this section, we briefly remind some unusual properties of such operators.

General properties

Let Θ_1 and Θ_2 be two operators.

If both Θ_1 and Θ_2 are antilinear, their product $\Theta_1\Theta_2$ is a linear operator. If Θ_1 – or Θ_2 – is antilinear and the other is linear, the product $\Theta_1\Theta_2$ is still antilinear.

If Θ_1 is an antilinear operator, its inverse Θ_1^{-1} and its Hermitian conjugate $\Theta_1^\dagger$ are antilinear too.

The time reversal operator Θ and the conjugation operator K

In the basis $|\mathbf{r},\sigma\rangle$, the expression of the *time reversal* operator Θ is:

$$\Theta = -i\sigma_y.K_{\mathbf{r}} \quad \text{with} \quad \sigma_y = \begin{pmatrix} 0 & -i \\ i & 0 \end{pmatrix} \tag{E.3}$$

where $K_{\mathbf{r}}$ is the conjugation operator in this same basis, or in other words:

$$\forall|\mathbf{r},\sigma\rangle \quad \forall\lambda \qquad K_{\mathbf{r}}\left(\lambda|\mathbf{r},\sigma\rangle\right) = \lambda^*|\mathbf{r},\sigma\rangle \tag{E.4}$$

More generally, it can be shown [112] that any antiunitary operator can be written as the product of the complex conjugation operator K times a linear "standard" operator:

$$\Theta = \Theta K^2 = (\Theta K)K = K(K\Theta) \quad \text{since} \quad K^2 = Id \tag{E.5}$$

Matrix representation of an antilinear operator

It is possible to use a matrix representation for K or any antilinear operator. In this case, it is necessary to impose the following convention: *all the matrices at the right-hand side of the "antilinear" matrix should be complex conjugate.*

Indeed, let $(\mathbf{e}_i)_{i\in I}$ be the basis of a $\mathbb{C}$-vector space and $T = \mathcal{D}(\Theta)$ the representation of the operator Θ in this vector space. Moreover, let $B = \mathcal{D}(f)$ be the representation of the endomorphism f.

$$\forall j \in I \quad \Theta.f(\mathbf{e}_j) = \Theta(\sum_k b_{kj}\mathbf{e}_k) = \sum_k b^*_{kj}\Theta(\mathbf{e}_k) = \sum_{i,k} t_{ik}b^*_{kj}\mathbf{e}_i \iff \mathcal{D}(\Theta.f) = T.B^* \tag{E.6}$$

$$\forall j \in I \quad f.\Theta(\mathbf{e}_j) = f(\sum_k t_{kj}\mathbf{e}_k) = \sum_k t_{kj}f(\mathbf{e}_k) = \sum_{i,k} b_{ik}t_{kj}\mathbf{e}_i \iff \mathcal{D}(f.\Theta) = B.T \tag{E.7}$$

If f is antilinear too, it can be shown in a similar way that:

$$\mathcal{D}(\Theta.f) = T.B^* \quad \text{and} \quad \mathcal{D}(f.\Theta) = B.T^* \tag{E.8}$$

As a result, in the particular case where Θ is bijective and $f = \Theta^{-1}$, we have the following relation:

$$T.(T^{-1})^* = T^{-1}.T^* = Id \tag{E.9}$$

Change of basis

As seen in (E.4), the definition of the K operator depends *explicitly* of the basis. This property holds also for any antilinear operator.

Let's now consider that f is an automorphism, that is to say a bijective endomorphism. Then if $f_i = f(\mathbf{e}_i)$, $(f_i)_{i\in I}$ is also a basis of our considered $\mathbb{C}$-vector space. Let $B = \mathcal{D}_{e_i}(f)$ and $C = B^{-1} = \mathcal{D}_{f_i}(f^{-1})$. We are now interested in the matrix representation of Θ in this new basis.

$$\forall j \in I \quad \Theta(f(\mathbf{e}_j)) = \Theta(\sum_l b_{lj}\mathbf{e}_l) = \sum_k b^*_{lj}\Theta(\mathbf{e}_l) = \sum_{k,l} t_{kl}b^*_{lj}\mathbf{e}_k = \sum_{i,k,l} c_{ik}t_{kl}b^*_{lj}f(\mathbf{e}_i) \tag{E.10}$$

and therefore

$$\mathcal{D}_{f_i}(\Theta) = C.\mathcal{D}_{e_i}(\Theta).B^* \qquad \text{or} \qquad T_{f_i} = B^{-1}.T_{e_i}.B^* \tag{E.11}$$

Hermitian adjoint of an antilinear operator

The usual definition – for a linear operator A – of its Hermitian adjoint is:

$$\langle A^\dagger y, x\rangle = \langle y, Ax\rangle \tag{E.12}$$

In the case of an antilinear operator Θ, this definition is slightly modified:[1]

$$\langle \Theta^\dagger y, x\rangle = (\langle y, \Theta x\rangle)^* \quad \text{or} \quad \langle x, \Theta^\dagger y\rangle = \langle y, \Theta x\rangle \tag{E.13}$$

Let then be $T = \mathcal{D}(\Theta)$ and $U = \mathcal{D}(\Theta^\dagger)$. The usual relation for linear operators – namely $U = {}^tT^*$ – doesn't hold anymore for antilinear operator:

$$\begin{aligned} \forall\ i,j\ \in\ I \qquad \langle e_i, \Theta^\dagger e_j\rangle &= \langle e_i, \sum_k u_{kj} e_k\rangle = \sum_k u_{kj}\langle e_i, e_k\rangle = u_{ij} \\ \langle e_i, \Theta^\dagger e_j\rangle &= \langle e_j, \Theta e_i\rangle = \langle e_j, \sum_k t_{ki} e_k\rangle = \sum_k t_{ki}\langle e_j, e_k\rangle = t_{ji} \end{aligned} \tag{E.14}$$

Therefore the *true* relation is merely: $U = {}^tT$

E.3 Action of a space group operation on the projectors

In order to obtain the formulas involving a sum over the irreducible Brillouin zone, the action of the space group operations on the Wannier and $\Theta-$projectors, $P^{\alpha,\sigma}_{lm,\nu}(\mathbf{k})$ and $\Theta^{\alpha,\sigma}_{lm,\nu j}(\mathbf{k})$, must be known. In this section, we calculate it explicitly.

In the following, we will only consider the ordinary point group operators[2] $\mathcal{R}$ and we will denote Θ the time reversal operator. According to section E.1, we thus have to study symmetry operations $\mathcal{S}$ of the form $\mathcal{R}$ or $\Theta\mathcal{R}$

E.3.1 Action of a space group operation on the Bloch states

From Bloch theorem, we have:

$$H\psi_{\mathbf{k},\nu}(\mathbf{r}) = \varepsilon_{\mathbf{k},\nu}\psi_{\mathbf{k}\nu}(\mathbf{r}) \qquad \Longleftrightarrow \qquad \psi_{\mathbf{k},\nu}(\mathbf{r}) = e^{i\mathbf{k}.\mathbf{r}}u_{\mathbf{k}}(\mathbf{r}) \quad \text{with} \quad u_{\mathbf{k},\nu}(\mathbf{r}+\mathbf{R}) = u_{\mathbf{k},\nu}(\mathbf{r}) \quad \forall\ \mathbf{R}\in\mathcal{B} \tag{E.15}$$

By definition, the symmetry operators $\mathcal{S}$ are such that $[H,\mathcal{S}] = 0$. Consequently, if $|\psi_{\mathbf{k}\nu}\rangle$ is an eigenvector of H, $\mathcal{S}|\psi_{\mathbf{k}\nu}\rangle$ is also an eigenvector of H with the same eigenvalue. We now precise the action of $\mathcal{S}$ on the momentum $\mathbf{k}$ and the spin index σ. We will not study the effect of the symmetry operation on the band index ν, since it really depends on what it is standing for. We will merely denote $\mathcal{S}\nu$ as the image by $\mathcal{S}$ of ν in the following.

If $\mathcal{S} = \mathcal{R}$,

$$\langle\mathbf{r}|\mathcal{S}|\psi_{\mathbf{k},\nu}\rangle = \langle\mathcal{R}^{-1}\mathbf{r}|\psi_{\mathbf{k},\nu}\rangle = \psi_{\mathbf{k}\nu}(\mathcal{R}^{-1}\mathbf{r}) = e^{i\mathbf{k}\cdot\mathcal{R}^{-1}\mathbf{r}}u_{\mathbf{k},\nu}(\mathcal{R}^{-1}\mathbf{r}) \tag{E.16}$$

Defining $u_{\mathcal{R}\mathbf{k},\mathcal{R}\nu}(\mathbf{r}) = u_{\mathbf{k},\nu}(\mathcal{R}^{-1}\mathbf{r})$ which still verifies $u_{\mathcal{R}\mathbf{k},\mathcal{R}\nu}(\mathbf{r}+\mathbf{R}) = u_{\mathcal{R}\mathbf{k},\mathcal{R}\nu}(\mathbf{r})\ \forall\ \mathbf{R}\in\mathcal{B}$, we can then write:

$$\langle\mathbf{r}|\mathcal{S}|\psi_{\mathbf{k},\nu}\rangle = e^{i\mathcal{S}\mathbf{k}\cdot\mathbf{r}}u_{\mathcal{R}\mathbf{k},\mathcal{R}\nu}(\mathbf{r}) = \psi_{S\mathbf{k},\mathcal{S}\nu}(\mathbf{r}) = \langle\mathbf{r}|\psi_{S\mathbf{k},\mathcal{S}\nu}\rangle \quad \text{hence} \quad \mathcal{S}|\psi_{\mathbf{k},\nu}\rangle = |\psi_{\mathcal{S}\mathbf{k},\mathcal{S}\nu}\rangle \tag{E.17}$$

[1] The existence of the Hermitian adjoint is shown by using the Riesz representation theorem. In order to apply it, the conjugate expression of the scalar product must indeed be considered.

[2] Taking into account the translation vector $\mathbf{v}$ of the more general space group operation $\mathcal{T}$ only introduce a phase factor, which will anyway disappear when local quantities are calculated.

If we add the spin quantum number, we have to consider the spinor $|\Psi_{\mathbf{k}}\rangle$ and the representation of the transformation $\mathcal{S}$ in the spin-space, $D^{\frac{1}{2}}(\mathcal{S})$, introduced in Appendix C:

$$|\Psi_{\mathbf{k},\nu}\rangle = \begin{pmatrix} |\psi^{\uparrow}_{\mathbf{k},\nu}\rangle \\ |\psi^{\downarrow}_{\mathbf{k},\nu}\rangle \end{pmatrix} \qquad \text{and} \qquad \mathcal{S}|\Psi_{\mathbf{k},\nu}\rangle = \mathcal{D}^{\frac{1}{2}}(\mathcal{S})|\Psi_{\mathcal{S}\mathbf{k},\mathcal{S}\nu}\rangle \Leftrightarrow \mathcal{S}|\psi^{\sigma}_{\mathbf{k},\nu}\rangle = \sum_{\tau=\uparrow,\downarrow} \mathcal{D}^{\frac{1}{2}}(\mathcal{S})_{\tau\sigma}|\psi^{\tau}_{\mathcal{S}\mathbf{k},\mathcal{S}\nu}\rangle \tag{E.18}$$

The result is similar if the computation includes the spin-orbit coupling:

$$\mathcal{S}|\Psi_{\mathbf{k},\nu}\rangle = \mathcal{D}^{\frac{1}{2}}(\mathcal{S})|\Psi_{\mathcal{S}\mathbf{k},\mathcal{S}\nu}\rangle \quad \text{with} \quad |\Psi_{\mathbf{k},\nu}\rangle = \begin{pmatrix} |\psi^{+}_{\mathbf{k},\nu}\rangle \\ |\psi^{-}_{\mathbf{k},\nu}\rangle \end{pmatrix} \Leftrightarrow \mathcal{S}|\psi^{i}_{\mathbf{k},\nu}\rangle = \sum_{j=+,-} \mathcal{D}^{\frac{1}{2}}(\mathcal{S})_{ji}|\psi^{\tau}_{\mathcal{S}\mathbf{k},\mathcal{S}\nu}\rangle \tag{E.19}$$

Before studying the case $\mathcal{S} = \Theta\mathcal{R}$, we consider the action of the time-reversal operator Θ alone on a Bloch state. Neglecting first the spin, we get:

$$\Theta|\psi_{\mathbf{k},\nu}\rangle = \Theta\left(\sum_{\mathbf{r}} e^{i\mathbf{k}\cdot\mathbf{r}} u_{\mathbf{k},\nu}(\mathbf{r})|\mathbf{r}\rangle\right) = \sum_{\mathbf{r}} e^{-i\mathbf{k}\cdot\mathbf{r}} u^{*}_{\mathbf{k},\nu}(\mathbf{r})|\mathbf{r}\rangle \tag{E.20}$$

since $\Theta|\mathbf{r}\rangle = |\mathbf{r}\rangle$. Moreover, defining $u_{-\mathbf{k},\Theta\nu}(\mathbf{r}) = u^{*}_{\mathbf{k},\nu}(\mathbf{r})$, we can finally write:

$$\Theta|\psi_{\mathbf{k},\nu}\rangle = \sum_{\mathbf{r}} e^{i(-\mathbf{k})\cdot\mathbf{r}} u_{-\mathbf{k},\Theta\nu}(\mathbf{r})|\mathbf{r}\rangle = |\psi_{-\mathbf{k},\Theta\nu}\rangle \tag{E.21}$$

Then, if we add the spin degree of freedom, the expression becomes:

$$\Theta|\Psi_{\mathbf{k},\nu}\rangle = -i\sigma_y.K_{\mathbf{r}} \begin{pmatrix} |\psi^{\uparrow}_{\mathbf{k},\nu}\rangle \\ |\psi^{\downarrow}_{\mathbf{k},\nu}\rangle \end{pmatrix} = -i\sigma_y \begin{pmatrix} |\psi^{\uparrow}_{-\mathbf{k},\Theta\nu}\rangle \\ |\psi^{\downarrow}_{-\mathbf{k},\Theta\nu}\rangle \end{pmatrix} = \begin{pmatrix} -|\psi^{\downarrow}_{-\mathbf{k},\Theta\nu}\rangle \\ |\psi^{\uparrow}_{-\mathbf{k},\Theta\nu}\rangle \end{pmatrix} \tag{E.22}$$

and the result is similar if the spin-orbit coupling is included – it is then enough to replace $\uparrow,\downarrow$ by $+,-$ respecitively.

If $\mathcal{S} = \Theta\mathcal{R}$, the result is merely derived from the previous relations:

$$\mathcal{S}|\psi^{\sigma}_{\mathbf{k},\nu}\rangle = \Theta\left(\sum_{\tau} \mathcal{D}^{\frac{1}{2}}(\mathcal{R})_{\tau\sigma}|\psi^{\tau}_{\mathcal{R}\mathbf{k},\mathcal{R}\nu}\rangle\right) = \sum_{\tau} \mathcal{D}^{\frac{1}{2}}(R)^{*}_{\tau\sigma}\Theta|\psi^{\tau}_{\mathcal{R}\mathbf{k},\mathcal{R}\nu}\rangle = \sum_{\tau,\mu}(-i\sigma_y)_{\mu\tau}\mathcal{D}^{\frac{1}{2}}(\mathcal{R})^{*}_{\tau\sigma}|\psi^{\mu}_{-\mathcal{R}\mathbf{k},\mathcal{S}\nu}\rangle \tag{E.23}$$

Taking into account the following relations:

$$\mathcal{S}\mathbf{k} = -\mathcal{R}\mathbf{k} \qquad \text{and} \qquad \mathcal{D}^{\frac{1}{2}}(\Theta\mathcal{R}) = \mathcal{D}^{\frac{1}{2}}(\Theta)\mathcal{D}^{\frac{1}{2}}(\mathcal{R})^{*} \qquad \text{with} \qquad \mathcal{D}^{\frac{1}{2}}(\Theta) = -i\sigma_y, \tag{E.24}$$

we finally can write:

$$\mathcal{S}|\psi^{\sigma}_{\mathbf{k},\nu}\rangle = \sum_{\tau} \mathcal{D}^{\frac{1}{2}}(\Theta\mathcal{R})_{\tau\sigma}|\psi^{\tau}_{\mathcal{S}\mathbf{k},\mathcal{S}\nu}\rangle,$$

which is analogous to the formulas (E.18) and (E.19).

E.3.2 Transformation of the projectors under a space group operation

case of a symmetry operation $\mathcal{S} = \mathcal{R}$

Let's assume first of all that $\mathcal{S}$ is a simple space group operation ($\mathcal{S} = \mathcal{R}$). As defined in section 2.3, the *temporary* Wannier projectors are written as follows:

$$\widetilde{P}^{\alpha,\sigma}_{lm,\nu}(\mathbf{k}) = \langle u^{\alpha,\sigma}_{l}(E^{\alpha}_{1l})Y^{l}_{m}|\psi^{\sigma}_{\mathbf{k}\nu}\rangle, \qquad \forall\ \nu \in \mathcal{W} \tag{E.25}$$

$$\begin{aligned}
\widetilde{P}^{\alpha,\sigma}_{lm,\nu}(\mathcal{S}\mathbf{k}) &= \langle u_l^{\alpha,\sigma}(E^{\alpha}_{1l})Y^l_m|\psi^{\sigma}_{\mathcal{S}\mathbf{k},\nu}\rangle = \langle u_l^{\alpha,\sigma}(E^{\alpha}_{1l})Y^l_m|\psi^{\mathcal{S}(\mathcal{S}^{-1}\sigma)}_{\mathcal{S}\mathbf{k},\mathcal{S}(\mathcal{S}^{-1}\nu)}\rangle \\
&= \langle u_l^{\alpha,\sigma}(E^{\alpha}_{1l})Y^l_m|\Big(\mathcal{S}|\psi^{\mathcal{S}^{-1}\sigma}_{\mathbf{k},\mathcal{S}^{-1}\nu}\rangle\Big) \\
&= \Big[\langle\psi^{\mathcal{S}^{-1}\sigma}_{\mathbf{k},\mathcal{S}^{-1}\nu}|\Big(\mathcal{S}^{-1}|u_l^{\alpha,\sigma}(E^{\alpha}_{1l})Y^l_m\rangle\Big)\Big]^* \qquad \text{since} \quad \mathcal{S}^{-1}=\mathcal{S}^{\dagger} \\
&= \sum_{m'}\mathcal{D}^l(\mathcal{S}^{-1})^*_{m',m}\ \ \langle\psi^{\mathcal{S}^{-1}\sigma}_{\mathbf{k},\mathcal{S}^{-1}\nu}|u_l^{\mathcal{S}^{-1}\alpha,\mathcal{S}^{-1}\sigma}(E^{\mathcal{S}^{-1}\alpha}_{1l})Y^l_{m'}\rangle^* \\
&= \sum_{m'}\mathcal{D}^l(\mathcal{S})_{m,m'}\ \ \langle u_l^{\mathcal{S}^{-1}\alpha,\mathcal{S}^{-1}\sigma}(E^{\mathcal{S}^{-1}\alpha}_{1l})Y^l_{m'}|\psi^{\mathcal{S}^{-1}\sigma}_{\mathbf{k},\mathcal{S}^{-1}\nu}\rangle
\end{aligned} \tag{E.26}$$

because $\mathcal{D}^l(\mathcal{S}^{-1}) = \mathcal{D}^l(\mathcal{S}^{\dagger}) = \mathcal{D}^l(\mathcal{S})^{\dagger} = [{}^t\mathcal{D}^l(\mathcal{S})]^*$. This finally leads to:

$$\widetilde{P}^{\alpha,\sigma}_{lm,\nu}(\mathcal{S}\mathbf{k}) = \sum_{m'}\mathcal{D}^l(\mathcal{S})_{m,m'}\ \widetilde{P}^{\mathcal{S}^{-1}\alpha,\mathcal{S}^{-1}\sigma}_{lm',\mathcal{S}^{-1}\nu}(\mathbf{k}) \tag{E.27}$$

It can then be shown that:

$$O^{\alpha,\alpha'}_{m,m'}(\mathcal{S}\mathbf{k},\sigma) = \sum_{q,q'}\mathcal{D}^l(\mathcal{S})_{m,q}\ O^{\mathcal{S}^{-1}\alpha,\mathcal{S}^{-1}\alpha'}_{q,q'}(\mathbf{k},\mathcal{S}^{-1}\sigma)\ \mathcal{D}^l(\mathcal{S}^{-1})_{q',m'} \tag{E.28}$$

$$\Big[O^{-1/2}(\mathcal{S}\mathbf{k},\sigma)\Big]^{\alpha,\alpha'}_{m,m'} = \sum_{q,q'}\mathcal{D}^l(\mathcal{S})_{m,q}\ \Big[O^{-1/2}(\mathbf{k},\mathcal{S}^{-1}\sigma)\Big]^{\mathcal{S}^{-1}\alpha,\mathcal{S}^{-1}\alpha'}_{q,q'}\ \mathcal{D}^l(\mathcal{S}^{-1})_{q',m'} \tag{E.29}$$

and thus the same relation as (E.27) also for the "true" projectors $P^{\alpha,\sigma}_{lm,\nu}(\mathcal{S}\mathbf{k})$:

$$P^{\alpha,\sigma}_{lm,\nu}(\mathcal{S}\mathbf{k}) = \sum_{m'}\mathcal{D}^l(\mathcal{S})_{m,m'}\ P^{\mathcal{S}^{-1}\alpha,\mathcal{S}^{-1}\sigma}_{lm',\mathcal{S}^{-1}\nu}(\mathbf{k}) \tag{E.30}$$

Moreover, when the calculation is paramagnetic – up and down states are thus degenerate –, the expression (E.30) can be used without paying attention to the indices σ and $\mathcal{S}^{-1}\sigma$.

When the spin-orbit coupling is taken into account, the *temporary* Wannier projectors are written as follows:

$$\Big[\widetilde{P}^{\alpha,\sigma}_{lm,\nu}\Big]^i(\mathbf{k}) = \langle u_l^{\alpha,\sigma}(E^{\alpha}_{1l})Y^l_m|\psi^i_{\mathbf{k}\nu}\rangle, \qquad \forall\ \nu\in\mathcal{W} \quad \text{and with} \quad i=\{+,-\}. \tag{E.31}$$

The relation (E.27) then becomes:

$$\begin{aligned}
\Big[\widetilde{P}^{\alpha,\sigma}_{lm,\nu}\Big]^i(\mathcal{S}\mathbf{k}) &= \sum_{m'}\mathcal{D}^l(\mathcal{S})_{m,m'}\ \Big[\widetilde{P}^{\mathcal{S}^{-1}\alpha,\mathcal{S}^{-1}\sigma}_{lm',\nu}\Big]^{\mathcal{S}^{-1}(i)}(\mathbf{k}) \\
&= \sum_{m',\tau,j}\mathcal{D}^l(\mathcal{S})_{m,m'}\ \mathcal{D}^{\frac{1}{2}}(\mathcal{S})_{\sigma,\tau}\ \mathcal{D}^{\frac{1}{2}}(\mathcal{S}^{-1})_{j,i}\ \ \langle u_l^{\mathcal{S}^{-1}\alpha,\tau}(E^{\mathcal{S}^{-1}\alpha}_{1l})Y^l_{m'}|\psi^{\ j}_{\mathbf{k},\mathcal{S}^{-1}\nu}\rangle \\
&= \sum_{m',\tau,j}\mathcal{D}^l(\mathcal{S})_{m,m'}\ \mathcal{D}^{\frac{1}{2}}(\mathcal{S})_{\sigma,\tau}\ \Big[\widetilde{P}^{\mathcal{S}^{-1}\alpha,\tau}_{lm',\nu}\Big]^j(\mathbf{k})\ \mathcal{D}^{\frac{1}{2}}(\mathcal{S}^{-1})_{j,i}
\end{aligned} \tag{E.32}$$

which leads to:

$$\Big[P^{\alpha,\sigma}_{lm,\nu}\Big]^i(\mathcal{S}\mathbf{k}) = \sum_{m',\tau,j}\mathcal{D}^l(\mathcal{S})_{m,m'}\ \mathcal{D}^{\frac{1}{2}}(\mathcal{S})_{\sigma,\tau}\ \Big[P^{\mathcal{S}^{-1}\alpha,\tau}_{lm',\nu}\Big]^j(\mathbf{k})\ \mathcal{D}^{\frac{1}{2}}(\mathcal{S}^{-1})_{j,i} \tag{E.33}$$

case of an antisymmetry operation $\mathcal{S} = \Theta\mathcal{R}$

Starting from the defintion of the *temporary* Wannier projectors (E.25), we get:

$$\begin{aligned}
\widetilde{P}^{\alpha,\sigma}_{lm,\nu}(\mathcal{S}\mathbf{k}) &= \langle u_l^{\alpha,\sigma}(E^\alpha_{1l})Y^l_m|\psi^\sigma_{\mathcal{S}\mathbf{k},\nu}\rangle = \langle u_l^{\alpha,\sigma}(E^\alpha_{1l})Y^l_m|\psi^{\mathcal{S}(\mathcal{S}^{-1}\sigma)}_{\mathcal{S}\mathbf{k},\mathcal{S}(\mathcal{S}^{-1}\nu)}\rangle \\
&= \langle u_l^{\alpha,\sigma}(E^\alpha_{1l})Y^l_m|\Big(\mathcal{S}|\psi^{\mathcal{S}^{-1}\sigma}_{\mathbf{k},\mathcal{S}^{-1}\nu}\rangle\Big) \\
&= \langle \psi^{\mathcal{S}^{-1}\sigma}_{\mathbf{k},\mathcal{S}^{-1}\nu}|\Big(\mathcal{S}^{-1}|u_l^{\alpha,\sigma}(E^\alpha_{1l})Y^l_m\rangle\Big) \qquad \text{since} \quad \mathcal{S}^{-1} = \mathcal{S}^\dagger \\
&= \sum_{m'} \mathcal{D}^l(\mathcal{S}^{-1})_{m',m} \;\; \langle \psi^{\mathcal{S}^{-1}\sigma}_{\mathbf{k},\mathcal{S}^{-1}\nu}|u_l^{\mathcal{S}^{-1}\alpha,\mathcal{S}^{-1}\sigma}(E^{\mathcal{S}^{-1}\alpha}_{1l})Y^l_{m'}\rangle \\
&= \sum_{m'} \mathcal{D}^l(\mathcal{S})_{m,m'} \;\; \langle u_l^{\mathcal{S}^{-1}\alpha,\mathcal{S}^{-1}\sigma}(E^{\mathcal{S}^{-1}\alpha}_{1l})Y^l_{m'}|\psi^{\mathcal{S}^{-1}\sigma}_{\mathbf{k},\mathcal{S}^{-1}\nu}\rangle^* \qquad \text{(E.34)}
\end{aligned}$$

because $\mathcal{D}^l(\mathcal{S}^{-1}) = \mathcal{D}^l(\mathcal{S}^\dagger) = \mathcal{D}^l(\mathcal{S})^\dagger = {}^t\mathcal{D}^l(\mathcal{S})$. This finally leads to:

$$\widetilde{P}^{\alpha,\sigma}_{lm,\nu}(\mathcal{S}\mathbf{k}) = \sum_{m'} \mathcal{D}^l(\mathcal{S})_{m,m'} \;\; \Big[\widetilde{P}^{\mathcal{S}^{-1}\alpha,\mathcal{S}^{-1}\sigma}_{lm',\mathcal{S}^{-1}\nu}(\mathbf{k})\Big]^* \qquad \text{(E.35)}$$

It can then be shown that:

$$O^{\alpha,\alpha'}_{m,m'}(\mathcal{S}\mathbf{k},\sigma) = \sum_{q,q'} \mathcal{D}^l(\mathcal{S})_{m,q} \;\; \Big[O^{\mathcal{S}^{-1}\alpha,\mathcal{S}^{-1}\alpha'}_{q,q'}(\mathbf{k},\mathcal{S}^{-1}\sigma)\Big]^* \;\; \Big[\mathcal{D}^l(\mathcal{S}^{-1})_{q',m'}\Big]^* \qquad \text{(E.36)}$$

$$\Big[O^{-1/2}(\mathcal{S}\mathbf{k},\sigma)\Big]^{\alpha,\alpha'}_{m,m'} = \sum_{q,q'} \mathcal{D}^l(\mathcal{S})_{m,q} \;\; \Big(\Big[O^{-1/2}(\mathbf{k},\mathcal{S}^{-1}\sigma)\Big]^{\mathcal{S}^{-1}\alpha,\mathcal{S}^{-1}\alpha'}_{q,q'} \;\; \mathcal{D}^l(\mathcal{S}^{-1})_{q',m'}\Big)^* \qquad \text{(E.37)}$$

and thus the same relation as (E.35) also for the "true" projectors $P^{\alpha,\sigma}_{lm,\nu}(\mathcal{S}\mathbf{k})$:

$$P^{\alpha,\sigma}_{lm,\nu}(\mathcal{S}\mathbf{k}) = \sum_{m'} \mathcal{D}^l(\mathcal{S})_{m,m'} \;\; \Big[P^{\mathcal{S}^{-1}\alpha,\mathcal{S}^{-1}\sigma}_{lm',\mathcal{S}^{-1}\nu}(\mathbf{k})\Big]^* \qquad \text{(E.38)}$$

Moreover, when the calculation is paramagnetic – up and down states are thus degenerate –, the expression (E.30) can be used without paying attention to the indices σ and $\mathcal{S}^{-1}\sigma$.

When the spin-orbit coupling is taken into account, the relation (E.35) then becomes:

$$\begin{aligned}
\Big[\widetilde{P}^{\alpha,\sigma}_{lm,\nu}\Big]^i(\mathcal{S}\mathbf{k}) &= \sum_{m'} \mathcal{D}^l(\mathcal{S})_{m,m'} \;\; \Big(\Big[\widetilde{P}^{\mathcal{S}^{-1}\alpha,\mathcal{S}^{-1}\sigma}_{lm',\nu}\Big]^{\mathcal{S}^{-1}(i)}(\mathbf{k})\Big)^* \\
&= \sum_{m',\tau,j} \mathcal{D}^l(\mathcal{S})_{m,m'} \; \mathcal{D}^{\frac{1}{2}}(\mathcal{S})_{\sigma,\tau} \;\; \Big[\mathcal{D}^{\frac{1}{2}}(\mathcal{S}^{-1})_{j,i}\Big]^* \;\; \langle u_l^{\mathcal{S}^{-1}\alpha,\tau}(E^{\mathcal{S}^{-1}\alpha}_{1l})Y^l_{m'}|\psi^{\;j}_{\mathbf{k},\mathcal{S}^{-1}\nu}\rangle^* \\
&= \sum_{m',\tau,j} \mathcal{D}^l(\mathcal{S})_{m,m'} \; \mathcal{D}^{\frac{1}{2}}(\mathcal{S})_{\sigma,\tau} \;\; \Big[\Big[\widetilde{P}^{\mathcal{S}^{-1}\alpha,\tau}_{lm',\nu}\Big]^j(\mathbf{k})\Big]^* \;\; \Big[\mathcal{D}^{\frac{1}{2}}(\mathcal{S}^{-1})_{j,i}\Big]^* \qquad \text{(E.39)}
\end{aligned}$$

which leads to:

$$\Big[P^{\alpha,\sigma}_{lm,\nu}\Big]^i(\mathcal{S}\mathbf{k}) = \sum_{m',\tau,j} \mathcal{D}^l(\mathcal{S})_{m,m'} \; \mathcal{D}^{\frac{1}{2}}(\mathcal{S})_{\sigma,\tau} \;\; \Big[\Big[P^{\mathcal{S}^{-1}\alpha,\tau}_{lm',\nu}\Big]^j(\mathbf{k})\Big]^* \;\; \Big[\mathcal{D}^{\frac{1}{2}}(\mathcal{S}^{-1})_{j,i}\Big]^* \qquad \text{(E.40)}$$

E.4 Local quantities and sum over the irreducible Brillouin zone:

We consider in this section a quantity $\mathcal{O}$ which has the following form in the Bloch basis $|\psi^{\sigma}_{\mathbf{k}\nu}\rangle$:

$$\langle\psi^{\sigma}_{\mathbf{k}\nu}|\mathcal{O}|\psi^{\sigma'}_{\mathbf{k}'\nu'}\rangle = \mathcal{O}^{\sigma\sigma'}_{\nu\nu'}(\mathbf{k})\delta_{\mathbf{k}\mathbf{k}'}, \tag{E.41}$$

and which commutes with any symmetry operation of the system $[\mathcal{O},\mathcal{S}]=0$. This is particularly the case of the Hamiltonian H, the Green function G, the charge density ρ.

We would like to compute the value of the elements $(\mathcal{O}^{\alpha}_{l})^{\sigma\sigma'}_{mm'}$ in the local basis $|w^{\alpha\sigma}_{lm}\rangle$ of Wannier functions:

$$(\mathcal{O}^{\alpha}_{l})^{\sigma\sigma'}_{mm'} = \langle w^{\alpha\sigma}_{lm}|\mathcal{O}|w^{\alpha\sigma'}_{lm'}\rangle \tag{E.42}$$

E.4.1 Case of a paramagnetic compound

without spin-orbit coupling

If we consider a *paramagnetic* compound – with a "*grey*" (type II) magnetic point group $\mathcal{G}+\Theta\mathcal{G}$ –, we have to perform the following computation:

$$\begin{aligned}(\mathcal{O}^{\alpha}_{l})^{\sigma\sigma'}_{mm'} &= \langle w^{\alpha\sigma}_{lm}|\left[\sum_{\mathbf{k}\in 1BZ}\sum_{\nu,\nu'}|\psi^{\sigma}_{\mathbf{k}\nu}\rangle\mathcal{O}^{\sigma\sigma'}_{\nu\nu'}(\mathbf{k})\langle\psi^{\sigma'}_{\mathbf{k}\nu'}|\right]|w^{\alpha\sigma'}_{lm'}\rangle \\ &= \sum_{\mathbf{k}\in 1BZ}\sum_{\nu,\nu'}P^{\alpha,\sigma}_{lm,\nu}(\mathbf{k})\ \mathcal{O}^{\sigma\sigma'}_{\nu\nu'}(\mathbf{k})\ \left[P^{\alpha,\sigma'}_{lm',\nu'}(\mathbf{k})\right]^{*}.\ \delta_{\sigma\sigma'}\end{aligned} \tag{E.43}$$

where *1BZ* is the first Brillouin zone of the original point group $\mathcal{G}$. In the following, we will note $\left(\mathcal{O}^{\alpha,\sigma}_{l}\right)_{mm'} = (\mathcal{O}^{\alpha}_{l})^{\sigma\sigma}_{mm'}$ and $\mathcal{O}^{\sigma}_{\nu\nu'}(\mathbf{k}) = \mathcal{O}^{\sigma\sigma}_{\nu\nu'}(\mathbf{k})$.

$$\begin{aligned}\left(\mathcal{O}^{\alpha,\sigma}_{l}\right)_{mm'} &= \sum_{\mathcal{S}\in\mathcal{G}}\sum_{\mathbf{k}\in IBZ}\sum_{\nu,\nu'}P^{\alpha,\sigma}_{lm,\nu}(\mathcal{S}\mathbf{k})\ \mathcal{O}^{\sigma}_{\nu\nu'}(\mathbf{k})\ \left[P^{\alpha,\sigma}_{lm',\nu'}(\mathcal{S}\mathbf{k})\right]^{*} \\ &= \frac{1}{2}\sum_{\mathcal{S}\in\mathcal{G}}\sum_{\mathbf{k}\in IBZ}\sum_{\nu,\nu'}P^{\alpha,\sigma}_{lm,\nu}(\mathcal{S}\mathbf{k})\ \mathcal{O}^{\sigma}_{\nu\nu'}(\mathcal{S}\mathbf{k})\ \left[P^{\alpha,\sigma}_{lm',\nu'}(\mathcal{S}\mathbf{k})\right]^{*} \\ &\qquad +\frac{1}{2}\sum_{\mathcal{S}\in\mathcal{G}}\sum_{\mathbf{k}\in IBZ}\sum_{\nu,\nu'}P^{\alpha,\sigma}_{lm,\nu}(-\Theta\mathcal{S}\mathbf{k})\ \mathcal{O}^{\sigma}_{\nu\nu'}(-\Theta\mathcal{S}\mathbf{k})\ \left[P^{\alpha,\sigma}_{lm',\nu'}(-\Theta\mathcal{S}\mathbf{k})\right]^{*} \\ &= \frac{1}{2}\sum_{\mathcal{S}\in\mathcal{G}}\sum_{\mathbf{k}\in IBZ}\sum_{\nu,\nu'}P^{\alpha,\sigma}_{lm,\nu}(\mathcal{S}\mathbf{k})\ \mathcal{O}^{\sigma\sigma'}_{\nu\nu'}(\mathcal{S}\mathbf{k})\ \left[P^{\alpha,\sigma}_{lm',\nu'}(\mathcal{S}\mathbf{k})\right]^{*} \\ &\qquad +\frac{1}{2}\sum_{\mathcal{S}\in\Theta\mathcal{G}}\sum_{\mathbf{k}\in IBZ}\sum_{\nu,\nu'}P^{\alpha,\sigma}_{lm,\nu}(\mathcal{S}\mathbf{k})\ \mathcal{O}^{\sigma}_{\nu\nu'}(\mathcal{S}\mathbf{k})\ \left[P^{\alpha,\sigma}_{lm',\nu'}(\mathcal{S}\mathbf{k})\right]^{*}\end{aligned} \tag{E.44}$$

where *IBZ* denotes the irreducible Brillouin zone of the original point group $\mathcal{G}$. Moreover, since we can always choose a Brillouin zone with $\mathbf{k}=0$ as center of symmetry, it is possible not to take into account the introduced sign of the $\mathbf{k}$ point in the second right-hand-side term. The two terms in (E.43) can be rewritten as follows:

- when $\mathcal{S} \in \mathcal{G}$:

$$\begin{aligned}
\left[\left(\mathcal{O}_l^{\alpha,\sigma}\right)_{mm'}\right]^{\mathcal{G}} &= \sum_{\mathcal{S}\in\mathcal{G}} \sum_{\mathbf{k}\in IBZ} \sum_{\nu,\nu'} P^{\alpha,\sigma}_{lm,\nu}(\mathcal{S}\mathbf{k})\ \mathcal{O}^{\sigma}_{\nu\nu'}(\mathcal{S}\mathbf{k})\ \left[P^{\alpha,\sigma}_{lm',\nu'}(\mathcal{S}\mathbf{k})\right]^* \\
&= \sum_{\mathcal{S}\in\mathcal{G}} \sum_{n,n'} \mathcal{D}^l(\mathcal{S})_{m,n}\ \left[\left(\mathcal{O}_l^{\mathcal{S}^{-1}\alpha,\mathcal{S}^{-1}\sigma}\right)_{nn'}\right]_{unsym}\ \mathcal{D}^l(\mathcal{S}^{-1})_{n',m'} \\
&\text{with}\quad \left[\left(\mathcal{O}_l^{\alpha,\sigma}\right)_{mm'}\right]_{unsym} = \sum_{\mathbf{k}\in IBZ} \sum_{\nu,\nu'} P^{\alpha,\sigma}_{lm,\nu}(\mathbf{k})\ \mathcal{O}^{\sigma}_{\nu\nu'}(\mathbf{k})\ \left[P^{\alpha,\sigma}_{lm',\nu'}(\mathbf{k})\right]^*
\end{aligned} \tag{E.45}$$

using formula (E.30) and the equality $\mathcal{O}^{\sigma}_{\nu\nu'}(\mathcal{S}\mathbf{k}) = \mathcal{O}^{\mathcal{S}^{-1}\sigma}_{\mathcal{S}^{-1}\nu\mathcal{S}^{-1}\nu'}(\mathbf{k})$ because of the commutation property of $\mathcal{O}$:

$$\begin{aligned}
\langle\psi^{\sigma}_{\mathcal{S}\mathbf{k},\nu}|\mathcal{O}|\psi^{\sigma}_{\mathcal{S}\mathbf{k}',\nu'}\rangle &= \langle\psi^{\mathcal{S}^{-1}\sigma}_{\mathbf{k},\mathcal{S}^{-1}\nu}|\mathcal{S}^{\dagger}\mathcal{O}\mathcal{S}|\psi^{\mathcal{S}^{-1}\sigma}_{\mathbf{k}',\mathcal{S}^{-1}\nu'}\rangle \\
&= \langle\psi^{\mathcal{S}^{-1}\sigma}_{\mathbf{k},\mathcal{S}^{-1}\nu}|\mathcal{S}^{-1}\mathcal{O}\mathcal{S}|\psi^{\mathcal{S}^{-1}\sigma}_{\mathbf{k}',\mathcal{S}^{-1}\nu'}\rangle \\
&= \langle\psi^{\mathcal{S}^{-1}\sigma}_{\mathbf{k},\mathcal{S}^{-1}\nu}|\mathcal{O}|\psi^{\mathcal{S}^{-1}\sigma}_{\mathbf{k}',\mathcal{S}^{-1}\nu'}\rangle \qquad \text{since} \qquad [\mathcal{O},\mathcal{S}] = 0
\end{aligned} \tag{E.46}$$

Moreover, for each $\mathbf{k}$ point, the set to which belong the band indices ν is the following:

$$\mathcal{E}_{\mathbf{k}} = \{\nu | E_{min} < \varepsilon^{\sigma}_{\mathbf{k}\nu} < E_{max}\} \tag{E.47}$$

Since $\varepsilon^{\sigma}_{\mathcal{S}\mathbf{k},\nu} = \varepsilon^{\mathcal{S}^{-1}\sigma}_{\mathbf{k},\mathcal{S}^{-1}\nu}$, it implies that $\mathcal{E}_{\mathcal{S}\mathbf{k}} = \mathcal{E}_{\mathbf{k}}$ and then the summation over ν is finally independent of the symmetry operation $\mathcal{S}$.

- and similarly, when $\mathcal{S} \in \Theta\mathcal{G}$:

$$\begin{aligned}
\left[\left(\mathcal{O}_l^{\alpha,\sigma}\right)_{mm'}\right]^{\Theta\mathcal{G}} &= \sum_{\mathcal{S}\in\Theta\mathcal{G}} \sum_{\mathbf{k}\in IBZ} \sum_{\nu,\nu'} P^{\alpha,\sigma}_{lm,\nu}(\mathcal{S}\mathbf{k})\ \mathcal{O}^{\sigma}_{\nu\nu'}(\mathcal{S}\mathbf{k})\ \left[P^{\alpha,\sigma}_{lm',\nu'}(\mathcal{S}\mathbf{k})\right]^* \\
&= \sum_{\mathcal{S}\in\Theta\mathcal{G}} \sum_{n,n'} \mathcal{D}^l(\mathcal{S})_{m,n}\ \left[\left(\mathcal{O}_l^{\mathcal{S}^{-1}\alpha,\mathcal{S}^{-1}\sigma}\right)_{nn'}\right]^*_{unsym}\ \left[\mathcal{D}^l(\mathcal{S}^{-1})_{n',m'}\right]^*
\end{aligned} \tag{E.48}$$

using formula (E.38) and the following relation:

$$\begin{aligned}
\langle\psi^{\sigma}_{\mathcal{S}\mathbf{k},\nu}|\mathcal{O}|\psi^{\sigma}_{\mathcal{S}\mathbf{k}',\nu'}\rangle &= \langle\psi^{\sigma}_{\mathcal{S}\mathbf{k},\nu}|\mathcal{O}\mathcal{S}|\psi^{\mathcal{S}^{-1}\sigma}_{\mathbf{k}',\mathcal{S}^{-1}\nu'}\rangle \\
&= \left[\langle\psi^{\mathcal{S}^{-1}\sigma}_{\mathbf{k},\mathcal{S}^{-1}\nu}|\mathcal{S}^{-1}\mathcal{O}\mathcal{S}|\psi^{\mathcal{S}^{-1}\sigma}_{\mathbf{k}',\mathcal{S}^{-1}\nu'}\rangle\right]^* \qquad \text{since} \qquad \langle\mathcal{S}u|v\rangle = \left[\langle u|\mathcal{S}^{\dagger}v\rangle\right]^* \\
&= \left[\langle\psi^{\mathcal{S}^{-1}\sigma}_{\mathbf{k},\mathcal{S}^{-1}\nu}|\mathcal{O}|\psi^{\mathcal{S}^{-1}\sigma}_{\mathbf{k}',\mathcal{S}^{-1}\nu'}\rangle\right]^* \qquad \text{since} \qquad [\mathcal{O},\mathcal{S}] = 0
\end{aligned} \tag{E.49}$$

Moreover, we can also write (E.48) as follows:

$$\left[\left(\mathcal{O}_l^{\alpha,\sigma}\right)_{mm'}\right]^{\Theta\mathcal{G}} = \sum_{\mathcal{R}\in\mathcal{G}} \sum_{n,n'} \mathcal{D}^l(\Theta\mathcal{R})_{m,n}\ \left[\left(\mathcal{O}_l^{\mathcal{R}^{-1}\alpha,-\mathcal{R}^{-1}\sigma}\right)_{nn'}\right]^*_{unsym}\ \left[\mathcal{D}^l(\mathcal{R}^{-1}\Theta^{-1})_{n',m'}\right]^* \tag{E.50}$$

since the time reversal operator Θ has no effect on the atomic position α and reverses the spin $\Theta\sigma = -\sigma$. However, the compound is assumed to be paramagnetic and thus the spin inversion can be ommited. As a result,

$$\left[\left(\mathcal{O}_l^{\alpha,\sigma}\right)_{mm'}\right]^{\Theta\mathcal{G}} = \sum_{n,n'} \mathcal{D}^l(\Theta)_{m,n} \left[\left(\mathcal{O}_l^{\alpha,\sigma}\right)_{nn'}\right]^{\mathcal{G}*} \left[\mathcal{D}^l(\Theta^{-1})_{n',m'}\right]^* \tag{E.51}$$

where the time-reversal operator Θ and the previous term $\left[\left(\mathcal{O}_l^{\alpha,\sigma}\right)_{mm'}\right]^{\mathcal{G}}$ appear now explicitly. Finally, the term $\left(\mathcal{O}_l^{\alpha,\sigma}\right)_{mm'}$ of (E.43) can be calculated by the following expression:

$$\begin{aligned}
\left(\mathcal{O}_l^{\alpha,\sigma}\right)_{mm'} &= \frac{1}{2}\left[\left[\left(\mathcal{O}_l^{\alpha}\right)_{mm'}^{\sigma\sigma}\right]^{\mathcal{G}} + \sum_{n,n'} \mathcal{D}^l(\Theta)_{m,n} \left[\left(\mathcal{O}_l^{\alpha,\sigma}\right)_{nn'}\right]^{\mathcal{G}*} \left[\mathcal{D}^l(\Theta^{-1})_{n',m'}\right]^*\right] \\
&\text{with} \quad \left[\left(\mathcal{O}_l^{\alpha,\sigma}\right)_{mm'}\right]^{\mathcal{G}} = \sum_{\mathcal{S}\in\mathcal{G}} \sum_{n,n'} \mathcal{D}^l(\mathcal{S})_{m,n} \left[\left(\mathcal{O}_l^{\mathcal{S}^{-1}\alpha,\mathcal{S}^{-1}\sigma}\right)_{nn'}\right]_{unsym} \mathcal{D}^l(\mathcal{S}^{-1})_{n',m'} \\
&\text{and} \quad \left[\left(\mathcal{O}_l^{\alpha,\sigma}\right)_{mm'}\right]_{unsym} = \sum_{\mathbf{k}\in IBZ} \sum_{\nu,\nu'} P^{\alpha,\sigma}_{lm,\nu}(\mathbf{k})\ \mathcal{O}^{\sigma}_{\nu\nu'}(\mathbf{k})\ \left[P^{\alpha,\sigma}_{lm',\nu'}(\mathbf{k})\right]^*
\end{aligned} \tag{E.52}$$

when the spin-orbit coupling is taken into account

Taking into account the spin-orbit coupling does not modify the "*grey*" magnetic point group – $\mathcal{G}+\Theta\mathcal{G}$ – of the compound. Nevertheless, it is now necessary to treat explicitly the spin indices:

$$\begin{aligned}
\left(\mathcal{O}_l^{\alpha}\right)^{\sigma\sigma'}_{mm'} &= \langle w^{\alpha\sigma}_{lm}| \left[\sum_{\mathbf{k}\in 1BZ} \sum_{\nu,\nu'} \sum_{i,j=+,-} |\psi^i_{\mathbf{k}\nu}\rangle \mathcal{O}^{ij}_{\nu\nu'}(\mathbf{k}) \langle\psi^j_{\mathbf{k}\nu'}|\right] |w^{\alpha\sigma'}_{lm'}\rangle \\
&= \sum_{\mathbf{k}\in 1BZ} \sum_{\nu,\nu'} \sum_{i,j} \left[P^{\alpha,\sigma}_{lm,\nu}(\mathbf{k})\right]^i\ \mathcal{O}^{ij}_{\nu\nu'}(\mathbf{k})\ \left[P^{\alpha,\sigma}_{lm',\nu'}(\mathbf{k})\right]^{j\,*}
\end{aligned} \tag{E.53}$$

where *1BZ* is still the first Brillouin zone of the original point group $\mathcal{G}$.

$$\begin{aligned}
\left(\mathcal{O}_l^{\alpha}\right)^{\sigma\sigma'}_{mm'} &= \frac{1}{2} \sum_{\mathcal{S}\in\mathcal{G}} \sum_{\mathbf{k}\in IBZ} \sum_{\nu,\nu'} \sum_{i,j} \left[P^{\alpha,\sigma}_{lm,\nu}(\mathcal{S}\mathbf{k})\right]^i\ \mathcal{O}^{ij}_{\nu\nu'}(\mathcal{S}\mathbf{k})\ \left[P^{\alpha,\sigma'}_{lm',\nu'}(\mathcal{S}\mathbf{k})\right]^{j\,*} \\
&\quad + \frac{1}{2} \sum_{\mathcal{S}\in\Theta\mathcal{G}} \sum_{\mathbf{k}\in IBZ} \sum_{\nu,\nu'} \sum_{i,j} \left[P^{\alpha,\sigma}_{lm,\nu}(\mathcal{S}\mathbf{k})\right]^i\ \mathcal{O}^{ij}_{\nu\nu'}(\mathcal{S}\mathbf{k})\ \left[P^{\alpha,\sigma'}_{lm',\nu'}(\mathcal{S}\mathbf{k})\right]^{j\,*}
\end{aligned} \tag{E.54}$$

where *IBZ* denotes the irreducible Brillouin zone of the original point group $\mathcal{G}$.

- when $\mathcal{S} \in \mathcal{G}$, one gets:

$$\begin{aligned}
\left[\left(\mathcal{O}_l^{\alpha}\right)^{\sigma\sigma'}_{mm'}\right]^{\mathcal{G}} &= \sum_{\mathcal{S}\in\mathcal{G}} \sum_{n,n'} \sum_{\tau,\tau'} \mathcal{D}^l(\mathcal{S})_{m,n} \mathcal{D}^{\frac{1}{2}}(\mathcal{S})_{\sigma,\tau} \left[\left(\mathcal{O}_l^{\mathcal{S}^{-1}\alpha}\right)^{\tau\tau'}_{nn'}\right]_{unsym} \mathcal{D}^l(\mathcal{S}^{-1})_{n',m'} \mathcal{D}^{\frac{1}{2}}(\mathcal{S}^{-1})_{\tau',\sigma'} \\
&\text{with} \quad \left[\left(\mathcal{O}_l^{\alpha}\right)^{\sigma\sigma'}_{mm'}\right]_{unsym} = \sum_{\mathbf{k}\in IBZ} \sum_{\nu,\nu'} \sum_{i,j} \left[P^{\alpha,\sigma}_{lm,\nu}(\mathbf{k})\right]^i\ \mathcal{O}^{ij}_{\nu\nu'}(\mathbf{k})\ \left[P^{\alpha,\sigma'}_{lm',\nu'}(\mathbf{k})\right]^{j\,*}
\end{aligned} \tag{E.55}$$

by using the formula (E.33) and the following equality:

$$\langle\psi^i_{\mathcal{S}\mathbf{k},\nu}|\mathcal{O}|\psi^j_{\mathcal{S}\mathbf{k}',\nu'}\rangle = \sum_{a,b} \mathcal{D}^{\frac{1}{2}}(\mathcal{S})_{i,a} \langle\psi^a_{\mathbf{k},\mathcal{S}^{-1}\nu}|\mathcal{O}|\psi^b_{\mathbf{k}',\mathcal{S}^{-1}\nu'}\rangle \mathcal{D}^{\frac{1}{2}}(\mathcal{S}^{-1})_{b,j} \tag{E.56}$$

- and when $\mathcal{S} \in \Theta\mathcal{G}$, one gets:

$$\left[(\mathcal{O}_l^\alpha)_{mm'}^{\sigma\sigma'}\right]^{\Theta\mathcal{G}} = \sum_{\mathcal{S}\in\Theta\mathcal{G}} \sum_{n,n'} \sum_{\tau\tau'} \mathcal{D}^l(\mathcal{S})_{m,n} \mathcal{D}^{\frac{1}{2}}(\mathcal{S})_{\sigma,\tau} \left[\left(\mathcal{O}_l^{\mathcal{S}^{-1}\alpha}\right)_{nn'}^{\tau\tau'}\right]^*_{unsym} \left[\mathcal{D}^l(\mathcal{S}^{-1})_{n',m'} \mathcal{D}^{\frac{1}{2}}(\mathcal{S}^{-1})_{\tau',\sigma'}\right]^* \tag{E.57}$$

by using formula (E.40) and the relation:

$$\langle \psi^i_{\mathcal{S}\mathbf{k},\nu} | \mathcal{O} | \psi^j_{\mathcal{S}\mathbf{k}',\nu'} \rangle = \sum_{a,b} \mathcal{D}^{\frac{1}{2}}(\mathcal{S})_{i,a} \left[\langle \psi^a_{\mathbf{k},\mathcal{S}^{-1}\nu} | \mathcal{O} | \psi^b_{\mathbf{k}',\mathcal{S}^{-1}\nu'} \rangle\right]^* \left[\mathcal{D}^{\frac{1}{2}}(\mathcal{S}^{-1})_{b,j}\right]^* \tag{E.58}$$

The term $(\mathcal{O}_l^\alpha)_{mm'}^{\sigma\sigma'}$ of (E.53) can finally be written as follows:

$$(\mathcal{O}_l^\alpha)_{mm'}^{\sigma\sigma'} = \frac{1}{2}\left[\left[(\mathcal{O}_l^\alpha)_{mm'}^{\sigma\sigma'}\right]^{\mathcal{G}} + \sum_{n,n'}\sum_{\tau,\tau'} \mathcal{D}^l(\Theta)_{m,n} \mathcal{D}^{\frac{1}{2}}(\Theta)_{\sigma,\tau} \left[(\mathcal{O}_l^\alpha)_{nn'}^{\tau\tau'}\right]^{\mathcal{G}*} \left[\mathcal{D}^l(\Theta^{-1})_{n',m'} \mathcal{D}^{\frac{1}{2}}(\Theta^{-1})_{\tau',\sigma'}\right]^*\right] \tag{E.59}$$

since $\mathcal{D}^{\frac{1}{2}}(\Theta) = -i\sigma_y$ and $\mathcal{D}^{\frac{1}{2}}(\Theta^{-1}) = \mathcal{D}^{\frac{1}{2}}(\Theta^\dagger) = \mathcal{D}^{\frac{1}{2}}(\Theta)^T = -\mathcal{D}^{\frac{1}{2}}(\Theta)$, this leads to:

$$\begin{aligned}
(\mathcal{O}_l^\alpha)_{mm'}^{\uparrow\uparrow} &= \frac{1}{2}\left[\left[(\mathcal{O}_l^\alpha)_{mm'}^{\uparrow\uparrow}\right]^{\mathcal{G}} + \sum_{n,n'} \mathcal{D}^l(\Theta)_{m,n} \left[(\mathcal{O}_l^\alpha)_{nn'}^{\downarrow\downarrow}\right]^{\mathcal{G}*} \left[\mathcal{D}^l(\Theta^{-1})_{n',m'}\right]^*\right] \\
(\mathcal{O}_l^\alpha)_{mm'}^{\downarrow\downarrow} &= \frac{1}{2}\left[\left[(\mathcal{O}_l^\alpha)_{mm'}^{\downarrow\downarrow}\right]^{\mathcal{G}} + \sum_{n,n'} \mathcal{D}^l(\Theta)_{m,n} \left[(\mathcal{O}_l^\alpha)_{nn'}^{\uparrow\uparrow}\right]^{\mathcal{G}*} \left[\mathcal{D}^l(\Theta^{-1})_{n',m'}\right]^*\right] \\
(\mathcal{O}_l^\alpha)_{mm'}^{\uparrow\downarrow} &= \frac{1}{2}\left[\left[(\mathcal{O}_l^\alpha)_{mm'}^{\uparrow\downarrow}\right]^{\mathcal{G}} - \sum_{n,n'} \mathcal{D}^l(\Theta)_{m,n} \left[(\mathcal{O}_l^\alpha)_{nn'}^{\downarrow\uparrow}\right]^{\mathcal{G}*} \left[\mathcal{D}^l(\Theta^{-1})_{n',m'}\right]^*\right]
\end{aligned} \tag{E.60}$$

E.4.2 Case of a spin-polarized calculation

without spin-orbit coupling

We consider now a *spin-polarized* calculation – with a "*black and white*" (type III) magnetic point group $\mathcal{H} + \Theta(\mathcal{G} \setminus \mathcal{H})$ –. In this case, we have to perform the following computation:

$$\begin{aligned}
\forall\ \sigma \in \{\uparrow,\downarrow\} \qquad \left(\mathcal{O}_l^{\alpha,\sigma}\right)_{mm'} &= \langle w_{lm}^{\alpha\sigma} | \left[\sum_{\mathbf{k}\in 1BZ} \sum_{\nu,\nu'} |\psi^\sigma_{\mathbf{k}\nu}\rangle \mathcal{O}^\sigma_{\nu\nu'}(\mathbf{k}) \langle \psi^\sigma_{\mathbf{k}\nu'}|\right] |w_{lm'}^{\alpha\sigma}\rangle \\
&= \sum_{\mathbf{k}\in 1BZ} \sum_{\nu,\nu'} P^{\alpha,\sigma}_{lm,\nu}(\mathbf{k})\ \mathcal{O}^\sigma_{\nu\nu'}(\mathbf{k})\ \left[P^{\alpha,\sigma}_{lm',\nu'}(\mathbf{k})\right]^* .\ \delta_{\sigma\sigma'} \\
&= \sum_{\mathcal{S}\in\mathcal{H}} \sum_{\mathbf{k}\in IBZ} \sum_{\nu,\nu'} P^{\alpha,\sigma}_{lm,\nu}(\mathcal{S}\mathbf{k})\ \mathcal{O}^\sigma_{\nu\nu'}(\mathcal{S}\mathbf{k})\ \left[P^{\alpha,\sigma}_{lm',\nu'}(\mathcal{S}\mathbf{k})\right]^* \\
&\qquad + \sum_{\mathcal{S}\in\Theta(\mathcal{G}\setminus\mathcal{H})} \sum_{\mathbf{k}\in IBZ} \sum_{\nu,\nu'} P^{\alpha,\sigma}_{lm,\nu}(\mathcal{S}\mathbf{k})\ \mathcal{O}^\sigma_{\nu\nu'}(\mathcal{S}\mathbf{k})\ \left[P^{\alpha,\sigma}_{lm',\nu'}(\mathcal{S}\mathbf{k})\right]^*
\end{aligned} \tag{E.61}$$

where *1BZ* (*IBZ*) is the first (respectively the irreducible) Brillouin zone of the original point group $\mathcal{G}$. Using the previous expressions (E.45) and (E.48), one obtains:

$$\begin{aligned}
\left(\mathcal{O}_l^{\alpha,\sigma}\right)_{mm'} &= \sum_{\mathcal{S}\in\mathcal{H}}\sum_{n,n'} \mathcal{D}^l(\mathcal{S})_{m,n} \left[\left(\mathcal{O}_l^{\mathcal{S}^{-1}\alpha,\mathcal{S}^{-1}\sigma}\right)_{nn'}\right]_{unsym} \mathcal{D}^l(\mathcal{S}^{-1})_{n',m'} \\
&\quad + \sum_{\mathcal{S}\in\Theta(\mathcal{G}\smallsetminus\mathcal{H})}\sum_{n,n'} \mathcal{D}^l(\mathcal{S})_{m,n} \left[\left(\mathcal{O}_l^{\mathcal{S}^{-1}\alpha,\mathcal{S}^{-1}\sigma}\right)_{nn'}\right]^*_{unsym} \left[\mathcal{D}^l(\mathcal{S}^{-1})_{n',m'}\right]^* \\
\text{with}\quad \left[\left(\mathcal{O}_l^{\alpha,\sigma}\right)_{mm'}\right]_{unsym} &= \sum_{\mathbf{k}\in IBZ}\sum_{\nu,\nu'} P^{\alpha,\sigma}_{lm,\nu}(\mathbf{k})\ \mathcal{O}^{\sigma}_{\nu\nu'}(\mathbf{k})\ \left[P^{\alpha,\sigma}_{lm',\nu'}(\mathbf{k})\right]^*
\end{aligned} \tag{E.62}$$

If we assume that the magnetization axis of the compound lies along the **z**-axis, the halving subgroup $\mathcal{H}$ of $\mathcal{G}$ is defined as the symmetry operations which do not change the orientation of the magnetization and thus keep the **z**-axis invariant. As a result,

$$\begin{array}{ccccccccc}
\mathcal{S}\in\mathcal{H} & \Longleftrightarrow & \beta_{\mathcal{S}}=0 & & \text{and} & \mathcal{R}\in\mathcal{G}\smallsetminus\mathcal{H} & \Longleftrightarrow & \beta_{\mathcal{R}}=\pi & \\
& \Longleftrightarrow & \forall\ \sigma\in\{\uparrow,\downarrow\} & \mathcal{R}\sigma=\sigma & & & \Longleftrightarrow & \forall\ \sigma\in\{\uparrow,\downarrow\} & \mathcal{S}\sigma=-\sigma
\end{array}$$

where $\beta_{\mathcal{S}}$ is the Euler angle β of the symmetry operation $\mathcal{S}$. Since $\Theta\sigma=-\sigma$ too, we finally can write:

$$\begin{aligned}
\forall\ \sigma\in\{\uparrow,\downarrow\} \qquad \left(\mathcal{O}_l^{\alpha,\sigma}\right)_{mm'} &= \sum_{\mathcal{S}\in\mathcal{H}}\sum_{n,n'} \mathcal{D}^l(\mathcal{S})_{m,n} \left[\left(\mathcal{O}_l^{\mathcal{S}^{-1}\alpha,\sigma}\right)_{nn'}\right]_{unsym} \mathcal{D}^l(\mathcal{S}^{-1})_{n',m'} \\
&\quad + \sum_{\mathcal{R}\in\mathcal{G}\smallsetminus\mathcal{H}}\sum_{n,n'} \mathcal{D}^l(\Theta\mathcal{R})_{m,n} \left[\left(\mathcal{O}_l^{\mathcal{R}^{-1}\alpha,\sigma}\right)_{nn'}\right]^*_{unsym} \left[\mathcal{D}^l(\mathcal{R}^{-1}\Theta^{-1})_{n',m'}\right]^*
\end{aligned} \tag{E.63}$$

when the spin-orbit coupling is taken into account

AS previously, taking into account the spin-orbit coupling does not modify the "*black and white*" magnetic point group of the system but the spin indices must now be explicitly treated.

$$\begin{aligned}
(\mathcal{O}_l^{\alpha})^{\sigma\sigma'}_{mm'} &= \langle w^{\alpha\sigma}_{lm}| \left[\sum_{\mathbf{k}\in 1BZ}\sum_{\nu,\nu'}\sum_{i,j=+,-} |\psi^i_{\mathbf{k}\nu}\rangle \mathcal{O}^{ij}_{\nu\nu'}(\mathbf{k}) \langle\psi^j_{\mathbf{k}\nu'}|\right] |w^{\alpha\sigma'}_{lm'}\rangle \\
&= \sum_{\mathbf{k}\in 1BZ}\sum_{\nu,\nu'}\sum_{i,j} \left[P^{\alpha,\sigma}_{lm,\nu}(\mathbf{k})\right]^i\ \mathcal{O}^{ij}_{\nu\nu'}(\mathbf{k})\ \left[P^{\alpha,\sigma}_{lm',\nu'}(\mathbf{k})\right]^{j\ *} \\
&= \sum_{\mathcal{S}\in\mathcal{G}}\sum_{\mathbf{k}\in IBZ}\sum_{\nu,\nu'}\sum_{i,j} \left[P^{\alpha,\sigma}_{lm,\nu}(\mathcal{S}\mathbf{k})\right]^i\ \mathcal{O}^{ij}_{\nu\nu'}(\mathcal{S}\mathbf{k})\ \left[P^{\alpha,\sigma'}_{lm',\nu'}(\mathcal{S}\mathbf{k})\right]^{j\ *} \\
&\qquad + \sum_{\mathcal{S}\in\Theta(\mathcal{G}\smallsetminus\mathcal{H})}\sum_{\mathbf{k}\in IBZ}\sum_{\nu,\nu'}\sum_{i,j} \left[P^{\alpha,\sigma}_{lm,\nu}(\mathcal{S}\mathbf{k})\right]^i\ \mathcal{O}^{ij}_{\nu\nu'}(\mathcal{S}\mathbf{k})\ \left[P^{\alpha,\sigma'}_{lm',\nu'}(\mathcal{S}\mathbf{k})\right]^{j\ *}
\end{aligned} \tag{E.64}$$

with *1BZ* (*IBZ*)the first (respectively the irreducible) Brillouin zone of the original point group $\mathcal{G}$. Using the previous expressions (E.55) and (E.57), one obtains:

$$\begin{aligned}
(\mathcal{O}_l^\alpha)^{\sigma\sigma'}_{mm'} &= \sum_{\mathcal{S}\in\mathcal{G}}\sum_{n,n'}\sum_{\tau,\tau'}\mathcal{D}^l(\mathcal{S})_{m,n}\mathcal{D}^{\frac{1}{2}}(\mathcal{S})_{\sigma,\tau}\ \left[\left(\mathcal{O}_l^{\mathcal{S}^{-1}\alpha}\right)^{\tau\tau'}_{nn'}\right]_{unsym}\ \mathcal{D}^l(\mathcal{S}^{-1})_{n',m'}\mathcal{D}^{\frac{1}{2}}(\mathcal{S}^{-1})_{\tau',\sigma'} \\
&+ \sum_{\mathcal{S}\in\Theta(\mathcal{G}\smallsetminus\mathcal{H})}\sum_{n,n'}\sum_{\tau\tau'}\mathcal{D}^l(\mathcal{S})_{m,n}\mathcal{D}^{\frac{1}{2}}(\mathcal{S})_{\sigma,\tau}\ \left[\left(\mathcal{O}_l^{\mathcal{S}^{-1}\alpha}\right)^{\tau\tau'}_{nn'}\right]^*_{unsym}\ \left[\mathcal{D}^l(\mathcal{S}^{-1})_{n',m'}\mathcal{D}^{\frac{1}{2}}(\mathcal{S}^{-1})_{\tau',\sigma'}\right]^* \\
\text{with}\quad \left[(\mathcal{O}_l^\alpha)^{\sigma\sigma'}_{mm'}\right]_{unsym} &= \sum_{\mathbf{k}\in IBZ}\sum_{\nu,\nu'}\sum_{i,j}\left[P^{\alpha,\sigma}_{lm,\nu}(\mathbf{k})\right]^i\ \mathcal{O}^{ij}_{\nu\nu'}(\mathbf{k})\ \left[P^{\alpha,\sigma'}_{lm',\nu'}(\mathbf{k})\right]^{j\ *}
\end{aligned} \tag{E.65}$$

This expression can be simplified further if we assume that magnetization axis of the compound lies along the **z**-axis. In this case, when $\mathcal{S}$ belongs to the subgroup $\mathcal{H}$ ($\beta = 0$), we indeed have in the basis $\{|\uparrow\rangle, |\downarrow\rangle\}$:

$$\mathcal{D}^{\frac{1}{2}}(\mathcal{S}) = \begin{pmatrix} \cos\frac{\beta}{2}e^{-i\frac{\alpha+\gamma}{2}} & -\sin\frac{\beta}{2}e^{i\frac{\alpha-\gamma}{2}} \\ \sin\frac{\beta}{2}e^{-i\frac{\alpha-\gamma}{2}} & \cos\frac{\beta}{2}e^{i\frac{\alpha+\gamma}{2}} \end{pmatrix} = \begin{pmatrix} e^{-i\frac{\alpha+\gamma}{2}} & 0 \\ 0 & e^{i\frac{\alpha+\gamma}{2}} \end{pmatrix} \tag{E.66}$$

whereas when $\mathcal{R}$ belongs to the subgroup $\mathcal{G}\smallsetminus\mathcal{H}$ ($\beta = \pi$),

$$\mathcal{D}^{\frac{1}{2}}(\mathcal{R}) = \begin{pmatrix} \cos\frac{\beta}{2}e^{-i\frac{\alpha+\gamma}{2}} & -\sin\frac{\beta}{2}e^{i\frac{\alpha-\gamma}{2}} \\ \sin\frac{\beta}{2}e^{-i\frac{\alpha-\gamma}{2}} & \cos\frac{\beta}{2}e^{i\frac{\alpha+\gamma}{2}} \end{pmatrix} = \begin{pmatrix} 0 & -e^{i\frac{\alpha-\gamma}{2}} \\ e^{-i\frac{\alpha-\gamma}{2}} & 0 \end{pmatrix} \tag{E.67}$$

thus leading to:

$$\mathcal{D}^{\frac{1}{2}}(\mathcal{S}) = \mathcal{D}^{\frac{1}{2}}(\Theta\mathcal{R}) = \begin{pmatrix} 0 & -1 \\ 1 & 0 \end{pmatrix}\begin{pmatrix} 0 & -e^{i\frac{\alpha-\gamma}{2}} \\ e^{-i\frac{\alpha-\gamma}{2}} & 0 \end{pmatrix} = \begin{pmatrix} -e^{i\frac{\alpha-\gamma}{2}} & 0 \\ 0 & -e^{-i\frac{\alpha-\gamma}{2}} \end{pmatrix} \tag{E.68}$$

As a result, we can rewrite (E.65) as follows[3]:

$$\begin{aligned}
(\mathcal{O}_l^\alpha)^{\uparrow\uparrow}_{mm'} &= \sum_{\mathcal{S}\in\mathcal{G}}\sum_{n,n'}\mathcal{D}^l(\mathcal{S})_{m,n}\ \left[\left(\mathcal{O}_l^{\mathcal{S}^{-1}\alpha}\right)^{\uparrow\uparrow}_{nn'}\right]_{unsym}\ \mathcal{D}^l(\mathcal{S}^{-1})_{n',m'} \\
&\quad + \sum_{\mathcal{R}\in(\mathcal{G}\smallsetminus\mathcal{H})}\sum_{n,n'}\mathcal{D}^l(\Theta\mathcal{R})_{m,n}\ \left[\left(\mathcal{O}_l^{\mathcal{R}^{-1}\alpha}\right)^{\uparrow\uparrow}_{nn'}\right]^*_{unsym}\ \left[\mathcal{D}^l(\mathcal{R}^{-1}\Theta^{-1})_{n',m'}\right]^* \\
(\mathcal{O}_l^\alpha)^{\downarrow\downarrow}_{mm'} &= \sum_{\mathcal{S}\in\mathcal{G}}\sum_{n,n'}\mathcal{D}^l(\mathcal{S})_{m,n}\ \left[\left(\mathcal{O}_l^{\mathcal{S}^{-1}\alpha}\right)^{\downarrow\downarrow}_{nn'}\right]_{unsym}\ \mathcal{D}^l(\mathcal{S}^{-1})_{n',m'} \\
&\quad + \sum_{\mathcal{R}\in(\mathcal{G}\smallsetminus\mathcal{H})}\sum_{n,n'}\mathcal{D}^l(\Theta\mathcal{R})_{m,n}\ \left[\left(\mathcal{O}_l^{\mathcal{R}^{-1}\alpha}\right)^{\downarrow\downarrow}_{nn'}\right]^*_{unsym}\ \left[\mathcal{D}^l(\mathcal{R}^{-1}\Theta^{-1})_{n',m'}\right]^* \\
(\mathcal{O}_l^\alpha)^{\uparrow\downarrow}_{mm'} &= \sum_{\mathcal{S}\in\mathcal{G}}\sum_{n,n'}\mathcal{D}^l(\mathcal{S})_{m,n}\ \left[\left(\mathcal{O}_l^{\mathcal{S}^{-1}\alpha}\right)^{\uparrow\downarrow}_{nn'}\right]_{unsym}\ \mathcal{D}^l(\mathcal{S}^{-1})_{n',m'}\ e^{-i(\alpha+\gamma)} \\
&\quad + \sum_{\mathcal{R}\in(\mathcal{G}\smallsetminus\mathcal{H})}\sum_{n,n'}\mathcal{D}^l(\Theta\mathcal{R})_{m,n}\ \left[\left(\mathcal{O}_l^{\mathcal{R}^{-1}\alpha}\right)^{\uparrow\downarrow}_{nn'}\right]^*_{unsym}\ \left[\mathcal{D}^l(\mathcal{R}^{-1}\Theta^{-1})_{n',m'}\right]^*\ e^{i(\alpha-\gamma)}
\end{aligned} \tag{E.69}$$

[3]We remind that if $\mathcal{S}$ belongs to the subgroup $\Theta(\mathcal{G}\smallsetminus\mathcal{H})$, $\mathcal{D}^{\frac{1}{2}}(\mathcal{S}^{-1}) = \mathcal{D}^{\frac{1}{2}}(\mathcal{S}^\dagger) = \mathcal{D}^{\frac{1}{2}}(\mathcal{S})^T (= \mathcal{D}^{\frac{1}{2}}(\mathcal{S})$ here).

Appendix F

From many-body spin-orbit interactions to one-electron spin-orbit coupling

The "*non-relativistic limit*" of the Dirac equation up to the order $(v/c)^2$ – and the "*scalar relativistic approximation*" – was introduced in section 3.3. In standard treatments of the spin-orbit coupling within the DFT framework, equations (3.43) and (3.45) are used with the effective Kohn-Sham potential $V_{KS}(\mathbf{r})$ instead of the mere external potential $V(\mathbf{r})$. As a result, the many-body effects induced by the Coulomb repulsion are included in this approach via the Hartree potential $V_H(\mathbf{r})$ and the exchange-correlation potential $V^{xc}(\mathbf{r})$. In this appendix, we address the question of how this spin-orbit coupling term – with $V_{KS}(\mathbf{r})$ instead of $V(\mathbf{r})$ – can be considered as a mean-field approximation to many-body interactions.

Indeed, if one considers the *non-relativistic limit* of the Dirac-Coulomb-Breit Hamiltonian [26], other many-body terms appear in addition to the "standard" electron-electron Coulomb interaction. Among them, the "*spin-same-orbit*" and "*spin-other-orbit*" terms are the general many-body expression of the spin-orbit interaction. The standard one-body term H_{SO} term can thus be seen as a mean-field approximation of the complete "spin-orbit interactions" which arise in the many-body problem.

In this appendix, we first introduce the many-body spin-orbit interaction terms, called "*spin-same-orbit*" and "*spin-other-orbit*". They must be taken into account in a *scalar relativistic approximation* of the Dirac-Coulomb-Breit Hamiltonian [26]. With the help of a generalization of Hedin's equation formalism [15, 65], we derive the generalized Hartree and Fock terms associated to these interactions and calculated the screened interaction. These developments are the first step towards a full treatment of "*many-body spin-orbit interactions*", which is however beyond the frame of this thesis.

F.1 The *spin-same-orbit* and *spin-other-orbit* interactions

F.1.1 Introduction of these interaction terms

According to Slater [153] and Breit [26], taking into account the magnetic effects in the many-body problem with a description of the electrons by the Dirac equation makes the following terms appear[1]:

the Coulomb interaction

$$\frac{1}{2}\sum_{i,j}\frac{e^2}{4\pi\varepsilon_0}\frac{1}{r_{ij}}, \tag{F.1}$$

[1] with the definition $\mathbf{s} = \frac{1}{2}\boldsymbol{\sigma}$, where σ_i (i=x,y,z) are the Pauli matrices.

the orbit-orbit interaction

$$\frac{1}{2}\sum_{i,j}\ \frac{e^2\hbar^2}{4\pi\varepsilon_0 m_0^2 c^2}\qquad \Big[-\frac{(-i\nabla_i)\cdot(-i\nabla_j)}{2r_{ij}} \\ -\frac{[(\mathbf{r}_i-\mathbf{r}_j)\cdot(-i\nabla_i)][(\mathbf{r}_i-\mathbf{r}_j)\cdot(-i\nabla_j)]}{2r_{ij}^3}+\frac{1}{4}\frac{(\mathbf{r}_i-\mathbf{r}_j)\cdot\nabla_i+(\mathbf{r}_j-\mathbf{r}_i)\cdot\nabla_j}{r_{ij}^3}\Big], \tag{F.2}$$

the spin-same-orbit interaction

$$\frac{1}{2}\sum_{i,j}\ -\frac{e^2\hbar^2}{4\pi\varepsilon_0 m_0^2 c^2}\frac{\mathbf{s}_i\cdot[(\mathbf{r}_i-\mathbf{r}_j)\times(-i\nabla_i)]+\mathbf{s}_j\cdot[(\mathbf{r}_j-\mathbf{r}_i)\times(-i\nabla_j)]}{2r_{ij}^3}, \tag{F.3}$$

the spin-other-orbit interaction

$$\frac{1}{2}\sum_{i,j}\ \frac{e^2\hbar^2}{4\pi\varepsilon_0 m_0^2 c^2}\frac{\mathbf{s}_i\cdot[(\mathbf{r}_i-\mathbf{r}_j)\times(-i\nabla_j)]+\mathbf{s}_j\cdot[(\mathbf{r}_j-\mathbf{r}_i)\times(-i\nabla_i)]}{r_{ij}^3}, \tag{F.4}$$

the spin-spin interaction

$$\frac{1}{2}\sum_{i,j}\ \frac{e^2\hbar^2}{4\pi\varepsilon_0 m_0^2 c^2}\Big[\frac{\mathbf{s}_i\cdot\mathbf{s}_j}{r_{ij}^3}-\frac{3[\mathbf{s}_i\cdot(\mathbf{r}_i-\mathbf{r}_j)][\mathbf{s}_j\cdot(\mathbf{r}_j-\mathbf{r}_i)]}{r_{ij}^5}\Big]. \tag{F.5}$$

However, the spin-orbit effects are generally supposed to be greater than those due to the other terms, except of course the Coulomb interaction. That is why we will only consider the *spin-same-orbit* and the *spin-other orbit* contributions in the following. The interaction term of our system is then:

$$\begin{aligned}\widehat{V} &= \frac{1}{2}\sum_{i,j}\ \frac{e^2}{4\pi\varepsilon_0}\frac{1}{r_{ij}}+\frac{e^2\hbar}{8\pi\varepsilon_0 m_0^2 c^2}[\nabla_{\mathbf{r}_i}\Big(\frac{1}{r_{ij}}\Big)\times(\mathbf{p}_i-2\mathbf{p}_j)]\cdot\boldsymbol{\sigma}_i \\ &= \frac{1}{2}\sum_{i,j}\ \frac{e^2}{4\pi\varepsilon_0}\frac{1}{r_{ij}}+\frac{e^2\hbar}{8\pi\varepsilon_0 m_0^2 c^2}[\nabla_{\mathbf{r}_i}\Big(\frac{1}{r_{ij}}\Big)\times\mathbf{p}_i]\cdot[\boldsymbol{\sigma}_i+2\boldsymbol{\sigma}_j].\end{aligned} \tag{F.6}$$

By performing an adimensionalization with respect to ε_F for the energies and k_F for the wave numbers, we find the following expressions where the relation between k_F and the Bohr radius a_0 is still to define:

$$v^C=\frac{2}{a_0^2k_F^2}\ \frac{1}{\widetilde{\mathbf{r}}}\ \varepsilon_F\quad\text{and}\quad v^{SO}=-\frac{2\alpha^2}{a_0k_F}\ \frac{1}{\widetilde{\mathbf{r}}^3}[\widetilde{\mathbf{r}}\times\widetilde{\mathbf{p}}]\cdot\frac{1}{2}\boldsymbol{\sigma}\ \varepsilon_F. \tag{F.7}$$

In the Hartree atomic units, the conventions lead to:

$$\varepsilon_F=(\hbar^2k_F^2)/(2m)=mc^2\alpha^2\qquad\text{i.e.}\qquad k_F^2a_0^2=2. \tag{F.8}$$

In the Rydberg atomic units however, the fundamental relation is:

$$\varepsilon_F=(\hbar^2k_F^2)/(2m)=(1/2)mc^2\alpha^2\qquad\text{i.e.}\qquad k_F^2a_0^2=1. \tag{F.9}$$

We will use the Hartree convention in the following and will then replace $(e^2\hbar^2)/(4\pi\varepsilon_0m_0^2c^2)$ by $\alpha^2\sqrt{2}$.

F.1.2 Pauli matrices representation of a general interaction

An interaction is a two-body operator which has the following general form in second quantization:

$$\widehat{V} = \frac{1}{2}\sum_{\alpha,\beta,\gamma,\eta}\iint\iint d1d2d3d4 \quad v_{\alpha\beta\gamma\eta}(1,2,3,4)\psi^\dagger_\alpha(1)\psi^\dagger_\beta(2)\psi_\eta(4)\psi_\gamma(3) \quad \text{with} \quad i=(\vec{r}_i,t_i) \tag{F.10}$$

with the two essential properties:

- $v_{\alpha\beta\gamma\eta}(1,2,3,4)$ must be proportional to $\delta(t_3-t_1)\delta(t_4-t_2)$ because of the *conservation of the number of particles at each time*. On the contrary, a term $\delta(t_2-t_1)$ appears only if the interaction is assumed instantaneous.
  In order to keep in mind this dependence on only two time parameters, we will use the following shortcuts $[i,j]=(\mathbf{r}_i,\mathbf{r}_j,t_i)$ if $t_i=t_j$ so that we can write:
$$v_{\alpha\beta\gamma\eta}(1,2,3,4) = v_{\alpha\beta\gamma\eta}([1,3];[2,4])\delta(t_3-t_1)\delta(t_4-t_2) \tag{F.11}$$
- $v_{\alpha\beta\gamma\eta}(1,2,3,4) = v_{\beta\alpha\eta\gamma}(2,1,4,3)$ or $v_{\alpha\beta\gamma\eta}([1,3];[2,4]) = v_{\beta\alpha\eta\gamma}([2,4];[1,3])$ because of the *invariance under particle interchange.*

This interaction can be expanded in the Pauli matrices (σ^X,σ^Y,σ^Z) and unit matrix ($\sigma^0=\mathbb{I}d$) as:

$$v_{\alpha\beta\gamma\eta}([1,3];[2,4]) = \sum_{I,J=0,X,Y,Z}\sigma^I_{\alpha\gamma}\ v_{IJ}([1,3];[2,4])\ \sigma^J_{\beta\eta} \tag{F.12}$$

In particular, the interaction term we consider can be written in this form:

$$v^C_{\alpha\beta\gamma\eta}([1,3];[2,4]) = \sigma^0_{\alpha\gamma}\delta(\mathbf{r}_3-\mathbf{r}_1)\frac{\delta(t_2-t_1)}{r_{12}}\delta(\mathbf{r}_4-\mathbf{r}_2)\sigma^0_{\beta\eta} \tag{F.13}$$

$$\begin{aligned} v^{SSO}_{\alpha\beta\gamma\eta}([1,3];[2,4]) &= \sigma^0_{\alpha\gamma}\ \frac{i\alpha^2}{2\sqrt{2}}[\nabla_{\mathbf{r}_2}\left(\frac{\delta(t_2-t_1)}{r_{12}}\right)\times\nabla_{\mathbf{r}_4}\delta(\mathbf{r}_4-\mathbf{r}_2)]_I\delta(\mathbf{r}_3-\mathbf{r}_1)\ \ \sigma^I_{\beta\eta} \\ &+ \sigma^I_{\alpha\gamma}\ \frac{i\alpha^2}{2\sqrt{2}}[\nabla_{\mathbf{r}_1}\left(\frac{\delta(t_2-t_1)}{r_{12}}\right)\times\nabla_{\mathbf{r}_3}\delta(\mathbf{r}_3-\mathbf{r}_1)]_I\delta(\mathbf{r}_4-\mathbf{r}_2)\ \ \sigma^0_{\beta\eta} \end{aligned} \tag{F.14}$$

$$\begin{aligned} v^{SOO}_{\alpha\beta\gamma\eta}([1,3];[2,4]) &= -\ \sigma^0_{\alpha\gamma}\ \frac{i\alpha^2}{2\sqrt{2}}[\nabla_{\mathbf{r}_2}\left(\frac{\delta(t_2-t_1)}{r_{12}}\right)\times\nabla_{\mathbf{r}_3}\delta(\mathbf{r}_3-\mathbf{r}_1)]_I\delta(\mathbf{r}_4-\mathbf{r}_2)\ 2\sigma^I_{\beta\eta} \\ &\quad -2\sigma^I_{\alpha\gamma}\ \frac{i\alpha^2}{2\sqrt{2}}[\nabla_{\mathbf{r}_1}\left(\frac{\delta(t_2-t_1)}{r_{12}}\right)\times\nabla_{\mathbf{r}_4}\delta(\mathbf{r}_4-\mathbf{r}_2)]_I\delta(\mathbf{r}_3-\mathbf{r}_1)\ \ \sigma^0_{\beta\eta} \end{aligned} \tag{F.15}$$

or, to be more clear:

$$v^C_{00}([1,3];[2,4]) = \delta(\mathbf{r}_3-\mathbf{r}_1)\frac{\delta(t_2-t_1)}{r_{12}}\delta(\mathbf{r}_4-\mathbf{r}_2) \tag{F.16}$$

$$\begin{aligned} v^{SSO}_{0J}([1,3];[2,4]) &= \frac{i\alpha^2}{2\sqrt{2}}[\nabla_{\mathbf{r}_2}\left(\frac{\delta(t_2-t_1)}{r_{12}}\right)\times\nabla_{\mathbf{r}_4}\delta(\mathbf{r}_4-\mathbf{r}_2)]_I\delta(\mathbf{r}_3-\mathbf{r}_1) \qquad \forall J\in\{X,Y,Z\} \\ v^{SSO}_{I0}([1,3];[2,4]) &= \frac{i\alpha^2}{2\sqrt{2}}[\nabla_{\mathbf{r}_1}\left(\frac{\delta(t_2-t_1)}{r_{12}}\right)\times\nabla_{\mathbf{r}_3}\delta(\mathbf{r}_3-\mathbf{r}_1)]_I\delta(\mathbf{r}_4-\mathbf{r}_2) \qquad \forall I\in\{X,Y,Z\} \end{aligned} \tag{F.17}$$

$$\begin{aligned} v^{SOO}_{0J}([1,3];[2,4]) &= -2\frac{i\alpha^2}{2\sqrt{2}}[\nabla_{\mathbf{r}_2}\left(\frac{\delta(t_2-t_1)}{r_{12}}\right)\times\nabla_{\mathbf{r}_3}\delta(\mathbf{r}_3-\mathbf{r}_1)]_I\delta(\mathbf{r}_4-\mathbf{r}_2) \qquad \forall J\in\{X,Y,Z\} \\ v^{SOO}_{I0}([1,3];[2,4]) &= -2\frac{i\alpha^2}{2\sqrt{2}}[\nabla_{\mathbf{r}_1}\left(\frac{\delta(t_2-t_1)}{r_{12}}\right)\times\nabla_{\mathbf{r}_4}\delta(\mathbf{r}_4-\mathbf{r}_2)]_I\delta(\mathbf{r}_3-\mathbf{r}_1) \qquad \forall I\in\{X,Y,Z\} \end{aligned}$$

We draw the reader's attention to the gradient operator in the expression $\nabla_{\mathbf{r}_i}(\frac{\delta(t_i-t_j)}{r_{ij}})$: this is just a shorter notation where the operator acts only on the following bracket contents. On the contrary, $\nabla_{\mathbf{r}_j}\delta(j-i)$ is an operator which acts on the whole expression, including creation and annihilation operators. Moreover, it is useful to notice that:

$$v_{0I}^{SSO}([1,3];[2,4]) = v_{I0}^{SSO}([2,4];[1,3]) \quad \text{and} \quad v_{0I}^{SOO}([1,3];[2,4]) = v_{I0}^{SOO}([2,4];[1,3]). \tag{F.18}$$

This equality ensures the invariance under particle exchange of the interactions.

F.2 Spin-Hedin equations in their most general form

F.2.1 A brief history on Hedin's equations

Inspired by the previous works of Schwinger, Hedin derived a closed set of equations for the electronic Green's function and self-energy, the screened Coulomb interaction and the polarization of a solid in 1965 [65]:

$$\begin{aligned}
\Sigma(1,2) &= i\hbar \iint d3d4 \quad G(1,3^+)W(1,4)\Lambda(3,2,4) \\
G(1,2) &= G_0(1,2) + \iint d3d4 \quad G_0(1,3)\Sigma(3,4)G(4,2) \\
P(1,2) &= -i\hbar \iint d3d4 \quad G(1,3)\Lambda(3,4,2)G(4,1^+) \\
W(1,2) &= v(1,2) + \iint d3d4 \quad v(1,3)P(3,4)W(4,2) \\
\Lambda(1,2,3) &= \delta(1-2)\delta(2-3) + \iint\iint d4d5d6d7 \quad \frac{\delta\Sigma(1,2)}{\delta G(4,5)}G(4,6)G(7,5)\Lambda(6,7,3)
\end{aligned} \tag{F.19}$$

with the convention $i = (\vec{r}_i, t_i, \sigma_i)$. In these equations, $\Sigma(1,2)$ is the self energy, $P(1,2)$ the polarization, $W(1,2)$ the screened interaction and $\Lambda(1,2,3)$ the vertex function. These equations are exact but the most common and simplest use of them is made by the so-called "*GW approximation*" which consists in writing:

$$\begin{aligned}
\Sigma(1,2) &= i\hbar\, G(1,2)W(2,1) \\
G(1,2) &= G_0(1,2) + \iint d3d4 \quad G_0(1,3)\Sigma(3,4)G(4,2) \\
P(1,2) &= -i\hbar\, G(1,2)G(2,1^+) \\
W(1,2) &= v(1,2) + \iint d3d4 \quad v(1,3)P(3,4)W(4,2) \\
\Lambda(1,2,3) &= \delta(1-2)\delta(2-3).
\end{aligned} \tag{F.20}$$

In 2008, a generalization of equations (F.19) for describing systems containing spin interactions,

such as spin-orbit and spin-spin interactions, was developed by Aryasetiawan and Biermann [15]:

$$\begin{aligned}
\Sigma_{\alpha\beta}(1,2) &= -\sigma^I_{\alpha\eta} G_{\eta\gamma}(1,3)\Lambda^J_{\gamma\beta}(3,2,4)W_{JI}(4,1) \\
G_{\alpha\beta}(1,2) &= G^0_{\alpha\beta}(1,2) + G^0_{\alpha\gamma}(1,3)\Sigma_{\gamma\eta}(3,4)G_{\eta\beta}(4,2) \\
P_{IJ}(1,2) &= \sigma^I_{\alpha\beta} G_{\beta\gamma}(1,3)\Lambda^J_{\gamma\eta}(3,4,2)G_{\eta\alpha}(4,1^+) \\
W_{IJ}(1,2) &= v_{IJ}(1,2) + v_{IK}(1,3)P_{KL}(3,4)W_{LJ}(4,2) \\
\Lambda^I_{\alpha\beta}(1,2,3) &= \delta(1-2)\delta(2-3)\sigma^I_{\alpha\beta} + \frac{\delta\Sigma_{\alpha\beta}(1,2)}{\delta G_{\gamma\eta}(4,5)} G_{\gamma\kappa}(4,6)\Lambda^I_{\kappa\mu}(6,7,3)G_{\mu\eta}(7,5).
\end{aligned} \tag{F.21}$$

where $i = (\vec{r}_i, \tau_i)$, τ is the imaginary time and σ^I are the Pauli spin matrices. Repeated indices are summed and repeated variables are integrated.

F.2.2 Spin-Hedin's equations for a general interaction term

Let's now rewrite the spin-Hedin's equations with the general expression (F.12) for the interaction term. To begin, the Heisenberg equations of motion are:

$$\begin{aligned}
-i\hbar\partial_t\psi_\kappa(5) &= [\widehat{H}, \psi_\kappa(5)] \quad \text{with} \quad \widehat{H} = \widehat{H}^0 + \widehat{V} \\
&= -h^0_{\kappa\beta}(5,1)\psi_\beta(1) - \frac{1}{2}\big(v_{\alpha\kappa\gamma\eta}(1,5,3,4) - v_{\kappa\alpha\gamma\eta}(5,1,3,4)\big)\psi^\dagger_\alpha(1)\psi_\eta(4)\psi_\gamma(3) \\
&= -h^0_{\kappa\beta}(5,1)\psi_\beta(1) - \frac{1}{2}\big(v_{\alpha\kappa\gamma\eta}(1,5,3,4) - v_{\alpha\kappa\eta\gamma}(1,5,4,3)\big)\psi^\dagger_\alpha(1)\psi_\eta(4)\psi_\gamma(3) \\
&= -h^0_{\kappa\beta}(5,1)\psi_\beta(1) - v_{\alpha\kappa\gamma\eta}(1,5,3,4)\psi^\dagger_\alpha(1)\psi_\eta(4)\psi_\gamma(3) \\
&= -h^0_{\kappa\beta}(5,1)\psi_\beta(1) - v_{\alpha\kappa\gamma\eta}([1,3];[5,4])\Big[\psi^\dagger_\alpha(1)\psi_\eta(4)\psi_\gamma(3)\Big]_{\substack{t_3=t_1\\ t_4=t_5}}
\end{aligned} \tag{F.22}$$

where we have used the invariance under particle interchange. As a result, one gets:

$$\begin{aligned}
-i\hbar\partial_t G_{\kappa\mu}(5,6) &= -i\hbar\partial_t\big(\frac{-i}{\hbar} < T[\psi_\kappa(5)\psi^\dagger_\mu(6)] > \big) \\
&= -h^0_{\kappa\beta}(5,1)G_{\beta\mu}(1,6) + i\hbar\, v_{\alpha\kappa\gamma\eta}([1,3];[5,4])G^{(2)}_{\eta\mu\gamma\alpha}(4,6,3,1^+) - \delta(5-6)\delta_{\kappa\mu}
\end{aligned} \tag{F.23}$$

where, as usual, $G^{(2)}_{\alpha\beta\gamma\eta}(1,2,3,4) = (-i/\hbar)^2 < T[\psi_\alpha(1)\psi_\eta(3)\psi^\dagger_\gamma(4)\psi^\dagger_\beta(2)] >$ and the notation 1^+ means $t_1 = t_3 + 0^+$.[2]

We will then use the Schwinger functional derivative technique, with the probing field:

$$\widehat{\phi} = \iint d1d2 \quad \psi^\dagger_\alpha(1)\,\Big(\varphi_I([1,2]).\delta(t_2-t_1)\Big)\sigma^I_{\alpha\beta}\,\psi_\beta(2) \quad \text{in} \quad \widehat{S} = T\Big[\exp\big(\frac{-i}{\hbar}\widehat{\phi}\big)\Big]. \tag{F.24}$$

It can then be shown that:

$$\frac{\delta G_{\alpha\beta}(1,2)}{\delta\varphi_I([3,4])} = \big[G_{\alpha\beta}(1,2)G_{\eta\gamma}(3,4^+) - G^{(2)}_{\alpha\beta\eta\gamma}(1,2,4,3^+)\big]\sigma^I_{\gamma\eta} \tag{F.25}$$

$$\text{and} \quad \frac{\delta G_{\alpha\beta}(1,2)}{\delta\varphi_I([3,4])} = -\iint d5d6 \quad G_{\alpha\gamma}(1,5)\,\frac{\delta G^{-1}_{\gamma\eta}(5,6)}{\delta\varphi_I([3,4])}\,G_{\eta\beta}(6,2). \tag{F.26}$$

[2] We remind the reader that the studied interactions contains a term $\delta(t_1 - t_3)$.

Consequently, the mass operator can be defined as:

$$\begin{aligned}\mathcal{M}_{\kappa\eta}(5,4)G_{\eta\mu}(4,6) &= -i\hbar\, v_{\alpha\kappa\gamma\eta}([1,3];[5,4])G^{(2)}_{\eta\mu\gamma\alpha}(4,6,3,1^+)\\ &= -i\hbar\, \sigma^I_{\alpha\gamma}\, v_{IJ}([1,3];[5,4])\, \sigma^J_{\kappa\eta}G^{(2)}_{\eta\mu\gamma\alpha}(4,6,3,1^+)\\ &= V^H_J(5,4)\sigma^J_{\kappa\eta}G_{\eta\mu}(4,6) + i\hbar\, v_{IJ}([1,3];[5,4])\sigma^J_{\kappa\eta}\frac{\delta G_{\eta\mu}(4,6)}{\delta\varphi_I([1,3])}\\ &= \left[V^H_J(5,4)\sigma^J_{\kappa\eta} + \Sigma_{\kappa\eta}(5,4)\right]G_{\eta\mu}(4,6) \qquad \text{(F.27)}\end{aligned}$$

with the following exact expression for the self-energy:

$$\Sigma_{\alpha\beta}(1,2) = -i\hbar\, v_{IJ}([0,3],[1,4])\sigma^J_{\alpha\gamma}G_{\gamma\eta}(4,5)\,\frac{\delta G^{-1}_{\eta\beta}(5,2)}{\delta\varphi_I([0,3])} \qquad \text{(F.28)}$$

and the generalized Hartree potential $V^H_I(1,3) = V^H_I([1,3]).\delta(t_3-t_1)$

$$\begin{aligned}\text{with}\quad V^H_I([1,3]) &= -i\hbar\, v_{JI}([2,4];[1,3])G_{\eta\gamma}(2,4^+)\sigma^J_{\gamma\eta}\\ &= -i\hbar\, v_{JI}([2,4];[1,3])G^J(2,4^+) = v_{IJ}([1,3];[2,4])\rho^J(2,4^+) \qquad \text{(F.29)}\end{aligned}$$

where $\rho^J(2,4^+) = -i\hbar\, G^J(2,4^+)$ is actually $\left[\rho^J(\mathbf{x}_4,\mathbf{x}_2)\right]_{t_2}$, i.e. the J-component of the density matrix in the Pauli matrices formalism. In particular, when $\mathbf{x}_4 = \mathbf{x}_2$, $\rho^0(2,2^+) = \left[\rho^0(\mathbf{x}_2)\right]_{t_2}$ is the total charge density in $(\mathbf{x}_2,t_2)$, and $\rho^I(2,2^+) = \left[\rho^I(\mathbf{x}_2)\right]_{t_2}$ (I=X,Y,Z) is the density of spin along the I-axis in $(\mathbf{x}_2,t_2)$.

We define now

- the total field as: $\Phi_I([1,2]) = \varphi_I([1,2]) + V^H_I([1,2])$
- the vertices[3]

$$\begin{aligned}\Lambda^I_{\alpha\beta}(1,2,[3,4]) &= -\frac{\delta G^{-1}_{\alpha\beta}(1,2)}{\delta\Phi_I([3,4])} = -\frac{\delta[G^0]^{-1}_{\alpha\beta}(1,2)}{\delta\Phi_I([3,4])} + \frac{\delta\Sigma_{\alpha\beta}(1,2)}{\delta\Phi_I([3,4])}\\ &= \left[\delta(3-1)\delta(4-2)\sigma^I_{\alpha\beta}\right]_{t_3=t_4} + \frac{\delta\Sigma_{\alpha\beta}(1,2)}{\delta\Phi_I([3,4])} \qquad \text{(F.30)}\end{aligned}$$

- the dielectric function

$$\varepsilon^{-1}_{IJ}([1,2];[3,4]) = \frac{\delta\Phi_I([1,2])}{\delta\varphi_J([3,4])} = \left[\delta(3-1)\delta(4-2)\delta_{IJ}\right]_{\substack{t_1=t_2\\ t_3=t_4}} + \frac{\delta V^H_I([1,2])}{\delta\varphi_J([3,4])} \qquad \text{(F.31)}$$

- the screened interaction as: $W_{IJ}([1,3];[2,4]) = \varepsilon^{-1}_{IK}([1,3];[5,6])v_{KJ}([5,6];[2,4])$
- and the polarization

$$P_{IJ}([1,2];[3,4]) = \frac{\delta\rho^I(2,1^+)}{\delta\Phi_J([3,4])} = -i\hbar\, \sigma^I_{\alpha\beta}\frac{\delta G_{\beta\alpha}(2,1^+)}{\delta\Phi_J([3,4])} \qquad \text{(F.32)}$$

[3]We remind the reader that:

$$\begin{aligned}[G^0]^{-1}_{\alpha\beta}(1,2) = H^0_{\alpha\beta}(1,2) &= i\hbar\partial_t - h^0_{\alpha\beta}(1,2) - \left[V^H_I([1,2])\delta(t_2-t_1)\right]\sigma^I_{\alpha\beta} - \left[\varphi^I([1,2])\delta(t_2-t_1)\right]\sigma^I_{\alpha\beta}\\ &= i\hbar\partial_t - h^0_{\alpha\beta}(1,2) - \left[\Phi^I([1,2])\delta(t_2-t_1)\right]\sigma^I_{\alpha\beta}\end{aligned}$$

which enable us to write the generalized spin-Hedin's equations[4]:

$$\begin{aligned}
\Sigma_{\alpha\beta}(1,2) &= i\hbar\,\sigma^I_{\alpha\eta}\Big[G_{\eta\gamma}(4,3)\Big]_{t_4=t_1}\Lambda^J_{\gamma\beta}(3,2,[5,6])W_{JI}([5,6];[1,4]) \\
G_{\alpha\beta}(1,2) &= G^0_{\alpha\beta}(1,2)+G^0_{\alpha\gamma}(1,3)\Sigma_{\gamma\eta}(3,4)G_{\eta\beta}(4,2) \\
P_{IJ}([1,3];[2,4]) &= -i\hbar\,\sigma^I_{\alpha\beta}\Big[G_{\beta\gamma}(3,5)\Big]_{t_3=t_1}\Lambda^J_{\gamma\eta}(5,6,[2,4])G_{\eta\alpha}(6,1^+) \\
W_{IJ}([1,3];[2,4]) &= v_{IJ}([1,3];[2,4])+v_{IK}([1,3];[5,6])P_{KL}([5,6];[7,8])W_{LJ}([7,8];[2,4]) \\
\Lambda^I_{\alpha\beta}(1,2,[3,4]) &= \Big[\delta(3-1)\delta(4-2)\sigma^I_{\alpha\beta}\Big]_{t_4=t_3}+\frac{\delta\Sigma_{\alpha\beta}(1,2)}{\delta G_{\gamma\eta}(5,6)}G_{\gamma\kappa}(6,7)\Lambda^I_{\kappa\mu}(7,8,[3,4])G_{\mu\eta}(8,6).
\end{aligned} \tag{F.33}$$

As a consequence, the GW approximation becomes:

$$\begin{aligned}
\Lambda^I_{\alpha\beta}(1,2,[3,4]) &= \Big[\delta(3-1)\delta(4-2)\sigma^I_{\alpha\beta}\Big]_{t_4=t_3} \\
P_{IJ}([1,3];[2,4]) &= -i\hbar\,\sigma^I_{\alpha\beta}\Big[G_{\beta\gamma}(3,2)\Big]_{t_3=t_1}\sigma^J_{\gamma\eta}\Big[G_{\eta\alpha}(4,1^+)\Big]_{t_4=t_2} \\
\Sigma_{\alpha\beta}(1,2) &= i\hbar\,\sigma^I_{\alpha\eta}\Big[G_{\eta\gamma}(4,3)\Big]_{\substack{t_4=t_1\\ t_3=t_2}}\sigma^J_{\gamma\beta}W_{JI}([3,2];[1,4]).
\end{aligned} \tag{F.34}$$

F.3 Generalized Hartree potential for our system

Our first approach of the problem will be to understand the meaning of the mean-field potential terms that we will find with the considered interactions.

F.3.1 The Coulomb interaction

$$\text{for } I=X,Y,Z \quad V^{CH}_I([1,3]) = v^C_{IJ}([1,3];[2,4])\rho^J(2,4^+)=0 \tag{F.35}$$

$$\begin{aligned}
\text{and} \quad V^{CH}_0([1;3]) &= v^C_{0J}([1,3];[2,4])\rho^J(2,4^+)=v^C_{00}([1,3];[2,4])\rho^0(2,4^+) \\
&= \delta(\mathbf{r}_3-\mathbf{r}_1)\frac{\delta(t_2-t_1)}{r_{12}}\delta(\mathbf{r}_4-\mathbf{r}_2)\;.\;\rho^0(2,4^+) \\
&= \int d2\;\;\frac{\rho^0(2,2^+)}{r_{12}}\delta(t_2-t_1)\;.\;\delta(\mathbf{r}_3-\mathbf{r}_1)
\end{aligned} \tag{F.36}$$

where $\rho^0(2,2^+)=G_{\uparrow\uparrow}(2,2^+)+G_{\downarrow\downarrow}(2,2^+)$. The result is thus the expected one: in a mean-field approach, an electron feels the potential created by the mean charge distribution ρ^0; the operator is diagonal – proportional to $\delta(3-1)$ – and can be rewritten in its usual form:

$$V^{CH}_0(1)=\int d\mathbf{r}_2\;\;\frac{\rho^0(2,2^+)}{r_{12}}\delta(t_2-t_1) \quad \text{or} \quad V^{CH}_0(\mathbf{r}_1,t_1)=\int d\mathbf{r}_2\;\;\frac{\rho^0(\mathbf{r}_2,t_1)}{r_{12}}. \tag{F.37}$$

[4]To get the equivalent equations in imaginary time, it's enough to replace $-i\hbar\,\sigma^I_{\alpha\beta}$ by $\sigma^I_{\alpha\beta}$ in the expression of the polarization $P_{IJ}([1,3];[2,4])$ and the self-energy $\Sigma_{\alpha\beta}(1,2)$.

F.3.2 The spin-same-orbit interaction

$$\begin{aligned}
\text{for } I=X,Y,Z \quad V_I^{SSOH}([1,3]) &= v_{IJ}^{SSO}([1,3];[2,4])\rho^J(2,4^+) = v_{I0}^{SSO}([1,3];[2,4])\rho^0(2,4^+) \\
&= \frac{i\alpha^2}{2\sqrt{2}}\Big[\nabla_{\mathbf{r}_1}\Big(\frac{\delta(t_2-t_1)}{r_{12}}\Big)\times\nabla_{\mathbf{r}_3}\delta(\mathbf{r}_3-\mathbf{r}_1)\Big]_I\delta(\mathbf{r}_4-\mathbf{r}_2)\ .\ \rho^0(2,4^+) \\
&= \frac{i\alpha^2}{2\sqrt{2}}\Big[\nabla_{\mathbf{r}_1}\Big(\int d2\ \ \frac{\rho^0(2,2^+)}{r_{12}}\delta(t_2-t_1)\Big)\times\nabla_{\mathbf{r}_3}\delta(\mathbf{r}_3-\mathbf{r}_1)\Big]_I \\
&= \frac{i\alpha^2}{2\sqrt{2}}\Big[\nabla_{\mathbf{r}_1}\Big(V_0^{CH}(\mathbf{r}_1,t_1)\Big)\times\nabla_{\mathbf{r}_3}\delta(\mathbf{r}_3-\mathbf{r}_1)\Big]_I \\
\text{or}\quad V_I^{SSOH}(\mathbf{r}_1,t_1;\mathbf{r}_3,t_3) &= \frac{\alpha^2}{2\sqrt{2}}\Big[\nabla_{\mathbf{r}_1}\Big(V_0^{CH}(\mathbf{r}_1,t_1)\Big)\times\big[i\nabla_{\mathbf{r}_3}\delta(\mathbf{r}_3-\mathbf{r}_1)\big]\Big]_I.\ \delta(t_3-t_1).
\end{aligned} \tag{F.38}$$

These three terms describe the spin-same-orbit interaction between an electron and the mean charge distribution ρ^0. They can be easier understood when we write:

$$\begin{aligned}
\sum_{I=X,Y,Z} V_I^{SSOH}([1,3])\sigma_{\alpha\gamma}^I &= \frac{\alpha^2}{2\sqrt{2}}\Big[\nabla_{\mathbf{r}_1}\Big(V_0^{CH}(\mathbf{r}_1,t_1)\Big)\times\big[i\nabla_{\mathbf{r}_3}\delta(\mathbf{r}_3-\mathbf{r}_1)\big]\Big]\cdot\boldsymbol{\sigma}_{\alpha\gamma} \\
\text{i.e.}\quad \text{“ }\widehat{V}^{SSOH}(\mathbf{r}_1,t_1)\text{ ”} &= -\frac{\alpha^2}{\hbar\sqrt{2}}\Big[\nabla_{\mathbf{r}_1}\Big(-V_0^{CH}(\mathbf{r}_1,t_1)\Big)\times\mathbf{p}_1\Big]\cdot\mathbf{s}_1 \quad \text{with "less strict" notations.}
\end{aligned}$$

We recognize the usual spin-orbit coupling between an electron and an external potential, which is here replaced by the Hartree potential of the system. We remind the reader that the expression for the spin-orbit coupling between an electron and an external potential (created by the nuclei of a solid for instance) is the following[5]:

$$\begin{aligned}
\widehat{V}^{SO}(\mathbf{r},t) &= -\frac{e\hbar}{2m_0^2c^2}\Big[\nabla_{\mathbf{r}}\Big(V_{nuclei}(\mathbf{r},t)\Big)\times\mathbf{p}\Big]\cdot\mathbf{s} = -\frac{e^2\hbar}{8\pi\varepsilon_0 m_0^2c^2}\Big[\nabla_{\mathbf{r}}\Big(\sum_N Z_N\frac{\delta(t-t_N)}{|\mathbf{r}-\mathbf{R}_N|}\Big)\times\mathbf{p}\Big]\cdot\mathbf{s} \\
&= -\frac{\alpha^2}{\hbar\sqrt{2}}\Big[\nabla_{\mathbf{r}}\Big(\sum_N Z_N\frac{\delta(t-t_N)}{|\mathbf{r}-\mathbf{R}_N|}\Big)\times\mathbf{p}\Big]\cdot\mathbf{s}.
\end{aligned} \tag{F.39}$$

Thus the previous Hartree terms can be seen as taking into account the electrostatic screening in the spin-orbit coupling since:

$$\widehat{V}^{SO}(\mathbf{r}_1,t_1)+V^{SSOH}(\mathbf{r}_1,t_1) = -\frac{\alpha^2}{\hbar\sqrt{2}}\Big[\nabla_{\mathbf{r}_1}\Big(\sum_N Z_N\frac{\delta(t_1-t_N)}{|\mathbf{r}_1-\mathbf{R}_N|}-V_0^{CH}(\mathbf{r}_1,t_1)\Big)\times\mathbf{p}_1\Big]\cdot\mathbf{s}_1. \tag{F.40}$$

On the contrary, the last Hartree term $V_0^{SSOH}([1,3])$ is diagonal in real space – i.e. it is a local operator – and gives the interaction of the mean spin-density of the system with the electric field

[5]The spin-orbit coupling is a non-local one-body operator. It has the following form with the chosen formalism:

$$\begin{aligned}
\sum_{I=X,Y,Z} V_I^{SO}([1,3])\sigma_{\alpha\gamma}^I &= -\frac{\alpha^2}{2\sqrt{2}}\Big[\nabla_{\mathbf{r}_1}\Big(V_{nuclei}(\mathbf{r}_1,t_1)\Big)\times\big[i\nabla_{\mathbf{r}_3}\delta(\mathbf{r}_3-\mathbf{r}_1)\big]\Big]\cdot\boldsymbol{\sigma}_{\alpha\gamma} \\
V_0^{SO}([1,3])\sigma_{\alpha\gamma}^0 &= 0
\end{aligned}$$

generated by an electron.

$$\begin{aligned} V_0^{SSOH}([1,3]) &= v_{0J}^{SSO}([1,3];[2,4])\rho^J(2,4^+) \\ &= \frac{i\alpha^2}{2\sqrt{2}}\Big[\nabla_{\mathbf{r}_2}\Big(\frac{\delta(t_2-t_1)}{r_{12}}\Big)\times\nabla_{\mathbf{r}_4}\delta(\mathbf{r}_4-\mathbf{r}_2)\Big]_J\delta(\mathbf{r}_3-\mathbf{r}_1)\ .\ \rho^J(2,4^+) \\ &= \frac{\alpha^2}{2\sqrt{2}}\int d2\ \ \nabla_{\mathbf{r}_2}\Big(\frac{\delta(t_2-t_1)}{r_{12}}\Big)\cdot\Big[\int d\mathbf{r}_4\ i\nabla_{\mathbf{r}_4}\delta(\mathbf{r}_4-\mathbf{r}_2)\times\vec{\rho}(2,4^+)\Big]\ .\ \delta(\mathbf{r}_3-\mathbf{r}_1) \\ &= \frac{\alpha^2}{2\sqrt{2}}\int d2\ \ \nabla_{\mathbf{r}_2}\Big(\frac{\delta(t_2-t_1)}{r_{12}}\Big)\cdot\big[-i\mathbf{curl}_{\mathbf{r}_4}\ \vec{\rho}(2,4^+)\big]_{4=2}\ .\ \delta(\mathbf{r}_3-\mathbf{r}_1) \end{aligned} \tag{F.41}$$

$$\begin{aligned} \text{or}\quad V_0^{SSOH}(\mathbf{r}_1,t_1) &= \frac{\alpha^2}{2\sqrt{2}}\int d\mathbf{r}_2\ \ \nabla_{\mathbf{r}_2}\Big(\frac{1}{r_{12}}\Big).[\mathbf{p}_2\times\vec{\rho}(\mathbf{r}_2,t_1)] \\ &= \frac{\alpha^2}{2\sqrt{2}}\int d\mathbf{r}_2\ \ \nabla_{\mathbf{r}_2}\Big(\frac{1}{r_{12}}\Big).\big[-i\mathbf{curl}_{\mathbf{r}_2}\ \vec{\rho}(\mathbf{r}_2,t_1)\big]\,. \end{aligned} \tag{F.42}$$

The mean energy associated to these Hartree terms has the following property:

$$\begin{aligned} <V_0^{SSOH}([1,3])\sigma^0_{\alpha\gamma}> &= \frac{\alpha^2}{2\sqrt{2}}\int d\mathbf{r}_2\ \ \Big[\nabla_{\mathbf{r}_2}\Big(V_0^{CH}(\mathbf{r}_2,t_1)\Big)\cdot\big[-i\mathbf{curl}_{\mathbf{r}_4}\ \vec{\rho}(2,4^+)\big]_{4=2} \\ &= <\sum_{I=X,Y,Z}V_I^{SSOH}([1,3])\sigma^I_{\alpha\gamma}>\,. \end{aligned} \tag{F.43}$$

There is thus an equipartition of the energy between the two aspects of the Hartree terms induced by the spin-same-orbit interaction.

F.3.3 The spin-other-orbit interaction

For $I=X,Y,Z$

$$\begin{aligned} V_I^{SOOH}([1,3]) &= v_{IJ}^{SOO}([1,3];[2,4])\rho^J(2,4^+) = v_{I0}^{SOO}([1,3];[2,4])\rho^0(2,4^+) \\ &= -2\frac{i\alpha^2}{2\sqrt{2}}\Big[\nabla_{\mathbf{r}_1}\Big(\frac{\delta(t_2-t_1)}{r_{12}}\Big)\times\nabla_{\mathbf{r}_4}\delta(\mathbf{r}_4-\mathbf{r}_2)\Big]_I\delta(\mathbf{r}_3-\mathbf{r}_1)\ .\ \rho^0(2,4^+) \\ &= -2\frac{\alpha^2}{2\sqrt{2}}\int d\mathbf{r}_2\ \ \Big[\nabla_{\mathbf{r}_1}\Big(\frac{\delta(t_2-t_1)}{r_{12}}\Big)\times\Big(-i\nabla_{\mathbf{r}_4}\rho^0(2,4^+)\Big)_{4=2}\Big]_I\ .\ \delta(\mathbf{r}_3-\mathbf{r}_1) \\ &= -2\frac{\alpha^2}{2\sqrt{2}}\left[\int d\mathbf{r}_2\ \frac{[\mathbf{r}_1-\mathbf{r}_2]\times[-i\nabla_{\mathbf{r}_4}\rho^0(2,4^+)]_{4=2\ \&\ t_2=t_1}}{r_{12}^3}\right]_I\ .\ \delta(\mathbf{r}_3-\mathbf{r}_1) \end{aligned} \tag{F.44}$$

$$\text{or}\quad V_I^{SOOH}(\mathbf{r}_1,t_1) = \frac{e\hbar}{m_0}\left[\frac{\mu_0}{4\pi}\int d\mathbf{r}_2\ \frac{[\mathbf{r}_1-\mathbf{r}_2]\times\mathbf{j}(\mathbf{r}_2,t_1)}{r_{12}^3}\right]_I\ .\ \delta(3-1). \tag{F.45}$$

As previously, these three terms describe the spin-other-orbit interaction between an electron and the mean charge distribution ρ^0. However, the Biot-Savart law[6] can be recognized, which enables us to

[6]The usual definition of the electrical current is

$$\mathbf{j}(\mathbf{r},t) = -\frac{e\hbar}{2m_0}\Big[\psi^\dagger(\mathbf{r},t)\big(-i\nabla\psi(\mathbf{r},t)\big)-\big(-i\nabla\psi^\dagger(\mathbf{r},t)\big)\psi(\mathbf{r},t)\Big]$$

give a purely magnetic interpretation:

$$\begin{aligned}\sum_{I=X,Y,Z} V_I^{SOOH}(\mathbf{r}_1,t_1)\sigma^I_{\alpha\gamma} &= \frac{e\hbar}{2m_0}\left[\frac{\mu_0}{4\pi}\int d\mathbf{r}_2\ \frac{[\mathbf{r}_1-\mathbf{r}_2]\times\mathbf{j}(\mathbf{r}_2,t_1)}{r_{12}^3}\right]\cdot\boldsymbol{\sigma}_{\alpha\gamma}\\ &= -\frac{gq}{2m_0}\mathbf{B}(\mathbf{r}_1,t_1)\cdot\left[\frac{1}{2}\hbar\boldsymbol{\sigma}\right]_{\alpha\gamma}\end{aligned} \tag{F.46}$$

with the electron g-factor $g=2$ and the electron charge $q=-e$. These terms thus describe the interaction between the spin of an electron and the magnetic field induced by the mean charge currents in the system.

On the contrary, the last Hartree term gives the interaction of the mean spin of the system with the magnetic field generated by the "motion of one electron".

$$\begin{aligned}V_0^{SSOH}([1,3]) &= v_{0J}^{SSO}([1,3];[2,4])\rho^J(2,4^+)\\ &= -2\frac{i\alpha^2}{2\sqrt{2}}\left[\nabla_{\mathbf{r}_2}\left(\frac{\delta(t_2-t_1)}{r_{12}}\right)\times\nabla_{\mathbf{r}_3}\delta(\mathbf{r}_3-\mathbf{r}_1)\right]_J\delta(\mathbf{r}_4-\mathbf{r}_2)\ .\ \rho^J(2,4^+)\\ &= -\frac{e\hbar}{m_0}\left[\frac{\mu_0}{4\pi}\int d\mathbf{r}_2\ \frac{\mathbf{r}_2-\mathbf{r}_1}{r_{12}^3}\times i\frac{e\hbar}{2m_0}\nabla_{\mathbf{r}_3}\delta(\mathbf{r}_3-\mathbf{r}_1)\right]\ .\ \vec{\rho}(\mathbf{r}_2,t_1).\end{aligned} \tag{F.47}$$

The mean energy associated to this term verifies also an equipartition of the energy between the two aspects of the interaction:

$$\begin{aligned}<V_0^{SOOH}([1,3])\sigma^0_{\alpha\gamma}> &= \int d\mathbf{r}_2\ \ \frac{e\hbar}{m_0}\left[\frac{\mu_0}{4\pi}\int d\mathbf{r}_1\ \frac{[\mathbf{r}_2-\mathbf{r}_1]\times\mathbf{j}(\mathbf{r}_1,t_1)}{r_{12}^3}\right]\ .\ \vec{\rho}(\mathbf{r}_2,t_1)\\ &= -\frac{gq}{2m_0}\int d\mathbf{r}_2\ \ \mathbf{B}(\mathbf{r}_2,t_1)\cdot\mathbf{S}(\mathbf{r}_2,t_1)\qquad\text{with}\qquad\mathbf{S}(\mathbf{r}_2,t_1)=\frac{1}{2}\hbar\vec{\rho}(\mathbf{r}_2,t_1)\\ &= <\sum_{I=X,Y,Z} V_I^{SOOH}(\mathbf{r}_1,t_1)\sigma^I_{\alpha\gamma}>\ .\end{aligned} \tag{F.48}$$

F.4 Exchange self-energy Σ^x – generalized Fock terms – in our system

In the usual Hedin's formalism, the screened interaction $W(1,2)$ is split up into the bare Coulomb potential $v(1,2)$ and the induced potential $W_c(1,2)$. Using the GW approximation, the self-energy is then written:

$$\Sigma(1,2)=i\hbar G(1,2^+)v(1,2)+i\hbar G(1,2^+)W_c(1,2). \tag{F.49}$$

The first term is referred to as the exchange (Fock) self-energy $\Sigma^x(1,2)$ and the second as the correlation self-energy $\Sigma^c(1,2)$. This section will now focus on the computation of the Fock terms we will obtain with the considered interactions, in the generalized spin-Hedin's formalism.

F.4.1 The Coulomb interaction

Since we use the same decomposition of the screened interaction $W_{IJ}([1,3];[2,4])$ and the GW approximation, the Fock self-energy $\Sigma^x_{\alpha\beta}(1,2)$ has (of course) the same expression as usual:

$$\begin{aligned}\Sigma^x_{C\ \alpha\beta}(1,2) &= i\hbar\ \sigma^I_{\alpha\eta}\left[G_{\eta\gamma}(4,3)\right]_{\substack{t_4=t_1\\ t_3=t_2}}\sigma^J_{\gamma\beta}v^C_{JI}([3,2];[1,4])\\ &= i\hbar\sum_{\eta\gamma}\iint d\mathbf{r}_3d\mathbf{r}_4\ \ \sigma^0_{\alpha\eta}\left[G_{\eta\gamma}(4,3)\right]_{\substack{t_4=t_1\\ t_3=t_2}}\sigma^0_{\gamma\beta}\delta(\mathbf{r}_2-\mathbf{r}_3)\frac{\delta(t_1-t_3)}{r_{31}}\delta(\mathbf{r}_4-\mathbf{r}_1)\\ &= i\hbar\ \frac{\delta(t_1-t_2)}{r_{12}}G_{\alpha\beta}(1,2)\end{aligned} \tag{F.50}$$

We remind the reader that the bare Coulomb interaction is instantaneous in the limit $t_2 = t_1^+$. We can thus rewrite $G_{\alpha\beta}(1,2)$ as $G_{\alpha\beta}(1,2^+)$ in the previous expression.

$$\Sigma^x_{C\ \alpha\beta}(1,2) = i\hbar\ \frac{\delta(t_1-t_2)}{r_{12}} G_{\alpha\beta}(1,2^+) = -\frac{\delta(t_1-t_2)}{r_{12}} < \psi^\dagger_\beta(2)\psi_\alpha(1) >_{t_2=t_1} \tag{F.51}$$

This argument will be also valid for the spin-same-orbit and spin-other-orbit interactions, which rely on the spatial gradient of the bare Coulomb interaction, and then will be used without repeating this justification.

F.4.2 The spin-same-orbit interaction

$$\begin{aligned}
\Sigma^x_{SSO\ \alpha\beta}(1,2) &= i\hbar\ \sigma^I_{\alpha\eta}\,[G_{\eta\gamma}(4,3)]_{\substack{t_4=t_1\\t_3=t_2}}\,\sigma^J_{\gamma\beta} v^{SSO}_{JI}([3,2];[1,4]) \\
&= i\hbar\ \Big[\sigma^0_{\alpha\eta}\,[G_{\eta\gamma}(4,3)]_{\substack{t_4=t_1\\t_3=t_2}}\,\sigma^J_{\gamma\beta} v^{SSO}_{J0}([3,2];[1,4]) \\
&\qquad\qquad +\sigma^I_{\alpha\eta}\,[G_{\eta\gamma}(4,3)]_{\substack{t_4=t_1\\t_3=t_2}}\,\sigma^0_{\gamma\beta} v^{SSO}_{0I}([3,2];[1,4])\Big] \\
&= \Sigma^{x\ (1)}_{SSO\ \alpha\beta}(1,2) + \Sigma^{x\ (2)}_{SSO\ \alpha\beta}(1,2)
\end{aligned} \tag{F.52}$$

In the following, we will compute separately these two terms in order to be clearer.

$$\begin{aligned}
\Sigma^{x\ (1)}_{SSO\ \alpha\beta}(1,2) &= i\hbar\ \sigma^0_{\alpha\eta}\,[G_{\eta\gamma}(4,3)]_{\substack{t_4=t_1\\t_3=t_2}}\ \sigma^J_{\gamma\beta}\ v^{SSO}_{J0}([3,2];[1,4]) \\
&= -\frac{\alpha^2\hbar}{2\sqrt{2}} \sum_\gamma\ \Big[\nabla_{\mathbf{r}_2}\Big(\frac{\delta(t_1-t_2)}{r_{12}}\Big) \times \nabla_{\mathbf{r}_2} G_{\alpha\gamma}(1,2)\Big]\cdot \boldsymbol{\sigma}_{\gamma\beta} \\
&= -\frac{i\alpha^2}{2\sqrt{2}} \sum_\gamma\ \Big[\nabla_{\mathbf{r}_2}\Big(\frac{\delta(t_1-t_2)}{r_{12}}\Big) \times < \nabla_{\mathbf{r}_2}\big[\psi^\dagger_\gamma(2)\big]\psi_\alpha(1) >_{t_2=t_1}\Big]\cdot \boldsymbol{\sigma}_{\gamma\beta}
\end{aligned} \tag{F.53}$$

$$\begin{aligned}
\Sigma^{x\ (2)}_{SSO\ \alpha\beta}(1,2) &= i\hbar\ \sigma^I_{\alpha\eta}\,[G_{\eta\gamma}(4,3)]_{\substack{t_4=t_1\\t_3=t_2}}\ \sigma^0_{\gamma\beta}\ v^{SSO}_{0I}([3,2];[1,4]) \\
&= +\frac{\alpha^2\hbar}{2\sqrt{2}} \sum_\eta\ \Big[\nabla_{\mathbf{r}_1}\Big(\frac{\delta(t_1-t_2)}{r_{12}}\Big) \times \nabla_{\mathbf{r}_1} G_{\eta\beta}(1,2)\Big]\cdot \boldsymbol{\sigma}_{\alpha\eta} \\
&= +\frac{i\alpha^2}{2\sqrt{2}} \sum_\eta\ \Big[\nabla_{\mathbf{r}_1}\Big(\frac{\delta(t_1-t_2)}{r_{12}}\Big) \times < \psi^\dagger_\beta(2)\nabla_{\mathbf{r}_1}\big[\psi_\eta(1)\big] >_{t_2=t_1}\Big]\cdot \boldsymbol{\sigma}_{\alpha\eta}
\end{aligned} \tag{F.54}$$

These two computed terms have the following property:

$$\begin{aligned}
\Sigma^{x\ (1)}_{SSO\ \alpha\beta}(1,2) &= -\frac{i\alpha^2}{2\sqrt{2}}\ \sum_\gamma \Big[\nabla_{\mathbf{r}_2}\Big(\frac{\delta(t_1-t_2)}{r_{12}}\Big) \times < \nabla_{\mathbf{r}_2}\big[\psi^\dagger_\gamma(2)\big]\psi_\alpha(1) >_{t_2=t_1}\Big]\cdot \boldsymbol{\sigma}_{\gamma\beta} \\
&= \Big[\frac{i\alpha^2}{2\sqrt{2}}\ \sum_\gamma \Big[\nabla_{\mathbf{r}_2}\Big(\frac{\delta(t_1-t_2)}{r_{12}}\Big) \times < \psi^\dagger_\alpha(1)\nabla_{\mathbf{r}_2}\big[\psi_\gamma(2)\big] >_{t_2=t_1}\Big]\cdot \boldsymbol{\sigma}_{\beta\gamma}\Big]^* \\
&= \Big[\Sigma^{x\ (2)}_{SSO\ \beta\alpha}(2,1)\Big]^* = \big[\Sigma^{x\ (2)}_{SSO}\big]^\dagger_{\alpha\beta}(1,2)
\end{aligned} \tag{F.55}$$

As a consequence, the operator $\Sigma^x_{SSO} = \Sigma^{x\ (1)}_{SSO} + \big[\Sigma^{x\ (1)}_{SSO}\big]^\dagger$ is hermitian and its mean value on a state of the system is real.

F.4.3 The spin-other-orbit interaction

$$\begin{aligned}
\Sigma^x_{SOO\ \alpha\beta}(1,2) &= i\hbar\ \sigma^I_{\alpha\eta}\,[G_{\eta\gamma}(4,3)]_{\substack{t_4=t_1\\t_3=t_2}}\,\sigma^J_{\gamma\beta} v^{SOO}_{JI}([3,2];[1,4]) \\
&= i\hbar\ \Big[\sigma^0_{\alpha\eta}\,[G_{\eta\gamma}(4,3)]_{\substack{t_4=t_1\\t_3=t_2}}\,\sigma^J_{\gamma\beta} v^{SOO}_{J0}([3,2];[1,4]) \\
&\qquad\qquad +\sigma^I_{\alpha\eta}\,[G_{\eta\gamma}(4,3)]_{\substack{t_4=t_1\\t_3=t_2}}\,\sigma^0_{\gamma\beta} v^{SOO}_{0I}([3,2];[1,4])\Big] \\
&= \Sigma^{x\ (1)}_{SOO\ \alpha\beta}(1,2) + \Sigma^{x\ (2)}_{SOO\ \alpha\beta}(1,2)
\end{aligned} \tag{F.56}$$

As previously, we will compute separately these two contributions.

$$\begin{aligned}
\Sigma^{x\ (1)}_{SOO\ \alpha\beta}(1,2) &= i\hbar\ \sigma^0_{\alpha\eta}\,[G_{\eta\gamma}(4,3)]_{\substack{t_4=t_1\\t_3=t_2}}\ \sigma^J_{\gamma\beta}\ v^{SOO}_{J0}([3,2];[1,4]) \\
&= -\frac{\alpha^2\hbar}{\sqrt{2}}\ \sum_\gamma\ \Big[\nabla_{\mathbf{r}_2}\Big(\frac{\delta(t_1-t_2)}{r_{12}}\Big)\times\nabla_{\mathbf{r}_1} G_{\alpha\gamma}(1,2)\Big]\cdot\boldsymbol{\sigma}_{\gamma\beta} \\
&= -\frac{i\alpha^2}{\sqrt{2}}\ \sum_\gamma\ \Big[\nabla_{\mathbf{r}_2}\Big(\frac{\delta(t_1-t_2)}{r_{12}}\Big)\times <\psi^\dagger_\gamma(2)\nabla_{\mathbf{r}_1}\big[\psi_\alpha(1)\big]>_{t_2=t_1}\Big]\cdot\boldsymbol{\sigma}_{\gamma\beta}
\end{aligned} \tag{F.57}$$

$$\begin{aligned}
\Sigma^{x\ (2)}_{SOO\ \alpha\beta}(1,2) &= i\hbar\ \sigma^I_{\alpha\eta}\,[G_{\eta\gamma}(4,3)]_{\substack{t_4=t_1\\t_3=t_2}}\ \sigma^0_{\gamma\beta}\ v^{SOO}_{0I}([3,2];[1,4]) \\
&= +\frac{\alpha^2\hbar}{\sqrt{2}}\ \sum_\eta\ \Big[\nabla_{\mathbf{r}_1}\Big(\frac{\delta(t_1-t_2)}{r_{12}}\Big)\times\nabla_{\mathbf{r}_2} G_{\eta\beta}(1,2)\Big]\cdot\boldsymbol{\sigma}_{\alpha\eta} \\
&= +\frac{i\alpha^2}{\sqrt{2}}\ \sum_\eta\ \Big[\nabla_{\mathbf{r}_1}\Big(\frac{\delta(t_1-t_2)}{r_{12}}\Big)\times <\nabla_{\mathbf{r}_2}\big[\psi^\dagger_\beta(2)\big]\psi_\eta(1)>_{t_2=t_1}\Big]\cdot\boldsymbol{\sigma}_{\alpha\eta}
\end{aligned} \tag{F.58}$$

With an analogous proof, it can be showed that these terms have the same property as highlighted in the previous section.

$$\Sigma^{x\ (1)}_{SOO\ \alpha\beta}(1,2) = \Big[\Sigma^{x\ (2)}_{SOO\ \beta\alpha}(2,1)\Big]^* = \Big[\Sigma^{x\ (2)}_{SOO}\Big]^\dagger_{\alpha\beta}(1,2) \tag{F.59}$$

The operator $\Sigma^x_{SOO} = \Sigma^{x\ (1)}_{SOO} + \big[\Sigma^{x\ (1)}_{SOO}\big]^\dagger$ is thus hermitian too and its mean value on a state of the system is real.

F.5 Expression of the screened interaction W

We now calculate the screened interaction W.

F.5.1 Matrix approach & Polarization computation

The expression of W in the generalized spin-Hedin's equations can be understood as a generalized matrix product:

$$\begin{aligned}
W_{IJ}([1,3];[2,4]) &= v_{IJ}([1,3];[2,4]) + v_{IK}([1,3];[5,6])P_{KL}([5,6];[7,8])W_{LJ}([7,8];[2,4]) \\
<1,3\ _I|\widehat{W}|2,4\ _J> &= <1,3\ _I|\widehat{V}|2,4\ _J> + <1,3\ _I|_I\widehat{V}|5,6\ _K><5,6\ _K|\widehat{P}|7,8\ _L><7,8\ _L|\widehat{W}|3,4\ _J>
\end{aligned} \tag{F.60}$$

We can thus use the same expression as usual:

$$\widehat{W} = \widehat{V} + \widehat{V}\widehat{P}\widehat{W} = \left[1 - \widehat{V}\widehat{P}\right]^{-1}\widehat{V} \tag{F.61}$$

Using then this matrix-like notation, the operator $\widehat{V}$ can be written as:

$$\widehat{V} = \left(\begin{array}{c|ccc} v_{00} & v_{0X} & v_{0Y} & v_{0Z} \\ \hline v_{X0} & & & \\ v_{Y0} & & \mathbb{O} & \\ v_{Z0} & & & \end{array}\right) \quad \text{with} \quad \begin{array}{rcll} v_{00} &=& v_{00}^{C} & \\ v_{0J} &=& v_{0J}^{SSO} + v_{0J}^{SOO} & \forall J \in \{X,Y,Z\} \\ v_{I0} &=& v_{I0}^{SSO} + v_{I0}^{SOO} & \forall I \in \{X,Y,Z\} \end{array} \tag{F.62}$$

where each v_{IJ} is actually a matrix $(< 1,3|v_{IJ}|2,4 >)_{(1,2,3,4)}$. We will use the decomposition in the same block matrices in the following.

In order to perform our computation further, we have to precise the form of the polarization matrix $\widehat{P}$ too. In a first approach, we will use the GW approximation:

$$P_{IJ}([1,3];[2,4]) = -i\hbar\, \sigma^{I}_{\alpha\beta}\left[G_{\beta\gamma}(3,2)\right]_{t_3=t_1} \sigma^{J}_{\gamma\eta}\left[G_{\eta\alpha}(4,1^{+})\right]_{t_4=t_2} \tag{F.63}$$

however, this expression strongly depends on the form of $G_{\alpha\beta}(1,2)$. For instance, considering a spin-diagonal Green function (but assuming that $G_{\uparrow\uparrow} \neq G_{\downarrow\downarrow}$) leads to the following expressions:

$$\widehat{G} = \left(\begin{array}{c|c} G_{\uparrow\uparrow} & \mathbb{O} \\ \hline \mathbb{O} & G_{\downarrow\downarrow} \end{array}\right) \quad \text{then} \quad \widehat{P} = \left(\begin{array}{c|cc|c} P_{00} & 0 & 0 & P_{0Z} \\ \hline 0 & P_{XX} & P_{XY} & 0 \\ 0 & P_{YX} & P_{YY} & 0 \\ \hline P_{Z0} & 0 & 0 & P_{ZZ} \end{array}\right) \tag{F.64}$$

with

$$\begin{array}{rcl}
P_{00}([1,3];[2,4]) &=& -i\hbar\left(\left[G_{\uparrow\uparrow}(3,2)\right]_{t_3=t_1}\left[G_{\uparrow\uparrow}(4,1^{+})\right]_{t_4=t_2} + \left[G_{\downarrow\downarrow}(3,2)\right]_{t_3=t_1}\left[G_{\downarrow\downarrow}(4,1^{+})\right]_{t_4=t_2}\right) \\
&=& P_{ZZ}([1,3];[2,4]) \\
P_{0Z}([1,3];[2,4]) &=& -i\hbar\left(\left[G_{\uparrow\uparrow}(3,2)\right]_{t_3=t_1}\left[G_{\uparrow\uparrow}(4,1^{+})\right]_{t_4=t_2} - \left[G_{\downarrow\downarrow}(3,2)\right]_{t_3=t_1}\left[G_{\downarrow\downarrow}(4,1^{+})\right]_{t_4=t_2}\right) \\
&=& P_{Z0}([1,3];[2,4]) \\
P_{XX}([1,3];[2,4]) &=& -i\hbar\left(\left[G_{\uparrow\uparrow}(3,2)\right]_{t_3=t_1}\left[G_{\downarrow\downarrow}(4,1^{+})\right]_{t_4=t_2} + \left[G_{\downarrow\downarrow}(3,2)\right]_{t_3=t_1}\left[G_{\uparrow\uparrow}(4,1^{+})\right]_{t_4=t_2}\right) \\
&=& P_{YY}([1,3];[2,4]) \\
P_{XY}([1,3];[2,4]) &=& -i\hbar\left(-i\left[G_{\uparrow\uparrow}(3,2)\right]_{t_3=t_1}\left[G_{\downarrow\downarrow}(4,1^{+})\right]_{t_4=t_2} + i\left[G_{\downarrow\downarrow}(3,2)\right]_{t_3=t_1}\left[G_{\uparrow\uparrow}(4,1^{+})\right]_{t_4=t_2}\right) \\
&=& -P_{YX}([1,3];[2,4])
\end{array}$$

F.5.2 Computation of the screened interaction W

As the expression of the screened interaction is $\widehat{W} = \left[1 - \widehat{V}\widehat{P}\right]^{-1}\widehat{V} = \widehat{\varepsilon}^{-1}\widehat{V}$, the dielectric function has to be computed first.

$$\widehat{\varepsilon} = 1 - \widehat{V}\widehat{P} = \left(\begin{array}{c|c} \varepsilon_{00} & \varepsilon_{0J} \\ \hline \varepsilon_{I0} & \varepsilon_{IJ} \end{array}\right) \quad \text{with} \quad \varepsilon_{00} = 1 - v_{00}P_{00} - v_{0Z}P_{Z0} \tag{F.65}$$

$$\begin{array}{rclcrcl} \varepsilon_{0X} &=& -(v_{0X}P_{XX} + v_{0Y}P_{YX}) & & \varepsilon_{X0} &=& -v_{X0}P_{00} \\ \varepsilon_{0Y} &=& -(v_{0X}P_{XY} + v_{0Y}P_{YY}) & & \varepsilon_{Y0} &=& -v_{Y0}P_{00} \\ \varepsilon_{0Z} &=& -(v_{00}P_{0Z} + v_{0Z}P_{ZZ}) & & \varepsilon_{Z0} &=& -v_{Z0}P_{00} \end{array} \qquad \varepsilon_{IJ} = \begin{pmatrix} 1 & 0 & -v_{X0}P_{0Z} \\ 0 & 1 & -v_{Y0}P_{0Z} \\ 0 & 0 & 1 - v_{Z0}P_{0Z} \end{pmatrix}$$

As each term of the matrix $\widehat{\varepsilon}$ is a matrix itself, the inversion operation must be done carefully, using the following identity:

$$\left(\begin{array}{c|c} A & B \\ \hline C & D \end{array}\right)^{-1} = \left(\begin{array}{c|c} A^{-1} + A^{-1}B\Delta^{-1}CA^{-1} & -A^{-1}B\Delta^{-1} \\ \hline -\Delta^{-1}CA^{-1} & \Delta^{-1} \end{array}\right) \qquad \text{with} \qquad \Delta = D - CA^{-1}B \tag{F.66}$$

It appears then, taking into account that only terms of order $O(\alpha^2)$ are relevant:

$$\begin{aligned} A_\varepsilon^{-1} &= \big[1 - v_{00}P_{00} - v_{0Z}P_{Z0}\big]^{-1} \\ &\approx \big[1 - v_{00}P_{00}\big]^{-1} + \big[1 - v_{00}P_{00}\big]^{-1} v_{0Z}P_{Z0}\big[1 - v_{00}P_{00}\big]^{-1} + O(\alpha^4) \end{aligned} \tag{F.67}$$

$$\text{and} \quad \Delta_\varepsilon^{-1} \approx \begin{pmatrix} 1 & 0 & v_{X0}\big[1 - P_{00}v_{00}\big]^{-1}P_{0Z} \\ 0 & 1 & v_{Y0}\big[1 - P_{00}v_{00}\big]^{-1}P_{0Z} \\ 0 & 0 & 1 + v_{Z0}\big[1 - P_{00}v_{00}\big]^{-1}P_{0Z} \end{pmatrix}$$

As a result, the expression of the dielectric function is:

$$\widehat{\varepsilon}^{-1} = \big[1 - \widehat{V}\widehat{P}\big]^{-1} \approx \left(\begin{array}{c|c} \varepsilon_{00}^{-1} & \varepsilon_{0J}^{-1} \\ \hline \varepsilon_{I0}^{-1} & \varepsilon_{IJ}^{-1} \end{array}\right) \quad + O(\alpha^4) \tag{F.68}$$

$$\begin{aligned} \text{with} \quad \varepsilon_{00}^{-1} &\approx \big[1 - v_{00}P_{00}\big]^{-1} + \big[1 - v_{00}P_{00}\big]^{-1} v_{0Z}P_{Z0}\big[1 - v_{00}P_{00}\big]^{-1} \\ &\quad + \big[1 - v_{00}P_{00}\big]^{-1} v_{00}P_{0Z}v_{Z0}P_{00}\big[1 - v_{00}P_{00}\big]^{-1} \end{aligned}$$

$$\begin{aligned} \varepsilon_{0X}^{-1} &\approx \big[1 - v_{00}P_{00}\big]^{-1}(v_{0X}P_{XX} + v_{0Y}P_{YX}) \\ \varepsilon_{0Y}^{-1} &\approx \big[1 - v_{00}P_{00}\big]^{-1}(v_{0X}P_{XY} + v_{0Y}P_{YY}) \\ \varepsilon_{0Z}^{-1} &\approx \big[1 - v_{00}P_{00}\big]^{-1}(v_{00}P_{0Z} + v_{0Z}P_{ZZ}) + \big[1 - v_{00}P_{00}\big]^{-1} v_{00}P_{0Z}v_{Z0}\big[1 - P_{00}v_{00}\big]^{-1}P_{0Z} \end{aligned}$$

$$\begin{aligned} \varepsilon_{X0}^{-1} &\approx v_{X0}P_{00}\big[1 - v_{00}P_{00}\big]^{-1} \\ \varepsilon_{Y0}^{-1} &\approx v_{Y0}P_{00}\big[1 - v_{00}P_{00}\big]^{-1} \\ \varepsilon_{Z0}^{-1} &\approx v_{Z0}P_{00}\big[1 - v_{00}P_{00}\big]^{-1} \end{aligned}$$

$$\varepsilon_{IJ}^{-1} = \Delta_\varepsilon^{-1}(I,J) \quad \forall I, J \in \{X, Y, Z\}$$

and the expression of the screened interaction has the following form:

$$\widehat{W} = \widehat{\varepsilon}^{-1}\widehat{V} \approx \left(\begin{array}{c|c} W_{00} & W_{0J} \\ \hline W_{I0} & \mathbb{O} \end{array}\right) \quad + O(\alpha^4) \tag{F.69}$$

$$\begin{aligned} \text{with} \quad W_{00} &= \big[1 - v_{00}P_{00}\big]^{-1} v_{00} + \big[1 - v_{00}P_{00}\big]^{-1} v_{0Z}P_{Z0}\big[1 - v_{00}P_{00}\big]^{-1} v_{00} \\ &\quad + \big[1 - v_{00}P_{00}\big]^{-1} v_{00}P_{0Z}v_{Z0}\big[1 - P_{00}v_{00}\big]^{-1} \end{aligned}$$

$$\begin{aligned} W_{0X} &= \big[1 - v_{00}P_{00}\big]^{-1} v_{0X} & W_{X0} &= v_{X0}\big[1 - P_{00}v_{00}\big]^{-1} \\ W_{0Y} &= \big[1 - v_{00}P_{00}\big]^{-1} v_{0Y} \quad \text{and} & W_{Y0} &= v_{Y0}\big[1 - P_{00}v_{00}\big]^{-1} \\ W_{0Z} &= \big[1 - v_{00}P_{00}\big]^{-1} v_{0Z} & W_{Z0} &= v_{Z0}\big[1 - P_{00}v_{00}\big]^{-1} \end{aligned} \tag{F.70}$$

The conclusion of this last study is thus the appearance of a screening of the spin-same-orbit and spin-other-orbit interactions by the Coulomb interaction and the existence of two new terms in the charge-charge channel, obtained by the coupling of the Coulomb and the spin-same-orbit and spin-other-orbit interactions.

Bibliography

[1] M. Aichhorn, L. Pourovskii, V. Vildosola, M. Ferrero, O. Parcollet, T. Miyake, A. Georges, and S. Biermann, *Dynamical mean-field theory within an augmented plane-wave framework: Assessing electronic correlations in the iron pnictide LaFeAsO*, Phys. Rev. B, 80 (2009), p. 085101.

[2] H. Alloul, *Physique des électrons dans les solides*, Editions de l'Ecole Polytechnique, France, 2007.

[3] B. Amadon, F. Lechermann, A. Georges, F. Jollet, T. O. Wehling, and A. I. Lichtenstein, *Plane-wave based electronic structure calculations for correlated materials using dynamical mean-field theory and projected local orbitals*, Phys. Rev. B, 77 (2008), p. 205112.

[4] O. K. Andersen, *Simple approach to the band-structure problem*, Solid State Communications, 13 (1973), p. 133.

[5] O. K. Andersen, *Linear methods in band theory*, Phys. Rev. B, 12 (1975), p. 3060.

[6] O. K. Andersen and T. Saha-Dasgupta, *Muffin-tin orbitals of arbitrary order*, Phys. Rev. B, 62 (2000), p. R16219.

[7] P. W. Anderson, *Localized Magnetic States in Metals*, Phys. Rev., 124 (1961), p. 41.

[8] P. W. Anderson, *Self-Consistent Pseudopotentials and Ultralocalized Functions for Energy Bands*, Phys. Rev. Lett., 21 (1968), p. 13.

[9] V. I. Anisimov, F. Aryasetiawan, and A. I. Lichtenstein, *REVIEW ARTICLE: First-principles calculations of the electronic structure and spectra of strongly correlated systems: the LDA+U method*, Journal of Physics: Condensed Matter, 9 (1997), p. 767.

[10] V. I. Anisimov, D. E. Kondakov, A. V. Kozhevnikov, I. A. Nekrasov, Z. V. Pchelkina, J. W. Allen, S.-K. Mo, H.-D. Kim, P. Metcalf, S. Suga, A. Sekiyama, G. Keller, I. Leonov, X. Ren, and D. Vollhardt, *Full orbital calculation scheme for materials with strongly correlated electrons*, Phys. Rev. B, 71 (2005), p. 125119.

[11] V. I. Anisimov, A. I. Poteryaev, M. A. Korotin, A. O. Anokhin, and G. Kotliar, *First-principles calculations of the electronic structure and spectra of strongly correlated systems: dynamical mean-field theory*, Journal of Physics: Condensed Matter, 9 (1997), p. 7359.

[12] V. I. Anisimov, I. V. Solovyev, M. A. Korotin, M. T. Czyżyk, and G. A. Sawatzky, *Density-functional theory and NiO photoemission spectra*, Phys. Rev. B, 48 (1993), p. 16929.

[13] V. I. Anisimov, J. Zaanen, and O. K. Andersen, *Band theory and Mott insulators: Hubbard U instead of Stoner I*, Phys. Rev. B, 44 (1991), p. 943.

[14] N. Argaman and G. Makov, *Density functional theory: An introduction*, American Journal of Physics, 68 (2000), p. 69.

[15] F. Aryasetiawan and S. Biermann, *Generalized Hedin's Equations for Quantum Many-Body Systems with Spin-Dependent Interactions*, Phys. Rev. Lett., 100 (2008), p. 116402.

[16] N. W. Ashcroft and D. N. Mermin, *Solid State Physics*, Thomson Learning, Inc., 1976.

[17] A. Auerbach, *Interacting Electrons and Quantum Magnetism*, Springer-Verlag, 1994.

[18] M. N. Baibich, J. M. Broto, A. Fert, F. N. Van Dau, F. Petroff, P. Etienne, G. Creuzet, A. Friederich, and J. Chazelas, *Giant Magnetoresistance of (001)Fe/(001)Cr Magnetic Superlattices*, Phys. Rev. Lett., 61 (1988), p. 2472.

[19] K. S. D. Beach, *Identifying the maximum entropy method as a special limit of stochastic analytic continuation*, arXiv:cond-mat/0403055 (unpublished), (2004).

[20] J. G. Bednorz and K. A. Müller, *Possible high T_c superconductivity in the Ba–La–Cu–O system*, Zeitschrift für Physik B Condensed Matter, 64 (1986), p. 189.

[21] B. A. Bernevig, T. L. Hughes, and S.-C. Zhang, *Quantum Spin Hall Effect and Topological Phase Transition in HgTe Quantum Wells*, Science, 314 (2006), p. 1757.

[22] G. Binasch, P. Grünberg, F. Saurenbach, and W. Zinn, *Enhanced magnetoresistance in layered magnetic structures with antiferromagnetic interlayer exchange*, Phys. Rev. B, 39 (1989), p. 4828.

[23] P. Blaha, K. Schwarz, G. Madsen, D. Kvasnicka, and J. Luitz, *Wien2k, An Augmented Plane Wave+Local Orbitals Program for Calculating Crystal Properties*, (2001).

[24] F. Bloch, *Über die Quantenmechanik der Elektronen in Kristallgittern*, Zeitschrift für Physik A Hadrons and Nuclei, 52 (1929), p. 555.

[25] C. J. Bradley and A. P. Cracknell, *The mathematical theory of symmetry in solids*, Clarendon Press, Oxford, 1972.

[26] G. Breit, *The Effect of Retardation on the Interaction of Two Electrons*, Phys. Rev., 34 (1929), p. 553.

[27] W. F. Brinkman and T. M. Rice, *Application of Gutzwiller's Variational Method to the Metal-Insulator Transition*, Phys. Rev. B, 2 (1970), p. 4302.

[28] R. Bulla, T. A. Costi, and D. Vollhardt, *Finite-temperature numerical renormalization group study of the Mott transition*, Phys. Rev. B, 64 (2001), p. 045103.

[29] Y. A. Bychkov and E. I. Rashba, *Oscillatory effects and the magnetic susceptibility of carriers in inversion layers*, Journal of Physics C: Solid State Physics, 17 (1984), p. 6039.

[30] M. Caffarel and W. Krauth, *Exact diagonalization approach to correlated fermions in infinite dimensions: Mott transition and superconductivity*, Phys. Rev. Lett., 72 (1994), p. 1545.

[31] G. Cao, J. Bolivar, S. McCall, J. E. Crow, and R. P. Guertin, *Weak ferromagnetism, metal-to-nonmetal transition, and negative differential resistivity in single-crystal Sr_2IrOs_4*, Phys. Rev. B, 57 (1998), p. R11039.

[32] K. Capelle, *A Bird's-Eye View of Density-Functional Theory*, Brazilian Journal of Physics, 36 (2006), p. 1318.

[33] S. A. Carter, B. Batlogg, R. J. Cava, J. J. Krajewski, W. F. Peck, and L. W. Rupp, *Mechanism for the metal-insulator transition in $Sr_2Ir_{1-x}Ru_xO_4$*, Phys. Rev. B, 51 (1995), p. 17184.

[34] R. J. Cava, B. Batlogg, K. Kiyono, H. Takagi, J. J. Krajewski, W. F. Peck, L. W. Rupp, and C. H. Chen, *Localized-to-itinerant electron transition in $Sr_2Ir_{1-x}Ru_xO_4$*, Phys. Rev. B, 49 (1994), p. 11890.

[35] D. M. Ceperley and B. J. Alder, *Ground State of the Electron Gas by a Stochastic Method*, Phys. Rev. Lett., 45 (1980), p. 566.

[36] G. Chen and L. Balents, *Spin-orbit effects in $Na_4Ir_3O_8$: A hyper-kagome lattice antiferromagnet*, Phys. Rev. B, 78 (2008), p. 094403.

[37] G. Chen, L. Balents, and A. P. Schnyder, *Spin-Orbital Singlet and Quantum Critical Point on the Diamond Lattice: $FeSc_2S_4$*, Phys. Rev. Lett., 102 (2009), p. 096406.

[38] S. Chikara, O. Korneta, W. P. Crummett, L. E. DeLong, P. Schlottmann, and G. Cao, *Giant magnetoelectric effect in the $J_{eff}=\frac{1}{2}$ Mott insulator Sr_2IrO_4*, Phys. Rev. B, 80 (2009), p. 140407.

[39] C. Cosio-Castaneda, G. Tavizon, A. Baeza, P. de la Mora, and R. Escudero, *Structure and magnetic properties of the weak ferromagnet $Sr_{2x}La_xIrO_4$*, Journal of Physics: Condensed Matter, 19 (2007), p. 446210.

[40] S. Cottenier, *Density Functional Theory and the family of (L)APW-methods: a step-by-step introduction*, Instituut voor Kern- en Stralingsfysica, K.U.Leuven, Belgium, 2002 (to be found at http://www.wien2k.at/reg_user/textbooks).

[41] M. K. Crawford, M. A. Subramanian, R. L. Harlow, J. A. Fernandez-Baca, Z. R. Wang, and D. C. Johnston, *Structural and magnetic studies of Sr_2IrO_4*, Phys. Rev. B, 49 (1994), p. 9198.

[42] M. T. Czyżyk and G. A. Sawatzky, *Local-density functional and on-site correlations: The electronic structure of La_2CuO_4 and $LaCuO_3$*, Phys. Rev. B, 49 (1994), p. 14211.

[43] J. Darriet, G. Demazeau, and M. Pouchard, *Une modelisation du comportement magnetique d'un compose de l'iridium pentavalent: $LaLi_{0.5}Ir_{0.5}O_3$*, Materials Research Bulletin, 16 (1981), p. 1013.

[44] S. Datta and B. Das, *Electronic analog of the electro-optic modulator*, Applied Physics Letters, 56 (1990), p. 665.

[45] J. Des Cloizeaux, *Orthogonal Orbitals and Generalized Wannier Functions*, Phys. Rev., 129 (1963), p. 554.

[46] J. Des Cloizeaux, *Analytical Properties of n-Dimensional Energy Bands and Wannier Functions*, Phys. Rev., 135 (1964), pp. A698–A707.

[47] J. Des Cloizeaux, *Energy Bands and Projection Operators in a Crystal: Analytic and Asymptotic Properties*, Phys. Rev., 135 (1964), p. A685.

[48] P. A. M. Dirac, *Note on Exchange Phenomena in the Thomas Atom*, Mathematical Proceedings of the Cambridge Philosophical Society, 26 (1930), p. 376.

[49] G. Dresselhaus, *Spin-Orbit Coupling Effects in Zinc Blende Structures*, Phys. Rev., 100 (1955), p. 580.

[50] G. Dresselhaus, A. F. Kip, and C. Kittel, *Spin-Orbit Interaction and the Effective Masses of Holes in Germanium*, Phys. Rev., 95 (1954), p. 568.

[51] R. J. Elliott, *Theory of the Effect of Spin-Orbit Coupling on Magnetic Resonance in Some Semiconductors*, Phys. Rev., 96 (1954), p. 266.

[52] B. Fisher, J. Genossar, A. Knizhnik, L. Patlagan, and G. M. Reisner, *Electronic transport under high electric fields in Sr_2IrO_4*, Journal of Applied Physics, 101 (2007), p. 123703.

[53] J. Friedel, *The Physics of Metals, Electrons*, in Ziman, J.M. (Ed), Cambridge University Press, Cambridge, 1969.

[54] L. Fu, C. L. Kane, and E. J. Mele, *Topological Insulators in Three Dimensions*, Phys. Rev. Lett., 98 (2007), p. 106803.

[55] A. Georges, *Strongly Correlated Electron Materials: Dynamical Mean-Field Theory and Electronic Structure*, AIP Conference Proceedings, 715 (2004), p. 3.

[56] A. Georges and G. Kotliar, *Hubbard model in infinite dimensions*, Phys. Rev. B, 45 (1992), p. 6479.

[57] A. Georges, G. Kotliar, W. Krauth, and M. J. Rozenberg, *Dynamical mean-field theory of strongly correlated fermion systems and the limit of infinite dimensions*, Rev. Mod. Phys., 68 (1996), p. 13.

[58] A. Georges and W. Krauth, *Numerical solution of the $d = \infty$ Hubbard model: Evidence for a Mott transition*, Phys. Rev. Lett., 69 (1992), p. 1240.

[59] A. Georges and W. Krauth, *Physical properties of the half-filled Hubbard model in infinite dimensions*, Phys. Rev. B, 48 (1993), p. 7167.

[60] D. Grieger and F. Lechermann, *to be published.*

[61] E. Gull, *Continuous-Time Quantum Monte Carlo Algorithms for Fermions*, PhD thesis, ETH Zurich, 2008.

[62] O. Gunnarsson and B. I. Lundqvist, *Exchange and correlation in atoms, molecules, and solids by the spin-density-functional formalism*, Phys. Rev. B, 13 (1976), p. 4274.

[63] H. Hafermann, *Numerical Approaches to Spatial Correlations in Strongly Interacting Fermion Systems*, PhD thesis, Universität Hamburg, Jul. 2009.

[64] M. W. Haverkort, I. S. Elfimov, L. H. Tjeng, G. A. Sawatzky, and A. Damascelli, *Strong Spin-Orbit Coupling Effects on the Fermi Surface of Sr_2RuO_4 and Sr_2RhO_4*, Phys. Rev. Lett., 101 (2008), p. 026406.

[65] L. Hedin, *New Method for Calculating the One-Particle Green's Function with Application to the Electron-Gas Problem*, Phys. Rev., 139 (1965), p. A796.

[66] K. Held, *Electronic structure calculations using dynamical mean field theory*, Advances in Physics, 56 (2007), p. 829.

[67] J. E. Hirsch, *Discrete Hubbard-Stratonovich transformation for fermion lattice models*, Phys. Rev. B, 28 (1983), p. 4059.

[68] J. E. Hirsch, *Erratum: Discrete Hubbard-Stratonovich transformation for fermion lattice models*, Phys. Rev. B, 29 (1984), p. 4159.

[69] J. E. Hirsch and R. M. Fye, *Monte Carlo Method for Magnetic Impurities in Metals*, Phys. Rev. Lett., 56 (1986), p. 2521.

[70] P. Hohenberg and W. Kohn, *Inhomogeneous Electron Gas*, Phys. Rev., 136 (1964), p. B864.

[71] D. Hsieh, D. Qian, L. Wray, Y. Xia, Y. S. Hor, R. J. Cava, and M. Z. Hasan, *A topological Dirac insulator in a quantum spin Hall phase.*

[72] Q. Huang, J. L. Soubeyroux, O. Chmaissem, I. Natali Sora, A. Santoro, R. J. Cava, J. J. Krajewski, and W. F. Peck, *Neutron Powder Diffraction Study of the Crystal Structures of Sr_2RuO_4 and Sr_2IrO_4 at Room Temperature and at $10k$*, Journal of Solid State Chemistry, 112, p. 355.

[73] J. Hubbard, *Electron Correlations in Narrow Energy Bands*, Proc. Roy. Soc. Lond. A, 276 (1963), p. 238.

[74] J. Hubbard, *Electron Correlations in Narrow Energy Bands II. The Degenerate Band Case*, Proc. Roy. Soc. Lond. A, 277 (1964), p. 237.

[75] J. Hubbard, *Electron Correlations in Narrow Energy Bands III. An Improved Solution*, Proc. Roy. Soc. Lond. A, 281 (1964), p. 401.

[76] M. Imada, A. Fujimori, and Y. Tokura, *Metal-insulator transitions*, Rev. Mod. Phys., 70 (1998), p. 1039.

[77] G. Jackeli and G. Khaliullin, *Mott Insulators in the Strong Spin-Orbit Coupling Limit: From Heisenberg to a Quantum Compass and Kitaev Models*, Phys. Rev. Lett., 102 (2009), p. 017205.

[78] M. Jarrell and J. E. Gubernatis, *Bayesian inference and the analytic continuation of imaginary-time quantum Monte Carlo data*, Physics Reports, 269 (1996), p. 133.

[79] H. Jin, H. Jeong, T. Ozaki, and J. Yu, *Anisotropic exchange interactions of spin-orbit-integrated states in Sr_2IrO_4*, Phys. Rev. B, 80 (2009), p. 075112.

[80] R. O. Jones and O. Gunnarsson, *The density functional formalism, its applications and prospects*, Rev. Mod. Phys., 61 (1989), p. 689.

[81] H. Kajueter and G. Kotliar, *New Iterative Perturbation Scheme for Lattice Models with Arbitrary Filling*, Phys. Rev. Lett., 77 (1996), p. 131.

[82] C. L. Kane and E. J. Mele, *Z_2 Topological Order and the Quantum Spin Hall Effect*, Phys. Rev. Lett., 95 (2005), p. 146802.

[83] M. Karolak, G. Ulm, T. Wehling, V. Mazurenko, A. Poteryaev, and A. Lichtenstein, *Double counting in LDA+DMFT – The example of NiO*, Journal of Electron Spectroscopy and Related Phenomena, 181 (2010), p. 11. Proceedings of International Workshop on Strong Correlations and Angle-Resolved Photoemission Spectroscopy 2009.

[84] B. J. Kim, H. Jin, S. J. Moon, J.-Y. Kim, B.-G. Park, C. S. Leem, J. Yu, T. W. Noh, C. Kim, S.-J. Oh, J.-H. Park, V. Durairaj, G. Cao, and E. Rotenberg, *Novel $J_{eff}=\frac{1}{2}$ Mott State Induced by Relativistic Spin-Orbit Coupling in Sr_2IrO_4*, Phys. Rev. Lett., 101 (2008), p. 076402.

[85] B. J. Kim, H. Ohsumi, T. Komesu, S. Sakai, T. Morita, H. Takagi, and T. Arima, *Phase-Sensitive Observation of a Spin-Orbital Mott State in Sr_2IrO_4*, Science, 323 (2009), p. 1329.

[86] B. J. Kim, J. Yu, H. Koh, I. Nagai, S. I. Ikeda, S.-J. Oh, and C. Kim, *Missing xy-Band Fermi Surface in 4d Transition-Metal Oxide Sr_2RhO_4: Effect of the Octahedra Rotation on the Electronic Structure*, Phys. Rev. Lett., 97 (2006), p. 106401.

[87] N. S. Kini, A. M. Strydom, H. S. Jeevan, C. Geibel, and S. Ramakrishnan, *Transport and thermal properties of weakly ferromagnetic Sr_2IrO_4*, Journal of Physics: Condensed Matter, 18 (2006), p. 8205.

[88] Y. Klein and I. Terasaki, *Insight on the electronic state of Sr_2IrO_4 revealed by cationic substitutions*, Journal of Physics: Condensed Matter, 20 (2008), p. 295201.

[89] W. Kohn, *Analytic Properties of Bloch Waves and Wannier Functions*, Phys. Rev., 115 (1959), p. 809.

[90] W. Kohn, *Construction of Wannier Functions and Applications to Energy Bands*, Phys. Rev. B, 7 (1973), p. 4388.

[91] W. Kohn, *Wannier functions and self-consistent metal calculations*, Phys. Rev. B, 10 (1974), p. 382.

[92] W. Kohn and J. R. Onffroy, *Wannier Functions in a Simple Nonperiodic System*, Phys. Rev. B, 8 (1973), p. 2485.

[93] W. Kohn and L. J. Sham, *Self-Consistent Equations Including Exchange and Correlation Effects*, Phys. Rev., 140 (1965), pp. A1133–A1138.

[94] M. Konig, S. Wiedmann, C. Brune, A. Roth, H. Buhmann, L. W. Molenkamp, X.-L. Qi, and S.-C. Zhang, *Quantum Spin Hall Insulator State in HgTe Quantum Wells*, Science, 318 (2007), p. 766.

[95] G. F. Koster, *Localized Functions in Molecules and Crystals*, Phys. Rev., 89 (1953), p. 67.

[96] G. Kotliar, *Landau theory of the Mott transition in the fully frustrated Hubbard model in infinite dimensions*, The European Physical Journal B - Condensed Matter and Complex Systems, 11 (1999), p. 27.

[97] G. Kotliar, E. Lange, and M. J. Rozenberg, *Landau Theory of the Finite Temperature Mott Transition*, Phys. Rev. Lett., 84 (2000), p. 5180.

[98] G. Kotliar, S. Y. Savrasov, K. Haule, V. S. Oudovenko, O. Parcollet, and C. A. Marianetti, *Electronic structure calculations with dynamical mean-field theory*, Rev. Mod. Phys., 78 (2006), p. 865.

[99] G. Kotliar and D. Vollhardt, *Strongly Correlated Materials: Insights from Dynamical Mean-Field Theory*, Physics Today, 57 (2004), p. 53.

[100] L. Laloux, A. Georges, and W. Krauth, *Effect of a magnetic field on Mott-Hubbard systems*, Phys. Rev. B, 50 (1994), p. 3092.

[101] F. Lechermann, A. Georges, A. Poteryaev, S. Biermann, M. Posternak, A. Yamasaki, and O. K. Andersen, *Dynamical mean-field theory using Wannier functions: A flexible route to electronic structure calculations of strongly correlated materials*, Phys. Rev. B, 74 (2006), p. 125120.

[102] M. Levy, *Electron densities in search of Hamiltonians*, Phys. Rev. A, 26 (1982), p. 1200.

[103] X. Li, *All-electron G_0W_0 code based on FP-(L)APW+lo and applications*, PhD thesis, Freie Universität Berlin, Jul. 2008.

[104] A. I. Lichtenstein and M. I. Katsnelson, *Ab initio calculations of quasiparticle band structure in correlated systems: LDA++ approach*, Phys. Rev. B, 57 (1998), p. 6884.

[105] A. I. Lichtenstein, M. I. Katsnelson, and G. Kotliar, *Finite-Temperature Magnetism of Transition Metals: An* ab initio *Dynamical Mean-Field Theory*, Phys. Rev. Lett., 87 (2001), p. 067205.

[106] E. H. Lieb, *Density functionals for Coulomb systems*, Int. J. Quantum Chem., 24 (1983), p. 243.

[107] G.-Q. Liu, V. N. Antonov, O. Jepsen, and O. K. Andersen., *Coulomb-Enhanced Spin-Orbit Splitting: The Missing Piece in the Sr_2RhO_4 Puzzle*, Phys. Rev. Lett., 101 (2008), p. 026408.

[108] G. K. H. Madsen, P. Blaha, K. Schwarz, E. Sjöstedt, and L. Nordström, *Efficient linearization of the augmented plane-wave method*, Phys. Rev. B, 64 (2001), p. 195134.

[109] Y. Maeno, H. Hashimoto, K. Yoshida, S. Nishizaki, T. Fujita, J. G. Bednorz, and F. Lichtenberg, *Superconductivity in a layered perovskite without copper*, Nature, 372 (1994), p. 532.

[110] C. Martins, *Tutorial on* dmftproj, 2011.

[111] N. Marzari and D. Vanderbilt, *Maximally localized generalized Wannier functions for composite energy bands*, Phys. Rev. B, 56 (1997), p. 12847.

[112] A. Messiah, *Mécanique Quantique Volumes I et II*, Dunod, Paris, 1959.

[113] W. Metzner and D. Vollhardt, *Correlated Lattice Fermions in $d = \infty$ Dimensions*, Phys. Rev. Lett., 62 (1989), p. 324.

[114] J. Minár, L. Chioncel, A. Perlov, H. Ebert, M. I. Katsnelson, and A. I. Lichtenstein, *Multiple-scattering formalism for correlated systems: A KKR-DMFT approach*, Phys. Rev. B, 72 (2005), p. 045125.

[115] S. J. Moon, H. Jin, W. S. Choi, J. S. Lee, S. S. A. Seo, J. Yu, G. Cao, T. W. Noh, and Y. S. Lee, *Temperature dependence of the electronic structure of the $J_{eff}=\frac{1}{2}$ Mott insulator Sr_2IrO_4 studied by optical spectroscopy*, Phys. Rev. B, 80 (2009), p. 195110.

[116] S. J. Moon, H. Jin, K. W. Kim, W. S. Choi, Y. S. Lee, J. Yu, G. Cao, A. Sumi, H. Funakubo, C. Bernhard, and T. W. Noh, *Dimensionality-Controlled Insulator-Metal Transition and Correlated Metallic State in 5d Transition Metal Oxides $Sr_{n+1}Ir_nO_{3n+1}$ ($n = 1$, 2, and ∞)*, Phys. Rev. Lett., 101 (2008), p. 226402.

[117] S. J. Moon, M. W. Kim, K. W. Kim, Y. S. Lee, J.-Y. Kim, J.-H. Park, B. J. Kim, S.-J. Oh, S. Nakatsuji, Y. Maeno, I. Nagai, S. I. Ikeda, G. Cao, and T. W. Noh, *Electronic structures of layered perovskite Sr_2MO_4 (M=Ru, Rh and Ir)*, Phys. Rev. B, 74 (2006), p. 113104.

[118] J. Moore, *Topological insulators: The next generation*, Nature Physics, 5 (2009), p. 378.

[119] J. E. Moore and L. Balents, *Topological invariants of time-reversal-invariant band structures*, Phys. Rev. B, 75 (2007), p. 121306.

[120] N. F. Mott, *The Basis of the Electron Theory of Metals, with Special Reference to the Transition Metals*, Proceedings of the Physical Society. Section A, 62 (1949), p. 416.

[121] N. F. Mott and R. Peierls, *Discussion of the paper by de Boer and Verwey*, Proceedings of the Physical Society, 49 (1937), p. 72.

[122] J. Mravlje, M. Aichhorn, T. Miyake, K. Haule, G. Kotliar, and A. Georges, *Coherence-Incoherence Crossover and the Mass-Renormalization Puzzles in Sr_2RuO_4*, Phys. Rev. Lett., 106 (2011), p. 096401.

[123] E. Müller-Hartmann, *Correlated fermions on a lattice in high dimensions*, Zeitschrift für Physik B Condensed Matter, 74 (1989), p. 507.

[124] E. Müller-Hartmann, *The Hubbard model at high dimensions: some exact results and weak coupling theory*, Zeitschrift für Physik B Condensed Matter, 76 (1989), p. 211.

[125] S. Nakatsuji, Y. Machida, Y. Maeno, T. Tayama, T. Sakakibara, J. v. Duijn, L. Balicas, J. N. Millican, R. T. Macaluso, and J. Y. Chan, *Metallic Spin-Liquid Behavior of the Geometrically Frustrated Kondo Lattice $Pr_2Ir_2O_7$*, Phys. Rev. Lett., 96 (2006), p. 087204.

[126] P. Novak, *Calculation of spin-orbit coupling*, 1997 (to be found at http://www.wien2k.at/reg_user/textbooks).

[127] Y. Okamoto, M. Nohara, H. Aruga-Katori, and H. Takagi, *Spin-Liquid State in the S=1/2 Hyperkagome Antiferromagnet $Na_4Ir_3O_8$*, Phys. Rev. Lett., 99 (2007), p. 137207.

[128] R. H. Parmenter, *Symmetry Properties of the Energy Bands of the Zinc Blende Structure*, Phys. Rev., 100 (1955), p. 573.

[129] G. Parzen, *Electronic Energy Bands in Metals*, Phys. Rev., 89 (1953), p. 237.

[130] E. Pavarini, S. Biermann, A. Poteryaev, A. I. Lichtenstein, A. Georges, and O. K. Andersen, *Mott Transition and Suppression of Orbital Fluctuations in Orthorhombic $3d^1$ Perovskites*, Phys. Rev. Lett., 92 (2004), p. 176403.

[131] D. Pesin and L. Balents, *Mott physics and band topology in materials with strong spin-orbit interaction*, Nature Physics, 6 (2010), p. 376.

[132] A. G. Petukhov, I. I. Mazin, L. Chioncel, and A. I. Lichtenstein, *Correlated metals and the LDA+U method*, Phys. Rev. B, 67 (2003), p. 153106.

[133] A. I. Poteryaev, M. Ferrero, A. Georges, and O. Parcollet, *Effect of crystal-field splitting and interband hybridization on the metal-insulator transitions of strongly correlated systems*, Phys. Rev. B, 78 (2008), p. 045115.

[134] L. V. Pourovskii, B. Amadon, S. Biermann, and A. Georges, *Self-consistency over the charge density in dynamical mean-field theory: A linear muffin-tin implementation and some physical implications*, Phys. Rev. B, 76 (2007), p. 235101.

[135] M. V. Rama Rao, V. G. Sathe, D. Sornadurai, B. Panigrahi, and T. Shripathi, *Metal to insulator transition in $Sr_2Ru_{1-x}Ir_xO_4$*, Journal of Physics and Chemistry of Solids, 61 (2000), p. 1989.

[136] J. J. Randall, L. Katz, and R. Ward, *The Preparation of a Strontium-Iridium Oxide Sr_2IrO_4*, Journal of the American Chemical Society, 79 (1957), p. 266.

[137] J. J. Rehr and W. Kohn, *Wannier functions in crystals with surfaces*, Phys. Rev. B, 10 (1974), p. 448.

[138] M. Rozenberg, G. Moeller, and G. Kotliar, *The metal-insulator transition in the hubbard model at zero temperatute II*, Modern Physics Letters B, 8 (1994), pp. 535–543.

[139] M. J. Rozenberg, G. Kotliar, and X. Y. Zhang, *Mott-Hubbard transition in infinite dimensions II*, Phys. Rev. B, 49 (1994), p. 10181.

[140] M. J. Rozenberg, X. Y. Zhang, and G. Kotliar, *Mott-Hubbard transition in infinite dimensions*, Phys. Rev. Lett., 69 (1992), p. 1236.

[141] A. N. Rubtsov, V. V. Savkin, and A. I. Lichtenstein, *Continuous-time quantum Monte Carlo method for fermions*, Phys. Rev. B, 72 (2005), p. 035122.

[142] S. Y. Savrasov and G. Kotliar, *Spectral density functionals for electronic structure calculations*, Phys. Rev. B, 69 (2004), p. 245101.

[143] S. Y. Savrasov, G. Kotliar, and E. Abrahams, *Correlated electrons in δ-plutonium within a dynamical mean-field picture*, Nature, 410 (2001), p. 793.

[144] K. Schwarz, P. Blaha, and G. K. H. Madsen, *Electronic structure calculations of solids using the WIEN2k package for material sciences*, Computer Physics Communications, 147 (2002), p. 71.

[145] T. Shimura, Y. Inaguma, T. Nakamura, M. Itoh, and Y. Morii, *Structure and magnetic properties of $Sr_{2-x}A_xIrO_4$ (A=Ca and Ba)*, Phys. Rev. B, 52 (1995), p. 9143.

[146] A. Shitade, H. Katsura, J. Kunes, X.-L. Qi, S.-C. Zhang, and N. Nagaosa, *Quantum Spin Hall Effect in a Transition Metal Oxide Na_2IrO_3*, Phys. Rev. Lett., 102 (2009), p. 256403.

[147] A. V. Shubnikov, *Symmetry and Antisymmetry of Finite Figures*, USSR Academy of Sciences, Moscow, 1951.

[148] D. J. Singh, *Ground-state properties of lanthanum: Treatment of extended-core states*, Phys. Rev. B, 43 (1991), p. 6388.

[149] D. J. Singh, *Planewaves, Pseudopotentials and the LAPW Method*, Kluwer Academic Publishers, Norwell, Massachusetts, USA, 1994.

[150] E. Sjöstedt, *Augmented Planewaves, Developments and Applications to Magnetism*, PhD thesis, Uppsala University, 2002.

[151] E. Sjöstedt, L. Nordstrm̈, and D. J. Singh, *An alternative way of linearizing the augmented plane-wave method*, Solid State Communications, 114 (2000), p. 15.

[152] J. C. Slater, *An Augmented Plane Wave Method for the Periodic Potential Problem*, Phys. Rev., 92 (1953), p. 603.

[153] J. C. Slater, *Quantum Theory of Atomic Structure, Vol. II*, McGraw-Hill Book Company, Inc., 1960.

[154] I. I. Sobelman, *Atomic Spectra and Radiative Transitions*, 2^{nd} edition Springer-Verlag, Berlin Heidelberg New York, 1992.

[155] I. Souza, N. Marzari, and D. Vanderbilt, *Maximally localized wannier functions for entangled energy bands*, Phys. Rev. B, 65 (2001), p. 035109.

[156] M. A. Subramanian, M. K. Crawford, R. L. Harlow, T. Ami, J. A. Fernandez-Baca, Z. R. Wang, and D. C. Johnston, *Sr_2RhO_4 and Sr_2IrO_4: Structural and magnetic studies of 4d and 5d transition metal analogs of La_2CuO_4*, Physica C: Superconductivity, 235 (1994), p. 743.

[157] S. Sugano, Y. Tanabe, and H. Kamimura, *Multiplets of Transition-Metal Ions in Crystal*, Academic Press, New York, 1970.

[158] J. Tomczak, *Spectral and Optical Properties of Correlated Materials*, PhD thesis, Ecole Polytechnique, 2007.

[159] M. Tovar, K. S. Raman, and K. Shtengel, *Dzyaloshinskii-Moriya interactions in valence-bond systems*, Phys. Rev. B, 79 (2009), p. 024405.

[160] U. von Barth and L. Hedin, *A local exchange-correlation potential for the spin polarized case I*, Journal of Physics C: Solid State Physics, 5 (1972), p. 1629.

[161] N. V. Vugman and S. R. Nogueira, *Spin-orbit coupling constant in divalent iridium*, Revista Brasileira de Fisica, 19 (1989), p. 606.

[162] I. Žutić, J. Fabian, and S. Das Sarma, *Spintronics: Fundamentals and applications*, Rev. Mod. Phys., 76 (2004), p. 323.

[163] G. H. Wannier, *The Structure of Electronic Excitation Levels in Insulating Crystals*, Phys. Rev., 52 (1937), p. 191.

[164] H. Watanabe, T. Shirakawa, and S. Yunoki, *Microscopic Study of a Spin-Orbit-Induced Mott Insulator in Ir Oxides*, Phys. Rev. Lett., 105 (2010), p. 216410.

[165] P. Werner, A. Comanac, L. de' Medici, M. Troyer, and A. J. Millis, *Continuous-Time Solver for Quantum Impurity Models*, Phys. Rev. Lett., 97 (2006), p. 076405.

[166] R. Winkler, *Spin-Orbit Coupling Effects in Two-Dimensional Electron and Hole Systems*, Springer-Verlag, Berlin Heidelberg, 2003.

Couplage Spin-Orbite et Interaction de Coulomb dans l'Iridate de Strontium Sr_2IrO_4

Thèse de Doctorat en Physique des Matériaux et des Milieux Denses — Cyril Martins

Résumé

Cette thèse s'intéresse à l'interaction entre le couplage spin-orbite et les corrélations électroniques dans la matière condensée. En effet, de plus en plus de matériaux – tels que les isolants topologiques ou les oxydes de métaux de transition 5d à base d'iridium – présentent des propriétés pour lesquels l'interaction spin-orbite joue un rôle essentiel. Parmi eux, l'iridate de strontium (Sr_2IrO_4) a récemment été décrit comme un "*isolant de Mott régi par les effets spin-orbite*": dans cette image, l'interaction de Coulomb entre les électrons et le couplage spin-orbite ($\zeta_{SO} \approx 0.4$ eV) se combinent pour rendre le composé isolant.

Nous avons étudié la phase isolante paramagnétique de ce matériau avec l'approche LDA+DMFT, une méthode qui combine la théorie de la fonctionnelle de la densité dans l'approximation de la densité locale (LDA) avec la théorie du champ moyen dynamique (DMFT). Sr_2IrO_4 s'est avéré être un isolant de Mott pour une valeur raisonnable des corrélations électroniques ($U = 1,4$ eV) une fois que le couplage spin-orbite et les distorsions structurales du cristal ont été pris en compte. En outre, nos résultats mettent en évidence les rôles respectifs joués par ces deux éléments dans l'obtention d'un état isolant et montrent que *seule leur action conjointe* permet d'ouvrir un gap de Mott dans un tel composé.

Afin de réaliser cette étude, le couplage spin-orbite a dû être inclus au sein du formalisme LDA+DMFT – plus précisément, dans la définition des orbitales de Wannier sur lequel le problème local d'impureté repose. L'intérêt d'un tel développement technique dépasse le cas de Sr_2IrO_4, cette implémentation, dite "*LDA+SO+DMFT*", pouvant être aussi utilisée pour prendre en compte les corrélations électroniques dans d'autres oxydes de métaux de transition $5d$ ou même au sein des isolants topologiques.

* * *

Interplay of Spin-Orbit Coupling and Electronic Coulomb Interactions in Strontium Iridate Sr_2IrO_4

Abstract

In this thesis, we were interested in the interplay between the spin-orbit coupling and electronic correlations in condensed matter physics. The spin-orbit interaction has indeed been found to play a significant role in the properties of a growing variety of materials, such as the topological band insulators or the iridium-based $5d$-transition metal oxides. Particularly, strontium iridate (Sr_2IrO_4) was recently described as a "*spin-orbit driven Mott insulator*": according to this picture, the cooperative interaction between electronic Coulomb interactions and the spin-orbit coupling ($\zeta_{SO} \approx 0.4$ eV) can explain the insulating state of the compound.

We have studied the paramagnetic insulating phase of this material within LDA+DMFT, a method which combines the density functional theory in the local density approximation (LDA) with dynamical mean-field theory (DMFT). Sr_2IrO_4 was found to be a Mott insulator for a reasonable value of the electronic correlations ($U = 1.4$ eV) once both the spin-orbit coupling and the lattice distortions were taken into account. Moreover, our results highlight the respective roles played by theses two features to reach the Mott insulating state and emphasize that *only their acting together* may open the Mott gap in such a compound.

In order to perform this study, the spin-orbit interaction was included in LDA+DMFT – more precisely, to define the Wannier orbitals on which the local impurity problem is based. The interest of such a technical development goes beyond the present case of Sr_2IrO_4 since this "*LDA+SO+DMFT implementation*" could be also used to take into account the electronic correlations in the description of other $5d$-transition metal oxides or even topological band insulators.

CPhT Ecole Polytechnique – Novembre 2010